To the Graduate Council:

I am submitting herewith a dissertation written by Prabhjot Mehta entitled "A Study of the Factors Influencing the Morphology of Diamond Thin Films Grown via Hot Filament Chemical Vapor Deposition." I have examined the final copy of this dissertation for form and content and recommend that it be accepted in partial fulfillment of the requirements for the degree of Doctor of Philosophy, with a major in Chemistry.

Charles S. Feigerle, Major Professor

We have read this dissertation
and recommend its acceptance:

Robert E. Clausing

Frederick A. Grimm

Robert N. Compton

Ziling B. Xue

David C. Joy

Accepted for the Council:

Associate Vice Chancellor and
Dean of The Graduate School

A STUDY OF THE FACTORS INFLUENCING THE MORPHOLOGY OF DIAMOND THIN FILMS GROWN VIA HOT FILAMENT CHEMICAL VAPOR DEPOSITION

A Dissertation

Presented for the

Doctor of Philosophy

Degree

The University of Tennessee, Knoxville

Prabhjot Mehta

August 1997

Acknowledgments

There are many people at the University of Tennessee and at Oak Ridge National Laboratory to whom I am grateful for making this study so rewarding. I have benefited greatly from knowing the faculty and graduate students in the Chemistry Department over the last four years and appreciate their friendship and help. I am particularly grateful to my research advisors Charles S. Feigerle and Robert E. Clausing for their guidance and encouragement throughout the course of this study.

There are other people whose assistance I must acknowledge. I would like to thank Lee Heatherly helped me with the experimental set up in the laboratory. I have received help from Thomas Thundat with Atomic Force Microscopy observations and Dorothy Coffey with Scanning Electron Microscopy for which I am very grateful. Sincere thanks to Anna Edwards for Raman Spectroscopy measurements and Robert Shaw for many suggestions and discussions as well as for making the neutron activation analysis possible. Cathy Cheverton has helped me with the manuscript for the dissertation and her help is very much appreciated.

Lastly, I would like to thank my parents for giving me the chance to pursue this study, my sister and brother-in-law for their constant affection, my friend Sudha Chidambaram for her support and my husband, Vinod for his immense patience and love.

Abstract

In this study the morphology of hot filament chemical vapor deposited diamond films as a function of growth parameters was investigated. Morphological studies are needed for a complete understanding of growth mechanisms responsible for diamond growth, which is still in the stages of development. These studies are needed in order to make the important connection between the extreme properties and various applications of CVD diamond films.

The effects of filament material, substrate temperature, methane concentration and addition of nitrogen to the input gas mixture were investigated. The films were deposited in a hot filament reactor and characterized using scanning electron microscopy. Atomic force microscopy was used to quantitatively analyze some of the growth features. High index planes, belonging to the {221} and {331} family of planes, were found to comprise a hopper shaped {111} "face", which is observed within a narrow range of growth parameters.

Rhenium, tungsten and tantalum filaments were used to investigate the possible effect of filament material on morphology. It was found that the contamination levels from the filament varied dramatically even when the filaments were used under identical conditions. Quantitative determination of the metal content in the films was carried out by neutron activation analysis. The filament material did not appear to affect the morphology or the growth rate of the growing film.

Diamond crystals with octahedral, cubo-octahedral and cube geometry were grown by various combinations of growth parameters. A morphology map was generated for the reactor using different concentrations of methane (0.5-1.5 %) and varying the substrate temperature (536-1140 °C). Such maps have been generated for microwave plasma enhanced CVD before and are very useful in controlling film morphology and thereby film properties. It was found that the growth rates in the various crystallographic directions differ in their dependence on the growth parameters, which supports the arguments that growth on different faces takes place by different mechanisms. Baseline morphology maps become essential if the effect of another parameter is to be studied. The effect of addition of nitrogen was studied by the addition of ammonia to the input gas mixture. The addition of nitrogen (N/C ~1/6) showed a dramatic effect on the crystal morphology. The extent of the effect was found to depend on the region of morphology map that was being studied. Addition of ammonia was found to increase the overall growth rate and decrease the growth rate ratio. The increase in the growth rate was much higher in the [111] direction than in the [100] direction. These morphological studies are important not only for understanding the mechanisms involved in growth but also for realizing the full extent of the properties of CVD diamond for various applications.

Table of Contents

Part 1: Introduction

General introduction to diamond 2

(1) Carbon and its phases 2

(2) Techniques for diamond growth 3

(I) Physical crystallization 3

(ii) Chemical crystallization 4

(iii) Activated chemical crystallization 5

(3) Current methods for diamond growth 7

(4) Hot filament chemical vapor deposition 9

Introduction to morphology 12

(1) Morphology: definition and meaning with reference to context 12

(2) Theory of crystal growth 12

(I) Surface free energy 15

(ii) Growth of a perfect crystal 17

(iii) Growth of an imperfect crystal 20

(iv) Periodic Bond Chain theory 22

(3) Morphology: General understanding in the case of diamond 23

(4) Chemical vapor deposition of diamond 29

(5) Control of Morphology in CVD grown material and the layout of this theses 30

References 34

Part 2: Experimental set-up

Film growth 42

(1) HFCVD reactor 42

(2) Residual gas analysis (RGA) 42

Characterization techniques 47

(1) Scanning electron microscopy 47

(2) Atomic force microscopy 48

Part 3: The effect of filament material on the quality of diamond films deposited via HFCVD

Introduction 52

Experimental 58

(1) Filament preparation (carburization) 60

(I) Tungsten 60

(ii) Rhenium 60

(iii) Tantalum 61

Results and Discussion 66

(1) Effects of filament material 66

(2) Growth morphology trends as a function of substrate temperature for W and TaC filaments 74

(3) Filament temperature 82

(4) Filament distance 82

Summary of results 86

Conclusions 87

References 89

Part 4: Growth morphology of hot filament chemical vapor deposited diamond films

Introduction 95

Experimental 99

Results and Discussion 101

(1) Overall growth rate 111

(2) Growth rate ratios 111

(3) Growth rates in the [100] and [111] directions 119

(4) Twinning 126

(5) Texture 129

Conclusions 129

References 130

Part 5: Indexing the hopper shaped {111} face produced in chemical vapor deposited diamond films

Introduction 133

Experimental 135

Results and Discussion 137

Conclusions 146

References 148

Part 6: A study of the effects on growth morphology of polycrystalline HFCVD diamond films due to the addition of ammonia in the input gas mixture

Introduction 152

Experimental 164

Results and Discussion 166

(1) Morphology analysis 166

(I) Film deposition at conventional filament temperatures 166

(a) Addition of air 166

(b) Addition of N_2 167

(ii) Growth at high filament temperatures 168

(a) Addition of varying amounts of ammonia 168

(b) Addition of ammonia to three different methane concentrations 168

(iii) General observations on nitrogen effect on morphology 176

(iv) Analysis of growth rates 184

(v) Growth rates in <100> and <111> directions 192

(2) RGA analysis 201

(3) Raman analysis 206

Conclusions 210

Future direction 210

References 211

Appendix

A1. Diamond Lattice showing a unit cell 217

A2. Diamond lattice showing the formation of a twin on a (111) plane 218

A3. Some characteristics of diamond chemical crystallization from an activated vapor phase 219

A4. RGA data for the addition of ammonia to 1.5% methane in hydrogen gas mixture using a TaC filament at ~2400 °C and substrate temperature ~915 °C 220

A5. RGA data for 0.5-1.5 % methane concentration with the addition of ammonia at different substrate temperatures using a TaC filament at ~2400 °C 223

List of Tables

Table		Page
	Part 1: Introduction	
1.	Some Anisotropic Properties of Diamond Single Crystals	13
	Part 3: The effect of filament material on the quality of diamond films deposited via HFCVD	
1.	Comparison between the three filaments used for growing diamond films under identical conditions	67
2.	The neutron activation data for the films grown with the three different filaments under identical growth conditions	71
3.	The neutron activation data for additional films grown at ~2400 °C filament temperatures and with the addition of NH_3 and O_2	71
4.	Growth conditions of films grown with a WC filament	75
5.	Growth conditions of films grown with a TaC filament	76
6.	Growth conditions used to study effect of the filament temperature on the morphology of the films	83
	Part 4: Growth morphology of hot filament chemical vapor deposited diamond films	
1.	Growth conditions used, growth rates and growth rate ratios observed for depositions with 0.5% methane concentrations	102
2.	Growth conditions used, growth rates and growth rate ratios observed for depositions with 1.0% methane concentrations	103

Table Page

3. Growth conditions used, growth rates and growth rate ratios observed for depositions with 1.5% methane concentrations 103

Part 5: Indexing the hopper shaped {111} face produced in chemical vapor deposited diamond films

1. Growth conditions used for observing the appearance of hoppered {111} faces 138
2. Comparison of the calculated and measured angles between planes comprising the hopper shaped {111} face 145

Part 6: A study of the effects on growth morphology of polycrystalline HFCVD diamond films due to the addition of ammonia in the input gas mixture

1. Addition of air to 1.0% methane in hydrogen gas mixture 166
2. Addition of 1.43% air to 1.0% methane in hydrogen gas mixture at filament temperature ~ 1950°C 167
3. Addition of N_2 to a 1.0% methane in hydrogen gas mixture 169
4. Addition of NH_3 to 1.5 % methane in hydrogen gas mixture for substrate temperature of ~915 °C 169
5. Addition of NH_3 to 0.5 % methane in hydrogen gas mixture 173
6. Addition of NH_3 to 1.0 % methane in hydrogen gas mixture 174
7. Addition of NH_3 to 1.5 % methane in hydrogen gas mixture 175
8. Addition of N_2 to different methane concentrations 196
9. Comparison of the addition of NH_3 and N_2 202

List of figures

Figure		Page
	Part 1: Introduction	
1.	Thermodynamic equilibria in the diamond-hydrogen system	6
2.	Pressure-temperature diagram showing regions producing characteristic growth forms	11
3.	Surface of a crystal at low temperature, showing a kink, A, at a step	18
4.	Unit cell of diamond	24
5.	Idealized growth morphologies for natural, synthetic CVD grown and synthetic HPHT grown diamond single crystals	26
6.	Different faces and axes in various crystal geometries of diamond crystals	26
7.	The cubo-octahedral shapes which result as the ratio of growth velocity in the <100> to that in <111> directions	27
	Part 2: Experimental set-up	
1.	A hot filament chemival vapor deposition reactor	43
2.	A schematic of the quartz tube reactor used for hot filament CVD depositions if diamond films	44
3.	A schematic of the experimental set up used for growing polycrystalline diamond films	46
4.	Block diagram for Tapping mode operation of an Atomic Force Microscope	49

Figure Page

Part 3: The effect of filament material on the quality of diamond films deposited via HFCVD

1. Scanning electron micrographs showing the surface and cross section of a WC filament 62
2. Scanning electron micrograph of a Re filament 64
3. Scanning electron micrograph of a TaC filament 65
4. Scanning electron micrographs of films grown using three different filaments 68
5. Raman spectra of the films grown under identical growth conditions using different filaments 73
6. Scanning electron micrographs of films grown using a WC filament 77
7. Scanning electron micrographs of films grown using a TaC filament 80
8. Scanning electron micrographs of the films using a WC filament 84
9. Vapor pressure of Re, W and Ta 90
10. Phase diagram of C-Ta system 91
11. Phase diagram of C-W system 91

Part 4: Growth morphology of hot filament chemical vapor deposited diamond films

1. Scanning electron micrographs of crystals showing a wide range of growth rate ratios 104
2. Scanning electron micrographs showing the {111} penetration twins 107

Figure Page

3. The Scanning electron micrograph of {111} and {100} penetration twins 109
4. Scanning electron micrographs showing contact twins 112
5. Growth rate as a function of substrate temperature for different levels of methane concentrations used 114
6. Growth rate ratio as a function of substrate temperature for different methane concentrations 115
7. An Isomorphic map for the HFCVD reactor 118
8. Overall growth rate and growth rates in the [100] and [111] directions as a function of substrate temperature for 0.5% methane concentrations 120
9. Overall growth rate and growth rates in the [100] and [111] directions as a function of substrate temperature for 1.0% methane concentrations 121
10. Overall growth rate and growth rates in the [100] and [111] directions as a function of substrate temperature for 1.5% methane depositions 122
11. A plot of growth rate in the [111] direction as a function of substrate temperature for different methane concentrations 124
12. A plot of growth rate in the [100] direction as a function of substrate temperature for the different methane concentrations 125

Figure Page

Part 5: Indexing the hopper shaped {111} face produced in chemical vapor deposited diamond films

1. An electron micrograph of a hopper shaped feature formed on a (111) face 138
2. Scanning electron micrographs of a film grown at filament temperature 2120° C 139
3. Scanning electron micrographs of a film grown at filament temperature 2020 °C 139
4. Scanning electron micrographs of a film grown at filament temperature 1980 °C 139
5. Scanning electron micrographs of a film grown using filament temperature 2100 °C and substrate temperature 1100 °C 141
6. Scanning electron micrographs of a film using filament temperature 2020 °C and substrate temperature 1030 °C 141
7. A tapping mode AFM image of a hopper shaped feature 142
8. The standard (001) projection of a cubic crystal 144
9. A schematic of a hopper shaped face 147

Part 6: A study of the effects on growth morphology of polycrystalline HFCVD diamond films due to the addition of ammonia in the input gas mixture

1. Scanning electron micrographs of films deposited with varying concentrations of NH_3 170

Figure Page

2. Scanning electron micrographs of films deposited with the addition of 0.08 % NH_3 to 0.5 % input CH_4 in H_2 gas mixtures 177
3. Scanning electron micrographs of films deposited with the addition of 0.17 % NH_3 to 1.0 % input CH_4 in H_2 gas mixtures 181
4. Scanning electron micrographs of films deposited with the addition of 0.26 % NH_3 to 1.5 % input CH_4 in H_2 gas mixtures 185
5. The effect on the growth rate, g, as a function of substrate temperature with the addition of 0.08 % NH_3 to 0.5 % input CH_4 in H_2 gas mixtures 189
6. The effect on the growth rate, g, as a function of substrate temperature with the addition of 0.17 % NH_3 to 1.0 % input CH_4 in H_2 gas mixtures 190
7. The effect on the growth rate, g, as a function of substrate temperature with the addition of 0.26 % NH_3 to 1.5 % input CH_4 in H_2 gas mixtures 191
8. The effect of addition of NH_3 on growth rate ratio for different methane concentrations at different substrate temperatures 195
9. Scanning electron micrographs of films deposited with the addition of N2 to different input CH_4 in H_2 gas mixtures 197
10. Comparison of the effect of addition of NH_3 and N_2 growth rates and growth rate ratios for different CH_4 concentrations 203
11. Change in the RGA peak intensities as a function of NH_3 concentration 205

Figure Page

12. Raman data reveals that the films grown with more than 830 ppm NH_3 showed a deterioration in crystalline quality of the films 207

13. Raman spectra of the films grown with 0.5% methane, with and without NH_3 addition, at different substrate temperatures 208

14. Raman spectra of the films grown with 0.5%, 1.0% and 1.5% methane, with and without NH_3 addition, at the intermediate substrate temperature ~980°C 209

Part 1 : Introduction

General introduction to diamond

(1) Carbon and its phases

Carbon is known to exist in three phases having different atomic arrangements. These are diamond (cubic and lonsdaleite), graphite (hexagonal and rhombohedral), and fullerenes. Cubic diamond is a metastable phase at pressures below 13,800 atm. Diamond is a tetrahedrally bonded carbon phase with framework of single sp^3 bonds coupling the carbon atoms such that the angle between these bonds is 109°28'. Both of these crystal lattices, cubic and lonsdaleite, have four nearest neighbors, and are polytypes differing in the stacking of the atomic planes. The graphite polytypes are built from flat hexagonal framework. In this framework, carbon atoms are bonded to three other carbon atoms by strong collective sp^2-π-bonds. The average strength of the carbon-carbon bond in graphite is 108 kcal/mol and the interatomic distance 1.42 Å, for diamond these values are 83 kcal/mol and 1.54 Å respectively. However, in graphite, strong inter atomic bonding is realized only in the plane of the hexagonal network. Interplanar van der Waals interaction gives rise to an equilibrium interplanar spacing of 3.35 Å in the direction perpendicular to these hexagonal planes. Carbon atoms in fullerene molecules are believed to have carbon bonding which is an angularly stressed combination of sp^2 and sp^3 bonds.

The thermodynamically most stable solid phase of carbon, at ordinary conditions of temperature and pressure, is graphite. The deposition of diamond in chemical vapor deposition processes occurs within the thermodynamic metastability region. The surface phase diagram of diamond is not yet known completely i.e. some phase changes are known in vacuum and hydrogen.

However, it has been established [1] that diamond can be deposited as a metastable phase up to rather high temperatures such as 1200°C.

(2) Techniques for diamond film growth

Spitsyn [2] has discussed the techniques for diamond film growth from a historical perspective. These techniques can be divided into three categories, (a) Physical crystallization, (b) Chemical crystallization, and (c) Activated chemical crystallization.

(i) Physical crystallization

Physical crystallization [3] is understood to be the crystalline state terminated by phase transition between the crystallization medium and the growing crystals with conservation of the chemical content at both sides of the crystallization boundary. Physical crystallization can take place at the interface between a vapor and a solid, or a liquid and a solid or between two solids. Physical crystallization of diamond via the interaction of a seed diamond surface with a carbon vapor giving condensation in the diamond structure has been discussed by Spitsyn [2]. The arguments imply that growth of diamond by graphite vaporization and subsequent carbon condensation is hardly probable. However, if the carbon atoms or ions are excited before becoming attached to the surface, then the bonding of these electronically excited atoms usually leads to the deposition of diamond-like carbon films [4,5], which are composed of sp^2 and sp^3 bonded carbon atoms with no long range order.

(ii) Chemical crystallization

In chemical crystallization, the chemical content of the crystallization medium is different from that of the growing crystal. According to Spitsyn [2], the growth of diamond on diamond seed crystalline was accomplished in the 1950's by researchers at the Union Carbide Corporation in the United states [6,7]. The basic idea was the thermal decomposition of methane and other simple methyl-containing organic compounds. These depositions were carried out in the pressure and temperature ranges of 10^{-4} to 100 atm and 600 to 1600° C, respectively. At about the same time Spitsyn [8] and co-workers in the former Soviet Union had proposed similar approach. Growth of solid diamond was also carried out, in the pressure and temperature ranges of 10^{-3} torr to 2.3 atm and 700 to 1600° C respectively, by isothermal decomposition of methyl containing organic compounds [9], methane and methane-hydrogen mixtures [10,11], ethylene [12], metal-organics and other vapor media [13,14]. Different methods (such as an optical furnace, radio-frequency induction, resistive furnace, and laser heating) were used for heating the diamond seed crystals. Diamond films were grown on (111) face of diamond single crystal at temperatures in the range 700-850° C at pressures of up to 2.3 atm by chemical decomposition of pure methane [15]. The main efforts of first researchers were directed to an investigation of the kinetics of the growth on the surface of the seed diamond particles [2]. The isothermal chemical crystallization of diamond is characterized by (a) low linear growth rates, and (b) co-deposition of non-diamond carbon along with diamond-film growth. As proposed by Spitsyn [2], the interaction of non diamond and diamond phases with the vapor phase is the main reason for selective growth of diamond without graphite co-deposition. The growth rates of diamond and graphite obtained by the decomposition of hydrocarbon-precursor

may be the same order of magnitude but the reactivities of diamond and graphite with etching agents differ drastically. Thus in a mixture of carbon containing compounds serving as growth precursors and active etchants the net processes can favor a positive growth rate of diamond and etching of graphite.

(iii) Activated chemical crystallization

The activation energy for the formation of diamond by the thermal decomposition of methane has been reported [9, 15] as 58 and 56 kcal mol^{-1} respectively. This implies that the isothermal crystallization of diamond by the heterogeneous decomposition of carbon containing molecules to elemental carbon in the form of diamond at the growing diamond surface requires rather high activation energy resulting in rather low growth rates, e.g. 5.2 X 10^{-3} nm sec^{-1} [9].

Figure 1 [2] shows the thermodynamic equilibrium in the diamond-hydrogen system in the 500-1500 K range and in the graphite-hydrogen system in the 1500-3000 K range, at a total pressure of 10^{-2} atm. The equilibrium content of the vapor phase near the surface of the graphite source of carbon was calculated by methods of chemical thermodynamics [16]. According to this data then, for the graphite-hydrogen system at T > 1500 K, the most prevalent species in the vapor phase at equilibrium are molecular hydrogen, atomic hydrogen, acetylene, and ethenyl. With the idea of achieving better growth rates, Spitsyn [17] proposed using products of high temperature equilibrium reactions between graphite and hydrogen as carbon containing precursors for diamond crystallization. This high thermal gradient chemical transport reaction for the chemical crystallization of diamond from an activated vapor phase was the first and simplest to be proposed, as discussed by Spitsyn [2]. In the high

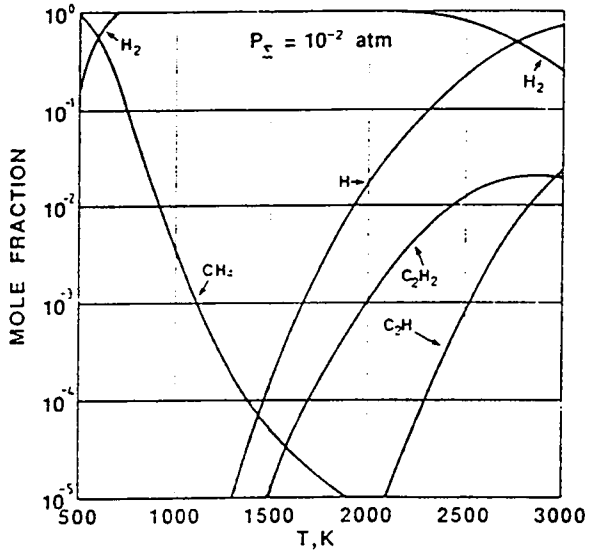

Figure 1 : Thermodynamic equilibria in the diamond-hydrogen system in the 500-1500 K range and in the graphite-hydrogen system in the 1500-3000 K range, at a total pressure of 10^{-2} atm. [Source : B. V. Spitsyn, in *Handbook of Crystal Growth*, edited by D. T. J. Hurle, Vol. **3**, 403 (1994)]

temperature high pressure set up proposed by Spitsyn [2], due the narrow gap between the diamond and graphite surfaces and high rates of diffusion at high temperatures, the active gas medium near the diamond surface is nearly identical to that near the graphite surface. This mixture of very active components can exist only because of permanent generation of active gas at the graphite source. Spitsyn [2] and co-workers were able to obtain the first epitaxial diamond film with growth rate of 1 μ/hr under the above mentioned conditions of special chemical transport reaction. Other methods were proposed and used with favorable results [18] in which epitaxial and polycrystalline films were produced.

(3) Current methods for diamond film growth

The present methods of diamond growth rely on various techniques for the generation of an active vapor phase. The most widely used techniques for growing diamond at low pressures can be conveniently divided into three basic categories [19] : hot filament chemical vapor deposition (HFCVD); high frequency plasma assisted chemical vapor deposition (PACVD), and DC plasma discharge. Hybrid techniques have also been used . A detailed account of the various techniques has been presented by Spitsyn [2]. Appendix lists the growth characteristics of various techniques.

In HFCVD a filament at 2000 to 2800 °K is used to dissociate gas mixtures containing 0.2% to 2.0% CH_4 in H_2, typically at about 6000 Pa but also up to atmospheric pressure. Hydrogen is dissociated by the filament thermally as well as catalytically. H• reacts with CH_4 via hydrogen abstraction reactions to form CH_3, CH_2 etc. which also condense to form C_2H_2. Filaments

of W, Ta, Mo, and Re have been used to produce diamond [20]. The filament is typically placed within 1 cm of the substrate surface and thus radiatively heats the substrate. Many experimental set ups have the capability of controlling the substrate temperature independent of the filament.

In PACVD [21-25] power at 2.45 GHz is coupled to a plasma in a small diameter tube within a waveguide or cavity. Diamond is deposited on an electrically floating substrate at about 40 torr pressure under gas phase compositions similar to the hot filament process. Substrate temperature is determined by the power density and the placement of the substrate. Independent heating or cooling of the substrate may be added to increase the versatility of the apparatus. Microwave and RF methods in which the substrate is removed from the plasma have been reported [26, 27]. Diamonds have also been grown in microwave discharges in a magnetic field, under conditions where electron-cyclotron resonance is considered modified by collisions. These "magneto-microwave" plasmas can have significantly higher densities and electron energies than isotropic plasmas and can be used to deposit diamond over large areas [28].

A stabilized DC plasma arc has produced growth rates of 20 μm/hr at the anode [29]. Only graphitic deposits formed at the cathode. DC glow discharges [30] and DC plasma jet [31] methods for producing diamond have also been used. Diamond has also been produced in transient experiments, for example, by irradiation of C_2H_2 in H_2 [32-34] with focused ArF excimer laser pulses at 193 nm.

Large number of methods have been utilized for the deposition of diamond. In the "thermal methods" such as the HFCVD, thermal plasmas and

the DC plasma jet the temperatures of the neutrals and the electrons are roughly equal and are much greater than the substrate temperature. In microwave plasmas and DC glow discharges however the electron temperature is typically much greater than the neutral and the substrate temperature. Yet both thermal and nonthermal methods produce diamond, although the highest rates have been achieved with the thermal methods.

Atomic hydrogen is used in all of these processes. It is believed to prevent surface reconstruction, suppress the formation of unsaturated carbon nuclei, and etches any graphitic nuclei that may form [19]. Dissociation of the carbon containing source gas is common to all these processes. However, significant ionization does not appear to be critical because there is little ionization in the hot filament method. Substrate temperatures are quite important and must be high enough (~550 °C) to impart mobility to adsorbed surface species.

4. Hot filament chemical vapor deposition (HFCVD)

The simplest and standard method for epitaxial and polycrystalline diamond growth is, perhaps, the hot-filament method. Simple set up and easy control of the growth parameters probably makes it so popular. General aspects of this technique have already been discussed above.

It is believed that the first stage of reactions is the conversion of methane into methyl radicals by its reaction with atomic hydrogen. In most cases, this process, leads to a high concentration of methyl radicals in the vapor phase. Secondary reactions resulting in the production of acetylene are also comparable to methyl radical concentrations. For the hot filament system, the

vapor phase gas composition in the reactor and near the growing surface depends on several parameters [36]. Most significant are : (a) gas phase content, (b) pressure, (c) level of gas phase excitation (or its average temperature), (d) gas flow rate in the activated zone, (e) gas flow near the growing surface, laminar or turbulent. The substrate temperature affects the growth kinetics and the crystallite orientation on the growing diamond surface. The irradiation of the substrate by electrons or photons and impurities in the vapor phase can also have major kinetic effects [2].

This dissertation presents a study of diamond growth via HFCVD. Within the region of metastability, there exist regions corresponding to different crystalline morphologies of diamond, as is shown in fig. 2. The next section outlines the introduction to and the importance of morphology in crystal growth. Various parameters affecting the growth process and morphology were investigated under this study. Part 2 describes the experimental method in detail and the various techniques used for characterization purposes. The effect of the changes in growth parameters on morphology can provide both; practical information leading to improved processes and materials, and, important insight into the growth mechanisms responsible for diamond growth. Parts 3,4,5 and 6 describe the experiments that were conducted to study the various factors affecting diamond film depositions. These parts are treated as separate topics each with its own introduction, experimental, results, discussion, conclusions and references, however, they are strongly interrelated and each builds on the preceding work.

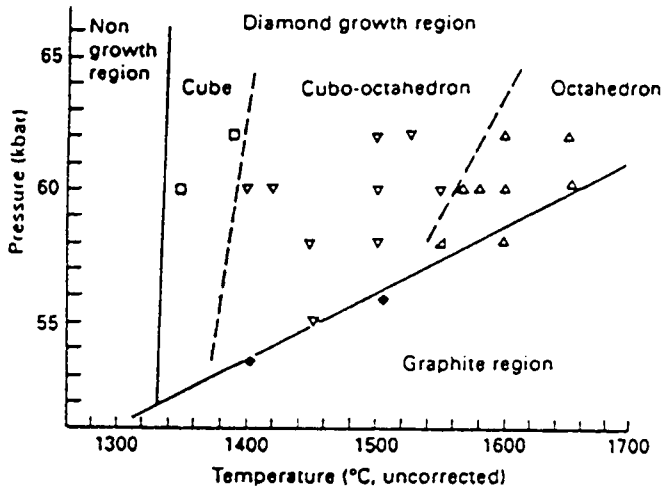

Figure 2 : Pressure-temperature diagram showing regions producing characteristic growth forms. [Source : R. E. Clausing, in *Industrial and Scientific Handbook on Diamond,* edited by M. Prelas, G. Popovici, L. K. Bigelow, Marcell Dekker publisher (to be published in summer '97)].

Introduction to morphology

(1) Morphology : definition and meaning with reference to context

Morphology used in this context has been defined [37] as the internal and external form and structure of diamond material, either as a single crystal or polycrystalline assembly. The understanding of morphology is especially important for a material such as diamond, which is known for it's excellent mechanical, physical and chemical properties, because of the anisotropic nature of its properties (table 1). Since it is impossible to change the structure of diamond once it is produced, one has to control the morphology during growth in order to optimize the properties of material. Morphology can be discussed quantitatively in terms of the quality and the rate of crystal growth in various crystallographic directions of the basic cubic crystal structure of diamond. These, the quality and the growth rates, have strong dependence on the growth conditions. The study of diamond crystal morphology as a function of the growth conditions, is not only expected to give control of the form and structure of the growing crystalline material, but more importantly, give useful insight into the growth mechanisms responsible for diamond growth. In order to correlate the growth features in the form of crystal morphology to the mechanism of growth of the crystal, one must, begin with the basic principles of crystal growth [38].

(2) Theory of crystal growth

Most substances form crystals in three general ways, by slow solidification from (a) solution, (b) liquid melts, (c) vapor. Crystals of a substance can also be formed in any of these ways by combination or decomposition of other substances. In order to grow large flawless crystals,

Table 1 : Some Anisotropic Properties of Diamond Single Crystals. [Source : R. E. Clausing, in *Industrial and Scientific Handbook on Diamond,* edited by M. Prelas, G. Popovici, L. K. Bigelow, Marcell Dekker publisher (to be published in summer '97)].

Property	Crystal face or direction	Relative Value	Reference
Abrasion/ Wear Rate	{111} face/ polishing direction 50 ° away from <111> toward cube	30	Wilks (1979)
	{111} face/ polishing direction 60 ° away from <111> toward cube	3	Wilks (1979)
Oxidation Rate	{111}	1.5	Evans (1979)
	{110}	0.8	
	{100}	0.2	
Cleavage Energy	{111}	10.6	Field (1979)
	{110}	13.0	
	{100}	18.4	

methods have been developed, through the control of the crystallization process, to create conditions similar to those at which some crystals have grown in nature. In certain cases even better crystals have been synthesized than those found in nature. A detailed account of the different crystal growth techniques has been given by Buckley [39].

As noted by Verma [38], the history of the development of the quantitative theory of crystal growth was initiated by Gibbs in 1878 [40] on thermodynamical grounds. Curie [41], Wulffe [42] and others followed it. Later, atomic theory of crystal growth was developed by Volmer [43], Kossel [44, 45], Stranski and his co-workers [46], Becker and Doring [47], also Becker [48, 49] and Frenkel [50, 51]. This theory considers the growth of an ideal crystal. Burton, Cabrera and Frank [52, 53] have developed a theory of crystal growth that takes into account the presence of imperfections, especially dislocations, and is referred to as the theory of imperfect crystals. A review of the historical development of crystal growth theories has been given by Buckley [39]. The theory developed by Burton et al. [53] has had a tremendous impact on the understanding of the experimental observations and is most commonly invoked for the understanding of the growth mechanisms in diamond film growth.

The form of a crystal is influenced by factors such as its internal structure, nature of the solvent and other external factors such as the concentration gradient etc. The theory of crystal growth can be understood in three steps, according to Mott [54] :

(a) Understanding of the theory of rate of growth of a crystal surface in contact with a vapor (or solution), with a given degree of supersaturation or in the case

of a crystal growing from the melt, for a given degree of supercooling. This will include the study of the rates of growth of different crystal faces, the effect on the growth rates of impurities which may be adsorbed on the surface, and of imperfections present in the crystals themselves.

(b) Applying the knowledge derived above, to determine, the crystal forms (in terms of dependence on diffusion of ions or atoms as in the case of growth from solution, or on the conduction of heat liberated in the case of growth from melt).

(c) As the final step, study of the crystal structure of the deposit (e.g. the formation of screw and edge dislocations during growth). One could, for example, as in this case, study the structure of crystalline films deposited on a crystalline substrate.

(i) Surface free energy

Gibbs in 1878 [40] made use of the analogy of liquid drops and applied the conditions governing the growth of water droplets in a mist to the growth of a crystal. As, Verma [38] notes, the condition for the stability of an isolated drop of a fluid is that its surface free energy, and hence its area is minimum. For a crystal in equilibrium with its surroundings at constant temperature and pressure, this condition implies that Gibbs free energy will be a minimum for a given volume. Assuming the volume free energy per unit volume to be a constant throughout the bulk of the crystal, the condition becomes that the sum, taken over the n faces of the crystal, of the product of the surface free energy per unit area of a face and the surface area of the face must be a minimum. This implies that those faces will develop which lead to a minimum total surface free energy for a given volume. Gibbs realized an essential difference between

a liquid drop and a crystal. In a drop the atoms or molecules are randomly arranged whereas in a crystal the structural units are arranged in a regular way in three dimensions according to certain symmetries.

Curie [41] took this theory a step further by calculating the shapes of crystals in equilibrium with solution or vapor, consistent with the minimum free energy concept. Wulffe [42] showed that the Gibbs' equilibrium shape of a crystal is related to the relative surface free energies of the faces in a very simple manner. The mathematical analysis of this relation, known as the Wulffe's theorem, shows that the crystal should form a polyhedron such that the perpendicular distances from a point, within the crystal, to the crystal faces, are proportional to the specific free energies of the appropriate faces. M. Von Laue [55] has discussed this theorem and Burton, Cabrera and Frank [53] have also given a proof of the generalized Wulffe's theorem. This simple theorem then implies that the velocities of growth of different faces in the directions of their normals are proportional to the appropriate specific surface free energies. It should be noted that Gibbs criterion is applicable only to a crystal in equilibrium with its surroundings.

The velocities of growth of the different faces of a crystal has also been explained by Bravais [56], who introduced the idea of densities of lattice points in the various planes, the reticular densities. According to him the velocities of growth of the different faces of a crystal will depend upon the reticular densities, and that the velocity of growth in a direction normal to a face would be the slowest for the planes of maximum density. The faster moving planes would grow out leaving only the slow moving planes of maximum reticular densities. The reticular densities alone, however, do not determine the rate of growth of a

crystal face, since, as is well known, isomorphous crystals do not possess identical habits. This simple Bravais law, that the most densely packed crystal planes will occur as crystal faces, was extended by Donnay and Harker [57-59] to take into account the effect of symmetry operations. After the Gibbs and Curie theories were put forward, Soehncke [60] further developed the idea of surface free energies by postulating that the faces which possess the greatest reticular densities are those with minimum surface energies, and hence have minimum velocities of growth. Only when all the factors that determine the relative growth rates of different faces are known can the shape of a crystal be defined.

(ii) Growth of a perfect crystal

The surfaces of crystals with perfect lattices may be divided, according to Burton, Cabrera and Frank [52], into two classes, (a) close-packed surfaces, (b) non-close-packed or stepped surfaces.

The equilibrium structure of a crystal surface maybe represented by a completely flat surface partially covered by another layer. Figure 3 shows the crystal surface at low temperature, having a kink marked A in the step [38]. The boundary line where there is a difference of level equal to an intermolecular spacing between the two sides is called a step. Any ideal crystal face with a step will continue to grow because of the presence of a large number of kinks due to thermal fluctuations. The concentration of kinks in a step has been mathematically calculated. For a temperature range between 0.5 and 0.8 times the boiling point Frenkel [50], Burton et al. [52, 53] have shown that there may be a kink for every four molecules in a step. This does not change even if the vapor is supersaturated. The process of growth of a crystal surface with steps

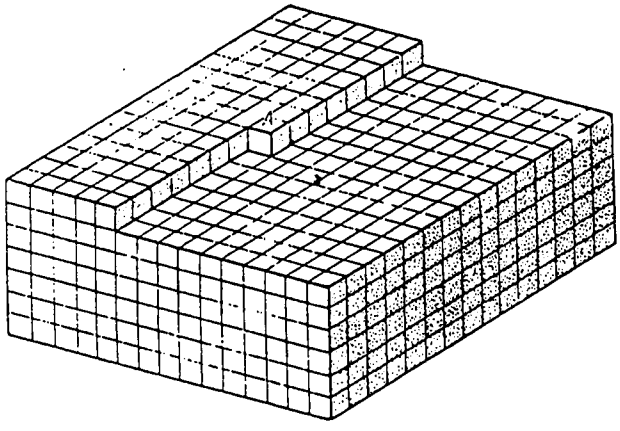

Figure 3 : Surface of a crystal at low temperature, showing a kink, A, at a step. [Source : A. R. Verma, in *Crystal Growth and Dislocations*, Butterworth Scientific Publications, London (1953).]

will be the result of a transport of molecules from the vapor to the adsorbed layer, the diffusion of adsorbed molecules towards the steps and the diffusion of the adsorbed molecules along the edge of the step towards a kink. Burton et al. [53] have shown mathematically that in growth from a vapor, the rate of direct arrival of molecules from vapor at any particular point on a crystal surface is generally small as compared with the rate of indirect arrival by way of surface migration. Mathematical calculations to determine the rate of advancement of a step have been calculated by Verma [2]. The analysis reveals that during the process of crystal growth all steps that are initially present on the crystal surface will travel towards the edge of the crystal and disappear, forming a completed surface. Thus all the high index planes or stepped surfaces will be eliminated leaving only the low-index surfaces to grow. Any further growth will be possible only if new steps can be formed. Detailed calculations by Burton, Cabrera and Frank [16, 17] show that steps will not be created by thermodynamic fluctuations on a low index face, unless the temperature is above a certain critical value, which for most of the close packed surfaces is of the order of, or higher than the melting point, when the surface rapidly becomes rough. Therefore for the growth to continue steps must be formed gradually, at ordinary temperatures.

Gibbs [4] first appreciated that this required the initiation or nucleation of a new layer. Once a nucleus is formed, growth can take place on its edges proceeding on to form a new layer. Such a layer will rapidly spread across the whole face and growth will again be halted unless another nucleus is formed. A generalized treatment of the nucleation theory has been given by Burton, Cabrera and Frank [17]. According to their analysis the probability of the formation of nuclei is a very sensitive function of supersaturation and is quite

negligible below a certain critical value. However real crystals have been observed to grow at low supersaturations, where, this theory predicts the formation of nuclei to be negligible.

In order to understand the growth at lower supersaturations, the assumption of the crystals being perfect needs to be reexamined. In reality crystals are not perfect, they have geometrical and compositional inhomogeneities. The theory of imperfect crystals, as proposed by Burton, Cabrera and Frank [17], provides with another mechanism by which a surface remains stepped no matter how far the steps advance. This theory is based on the nature of imperfections in the crystal lattice.

(iii) Growth of an imperfect crystal

The imperfections in a crystal lattice play an extremely important role since many properties of a crystal depend upon its structure, for e.g. the diffusion phenomena, the ionic and electronic conductivity in insulating crystals and semi-conductors, the crystal strength etc. The imperfections in a crystal have been categorized as : (a) a crystal defect consisting of lattice flaws where foreign atoms have taken up the normal positions of the atoms in the crystal lattice (such as a vacancy), (b) a crystal defect consisting of either a foreign atom or atoms of the crystal material, outside the regular geometrical arrangement of the crystal lattice (known as interstitial atom), and (c) a dislocation which consists of purely geometrical faults in the crystal lattice. Of the three only the last has any effect on the lattice at distances greater than a few inter-atomic spacings. There are two basic types of dislocations , the 'edge' and the 'screw' dislocations, with a series of intermediate cases which maybe

regarded as composed of these two standard types. Cottrell [61] and Read [62] have given an excellent account on the theory of dislocations.

A closer look at the dislocations that are of the screw type reveals that they may be responsible for the continuation of growth on a crystal face. A screw dislocation emerging on the face of a crystal provides it with a step. This step is self perpetuating and hence the steps needed for the growth of the crystal are provided [38]. Thus the need for a two dimensional nucleation does not arise. This theory offers a mechanism for crystal growth at low supersaturations, where the nucleation theory fails to explain the growth of a crystal.

The theory of imperfect crystals put forward by Burton et al. [17] predicts that on the surfaces of crystals which have grown by this screw dislocation mechanism, flat molecular spiral pyramids should be observed. The faces of spiral growth pyramids will be the vicinal faces, and thus the occurrence of such faces is naturally explained by the theory. Since the screw dislocations are almost always present at all temperatures used for growth, they provide a perpetual source of steps (and kinks) on which growth can take place.

The surfaces that have screw dislocations can grow by the step mechanism where as layered growth takes place on vicinal faces which have kinks at rough edges or other structural boundaries etc. The mechanism by which a large perfect crystal surface grows layer upon layer depends upon the nature of the surface. The Periodic Bond Chain Theory predicts the atomic level topography and existence of different faces in a crystal system depending upon the nearest neighbor arrangements of atoms on a crystal plane.

(iv) Periodic Bond Chain theory

The Periodic Bond Chain (PBC) Theory was formulated by Hartman and Perdok [63] and assumes a crystal surface to be a section of the bulk crystal. This theory has been used to connect the external crystal morphology, and the properties of the crystal surface to the crystallographic structure. According to this theory then, each crystal can be considered to be made up of chains of strongly connected atoms, called the PBC's. In the cubic diamond crystal, the zigzag chain of atoms in the <110> direction is the only type of PBC. Crystallographic planes are categorized according to the number of PBCs within a slice of the plane (which is determined by the crystallographic extinction conditions), into an F (flat), an S (stepped) or a K (kinked) face i.e. containing two or more, one and no PBCs respectively. F faces are predicted to grow by a step mechanism (they are thus relatively flat) and are expected to be the slowest growing faces. S faces on the other hand are entirely made up of steps, so there is no nucleation barrier for growth on these faces. These faces are thus very fast growing. Lastly, the K faces are atomically rough and are very fast growing like the S faces. These faces do not have a nucleation barrier for growth. Crystals, in general are then observed to be bounded by only the slow growing F faces as the S and the K faces grow out quickly to point or edges.

According to surface energy considerations diamond crystal is expected to have the {100}, {110} and the {111} families of crystal planes. Higher index faces have been observed in both natural and synthetic diamond, however, they are rather uncommon. According to the PBC theory, for diamond crystals, the {110}, {111} and {100} are S, F and K type faces respectively. Accordingly the {110} and the {100} faces should grow out, and the slow growing {111} faces

should persist. This prediction seems to hold good for the {110} and the {111} faces, but not for the {100} faces. As a matter of fact the {100} faces are as commonly observed as the {111} faces in CVD growth. This contradiction is explained by the 2X1 surface reconstruction of the {100} surface, making it an F type surface. Gilling et al. [64] have explained this classification of the reconstructed {100} surface in detail.

(3) Morphology : General understanding in the case of diamond

The diamond crystal structure has a cubic lattice and belongs to the space group Fd3m. Figure 4 shows the unit cell representing the diamond crystal lattice [65]. The most common facets on natural and synthetic crystals are {111} followed by {100}. The {111} plane is the only twinning plane and the only cleavage plane in practice. The {111} faces have the lowest free energy which is half the free energy of the {100} faces.

The differences in the rates of growth of the various crystallographic planes determine the shape of the crystal. The flatness and other topographical features of the faces are a consequence of the details of the growth processes. In twinned and polycrystalline material the morphology is also a function of the nucleation probability, preferential orientation of nuclei, and in the case of twins, the twin symmetry and competitive growth of twins or other new crystallites.

If only one crystal is considered and is allowed to grow freely in all directions, then the crystal would be bounded by the slowest growing crystal faces, having the slowest growth velocity in the direction perpendicular to these faces (and having the lowest surface free energy). The faster growing directions would have grown their corresponding faces out to a point or an edge

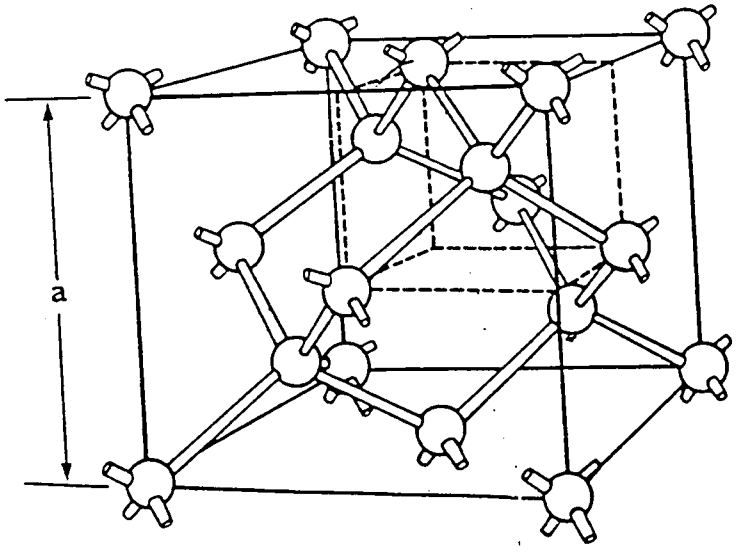

Figure 4 : Unit cell of diamond showing a face centered cubic crystal structure corresponding to Fd3m space group. The lattice spacing a, in diamond, is 3.56 Å. The interatomic distance is 1.54 Å. [Source : M. N. Yoder, in *Diamond and Diamond-like films and coatings*, Edited by R. E. Clausing, L. L. Horton, J. C. Angus and P. Koidl, NATO ASI series B **266**, 1 (1991)].

or to small facet. A diamond crystal in such a situation will have the shape of an octahedron bounded by the family of eight {111} planes. Synthetic crystals are usually in the shape of cubo-octahedra bounded by {111} and {100} planes. Figure 5 shows natural, synthetic CVD grown and synthetic high pressure high temperature (HPHT) grown diamond single crystals [37]. Cubes and octahedra can be grown by both synthetic processes but usually a combination of {111} and {100} facets form various cubo-octahedral shapes. Note that edges of all of the facets in cubo-octahedra are <110> directions and that the square {100} facets are not bounded by <100> directions but by <110> directions (at 45 ° to the crystal axes).

The {100} faces often referred to as cube faces, or 4 point surfaces have four fold symmetry. The {111} faces often referred to as octahedral or 3 point surfaces, have three fold symmetry. In synthetic diamond {110} and sometimes higher index faces such as {113}, {115}, {117}, {221} or {331} are occasionally seen but are seldom dominant features. Figure 6(b) shows a dodecahedron with all the {110} faces and fig. 6(c) shows a cubo-octahedron with added {110} faces. The {110} faces have 2 fold symmetry and are referred to as 2 point surfaces. Another way of looking at it is a {100} cube surface has four equivalent directions at 90 ° to each other, an {111} octahedral surface has three equivalent directions at 120 ° to each other, and a {110} dodecahedral surface has only two equivalent directions at 180 ° to each other.

The shape of cubo-octahedra vary depending on the ratio of the growth velocities in the <100> and <111> directions. The shapes can therefore be used to determine the ratio of growth rates. Figure 7 shows the shapes that result for different growth rate ratios [37]. These crystal shapes assume that the limiting

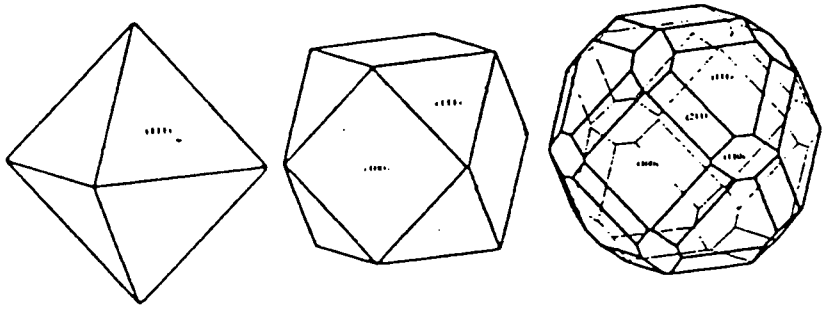

Figure 5 : Idealized growth morphologies for natural, synthetic CVD grown and synthetic HPHT grown diamond single crystals. [Source : R. E. Clausing, in *Industrial and Scientific Handbook on Diamond,* edited by M. Prelas, G. Popovici, L. K. Bigelow, Marcell Dekker publisher (to be published in summer '97)].

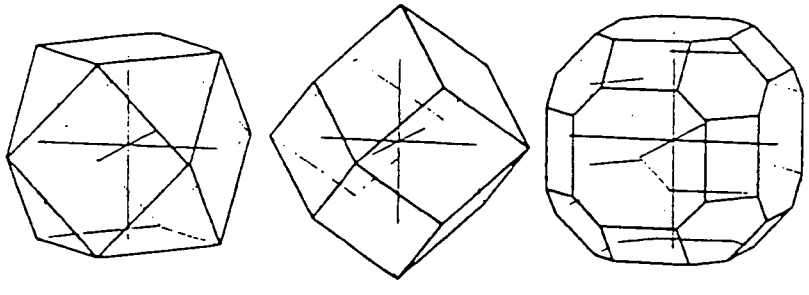

Figure 6 : (a) The {100} axes in a cubo-octahedron, (b) a dodecahedron with all {110} faces and (c) a cubo-octahedron with added {110} faces. [Source : R. E. Clausing, in *Industrial and Scientific Handbook on Diamond,* edited by M. Prelas, G. Popovici, L. K. Bigelow, Marcell Dekker publisher (to be published in summer '97)].

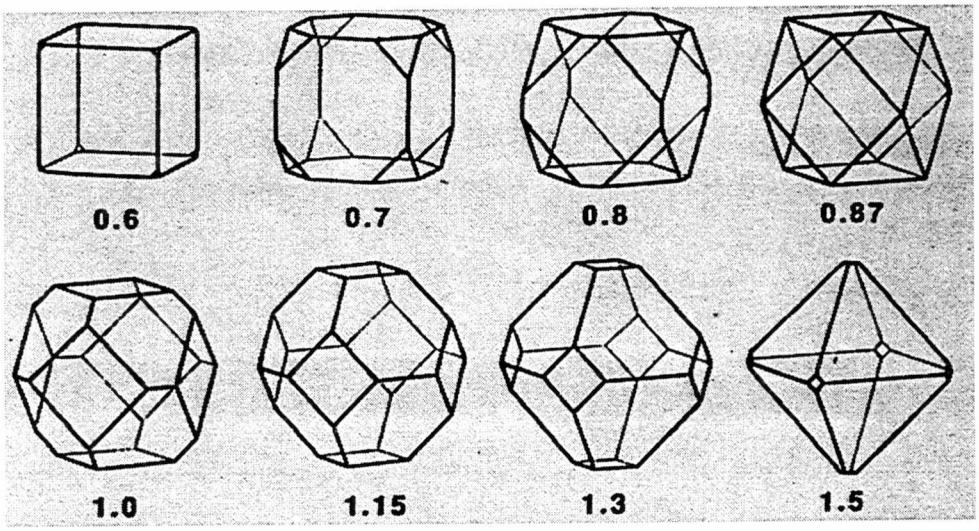

Figure 7 : The cubo-octahedral shapes which result as the ratio of growth velocity in the <100> to that in <111> varies from 0.577 to 1.732. [Source : R. E. Clausing, in *Industrial and Scientific Handbook on Diamond,* edited by M. Prelas, G. Popovici, L. K. Bigelow, Marcell Dekker publisher (to be published in summer '97)].

faces are the {100} and {111} facets but that the crystal grows at different rates on the two types of facets. The distance from the center of the crystal to the center of each face is proportional to the growth rate in the direction perpendicular to that face. The slower growth rates produce the larger corresponding faces. The longest dimension in the crystallite defines the fastest growing direction. This direction is always to a corner and is indicated in the figures by an arrow. The shapes of these crystals reveal the ratio of growth rates in the <100> and the <111> directions. The ratio of growth rates, $r = v_{<100>} / v_{<111>}$ is given under each shape. Note that the longest dimension in the cube is the <111> direction while that in the octahedron is in the <100> direction. For a ratio of growth rate equal to 0.87 the longest dimension is in a <110> direction.

The structural evolution of a polycrystalline film has been modeled by van der Drift [66]. He called it the principle of evolutionary selection. According to this theory, nuclei are formed with random orientations on a substrate. These nuclei grow uniformly, perpendicular to each facet of the crystallite so as to maintain the original shape. (This model assumes that growth occurs on all faces uniformly). The crystallites grow until they meet the growing surface of another crystal. The nuclei with their fastest growing crystallographic direction perpendicular to the substrate envelop and overgrow the less favorably oriented ones. This model should be modified somewhat if some face forms grow faster than others or if bulk or surface diffusion is important; however that does not change the final conclusion that the texture (crystallite orientation) is determined by the fastest growing direction [37]. The control of the fastest growing direction

can thus dictate the growth of oriented diamond films essential for various applications.

(4) Chemical vapor deposition of diamond

The ability to fabricate diamond material into coatings, films and bulk objects with dimensions greatly exceeding those available from natural or HPHT synthetic diamond gives CVD process great importance. Nearly all CVD diamond being produced at present is polycrystalline. The interest in growing single crystal material is immense due to its possible applications in the electronic industry as well as for the basic understanding of the growth processes in CVD diamond.

The morphologies in synthetic diamond are strongly dependent on the growth conditions. The connection between the growth conditions and morphology, and that between morphology and properties has been recognized but not completely understood. Substrate temperature, carbon supersaturation and impurities have especially strong effects on morphology. The growth morphology, on the other hand, is strongly related to the incorporation of film and crystal defects ranging from grain boundaries and voids in polycrystalline films, to twins, point defects and the incorporation of impurities in individual crystallites. The residual stresses, strength, fracture toughness, thermal conductivity, electronic and optical properties of films are all strongly related to growth morphology. A better understanding of the relationship between the growth morphology and growth conditions would facilitate the design and growth of diamond films and crystals for specific applications.

(5) Control of morphology in CVD grown material and the layout of this theses

CVD diamond has great potential for producing engineered diamond material and structures since it provides the ability to grow single crystals and large area films with controlled morphology, defects, and impurities.

It is possible to grow any of the basic single crystal cubo-octahedral shapes based on {111} and {100} facets (shown in fig. 7) and many more produced by twinning and nucleation. Under special condition forms resulting from the stabilization of higher index planes including the {110}, the {221}, {331} and {113} can be grown. The parameters chosen by most experimentalists until now however tend to produce mostly minor variations of the basic cubo-octahedral shapes having growth rate ratios, **r**, between 0.8 and 1.1 (growth parameter α=1.5-2.0, where α has been defined as $\mathbf{r}\sqrt{3}$). There are several reports in the literature relating the morphological development to the deposition parameters.

It is very useful to construct maps relating the changes in morphology to changes in growth parameters, particularly changes in temperature and changes in hydrocarbon concentration. Zhu et al. [67] have made such maps labeling the various regions according to the morphology. Some dependencies of morphology on individual parameters as well as morphology maps have been developed for various experimental set ups. Since the ratio of growth rates, **r**, is such a determining factor in morphological development, a map based on isomorphic contours of growth rate ratio has been developed for microwave plasma systems [68, 69]. Such maps are very useful as a guide for any given reactor system. Part 4 describes the generation of such an isomorphic map for the hot filament system used for this study. This is the first isomorphic map for a

hot filament system. It not only provides the standardization for this reactor system but also the basis for comparison between the two most common techniques used in diamond CVD, i.e. the microwave plasma and the hot filament systems. Part 4 also includes detailed experimental observations regarding the appearance of twins and texture of the films.

The basic difference between a hot filament reactor and a microwave plasma or any other reactor is the mode of generation of gas phase species. As is evident from the names of the techniques, in a hot filament reactor, gases are made to pass over a heated metal in the form of a filament that ionizes the input gas molecules into various gas phase species. In a microwave plasma system the mode of excitation are the microwaves. The role of the filament is being studied actively in terms of its performance. Part 3 describes several different aspects of the filament. Three different materials were used for the filament and the effect of the filament material on the growth morphology was studied. An aspect of the filament material that has not here to fore been fully explored is the filament as a source of contamination. For the hot filament process to be used commercially, to produce diamond films for specific applications, this aspect of the filament is of great importance. Neutron activation analysis was done and the contamination from the three materials were compared. The experimental details and results are described in Part 3.

It has been shown that internal defects and impurity levels of diamond crystals can be related to the crystal facet from which the section grew. Details of the growth processes on the {100} and {111} facets can be quite different because of the surface structure. As the crystal grows, the material added to

these different facets forms zones within the crystals having different kinds and concentrations of defects and impurities i.e. different crystal quality.

Details of the growth processes can be inferred from the characteristic topographical features of the faces, e.g. evidence of steps on the faces, flatness of the faces, presence of screw dislocations, sharpness of edges etc. These atomic level features can be investigated using atomic probe microscopy. Part 5 gives details of the observations made from scanning tunneling (STM) and atomic force microscopies (AFM). Spiral growth pyramids have been imaged on the {111} faces using STM [70]. These features support the theory that under the selected growth conditions growth on these {111} faces took place by layer mechanism. A screw dislocation in the lattice is probably the source for the steps of these growth spirals. Other growth features, such as an indented {111} face, called the hopper {111} face has been investigated under an AFM. The faces comprising the hopper face were indexed. This feature has been previously observed but hopper faces have been assigned as the {110} faces without any quantitative measurements. The analysis presented in part 5 reveals these faces to be higher index planes belonging to the [110] zone. Other topographical features as well as these give clues regarding the details of the growth mechanism and are discussed in part 5.

Defects and impurities play an important part in the growth processes responsible for growth. Since the properties of diamond depend so strongly on morphology and impurities they are graded and selected according to their applications. In natural diamonds nitrogen is the most common impurity, other common impurities being boron and oxygen. Natural diamond has been classified into type I and type II according to the optical absorption by the

nitrogen impurity. Type I exhibits pronounced optical absorption due to nitrogen impurities while in type II this is too weak to be detected. Nitrogen is the dominant impurity in type I diamond and may range up to 2500 ppm in type Ia where it is mostly present as aggregates. Type Ib refers to diamond with nitrogen present mostly as single substitutional atoms which exhibit electron paramagnetic resonance. Type Ib is rare in nature and has up to 300 ppm of substitutional nitrogen. Type IIa is the very low in nitrogen (below 1 or 2 ppm) and is considered the most pure form of diamond. Type IIb maybe even lower in nitrogen but it is semiconducting due to the presence of boron impurity. Both IIa and IIb can exhibit high degrees of crystal perfection.

The incorporation of substitutional nitrogen into diamond crystals increases the lattice parameter [71]. The lattice dilation is about 0.00007 Å for 100 ppm atomic nitrogen. Nitrogen can be incorporated into the crystal in many ways; as a single atom substitution, as N-N pairs, as N-V pairs, N3 centers etc. [72, 73]. Although these different possibilities are realized in the case of natural diamond, most nitrogen in synthetic diamond is believed to be single atom substitutional.

The incorporation of modest amounts of nitrogen (up to several hundreds ppm) into the atmosphere for diamond film growth by microwave plasma assisted CVD has the effect of increasing the overall growth rate and decreasing the relative growth rate parameter, **r** [34]. The size and smoothness of {100}, cube faces developed on <100> textured thick films increase as the nitrogen increases up to these levels. Nitrogen is not incorporated strongly into the deposited diamond but is incorporated into the {111} growth sectors as much as

100 times more effectively than into the {100} or the {110} growth sectors [74, 75]. Typical levels for microwave activated CVD are less than 100 ppm.

Very little information on the addition of nitrogen in a HFCVD system has been reported in literature. Part 6 gives the background and details of the experiments that were carried out to see the effects of nitrogen addition. Nitrogen was added in the form of ammonia and nitrogen gas. Results obtained regarding the growth rates and relative growth rate ratios are similar to those reported for the microwave plasma system, however the amounts of atomic nitrogen introduced in the gas phase, to produce these effects are quite different. A detailed description of these experiments and results are presented in Part 6.

References

1. J. J. Lander and J. Morrison, Surf. Sci. **4**, 241 (1966).

2. B. V. Spitsyn, in *Handbook of Crystal Growth*, edited by D. T. J. Hurle, Vol. **3**, 403 (1994).

3. B. V. Spitsyn, L. L. Bouilov and B. V. Deryagin, Progr. Cryst. Growth Charact. **17**, 79 (1988).

4. V. M. Golyanov and A. P. Demidov, US Pat. 3 840 451 (1974).

5. E. G. Spencer, P. K. Schmidt, P. C. Joy and F. J. Sansalone, Appl. Phys. Lett. **29**, 118 (1976).

6. W. G. Eversole, Us Pat. 3 030 187. Synthesis of Diamond (1958).

7. W. G. Eversole, Us Pat. 3 030 188. Synthesis of Diamond (1958).

8. B. V. Spitsyn and B. V. Deryagin, Inventors certificate 339, 134 (USSR). A technique of Diamond growth on diamond's face (1956).

9. S. P. Chauhan, J. C. Angus and N. C. Gardner, J. Appl. Phys. **47**, 4746 (1976).

10. V. Shanov and D. Dzhoglev, God. Vissh. Khim. Tekhnol. Inst. Sofia 27 (1980).

11. V. I. Trefilov, P. A. Tesnor, G. I. Sabbakin and L. P. Borodina, Dokl. Akad. Nauk SSSR **273**, 1431 (1983).

12. D. V. Fedoseev, K. S. Uspenskaya and B. V. Deryagin, Zh. Fiz. Khim. **49**, 2473 (1975).

13. B. E. Dzevitsky, B. V. Spitsyn, D. A. Kochkin and B. V. Deryagin, US Pat. 3 705 937 (1972).

14. V. V. Digonski, M. S. Drui, M. I. Sokchor, V. G. Syrkin, L. I. Feldgun and A. A, Uelskii, Inventor Certificate 444 448 (USSR). From Ptkrytiya, Izobr., Prom. Obraz., Tovarnye Zhaki, No. 47 (1981).

15. P. A. Tesner, A. E. Gorodetsky, E. V. Denisevitch, A. P. Zakharov and T. V. Tekunova, Dokl. Akad. Nauk SSSR **222**, 1384 (1975).

16. B. V. Spitsyn, J. Cryst. Growth **99**, 1162 (1990).

17. B. V. Spitsyn and A. V. Smol'yaninov, USSR Author's Certificate N 987912, Appl. 1533329/23-36, filed April 21 (1971).

18. B. V. Spitsyn, Proc. of 3rd Int. Symp. on Diamond Materials (Honolulu, May 16-21, 1993) p. 345.

19. J. C. Angus and C. C. Hayman, Science **241**, 913 (1988).

20. T. Anthony, Symposium N, fall meeting, Materials Research Society Meeting, Boston, 30 Nov. to 5 Dec. 1985.

21. N. Setaka, Proceedings of the Electrochemical Society Meeting, Honolulu, Hawaii, October 1987, p. 1156.

22. M. Kamo, Proceedings of the Eighth International Symposium on Plasma Chemistry, Tokyo (1987), p. 2481.

23. N. Fujimori, I. Imai and A. Doi, Vacuum **36**, 99 (1986).

24. O. Matsumoto, H. Toshima and Y. Kanzaki, Thin Solid Films **128**, 341 (1985).

25. O. Matsumoto and T. Katagiri, Thin Solid Films **146**, 283 (1986).

26. N. Setaka, Symposium N, Materials Research Society Meeting, Boston, 30 Nov. to 5 Dec. 1985.

27. G. Lucovsky, P. V. Tsu and R. J. Markunas, Mater. Res. Soc. Symp. Proc. **68**, 323 (1986).

28. H. Kawarada, K. Sheng Mar and A. Hiraki, Jpn. J. Appl. Phys. **26**, L1032 (1987).

29. K. Suzuki, A. Sawabe, H. Yasuda and T. Inuzuka, Jpn. J. Appl. Phys. **50**, 728 (1987).

30. M. Peters, paper presented at Society of Photo-optical Instrumentation Engineers (SPIE), Los Angeles Meeting, January 1988.

31. K. Kurihara, K. Sasaki, M. Kawaradi and N. Koshino, Appl. Phys. Lett. **52**, 437 (1988).

32. K. Kitahama, K. Hirata, H. Nakamatsu and S. Kawai, Appl. Phys. Lett. **49**, 634 (1986).

33. H. Okabe, R. J. Cody and J. E. Allen, Chem. Phys. **92**, 67 (1985).

34. M. P. Irion and K. L. Kompa, Appl. Phys. **B27**, 1983 (1982).

35. M. Kitabatake and K. Wasa, J. Appl. Phys. **58**, 1693 (1985).

36. B. V. Spitsyn, in *Applications of Diamond Films and Related Materials*, eds. Y. Tzeng, M. Yoshikawa, M. Murukawa and A. Feldman (Elsevier Science Publishers, Amsterdam, 1991), Mater. Sci. Monogr. **73**, 475 (1991).

37. R. E. Clausing, in *Industrial and Scientific Handbook on Diamond,* edited by M. Prelas, G. Popovici, L. K. Bigelow, Marcell Dekker publisher (to be published in summer '97).

38. A. R. Verma, *Crystal Growth and Dislocations*, Butterworth Scientific Publications, London (1953).

39. H. E. Buckley, *Crystal Growth*, John Wiley and Sons, Inc., New York (1951).

40. J. W. Gibbs, *Collected Works*, Longmans Green & Co., London (1928).

41. P. Curie, Bull. Soc. Franc. Miner. **8**, 145 (1885).

42. G. Wulffe, Z. Kristrallogr. **A 100**, 272 (1938).

43. M. Volmer, Kinetik der phasenbildung, Steinkopff, Dresden and Leipzig (1939).

44. W. Kossel, Nachr. Ges. Wiss. Gottingen, 135 (1927).

45. W. Kossel, *Falkenhagen, Quantentheorie und Chemie*, 46 Leipzig (1928).

46. I. N. Stranski, Z. Phys. Chem. **136**, 259 (1928).

47. I. N. Stranski, Disc. Faraday Soc. **5** (Crystal Growth), 13 (1949).

48. R. Becker and W. Doring, Ann. Phys. **24**, 719 (1935).

49. R. Becker, Disc. Faraday Soc. **5** (Crystal Growth), 55 (1949).

50. J. Frenkel, F. Phys., Moscow **9**, 392 (1945).

51. J. Frenkel, *Kinetic Theory of Liquids*, Clarendon Press, Oxford (1946).

52. W. K. Burton, N. Cabrera and F. C. Frank, Nature, London **163**, 398 (1949).

53. W. K. Burton, N. Cabrera and F. C. Frank, Phil. Trans. **A 243**, 299 (1951).

54. N. F. Mott, Disc. Faraday Soc. **5** (Crystal Growth), 11 (1949).

55. M. Von Laue, Z. Kristallogr. **105**, 124 (1943).

56. A. Bravais, *A Etdudes Cristallographiques*, Gauthier Villars, Paris (1866).

57. J. D. H. Donnay and D. Harker, C. R. Acad. Sci. **204**, 274 (1937).

58. J. D. H. Donnay and D. Harker, Amer. Min. **23**, 5 (1938).

59. J. D. H. Donnay and D. Harker, Amer. Min. **24**, 184 (1939).

60. L. Soehncke, *Entwickelung einer Theorie d. Krystalstruktur*, Liepzig (1879).

61. A. H. Cottrell, *Theory of dislocations, progress in Metal Physics* **1**, 77, Butterworth Scientific Publications, London (1949).

62. W. T. Read, *Dislocations in Crystals*, McGraw Hill Publishing Co. Inc., New York (1953).

63. P. Hartman and W. G. Perdok, Acta Crystallog. **8**, 49,521 & 525 (1955).

64. L. J. Giling and J. P. W. Van Enckevort, Surface Science **161**, 567 (1985).

65. M. N. Yoder, in *Diamond and Diamond-like films and coatings*, Edited by R. E. Clausing, L. L. Horton, J. C. Angus, and P. Koidl, NATO ASI series B **266**, 1 (1991).

66. A. van der Drift, Philips Research Report **22**, 267 (1967).

67. W. Zhu, A. R. Badzian and R. Messier, Proceedings of SPIE on Diamond Optics III **1325**, 187 (1990).

68. M. A. Tamor and M. P. Everson, J. Mater. Res. **9**, 1839 (1994).

69. C. Wild, R. Kohl, N. Herres, W. Muller-Sebert and P. Koidl, Dia. and Rel. Mat. **3**, 373 (1994).

70. T. J. Kreutz, R. E. Clausing, L. Heatherly, Jr., R. J. Warmack, T. Thundat, C. S. Feigerle, and K. Wandelt, Phys. Rev. B **51**, 14554 (1995).

71. A. R. Lang, in *Properties and Growth of Diamond*, edited by G. Davies, INSPEC, the institution of Electrical Engineers, London, 111-115.

72. G. S. Woods, in *Properties and Growth of Diamond*, edited by G. Davies, INSPEC, the institution of Electrical Engineers, London, p. 81-98.

73. J. P. W. Van Enckevort, in *Synthetic Diamond : Emerging CVD Science and Technology*, edited by Karl E. Spear and John P. Dismukes, John Wiley & Sons Inc., 307-353.

74. R. Locher, C. Wild, N. Herres, D. Behr and P. Koidl, Appl. Phys. Lett. **65**, 34 (1994).

75. Y. Yakota, H. Kawarada and A. Hiraki, Mat. Res. Soc. Symp. Proc. **162**, 231 (1990).

Part 2 : Experimental set-up

Film growth

(1) Hot filament chemical vapor deposition reactor

The films were grown via hot filament assisted chemical vapor deposition (HFCVD). A gas mixture of CH_4 in H_2 (with addition of NH_3 or N_2 in some experiments) was flowed at a total flow rate of 50 cc/min into a quartz tube of 25 mm diameter, which forms the main body of the CVD reactor. The pressure in the reactor was maintained at ~40 torr by throttling the inlet of the mechanical pump which exhausts the system. A carburized tungsten (or tantalum) wire filament was used to activate the gases and to indirectly heat the substrate.

Figure 1 shows the photograph of a quartz tube reactor. During the course of this study the reactor was modified to allow improved control of growth conditions. The reactor now has the additional capability of controlling the substrate temperature independently by means of a substrate heater block. Also the reaction chamber was redesigned and built with ultra high vacuum fittings to enable additions of small amounts (ppm) of NH_3 and N_2 to the input gas mixture. Figure 2 shows a schematic of the modified quartz tube reactor.

Filament holder and substrate heater assemblies form the main components of the quartz tube reactor. The filament holder assembly consisted of molybdenum rods which were connected to electrical feedthroughs on a conflat flange. A tightly wound filament (filament preparation is described in detail in Part 3) was inserted into these rods and held securely with molybdenum screws. A block made of machinable glass (maycor) was slid over the molybdenum rods. The substrate heater assembly consisted of a heater/holder block, also made out of molybdenum, and a heater element. The block had two

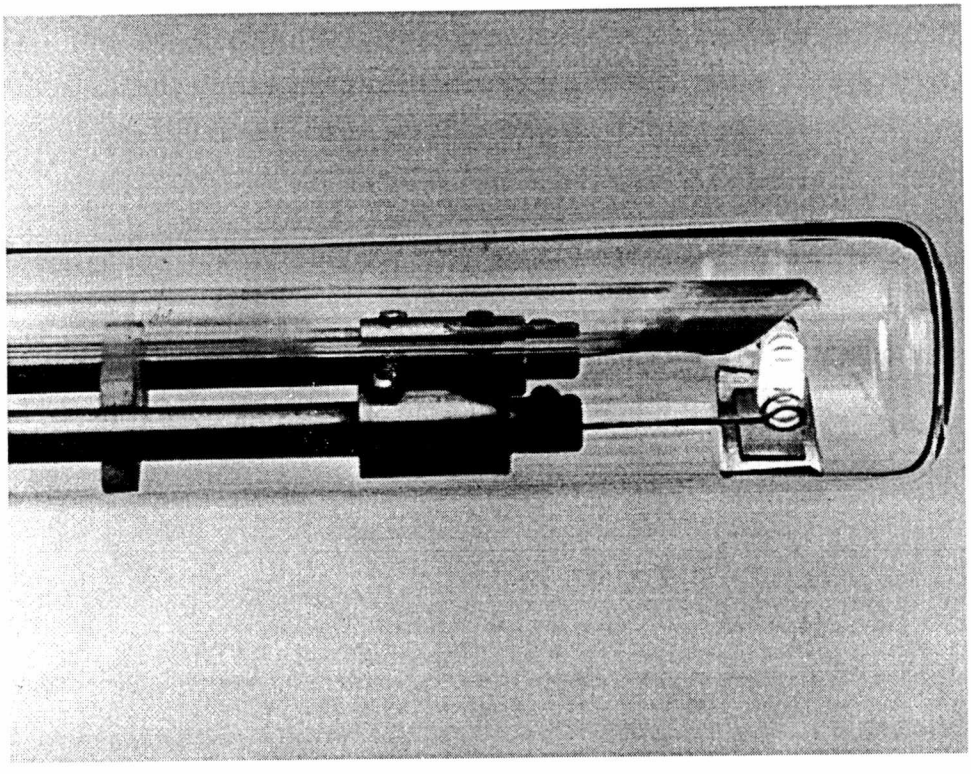

Figure 1 : A HFCVD reactor during film growth (ORNL photograph YP-5852). The substrate is placed directly underneath the filament for indirect heating. The modified reactor has the capability of controlling the substrate temperature independent of the filament by providing conductive heating from the substrate holder equipped with a heater element.

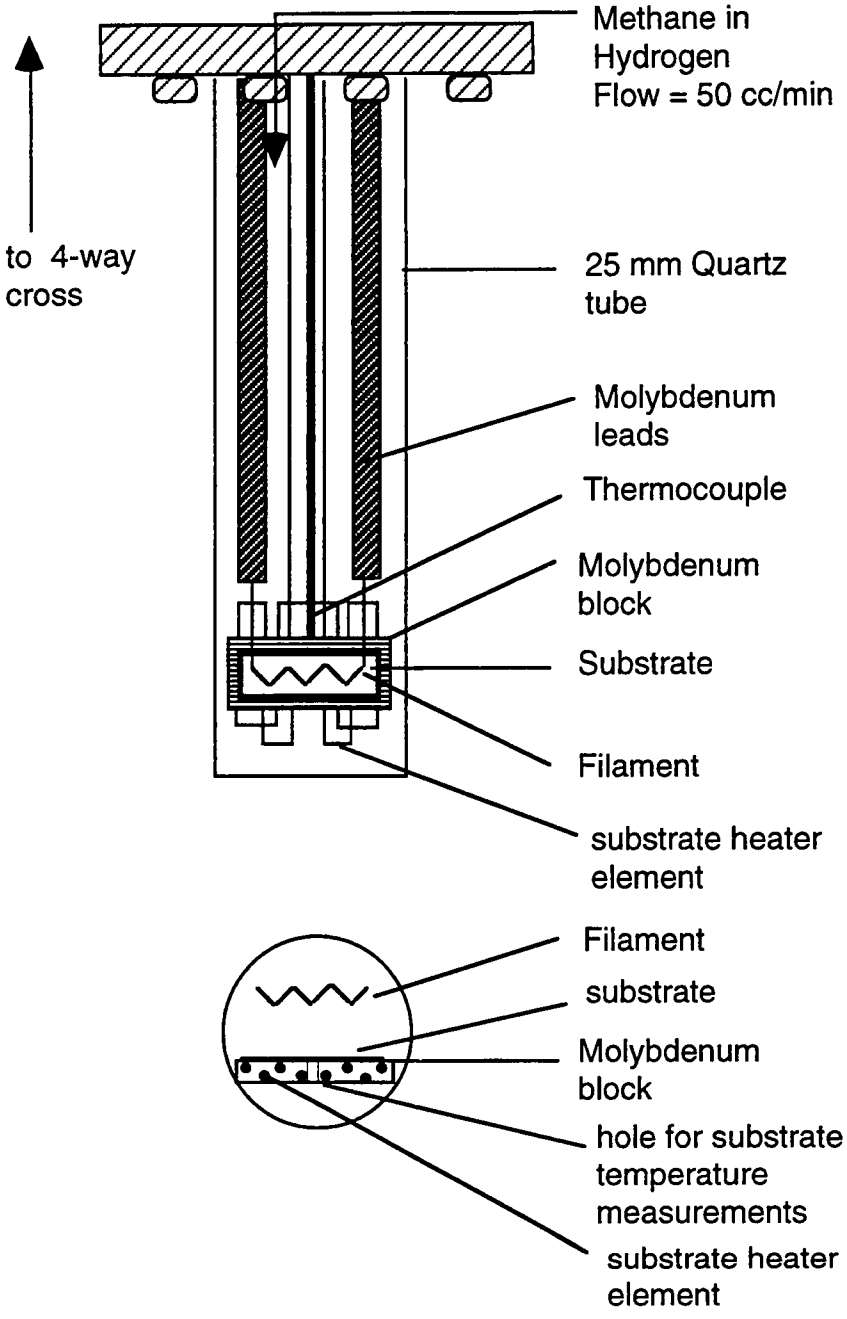

Figure 2 : A schematic of the quartz tube reactor used for hot filament CVD depositions if diamond films.

rods which were inserted into the machinable glass block, thus, holding the substrate heater block in place and isolating it from the filament leads, exactly below the filament. The filament and substrate holder assembly were fixed rigidly inside the quartz tube by the machinable glass block. A rhenium wire (0.5 mm diameter) heater element inside of ceramic tubing was used to heat this substrate holder. A Pt-Pt 10% Rh (Type S) thermocouple was placed inside this block to measure its temperature. The substrate was placed on this block, directly below the filament, enabling it to be radiatively heated from the filament as well as conductively heated from the heater block. The substrate temperature was measured using a disappearing filament type optical pyrometer, without employing any corrections for emissivity or reflections. The substrate holder block had a through hole drilled into it to enable viewing the back of the substrate with the pyrometer.

Figure 3 shows the schematic of the experimental set up. The flange containing the electrical feedthroughs for the filament, the substrate heater element and the gas inlet line was connected to one of the ports on a 4-way stainless steel high vacuum cross. The quartz tube was slid over the filament and substrate assemblies and connected to a Cajon O-ring seal on the opposite port on this cross. The mechanical pump which exhausts the system (Varian direct drive, model # SD 200), was connected to one of the side ports. A quadrupole mass spectrometer; which samples the exhaust gases and serves as a residual gas analyzer, was also connected to this port through a leak valve (Varian ultra high vacuum leak valve, model # 951-5100). The fourth port contained the feedthroughs for the thermocouple that was used to measure the temperature of the substrate heater block. The inlet line was connected to the

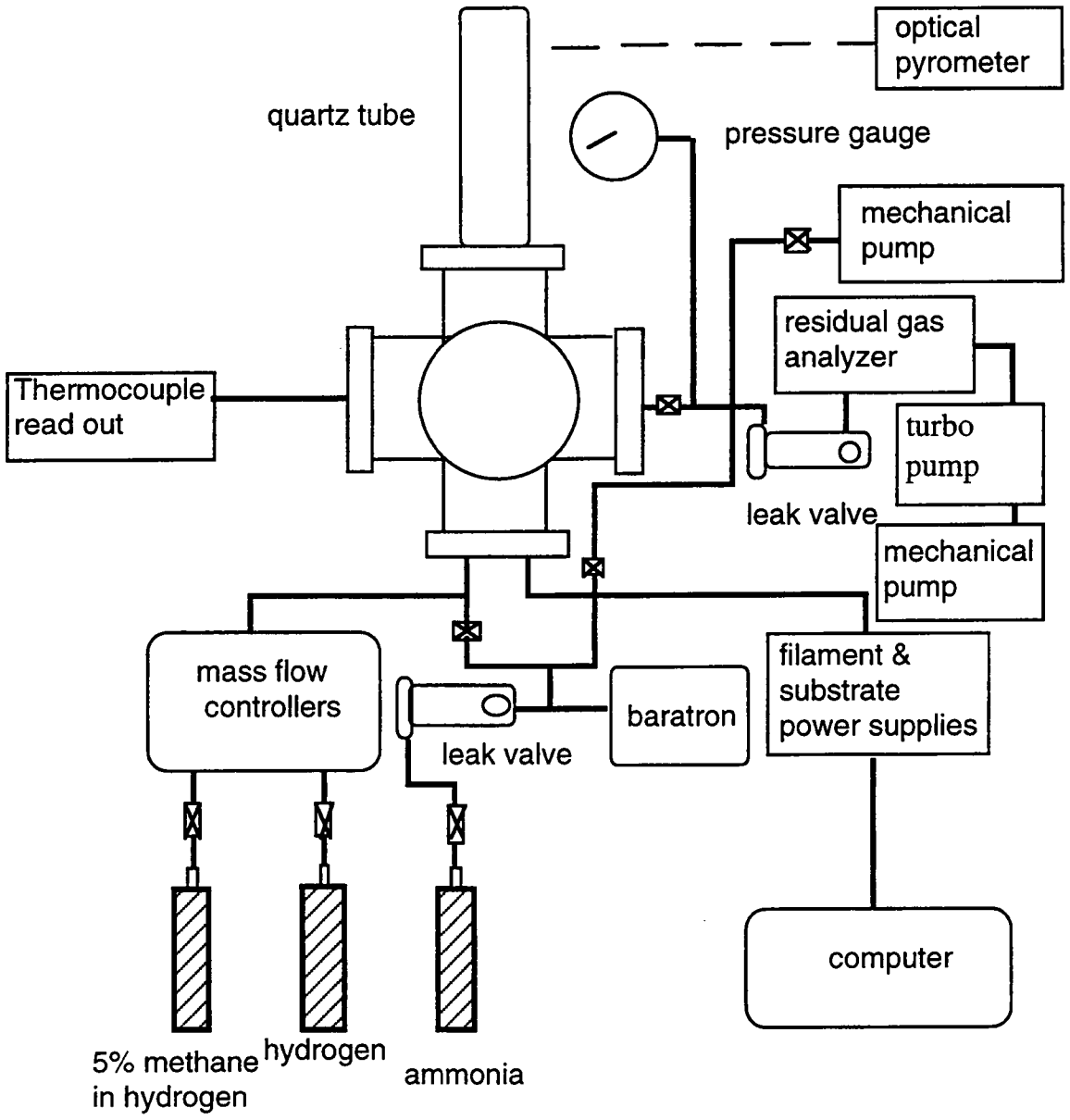

Figure 3 : A schematic of the experimental set up used for growing polycrystalline diamond films.

mass flow controllers (MKS, model # 1259B), a baratron (MKS pressure transducer type 627A, range 0-1000 torr), a safety switch, and a leak valve (Varian model # 951-5100) connected to the NH_3 gas tank for small additions to the input gas mixture. The flow rates of NH_3 were determined by slowly leaking the gas into a known volume and measuring the increase in pressure.

(2) Residual gas analysis

A mass spectrometer was used to analyze the residual gases being exhausted from the HFCVD reactor before, during and after diamond film growth. It was also used to monitor and detect leaks in the system. Variations in the peak intensities were observed when changes in the growth parameters; such as filament temperature, substrate temperature, addition of NH_3, etc. were made. Mass spectra were recorded using a commercially available differentially pumped UTI model 100 C quadrupole mass spectrometer with a closed ion source. The mass spectrometer used in this study had a sensitivity of better than 10^{-10} torr, mass range of 0-300 amu, and a resolving power of better than 1 amu.

Characterization techniques

(1) Scanning electron microscopy (SEM)

A scanning electron microscope (SEM) was used to study the surface morphology of the diamond films deposited during this study. In an SEM, a beam of high energy electrons (5-40 keV) is made to raster over the sample and low energy secondary electrons from the sample are collected using a secondary electron detector. The number of electrons being detected depends

upon the surface topography and composition of the sample and provides the contrast in the image. Most of the SEMs are also equipped with detectors that receive back scattered electrons, thus providing information regarding the atomic numbers of elements. The resolution in an SEM is determined by the size of the electron beam, and high resolution can be achieved when the electron beam is focused into a small and bright spot. The SEM provides information regarding the surface at the micrometer range. In this study, secondary electron detection was used to record the surface morphology of the films. In a few cases the films were fractured, and their thicknesses were measured by viewing the cross sections of the films.

A Hitachi S-800 SEM, equipped with a field emission gun for an electron source, which had a resolution of 5-10 Å, was used for most of this study. The images provided information from mm to sub micron levels. The images were digitally recorded on this instrument. Another SEM, an ISI-40, was also used for routine purposes. It had a resolution of ~1000 Å, and images from this instrument were recorded on Polaroid film, which were later scanned and converted into digital files.

(2) Atomic Force Microscopy (AFM)

An atomic force microscope (AFM) was used to image the morphology of the surface at the nanometer scale. It was also utilized to study the geometry of various features and to identify the orientation of some of the surface facets.

In an AFM, the schematic of which is shown in fig. 4, a flexible cantilever with a very low spring constant is scanned over the surface. This cantilever is made to vibrate and is brought near the surface. The force gradient due to the

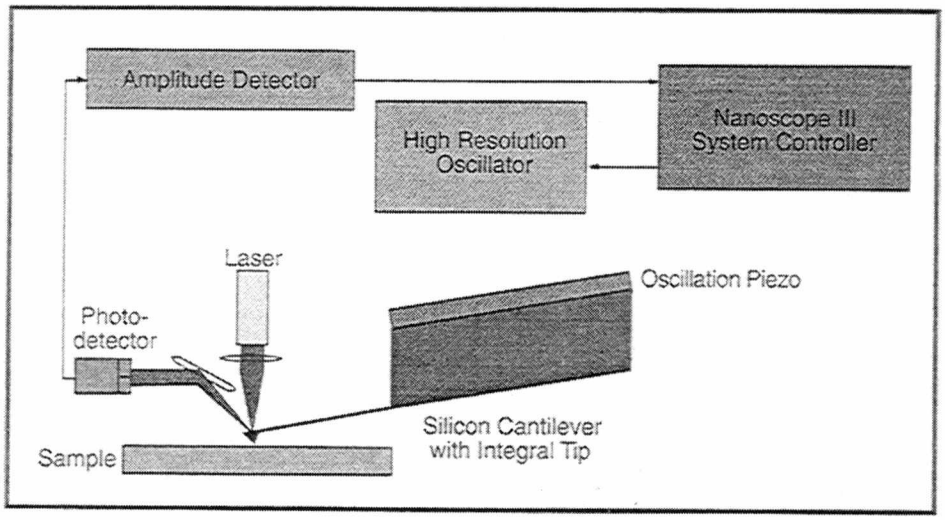

Figure 4 : Block diagram for Tapping mode operation of an Atomic Force Microscope. [Source : TappingMode Imaging Applications and Technology, C. B. Prater, P. G. Maivald, K. J. Kjoller, M. G. Heaton, Digital Instruments publication].

interaction between the tip and the sample surface changes its resonance frequency. In the tapping mode of AFM, the cantilever is made to vibrate with a certain amplitude, a shift in the vibration amplitude of the cantilever changes the response to the vibration source in a detectable way. The root mean square value of the cantilever vibration is used as the feedback signal which controls the height of the sample. The operating mode relies on a piezoelectric tube scanner to produce scans in the XY plane. An optical head is used to sense the cantilever deflection. Lateral resolution is defined by the shape of the tip.

Images of the films were obtained using a Digital Instruments Nanoprobe III atomic force microscope. The images were recorded in air and at room temperature using the tapping mode of operation. Commercially available micro fabricated silicon cantilevers were used which had a spring constant of ~ 35 N/m. The microscope has lateral resolution in the range of 5-10 nm, and vertical resolution of ~0.5 Å. for this instrument. The AFM images were analyzed quantitatively using Nanoscope III software to determine the geometry of certain growth features.

Part 3 : The effect of filament material on the quality of diamond films deposited via hot filament chemical vapor deposition

Introduction

The filament in hot filament chemical vapor deposition (HFCVD) of diamond plays the essential role of activating the gas phase species that enable and influence the growth of diamond. There are a limited number of materials which can potentially be used for filaments due to the high temperature and reactive environments employed in diamond growth. In this part, the performance of three of the most commonly utilized filament materials, W, Re and Ta, is investigated. The effects of the filament's attributes (the filament material, geometry and temperature) on the morphology of the growing film have been of interest for a variety of reasons. Performance of the filament has two broad aspects to it. First, the gas phase species that participate in diamond growth are generated at the filament, so its performance can be gauged in terms of production of these species and the interaction of the filament material with these gases. Second, good mechanical stability is required for the filament at the high operating temperatures typically used in diamond growth, if consistent growth conditions are to be established. Both aspects of performance depend on the material of the filament, and are equally important for the deposition of high quality crystalline diamond films suitable for various applications.

Sommer et al. [1] have done a detailed study on the state of the filament activity as it pertains to diamond CVD for tungsten and rhenium filaments. Filament activity is defined as the efficiency of the filament in dissociating the reactant gases. They measured the resistance, emissivity, and power consumption for W and Re filaments heated to 2500 °C in CH_4 and C_2H_2. They found that these properties as well as the partial pressures of the reactant gases depended critically on the filament temperature and the reactant ratio. The

power consumption for both filaments showed an increase at the same temperature implying an increase in filament activity and thus an increase in the production of atomic hydrogen. They proposed the removal of non-reactive carbon from the surface of the filament via etching by atomic hydrogen to be the reason for the increased filament activity, as predicted by their proposed thermodynamic model for the C-H system. They observed the emissivities of the W and Re filaments to have very different temperature dependencies and explained this observation on the basis of differences in the phase diagrams for the W-C and Re-C systems. They suggested that the optimum conditions for diamond growth require the filament to be free of carbon and hence be most active. Their observations as well as predictions from the thermodynamic model are independent of pressure, type of filament (W or Re) and hydrocarbon (CH_4 or C_2H_2). They recognized that Re filaments have an advantage over W filaments due to their superior mechanical stability. They have also reported [2] the effect of oxygen on the filament activity. They found the improvement in filament activity to be due to the removal of carbon from an oxygen related surface of the filament by formation of CO in agreement with the predictions of their quasi-equilibrium thermodynamic model.

More recently modulated-beam mass spectrometry and XPS have been used to study the filament reactions and film growth in HFCVD [3,4]. The researchers have shown that a carburized filament can produce carbon monomers, dimers and trimers as well as atomic hydrogen, from hydrocarbon/hydrogen gas mixture independent of the precursor hydrocarbon. They did not observe, under any conditions, etching reactions involving hydrogen for the removal of carbon from a hot, carburized tungsten filament, as proposed by Sommer et al. [1]. A carburized tungsten surface was, however,

found to be less effective in producing hydrogen atoms than a non-carburized surface. They suggest that carburization of a tungsten filament probably takes place as a result of generation of hydrogen atoms which subsequently react in the gas phase with methane to produce methyl radicals, acetylene, ethylene, etc., which in turn react with the tungsten to produce a carbide. They identified operating regimes at varying coverage, temperature and pressure which lead to a WC or W_2C surface. Their Rutherford backscattering measurements revealed that carburization of tungsten leads to the WC bulk composition. They observed that the surface concentration of carbon depended on the balance between carbide and graphite growth and carbon evaporation. Their XPS measurements showed an increased graphite content with increasing degree of carburization of the filament.

The fundamental mechanisms for growth of diamond and suppression of graphite are still under development. Several groups have shown [5-8] methyl radicals to be dominant growth species under typical growth conditions, however, under some conditions diamond growth from acetylene has also been shown to be possible [7]. Mechanisms have been proposed with either methyl or acetylene being the active growth species [9-13].

Various groups have investigated the dependence of key species on growth parameters. Corat et al. [14] measured the concentration of gas phase species very near the substrate using resonance enhanced multiphoton ionization spectroscopy (REMPI) for different substrate temperatures. They found the CH_3 concentration to be significantly depleted near the substrate at temperatures below 1000 K, whereas, CH_4 and C_2H_2 concentrations were found to be only weakly dependent on substrate temperature. They explained this

behavior by the recombination of CH_3 to CH_4 or C_2H_6 at low substrate temperatures, either through homogenous chemistry near the substrate or heterogeneous chemistry on the substrate.

Celii et al. [15] have shown the hydrogen atom production to be exponentially dependent on filament temperature using the REMPI technique to detect gas phase atomic hydrogen. A later analysis showed the production rates to exhibit differing activation energies at high and low temperatures, due to the conversion from catalytic to pyrolytic decomposition as the source of H. Connell et al. [16] have reported a direct measurement of the spatially resolved atomic hydrogen concentration profiles during HFCVD of diamond films. They obtained the absolute hydrogen atom concentration from titration experiments. They found that the observed H atom concentration exceeded the computed equilibrium concentrations based on the measured gas temperatures. They also concluded that diffusion is the principal mechanism controlling the H atom distribution.

Toyoda et al. [17] used ultraviolet spectroscopy to determine the methyl radical density and acetylene mole fraction when C_2H_2 and H_2 were used as the input gas. Both are found to depend greatly on the degree of filament surface poisoning. In particular filament poisoning is very important at either low temperatures or high concentrations of acetylene. They proposed that poisoning blocks dissociation sites for H_2 and may block dissociation sites for C_2H_2 and thus decreases the production of methyl radicals, as they observed. They conclude that atomic hydrogen as well as methyl radicals are critical for diamond growth.

Significant progress has also been achieved in modeling the extensive gas and surface chemistry that is integral to diamond growth. For instance, Dandy et al. [18] studied the effects of temperature and filament poisoning on diamond growth using a model designed to study diamond growth under conditions relevant to HFCVD. They were able to match the experimental observations by assuming that [H] and [H_2] near the filament reach equilibrium values at the filament temperature when there are no hydrocarbons present in the system. They found that diffusion is the dominant mode of transport from the filament to the substrate for a hydrogen-only system, and the value of the inlet mass-average velocity has negligible impact on the predicted results. For the case of the CH_4/H_2 system, the computed results were in agreement with experiments only when the effects of filament poisoning were taken into account. They found that as the inlet concentration of methane was increased, it became the dominant species near the substrate. The amount of atomic hydrogen near the substrate drops by an order of magnitude when the inlet methane was increased from 0.4% to 7.2%.

They also discussed the effect of temperature discontinuity on the predicted results. Temperature drops of as much as 1000K have been observed [19, 20] in the gas temperature in the vicinity of the filament. This discontinuity was found to be dependent on pressure, increasing in magnitude with decreasing pressure. They found that if a large discontinuity was employed, significantly more C_2H_4 is predicted to exist near the substrate for large inlet methane concentrations than is reported from experiment. At the same time, better agreement was seen between experiment and calculations for near-surface mole fractions of H, CH_3, and CH_4 when the discontinuity was taken into account.

In contrast, there have been studies which explore the effects of changing filament material. Okoli et al. [21] presented a direct comparison of W, Re, and Ta filaments. They reported that by the proper choice of growth parameters, uniform, well faceted diamond films could be grown using all three filaments. The filament material does not fundamentally influence the effects of the other deposition parameters. They reported that the maximum methane concentration, at which the filament is still active, was different for the three materials. This is understandable based on the thermodynamic characteristics of the three metals for carbide layer formation. They noted that the rate of carburization determines the deformation produced in a filament and found that W carburizes faster than Ta and deforms to a larger extent compared with Ta. Re does not form a stable carbide, they note, and thus does not exhibit geometric deformation. They reported that Re filaments were mechanically more stable than either W or Ta. Comparable growth rates were observed, by them, using all three filaments.

These authors also [22] reported, in detail, the carburization of Ta and W filaments. They found that W filaments converted to WC/W_2C at 2000 °C in 24 hours. The carburization rate did not seem to change with an increase in methane concentration (0.5% to 1.0%) or pressure (10 and 40 torr). The tantalum took longer to convert to TaC/Ta_2C. The carburization rate of the Ta filament increased with increasing methane concentration, gas pressure and filament temperature. At higher methane concentrations the Ta filaments were coated with carbon at 2000 °C and 2200 °C but at 2400 °C they did not find any carbon coating. For W, no carbon coatings were observed.

Based upon these studies one concludes that as far as the filament material is concerned, Re is preferred due to its mechanical stability, and Ta is favored due to the high melting point of its carbide. All three filaments have similar activities. High quality diamond films with comparable growth rates have been produced using filaments of all three materials. However, the filament as a source of contamination of the deposited films has not been investigated, to the best of our knowledge. It is, essential, for application purposes, to know what levels of metal are incorporated into films before HFCVD can be used as a commercial method for various applications of polycrystalline diamond films.

This study reports the effects of the filament material, temperature and distance from the substrate for a HFCVD reactor. The deposited films were characterized using scanning electron microscopy (SEM) for crystal morphology. Quantitative determination of the amount of filament material incorporated into the film was accomplished by using neutron activation analysis. Films were also characterized by Raman spectroscopy for film quality.

The advantages and disadvantages of the three filament materials are discussed. Filament performance has a new meaning in light of the film contamination produced by each filament material, as detected using neutron activation analysis. The effects of the filament temperature and distance on crystal morphology are also discussed.

Experimental

The films were deposited in a HFCVD reactor, described in Part 2. A wide range of growth conditions were used for depositing the films discussed in this Part. Two levels of methane concentration, 0.5% and 1.0%, in hydrogen

(total flow rate of 50 sccm), substrate temperatures in the range of 600 to 1050 °C and deposition durations ranging from 16 to 64 hours were used for these depositions. The pressure in the growth chamber was maintained at 40 torr by throttling the inlet of the mechanical pump which exhausted the system. The films were deposited on Si (001) substrates which had half of the growth surface scratched with diamond paste followed by rinsing with acetone and methanol in an ultrasonic bath. The scratched portion resulted in continuous film growth, while the other half had individual crystals. Filaments made out of W, Re and Ta were used at temperatures varying from 1700 to 2400 °C. The filament distance was maintained ~10 mm (unless its effect was being studied, in which case, it was changed to 5 mm).

The attributes of the filaments studied can be categorized into three features : (1) the filament material, (2) the filament temperature, and (3) the filament distance. In this study tungsten, rhenium and tantalum filaments were used. Films were grown under identical growth conditions using these three filaments and were compared to see the effects on growth morphology, crystalline quality, and the amount of metal being incorporated into the film. This was accomplished using SEM, Raman spectroscopy and neutron activation analysis, respectively. The effect of change in substrate temperature on the growth morphology and growth rate was observed for WC and TaC filaments. Filament temperature and distance were, similarly, found to affect the growth morphology and growth rate.

(1) Filament preparation (Carburization)

(i) Tungsten

A typical tungsten filament was made from a 12 cm long piece of a 0.5 mm diameter tungsten wire. This wire was then wound on a mandrel, to form a helical filament. Since W is not as soft as Re or Ta, the wire broke easily during winding if it was bent suddenly. The filament at this point had the appearance of a helical spring (~10 mm in length), with 5 to 7 turns and straight wire leads at the ends (2.0 cm long). In order to ensure uniform substrate temperature the helical spring portion of the filament was stretched to match the length of the substrate (length of the helical part was ~1.5 cm). It was quite difficult to stretch the tungsten wire filament due to its stiffness, and one needs to be careful because any stress present in the filament will distort it during carburization. The filament leads were inserted into holes in molybdenum support rods, and secured by screws.

Before utilizing the filament for growth it was typically heated in vacuum to a temperature of about 1800 °C for 2-3 minutes in order to relieve stress in the wire and then carburized. Typically, a tungsten filament was carburized under the following conditions : (a) methane concentration : 0.5%, (b) total flow : 50 cc/min, (c) total pressure : 40 torr , (d) filament temperature : 1950° C, (e) carburization time : 16 hours. The power to the filament was held constant during carburization.

Many times during carburization the filament became distorted. When this occurred it was discarded and the procedure repeated until a suitable filament was obtained. Typical distortions include touching of two of the turns on

the helical part of the filament or one of the ends of the filament bending closer to the substrate. At the end of carburization the tungsten filament appeared light gray in color with a black streak running through the coil. Figure 1 shows scanning electron micrographs of a WC filament which was fractured to enable viewing of both the surface and the interior structure. The micrograph of the fractured end of the wire reveals complete carburization (see fig. 1a). Figures 1b and 1c show the surface of the filament at higher magnification.

The most inconvenient characteristic of tungsten carbide filaments is their fragility due to brittleness. A small mechanical disturbance to the apparatus often resulted in a broken filament. This problem was partially solved by using a thicker W wire (0.625 mm diameter). Due to its brittleness, tungsten carbide filaments had a short life, typically three to four days. It was noted that higher gas phase carbon content deteriorated the filament faster. The filament turned dark gray as it aged and the surface appeared to have cracks and bubbles. Also the filament tends to expand with use, probably due to an increase in the diameter with the formation of a carbide layer.

(ii) Rhenium

A few experiments were done with Re wire filaments. These filaments were geometrically the same as the W filaments, but Re wire of 0.5 mm diameter was used. Since Re does not form a stable metal carbide, carburization procedures were not required. While these did not distort like the W filaments, one drawback in using a Re filament is that it sags with time. This leads to a change in the distance between the substrate and the filament introducing variation in growth parameters. Re filaments might be suitable for other CVD chambers with a different geometry, however, due to variability, their

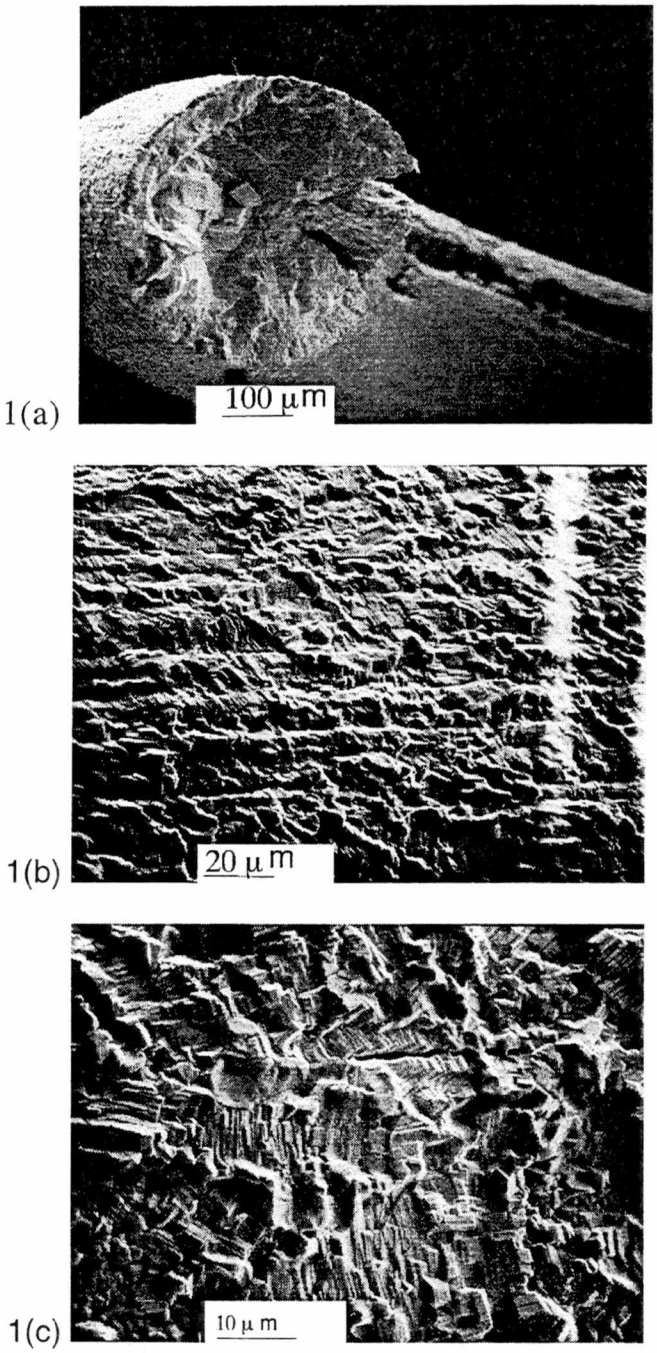

Figure 1 : Scanning electron micrographs showing the surface and cross section of a WC filament.

use was limited in this study. Figure 2 shows scanning electron micrographs of a Re filament. The surface appears to be smooth with small cracks on the surface.

(iii) Tantalum

Ta filaments were made using 0.5 mm Ta wire, wound in the same manner as tungsten, however, since Ta is a softer material than W, the two wire ends were wrapped around W rods (1.0 mm diameter) to form the leads of higher rigidity. These leads were then held securely in the molybdenum support rods. The carburization of Ta was a little different from that described for W. It was carried out in two stages. In the first stage, the conditions were : (a) methane concentration : 0.5%, (b) total flow : 50 cc/min, (c) total pressure : 40 torr, (d) filament temperature : 1950 °C, (e) carburization time : 16 hours. In the second stage, filament temperature was increased to 2350 °C and carburization was continued for another 16 hours. During each stage of carburization the power to the filament was held constant. The carburized filament was golden yellow in color. Figure 3 shows a scanning electron micrograph of a TaC filament. The surface of the filament appears to be smooth having small cracks, similar to those seen on the surface of Re filaments.

Quantitative determination of the amount of filament material incorporated into the film was accomplished by using neutron activation analysis. In this analysis [23, 24], a sample made up of stable isotopes of elements, by nuclear reactions, is made to produce radioactive isotopes. The radioactive isotopes emit radiation which is measured and qualitative as well as quantitative inferences are made of the elemental composition of the original sample. The

2(a)

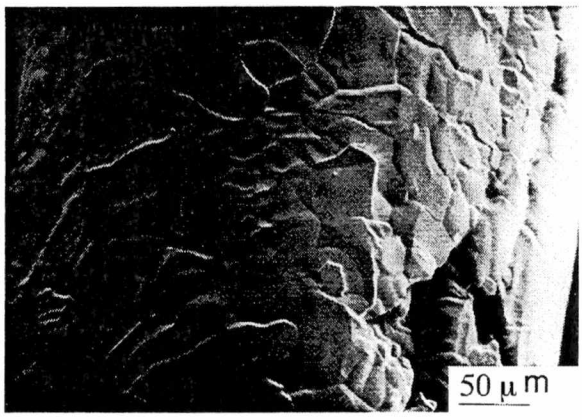

2(b)

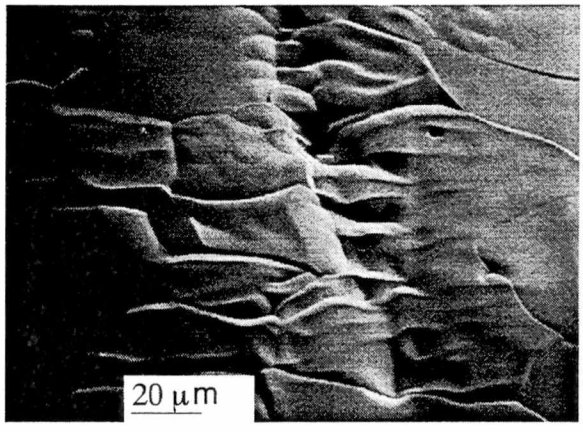

Figure 2 : Scanning electron micrographs showing the surface of a Re filament.

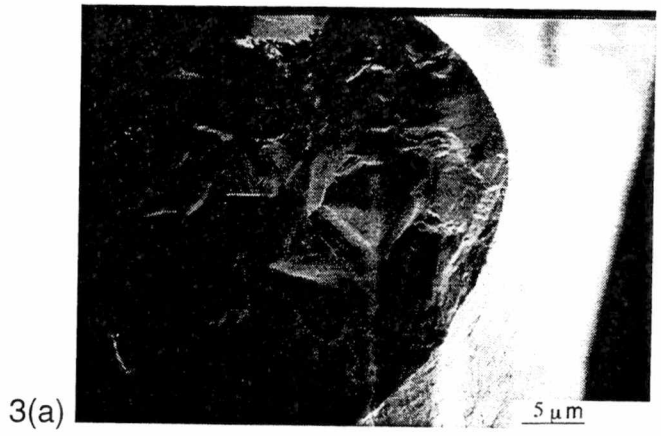

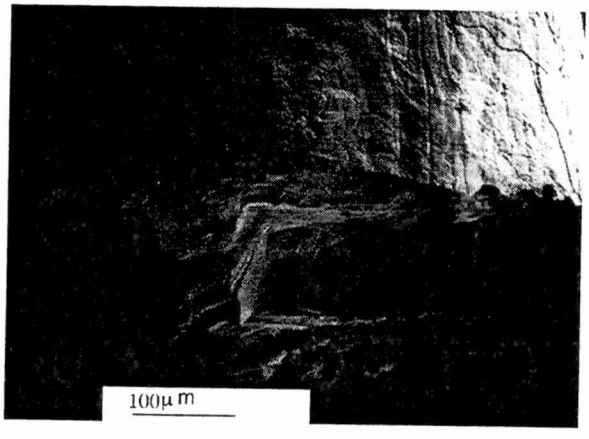

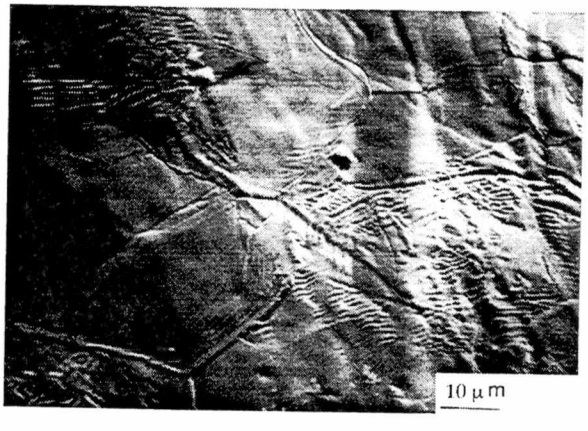

Figure 3: Scanning electron micrographs showing the surface and cross section of a TaC filament.

qualitative analyses is based on the fact that the radioactive isotopes exhibit characteristic beta and gamma ray energies and half lives. Since the induced activity due to a particular element in a sample is proportional to the amount of that element in the sample, very precise quantitative inferences can be made.

Results and Discussion

(1) Effects of filament material

The effect of the filament material on film morphology was studied in two settings. In the first case the depositions were carried out under identical growth conditions using filaments made from three different materials. These three films were then compared for growth morphologies and metal content. In the second case a set of experiments was carried out, first with a tungsten filament and then with a tantalum filament, to study the effect of change in the substrate temperature on growth morphology. The trends in growth morphologies were then compared, for the two filaments.

Comparison between W, Re and Ta filaments

The growth conditions for the films grown using the three different filaments are listed in Table 1. The gas composition was 1.0% methane in hydrogen. The pressure was held constant at 40 torr. The filaments were constructed to be identical. Wires of thickness 0.5 mm were used, and a filament with 7 turns was made. The rhenium wire filament sagged during deposition, so that it was closer to the substrate at the end of the deposition than it was at the beginning. The tantalum wire filament had W leads as described previously. All the three films were grown for 64 hours on silicon substrates.

Table 1 : Growth conditions for film deposition using Re, W and Ta filaments

Sample	Filament	Filament temp. (°C)	Substrate temp. (°C)	Growth rate (μm/hr)	Growth rate ratio
217	Re	1950	1018	0.63	0.87
218	W	1950	1010	0.81	0.87
308	Ta	1960	1010	0.67	0.87

Sections of Si (100) wafers, 2 cm X 1 cm X 0.05 cm, were prepared by scratching one half of the substrate surface with diamond paste, rinsing clean with acetone, and then cleaning it in an ultrasonic bath with methanol. The deposited films were imaged using a field emission scanning electron microscope (Hitachi S-800). Film quality was determined by Raman spectroscopy and metal content by neutron activation analysis.

Figures 4 (a-c) show scanning electron micrographs of the films grown with Re, W and Ta filaments. The morphology of the individual crystals as well as the continuous film appeared similar for all three samples compared. The filament material did not seem to affect the film morphology appreciably. The thickness of the film was measured by taking scanning electron micrograph of its cross section. For example, fig. 4 (d) shows the cross section image of the film grown with a Ta filament. The film thicknesses were found to be ~40 μm, ~52 μm and ~43 μm for the films grown with Re, W and Ta filaments, respectively.

4(a) 4(b)

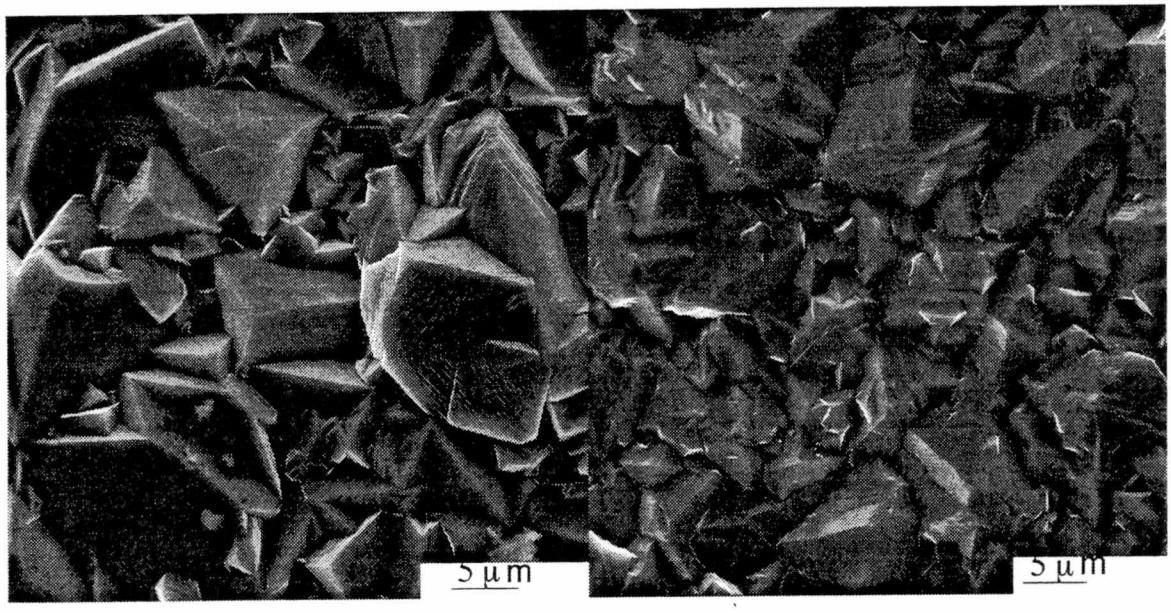

4(c)

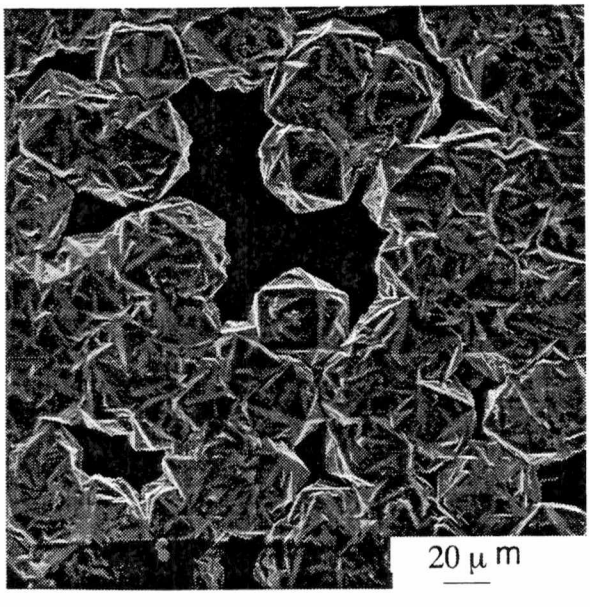

Figure 4 : Scanning electron micrographs showing the morphology of the films grown using the three different filaments.

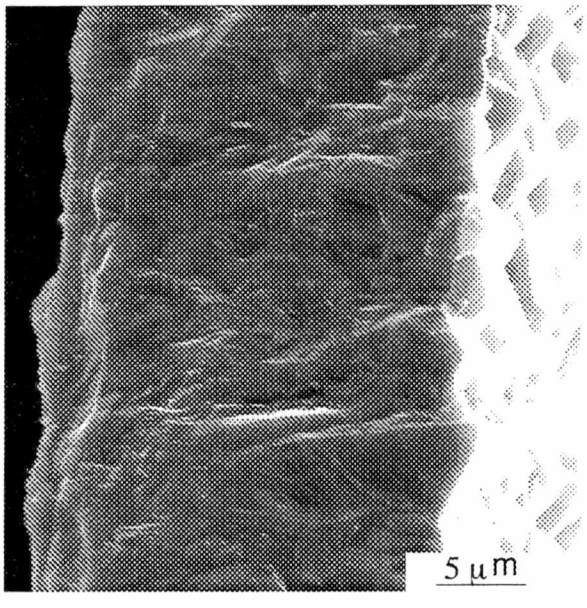

Figure 4(d) shows a cross section of the film showing the film thickness.

The growth rates obtained with the three filaments indicate that the film grown with a WC filament had the highest growth rate. A complicating factor in comparing growth rates for these is the distance of the filament from the substrate was different in each case. It is well established that the growth rate decreases with increasing filament distance.

Neutron activation analysis experiments were carried out to determine quantitatively how much metal from the filament was incorporated into the films. Table 2 gives the results of these analyses. The film that was grown using a Re filament had 2700 ppm Re in the film, whereas, the film grown using a W filament had only 1.0 ppm W in the film. This film also had 0.024 ppm Re. The molybdenum block that holds the substrate was resistively heated using a Re wire, which may be the source of Re in this film. The film grown using a TaC filament had 37 ppm of Ta incorporated in it. However, a TaC filament has other useful properties, including, that it is much less fragile than WC, and hence has a longer lifetime, as well as the fact that a TaC filament can be operated to a much higher temperature (up to 2500 °C). Therefore, additional experiments were done to examine the contamination levels at higher temperatures. This interest in higher filament temperature stems from the observations made while studying the effect of nitrogen incorporated in the growth of these polycrystalline diamond films. This is discussed in the Part 6 in greater detail.

The effect of the addition of impurities such as oxygen and nitrogen to the gas mixture has been of special interest to researchers in the diamond field. Samples that were grown in the presence of oxygen and NH_3 were analyzed to determine their effect on metal incorporation into the films. With the above arguments in mind, three more samples, listed in Table 3, were analyzed in

Table 2 : Neutron activation results showing the metal content in the films grown with different filaments

Sample	Filament type	Filament temp.	Subs. temp.	CH_4 (%)	W (ppm)	Re (ppm)	Ta (ppm)
217	Re	1950	1010	1.0	--	2700	--
218	W	1950	1018	1.0	1.0	0.024	--
308	Ta	1960	1010	1.0	--	--	330

Table 3 : The effect of filament temperature and addition of NH_3 and O_2 to the input gas mixture on the incorporation of the metal in the deposited film (Neutron activation analysis)

Sample	Filament type	Filament temp.	Subs. temp.	CH_4 (%)	W (ppm)	Re (ppm)	Ta (ppm)
308	Ta	1960	1010	10	--	--	330
309	Ta	2380	1010	1.0	200	--	17,400
310*	Ta	2400	1010	1.0	70	--	5350
0630†	W	1700	580	0.5	3360	7.3	--
218	W	1950	1018	1.0	1.0	0.024	--

*NH_3 was added.

†O_2 was added

From this analysis it is concluded that the contamination levels from a TaC filament were lower than from Re, but were not as good as those from WC. addition to those mentioned in Table 2. The sample that was grown with a TaC filament at 2380 °C had 17,400 ppm of Ta and 200 ppm of W in the film. The amount of Ta in the film increased by almost three orders of magnitude as the filament temperature was increased to 2380 °C. The amount of W coming from the filament leads (200 ppm) is also quite large especially when compared with the film that was grown at 1960 °C filament temperature. The addition of NH_3 at higher temperature, however brings the level of Ta to 5350 ppm and that of W to 70 ppm. In contrast, addition of oxygen increases the incorporation of metal in the film due to the formation of volatile metal oxides. The sample (0630) listed in Table 3 was grown at 1700 °C filament temperature with a WC filament in the presence of oxygen. This sample had 3360 ppm W and 7.3 ppm Re in the film; an increase of over 3 orders of magnitude in what was found without oxygen at 250 °C higher filament temperature. It must be noted, however, that substrate temperatures and methane concentrations were different for the samples (0630 and 218) being compared here.

Raman spectra of the films are shown in fig. 5. All samples show the characteristic diamond peak at 1332 cm^{-1}. The film grown with the Re filament had the sharpest peak with a FWHM of 6.0 cm^{-1}, an extremely low fluorescent background, and a very high diamond to graphite peak ratio, indicating a very high quality diamond film. The films grown with the W and Ta filaments had much larger FWHM of 17.9 and 13.6 cm^{-1}, respectively, showed considerable fluorescent background and a significant sp^2 carbon peaks. This data clearly shows the pronounced difference in crystalline quality of these films. The films

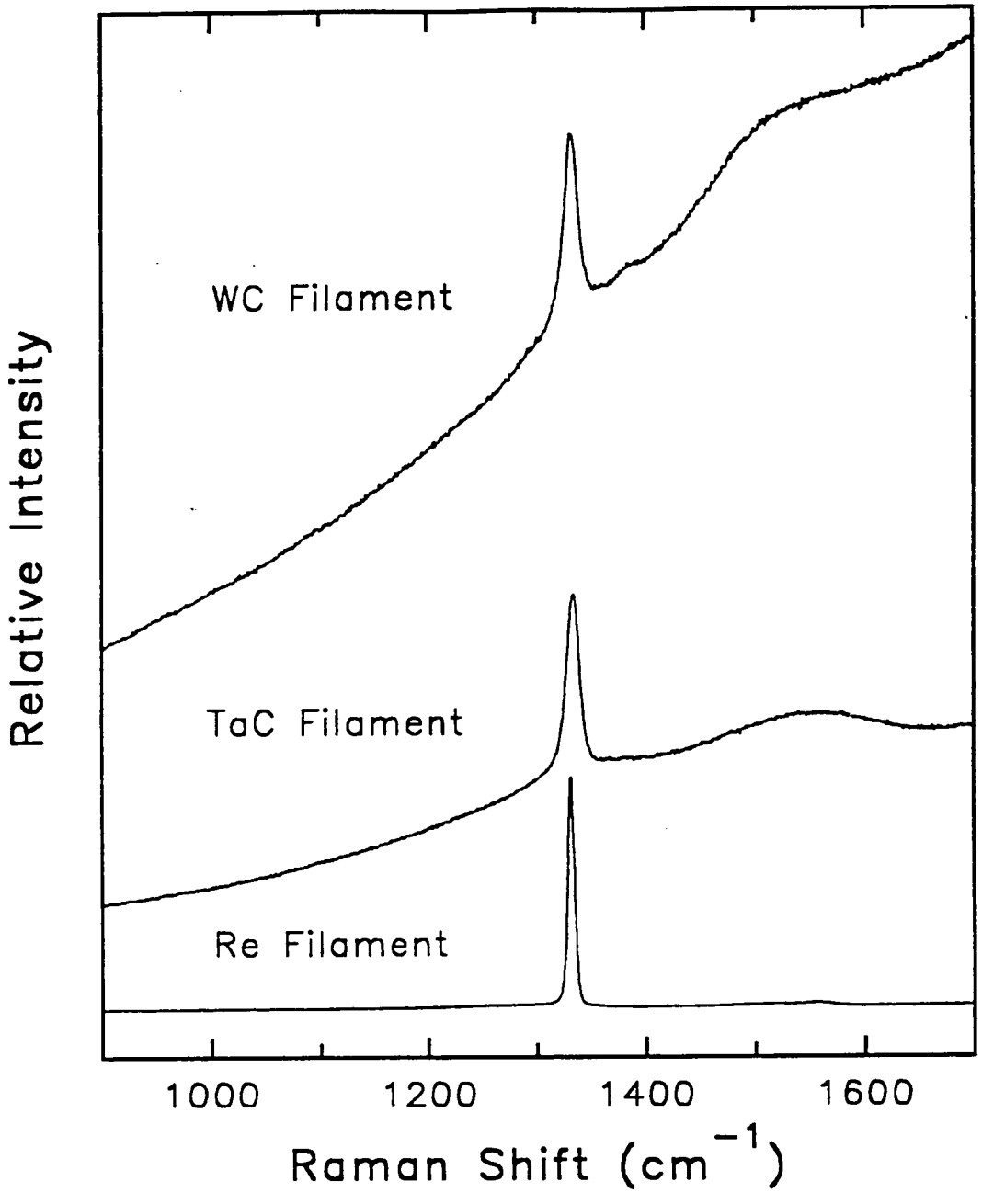

Figure 5 : Raman spectra of the films grown under identical growth conditions using : (a) Re, (b) WC, and (c) TaC filaments.

grown with Re and WC (with the addition of O_2) filaments exhibit better crystalline quality than the other samples. Both of these samples also had much higher metal content, as reported by neutron activation analysis.

(2) Growth morphology trends as a function of substrate temperature for W and Ta filaments

The growth conditions for the experiments carried out to study the relationship between the substrate temperature and the film morphology are listed in Tables 4 and 5 for WC and TaC filaments, respectively. Figure 6 shows electron micrographs for the samples listed in the Table 4. From analysis of these data, the growth rate ratio, was found to change from 1.5 to 1.15, i.e. from octahedral to irregular cubo-octahedral geometry, as the substrate temperature was increased from 704 °C to 736 °C. Figure 7 shows the scanning electron micrographs of films deposited using a TaC filament. As the temperature was further increased from 766 °C to 946 ° C the crystals changed to cubes corresponding to a growth rate ratio of 0.6. The overall growth rate, in this temperature regime, initially increased from 0.2 μm/hr at 704 °C to 0.24 μm/hr at 736 °C and then tapered off to 0.17 μm/hr at 946 °C. Similar trends regarding the morphology as well as the growth rate were seen for films grown using a TaC filament. As the temperature was changed from 706 °C to 775 °C the crystal morphology changed from being nearly octahedral to irregular cubo-octahedral and at 963 °C the crystal were nearly cubes with small (111) faces at the corners. The corresponding growth rate ratios for the temperatures mentioned above, were 1.4, 1.07 and 0.75 μm/hr, respectively. The overall growth rates increased from 0.350 μm/hr at 706 °C to 0.406 μm/hr at 775 °C and then decreased to 0.375 μm/hr at 963 °C. Thus the growth morphology and

Table 4 : Growth conditions used in the deposition of films using a tungsten filament

Sample	CH_4 (%)	Filament type	Filament temp. (°C)	Subs. temp (°C)	Growth rate (μm/hr)	Growth rate ratio	Alpha
270	0.5	W	1970	704	0.20	1.5	2.6
269	0.5	W	1970	736	0.24	1.15	1.9
276	0.5	W	1965	766	0.18	0.6	1.0
277	0.5	W	1960	815	0.18	0.6	1.0
278	0.5	W	1960	908	0.18	0.6	1.0
279	0.5	W	1950	946	0.17	0.6	1.0

Table 5 : Growth conditions used in the deposition of films using a tantalum filament

Sample	CH_4 (%)	Filament type	Filament temp. (°C)	Subs. temp (°C)	Growth rate (μm/hr)	Growth rate ratio	Alpha
264	0.5	Ta	1950	706	0.35	1.4	2.4
267	0.5	Ta	1940	775	0.41	1.0	1.7
266	0.5	Ta	1950	963	0.38	0.7	1.3

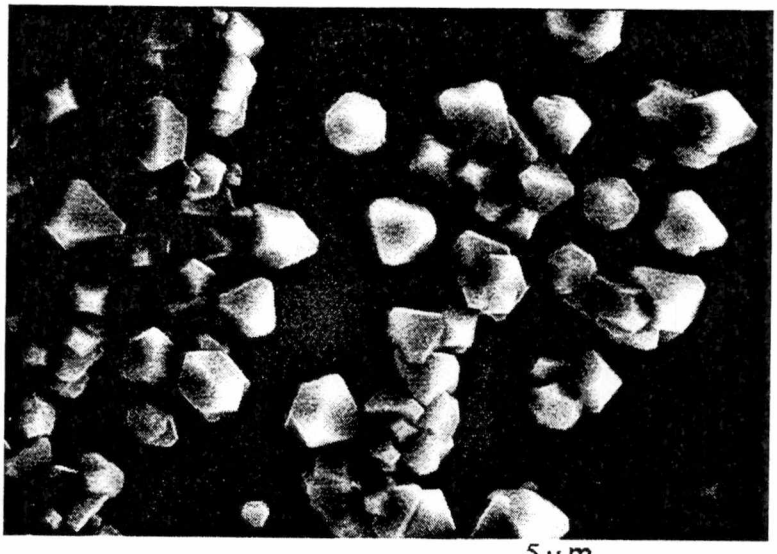

6(a)

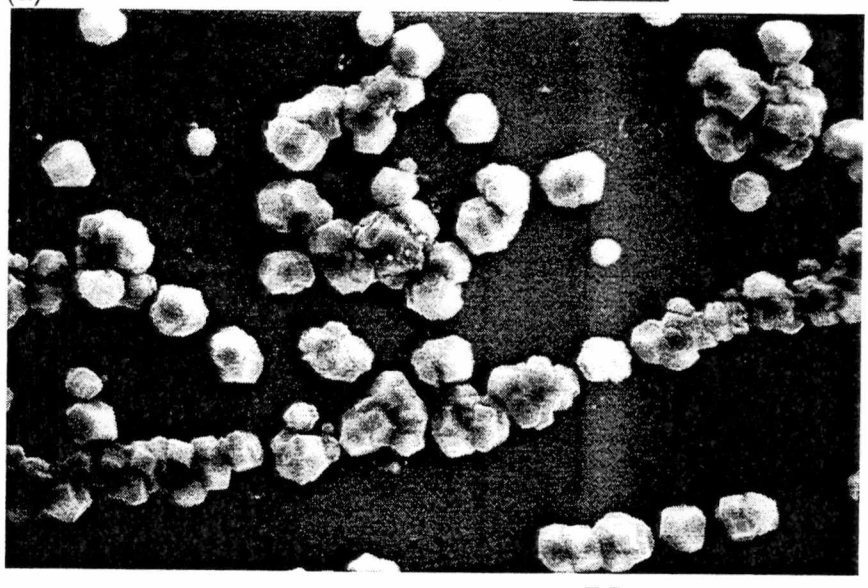

6(b)

Figure 6 : Scanning electron micrographs showing the morphology of films grown with a WC filament. The growth conditions for these films were as follows, filament temperature 1950-1970 °C, methane concentration 0.5%, and, substrate temperature : (a) 704 °C,(b) 736 °C.

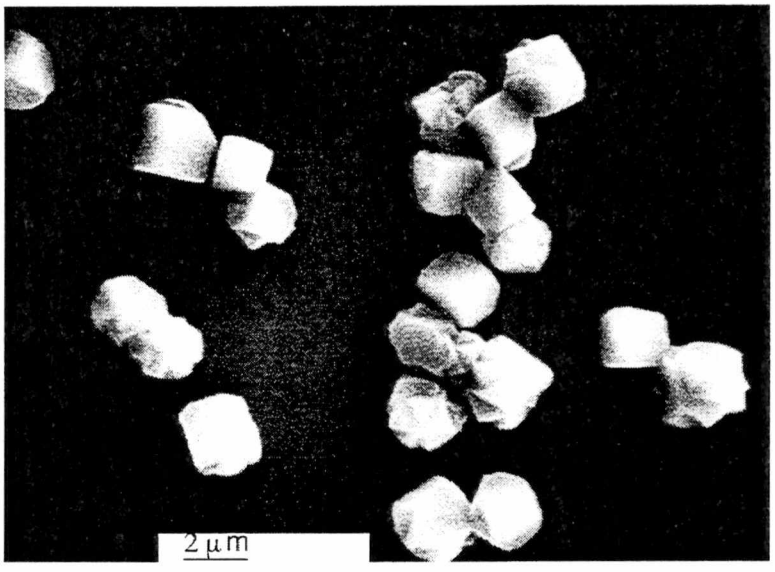

6(c)

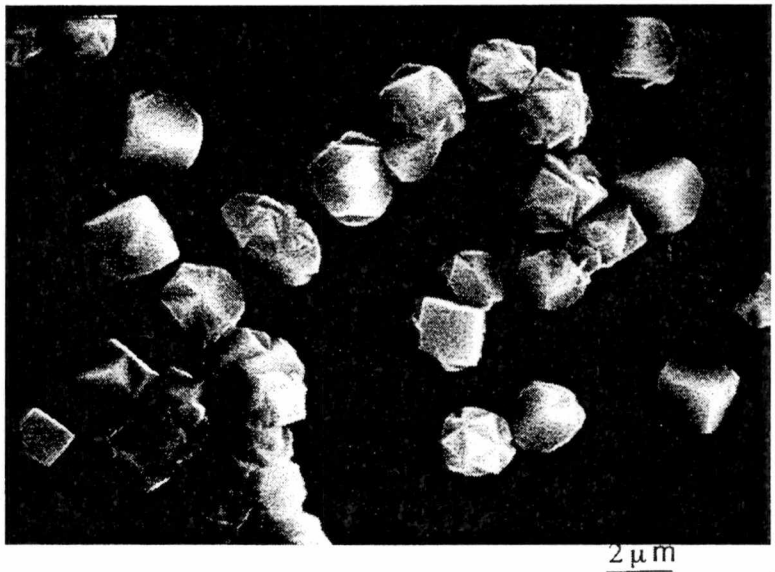

6(d)

Figure 6 : Scanning electron micrographs showing the morphology of films grown with a WC filament. The growth conditions for these films were as follows, filament temperature 1950-1970 °C, methane concentration 0.5%, and, substrate temperature : (c) 766 °C, (d) 815 °C.

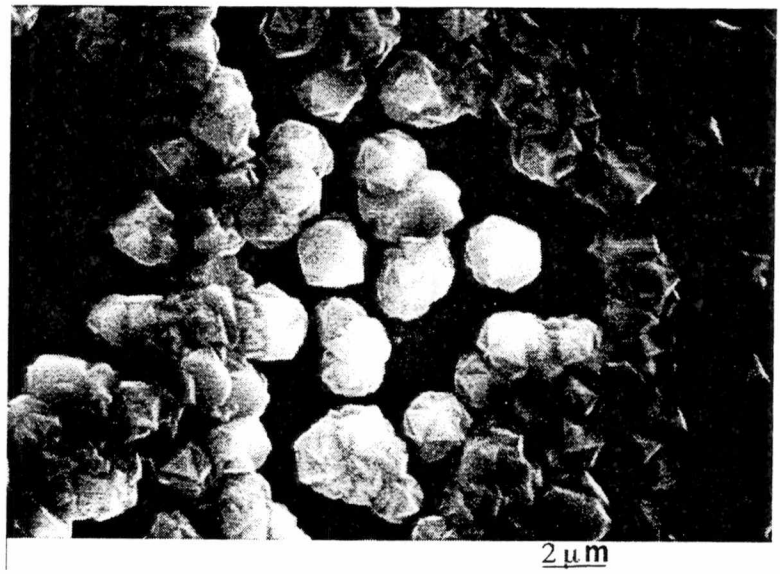

6(e)

Figure 6 : Scanning electron micrographs showing the morphology of films grown with a WC filament. The growth conditions for these films were as follows, filament temperature 1950-1970 °C, methane concentration 0.5%, and, substrate temperature : (e) 908 °C.

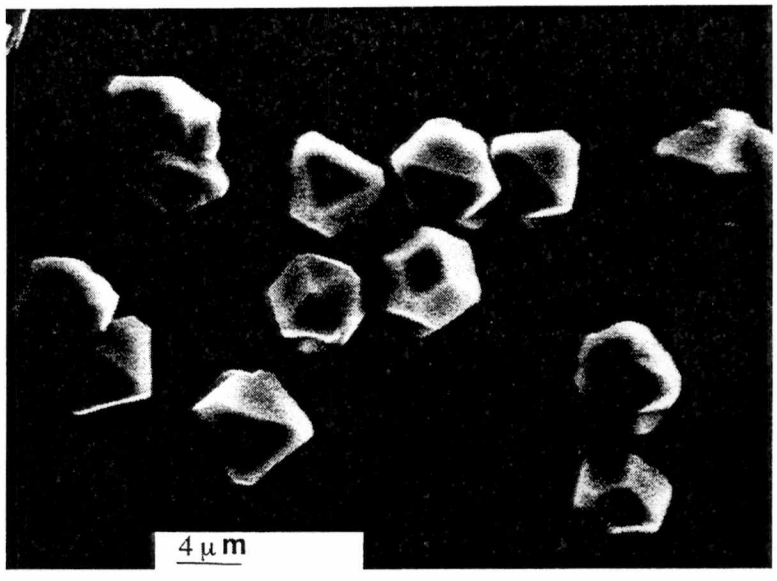

7(a)

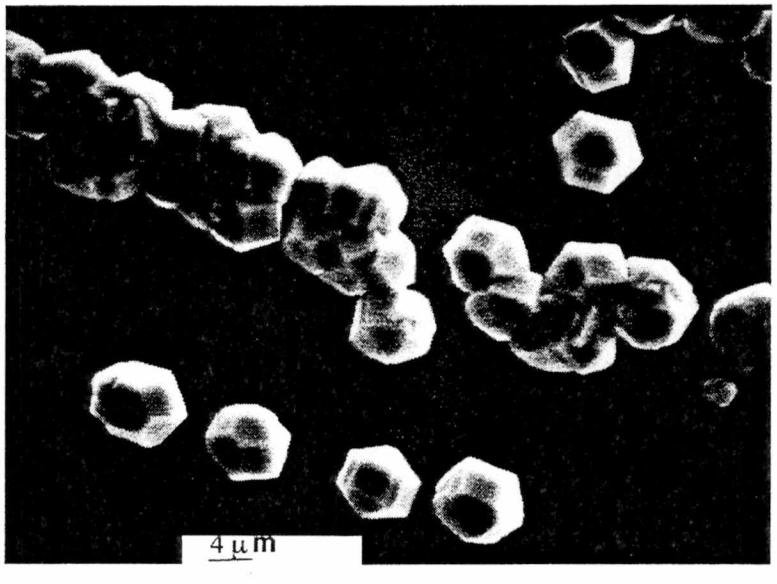

7(b)

Figure 7 : Scanning electron micrographs showing the morphology of films grown with a TaC filament. The growth conditions for these films were as follows, filament temperature ~1950 °C, methane concentration 0.5%, and, substrate temperature : (a) 706 °C,(b) 775 °C.

7(c) 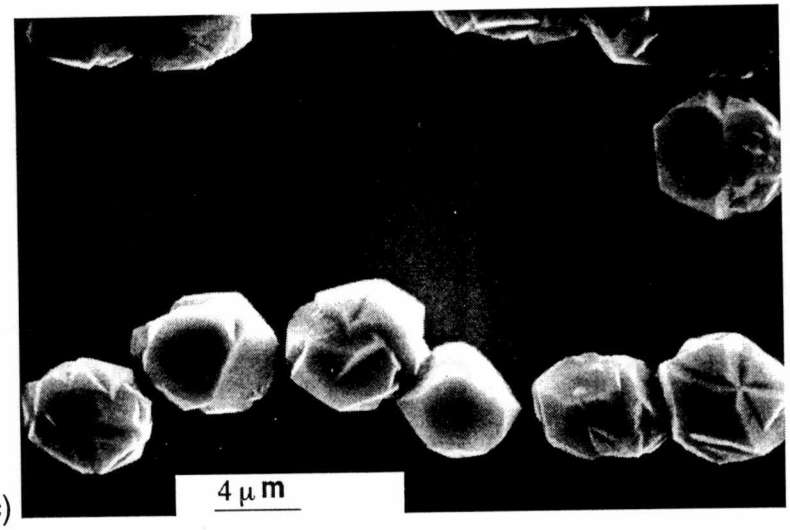

Figure 7 : Scanning electron micrographs showing the morphology of films grown with a TaC filament. The growth conditions for these films were as follows, filament temperature ~1950 °C, methane concentration 0.5%, and, substrate temperature : (c) 963 °C.

overall growth rates do not appear to depend significantly on the filament material.

(3) Filament temperature

Experiments were carried out, to study the effect of filament temperature on the morphology and growth rate of films. These experiments were accomplished using a WC filament having 5 turns, made from 0.625 mm diameter tungsten wire. Table 6 lists the growth conditions used in this series. The filament temperature was changed from 1880 °C to 2050 °C. The scanning electron micrographs of these films are presented in fig. 8.

At the lowest filament temperature (1880 °C) mostly sp^2 carbon was deposited, however as the filament temperature was increased to 1950 °C, crystals with octahedral geometry were deposited. As the filament temperature was further increased to 2000 °C and then to 2050 °C, the crystal morphology did not change, however a small change in growth rate was observed. The growth rate, increased from 0.21 to 0.33 μm/hr with the increase in filament temperature from 1950 to 2000 °C.

(4) Filament distance

Filament distance is known to affect the growth rate of the deposited film. The larger the distance between the filament and the substrate, the lower the growth rate. Two films were deposited under identical growth conditions of filament temperature (1980 °C), substrate temperature (~950 °C) and methane concentration (1.0%), but with different filament distance. The first sample was placed 10 mm, whereas the second, only 5 mm away from the lowest point of

Table 6 : Growth conditions used to study the effect of filament temperature on the morphology of the films deposited using a tungsten filament.

Sample	CH_4 (%)	Filament type	Filament temp.	Subs. temp	Growth rate (μm/hr)	Growth rate ratio	Alpha
268	0.5	W	1880	640	--	--	--
275	0.5	W	1950	647	0.21	1.5	2.6
296	0.5	W	2000	650	0.33	1.5	2.6
297	0.5	W	2050	647	0.33	1.5	2.6

8(a)

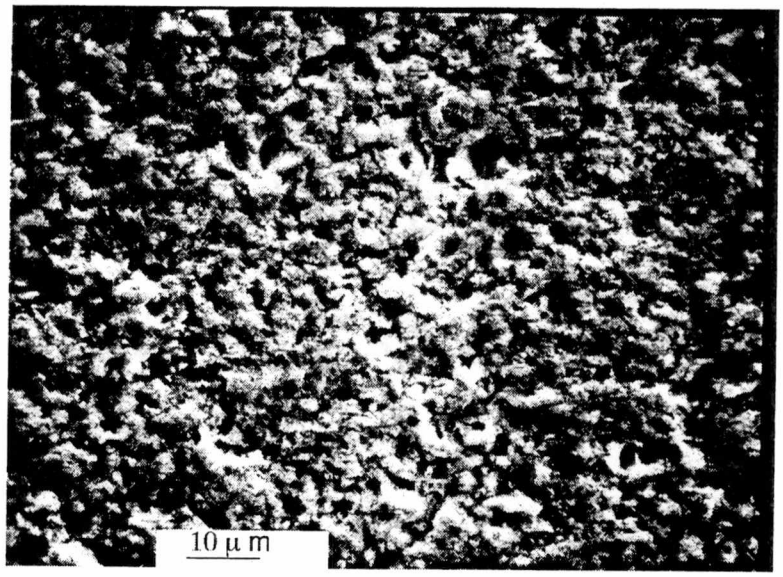

8(b)

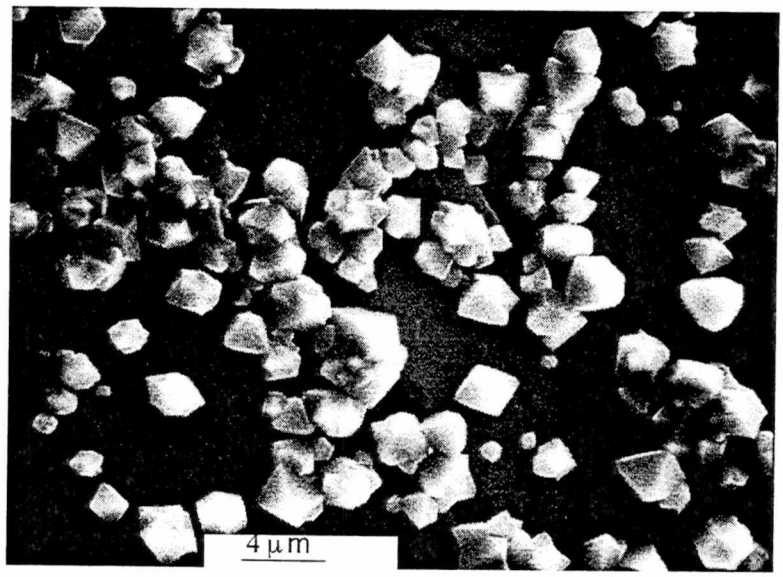

Figure 8 : Scanning electron micrographs showing the morphology of the films grown at different filament temperatures using a WC filament. The growth conditions used were as follows, substrate temperature ~650 °C, methane concentration 0.5%, and the filament temperature : (a) 1880 °C, (b) 1950 °C.

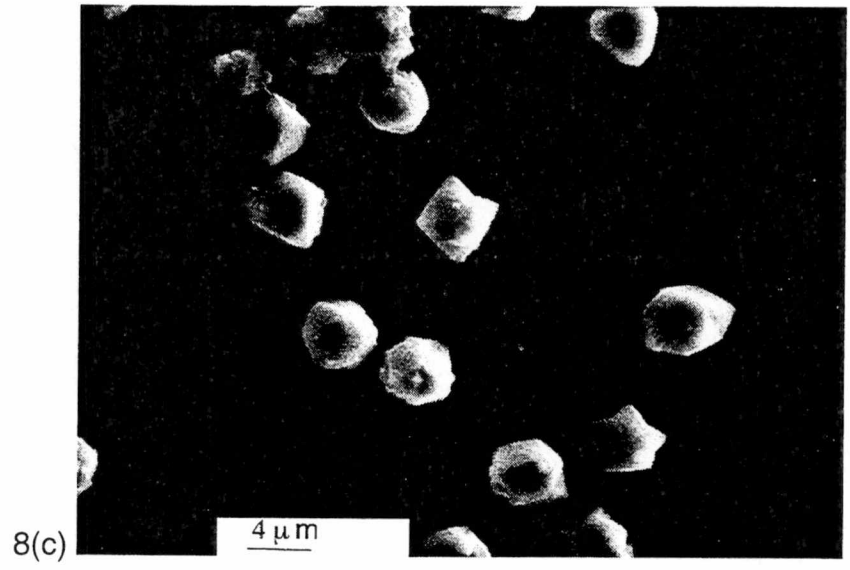

8(c)

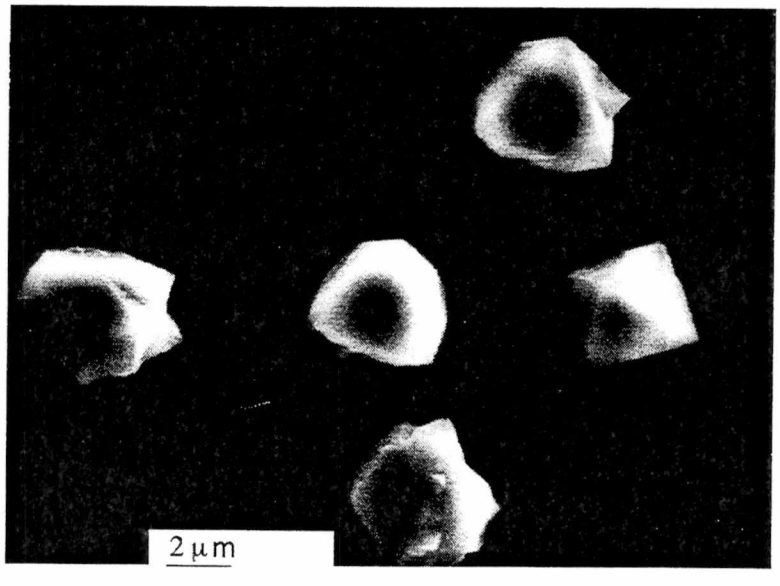

8(d)

Figure 8 : Scanning electron micrographs showing the morphology of the films grown at different filament temperatures using a WC filament. The growth conditions used were as follows, substrate temperature ~650 °C, methane concentration 0.5%, and the filament temperature : (c) 2000 °C, (d) 2050 °C.

the filament. The two films showed similarity in film morphology, both had crystallite shapes corresponding to growth rate ratio of 0.87 (α =1.5). However, the two films differed in thickness. The film deposited on the substrate placed closer to the filament (d=5 mm) had a growth rate of 0.90 μm/hr whereas the other deposited film (d=10 mm) had a growth rate of 0.30 μm/hr.

Summary of Results

(1) Mechanical stability renders Re filaments longer lasting than WC or TaC filaments. TaC lasted longer than the WC filament. The TaC filament is operable at much higher temperatures than any other filament.

(2) Films grown using all three filaments appeared similar in crystal morphology and had comparable growth rates. Films grown using TaC and WC filaments showed similar trends in morphology as the substrate temperature was changed.

(3) Metal contamination by the filament, as determined using neutron activation analysis, showed great variability for the three filaments. At 1950 °C the film grown using the Re filament had the highest amount of metal in the film, next was TaC and the film grown using the WC filament showed the least amount of metal. At 2400 °C, however, the amount of metal increased by a factor of 50. Addition of oxygen substitutionally increased the amount of W in the film whereas addition of NH_3 decreased the amount of Ta in the film.

(4) Raman data from the three samples showed pronounced differences for the three samples grown using different filaments. The film grown with Re appeared to have the highest crystalline quality as exhibited by the peak width at 1332

cm^{-1} and low background. It also had the highest metal content. Another film that had high metal content, which was deposited using a WC filament with O_2 addition, also showed good crystalline quality. There appeared to be a correlation between the metal content and crystalline quality of the film.

(5) Filament temperature does not appear to affect the growth morphology after a certain critical temperature. The growth rate increases with increasing filament temperature.

(6) Filament distance does not affect the crystal morphology; however, the growth rate increases with decreasing distance between the filament and the substrate.

Conclusions

The filament material affects reactor performance due to the difference in the thermodynamic characteristics responsible for metal carbide formation. The W filaments carburized faster than the Ta filaments and deformed to a higher degree as well. Re showed no deformation since it does not form a stable carbide, and had higher mechanical stability. A drawback for Re filaments is that they sagged appreciably and exhibited high contamination levels in the deposited films. WC and TaC both break easily, however, TaC filaments had a longer life than did the WC filaments. On the other hand, the films grown with WC showed the least contamination, one and three orders of magnitude less than that produced by TaC and Re filaments, respectively. In contrast to these observations, films grown with the Re filament showed the best crystalline quality. Films grown under similar conditions of filament and substrate

temperatures, and methane concentrations, had similar morphologies irrespective of the filament material.

Ta, W and Re are members of groups V-A, VI-A and VII-A in the periodic table of the elements, with atomic numbers 73, 74 and 75, respectively. All have incomplete d-shells of a lower quantum state while the next higher state is already filled with 's' electrons. They fall under the category of refractory metals with melting points of 2996, 3410 and 3180 °C, respectively [25]. They exhibit high mechanical strength at elevated temperatures.

Rhenium is a rare and precious metal, is thus quite expensive. It has a vapor pressure which is 1.5 times that of Ta and 10 times that of W. It has 4 oxides --- Re_2O_3, ReO_2, ReO_3 and Re_2O_7. Above 600 °C it undergoes rapid oxidation, in air, to form Re_2O_7, which has a melting point of 297 °C and is readily formed at grain boundaries when metal is worked in hot air. Re does not form a carbide and is thus not embrittled. The thermal conductivity of Re is much lower than that of W and only slightly higher than that of Ta. Re has one of the highest values of Young's modulus of elasticity among the metals, and it exhibits great strength at high temperatures. It is not embrittled by recrystallization to the same extent as tungsten and retains some degree of ductility at high temperature.

Tungsten has three oxides --- WO_3, W_2O_5 and WO_2. It undergoes rapid oxidation in air and in the presence of water vapor above 500 °C. The "water cycle" rapidly destroys tungsten filaments when they operate in presence of traces of water. It does not react with nitrogen up to 2000 °C, however, forms a dinitride with absorbed nitrogen at 2300 °C. It forms a carbide above 1200 °C which decomposes at 2430 °C.

Tantalum also has a high melting point and very low vapor pressure at high temperatures, which is lower than that of Re but slightly higher than that of W. Figure 9 shows the vapor pressure data for the three metals used for making filaments. Ta has ductility over a broad temperature range and undergoes rapid oxidation in air, oxygen and water vapor at temperatures greater than 600 °C. It forms two oxides ---- Ta_2O_4 and Ta_2O_5. It forms TaN when reacted with N_2 at 100 °C. TaN is an interstitial compound, a substantial volume change accompanies its formation. At 1200 °C it forms a partial carbide, which is complete at 1400 °C.

Figures 10 and 11 show the phase diagrams of the C-Ta and C-W systems, respectively. Ta forms two carbides, TaC and Ta_2C that have high melting points, 3800 and 3400 °C, respectively [26]. The crystal structure of TaC is cubic, whereas Ta_2C is hexagonal. Tungsten forms two carbides --- WC and W_2C as shown in fig. 11. The melting point of WC is 2600 °C and that of W_2C is 2750 °C. The crystal structure of W_2C is hexagonal with two W and one C atom per unit cell. WC has a simple hexagonal structure consisting of two interpenetrating simple hexagonal lattices of the W and C atoms.

References

1. M. Sommer and F. W. Smith, J. Mater. Res. **5**, 2433 (1990).

2. M. Sommer and F. W. Smith, J. Vac. Sci. Technol. A 9 (3), 1134 (1991).

3. R. R. Rye, J. Appl. Phys. **76**, 1220 (1994).

4. H. F. Winters, H. Seki, R. R. Rye and M. E. Coltrin, J. Appl. Phys. **76**, 1228 (1994).

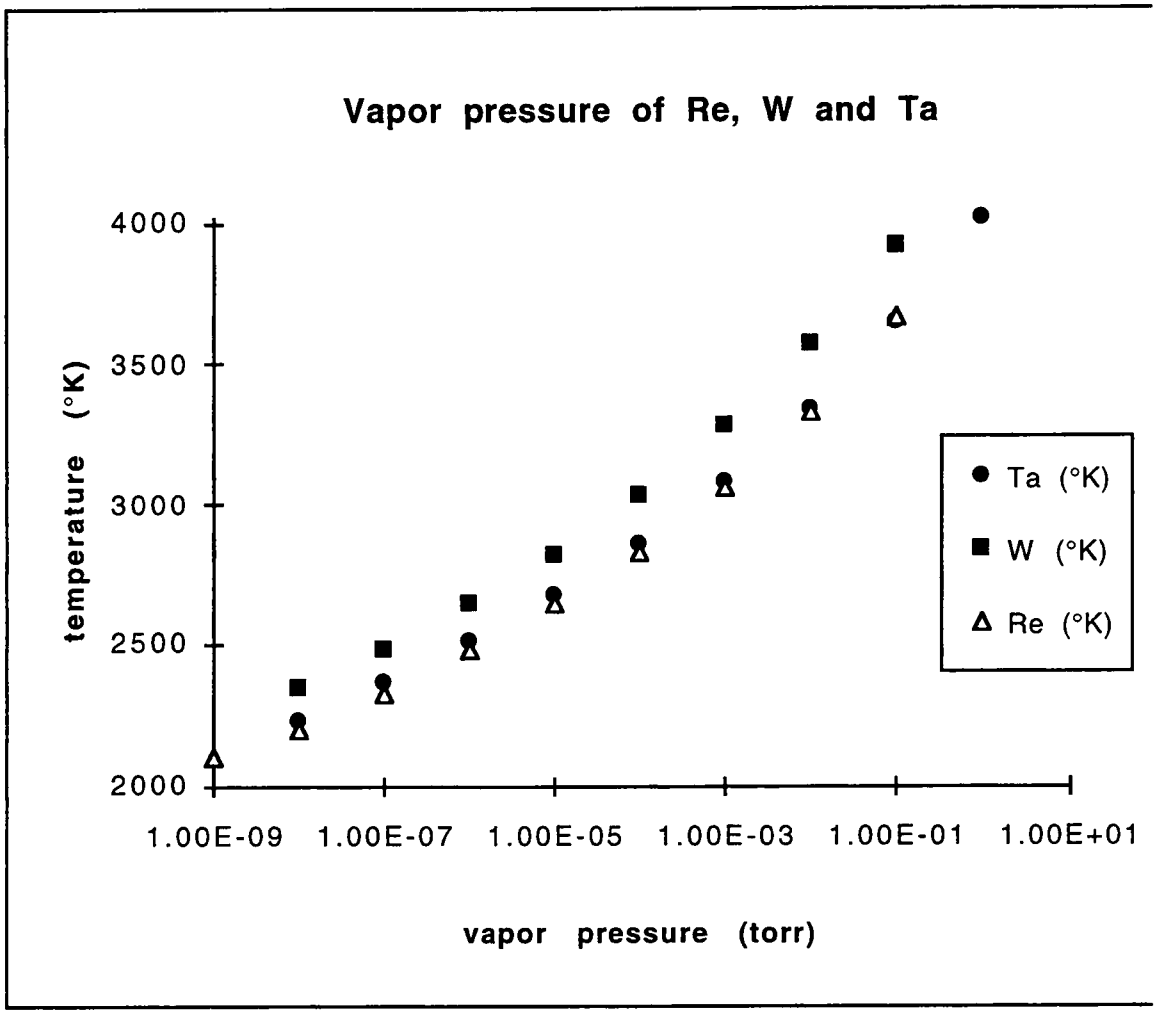

Figure 9 : Vapor pressure of Re, W and Ta. [Source : W. H. Kohl, *Handbook of Materials and Techniques for Vacuum Devices*, Reinhold Publishing Corporation (1967).]

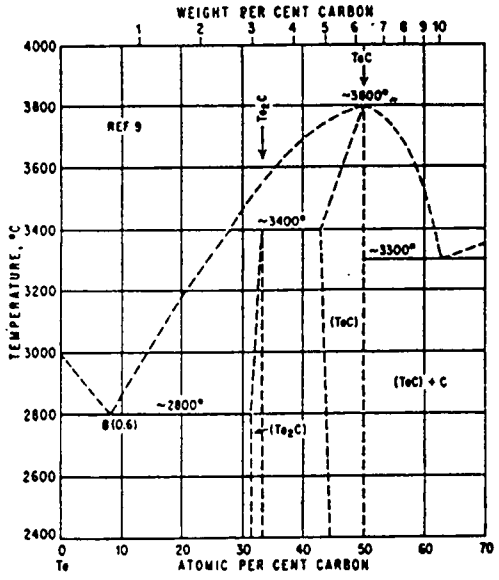

Figure 10 : Phase diagram of C-Ta system. [Source : J. G. Hansen, Constitution of Binary alloys, Metallurgy and Metallurgical engineering series, Mc Graw Hill Book Company.]

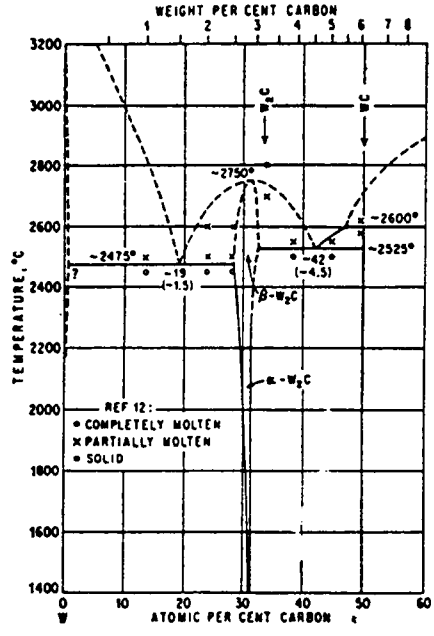

Figure 11 : Phase diagram of C-W system. [Source : J. G. Hansen, Constitution of Binary alloys, Metallurgy and Metallurgical engineering series, Mc Graw Hill Book Company.]

5. C. J. Chu, M. P. D'Evelyn, R. H. Hauge and J. L. Margrave, J. Mater. Res. **5**, 2405 (1990).

6. C. J. Chu, M. P. D'Evelyn, R. H. Hauge and J. L. Margrave, J. Appl. Phys. **70**, 1695 (1991).

7. S. J. Harris and A. M. Weiner, J. Appl. Phys. **70**, 1385 (1991).

8. S. J. Harris and L. R. Martin, J. Mater. Res. **5**, 2313 (1990).

9. D. Huang and M. Frenklach, J. Phys. Chem. **96**, 1868 (1992).

10. M. Frenklach and K. E. Spear, J. Mater. Res. **3**, 133 (1991).

11. D. Huang, M. Frenklach and M. Maroncelli, J. Phys. Chem. **92**, 6379 (1988).

12. D. N. Belton and S. J. Harris, J. Chem. Phys. **96**, 2371 (1992).

13. E. Kondoh, T. Ohta, T. Mitomo and K. Ohtsuka, Appl. Phys. Lett. 59, 488 (1991).

14. E. J. Corat and D. G. Goodwin, J. Appl. Phys. **74**, 2021 (1993).

15. F. G. Celii and J. E. Butler, Appl. Phys. Lett. 54, 1031 (1989).

16. L. L. Connell, J. W. Fleming, H. N. Chu, D. J. Vestyck, Jr., M. E. Jensen and J. E. Butler, J. Appl. Phys. **78**, 3622 (1995).

17. H. Toyoda, M. A. Childs, K. L. Menningen, L. W. Anderson and J. E. Lawler, J. Appl. Phys. **75**, 3142 (1994).

18. D. S. Dandy and M. E. Coltrin, J. Appl. Phys. **76**, 3102 (1994).

19. S. J. Harris, A. M. Weiner and T. A. Perry, Appl. Phys. Lett. **53**, 1605 (1988).

20. G. Leyendecker, J. Doppetbauer, D. Bauerle, P. Geittner and H. Lydtin, Appl. Phys. A **30**, 237 (1983).

21. S. Okoli, R. Haubner and B. Lux, Journal de Physique IV, (1991).

22. S. Okoli, R. Haubner and B. Lux, Surface and Coatings Technology **47**, 585 (1991).

23. W. S. Lyon, Jr., Guide *to Activation Analysis*, edited by W. S. Lyon, Jr., D. Van Nostrand Company, Inc. (1964).

24. P. Kruger, *Principles of Activation Analysis*, Wiley-Interscience (1971).

25. W. H. Kohl, *Handbook of Materials and Techniques for Vacuum Devices*, Reinhold Publishing Corporation (1967).

26. J. G. Hansen, *Constitution of Binary alloys, Metallurgy and Metallurgical engineering series*, Mc Graw Hill Book Company.

Part 4 : Growth morphology of hot filament chemical vapor deposited diamond films

Introduction

The growth of polycrystalline diamond films, whether by microwave plasma or by hot filament, can produce high crystalline quality diamond films over a narrow range of growth parameters [1] (such as the substrate temperature, methane concentration, etc.). High crystalline quality is usually characterized by clean facets, large grain size and a prominent Raman peak at 1332 cm^{-1}. Texture and morphology of these films can be controlled to a certain extent within this high quality growth regime. While significant progress has been made in the development of models for diamond growth [2-4], particularly for the {100} surfaces [5], no comprehensive models which can account for the range of growth morphologies observed has been established. The relation between the chemical aspects of the diamond growth mechanisms and film properties is not clear. Parametric studies of crystal structure and film morphology are essential for establishing this connection [6].

The competition of growth velocities in different crystallographic directions has been recognized [7] as a determining factor in film morphology and can be used to grow highly textured films [8,9]. Studies on homoepitaxial diamond growth reveal differences in the kinetics of growth in various growth directions [10,11]. The origin and role of twins and stacking faults has also been recognized but not completely understood yet. Geometric arguments which relate the growth velocities to the suppression or promotion of twin growth have been developed [12]. Some of these arguments have been verified by computer simulations and experimental observations for a microwave plasma system [13]. Both of these groups [12, 13] have presented an "alpha map" for their microwave plasma systems. Alpha (α) is defined as $\sqrt{3}$ times the ratio (**r**) of the

growth rate in the <100> direction to that in the <111> direction. This map is a graphical representation of the relation between growth parameters, specifically the methane concentration and substrate temperature, and the ratio of the rate of growth in the [100] and [111] crystallographic directions.

No comparable studies have been found in the literature for a hot filament system. This is not very surprising, considering that the data needed for such a map should be obtained using the same filament and the fact that the lifetime of a filament is relatively short. One could use more than one filament but these filaments would have to be identical to avoid inconsistency in the growth conditions. The issue of the filament material, relating its performance and lifetime to morphology has been discussed in Part 3.

We have generated an α map for our HFCVD system using a single filament for all depositions and here present results on how the morphology and the presence of twins depend on growth parameters. These results are compared to the microwave plasma studies that have been previously reported by others. The growth charts that are reported here are typical of our experimental apparatus which is based on a quartz tube reactor. It is expected that similar trends should be observable in other HFCVD systems, however differences in system configuration may modify the specifics in the relationships between the growth conditions and morphology.

Strong trends have been observed regarding the presence and appearance of twins on crystallite faces. These trends are categorized, in this study, according to the growth parameters, specifically the methane concentration and the substrate temperature and are compared with the theoretical predictions of Tamor et al. [12] and computer simulations of Wild et

al. [13]. Our observations appear to agree quite well with these predictions and with the experimental observations made on films grown via microwave plasma chemical vapor deposition (MPCVD) [12,13].

There are various subtleties in the relationship between the growth rates, the competition of growth in different crystallographic directions, and the developed crystal shape and film texture. In general, faces perpendicular to the fastest growth direction tend to be eliminated in individual crystallites. For example, the growth in the [110] direction is the fastest of the three directions, so that one never observes the {110} faces. For a cube, the rate of growth in the [111] direction is much faster than that in the [100], in fact so much so, that the {111} faces grow out and the crystal is left with only {100} faces, which gives rise to the cube. For a perfect cube the growth rate in the [111] direction is $\sqrt{3}$ times that in the [100] direction, which corresponds to an $\mathbf{r} = 0.58$ ($\alpha = 1$) . The longest dimension of the cube is the body diagonal, which is along the [111] direction.

Similarly for an octahedron, growth in the [100] direction is much faster than in the [111] direction, yielding a crystal consisting of only the slower growing {111} faces. A perfect octahedron corresponds to $\mathbf{r} = 1.5$ ($\alpha = 2.6$), and its longest dimension is along the [100] direction. It is in the region where cubo-octahedron geometry is observed that the competition between the growth rates in the [100] and the [111] directions is close. In this growth regime the fastest growing direction is along the [100] direction of the crystal. Thus the longest dimension in the crystal is changing from [111] to [110] and then to [100] as the crystal shape is transforming from a cube to a cubo-octahedron and then to an octahedron. These directions are important because, growth rate is usually

determined from the largest linear dimension that is reported and the growth rate ratio (or α) provides the information regarding the ratio of the growth rates in the [100] and the [111] growth directions. The growth parameters affect both the growth rate as well as the growth rate ratio, hence growth in these crystallographic directions is being affected differently by the change in the growth conditions.

Homoepitaxial studies [10,11] show that rates in different crystallographic directions indeed depend upon growth parameters. Its implications on the growth kinetics has also been presented [11]. Another aspect of growth rates in the [100] and [111] directions is that once the crystal has reached the geometry of a perfect cube, since the growth in the [111] has already reached its maximum, further increase in growth rate in that direction can't be measured. Maeda et al. [10] have very clearly and elegantly taken that into account in their analyses.

Growth rates along the [100] and [111] directions has been determined as a function of growth parameters in this study. Maeda et al. [10] have previously determined the rates in the [100] and [111] directions for homoepitaxial growth by the use of trigonometric relations involving dimensions measured from a two dimensional SEM. They have accomplished this by initially carrying out the growth under conditions that gave cubo-octahedron geometry, then, imaged the sample under an SEM and then continued the growth under conditions facilitating either an octahedron or a cube. By measuring the change in the dimensions of the crystals they are able to report the absolute change in growth rates in the different crystallographic directions. Chu et al. [11] have determined the growth rates for homoepitaxial growth in the different crystallographic

directions. They have determined the growth rates by measuring the change in the thickness of the substrate from the interference fringes in transmission Fourier transform infrared spectra. Both of these studies reveal that a change in the substrate temperature affects the growth in the various crystallographic directions differently.

The present study includes the dependence of the overall growth rate and the growth rates in the [100] and the [111] directions on the substrate temperature, for a polycrystalline film grown on [100] silicon substrate. Here the interplay of changes in growth rates in [100] and [111] directions with the rapid change in crystal habit with temperature is demonstrated.

Experimental

The films were grown in a hot filament assisted chemical vapor deposition (HFCVD) reactor which was described in Part 2. In these experiments, the pressure of the growth chamber was maintained at 40 torr, and a mixture of CH_4 and H_2 gas was used at a rate of 50 sccm. Depositions were performed at three levels of CH_4 concentration : 0.5%, 1.0% and 1.5%. A carburized tungsten wire filament was used in the range 1950 to 1980° C to activate the gases and to indirectly heat the substrate. Within this filament temperature range, the substrate heater allowed the substrate to be maintained at any temperature in the range 530 to 1140 °C. The substrate was mounted on a molybdenum block that was threaded with rhenium wire to resistively heat the sample. A Pt-Pt-10%Rh (type "S") thermocouple, placed inside the block, was used to measure the substrate temperature. The filament temperatures were measured using a disappearing filament type optical pyrometer without employing any corrections for emissivity or reflections.

The films were grown on Si (001) substrates which had half of the growth surface scratched with diamond paste, followed by rinsing with acetone and methanol in an ultrasonic bath. The substrate was positioned ~ 10 mm from the filament and the films were grown for 16 hours with a few exceptions. The scratched half of the substrate typically developed a continuous diamond film and was used to study the texture. The other side had individual crystallites which provided information regarding the growth rate ratio, appearance of twins and other growth features.

The morphology of these films was studied using scanning electron microscopy (SEM). Film texture was qualitatively determined from the observations of the crystal orientations on the continuous film side of the sample. The growth rates were determined by measuring the dimensions of the individual crystals and dividing the longest dimension by the growth time. The crystal shape chart generated by Clausing et al. [9] was used as the standard for determining the growth rate ratio of the individual crystals. This was accomplished by comparing the individual crystal shapes as seen in the scanning electron micrograph with those in the standard chart.

The determination of growth rates in different crystallographic directions from two-dimensional images provided by the SEMs, is a little tricky because different geometries provide dimensions in different crystallographic directions. However, the growth rate ratios, which basically relate the dependence of the rates of growth in the [100] and the [111] directions, make it possible to extract important information. By measuring the dimensions of individual crystals and using simple trigonometric relations as well as the growth rate ratios we have been able to calculate the growth rates in the [100] and the [111] directions, for a

crystal with growth rate ratio between 0.6 and 1.5. The overall growth rate, which is the longest dimension of the crystal, was also measured. Trends in the overall growth rates and in the different crystallographic directions were compared and are reported here.

Tables 1,2 and 3 list the experimental conditions used and the observations regarding the growth rates and growth rate ratios. All twenty five depositions were carried out at approximately the same filament temperature, pressure and using the same filament. The films were grown for 16 hours with a few exceptions. The growth durations used did not appear to affect the growth rate ratio or the growth rates. The experimental data is arranged in three different tables based on methane concentration. Each table is further arranged in the increasing order of substrate temperature. The growth rate (**g**), and the growth rate ratio (**r**) are reported for each deposition. We chose to use the growth rate ratio rather than alpha for the simple reason that we would like to discuss the growth rates in the two crystallographic directions individually as well as their ratio for the crystal morphology.

Results and Discussion

The changes in the crystal morphology is a well established observation for CVD diamond. The range and the specific values of the parameters at which these changes occur, however are specific not only for a particular technique but also for a particular apparatus. Figure 1 shows the scanning electron micrographs of samples having different crystal shapes, from octahedra to cubo-octahedron to cubes. These samples were all grown under different growth conditions of methane concentrations and substrate temperature. For the samples shown in fig. 1 these parameters had the values : (a) 1.5% and 612 °C;

Table 1 : Growth conditions used, growth rates and growth rate ratios observed for depositions with 0.5% methane concentrations.

Methane conc.(%)	Fil. temp. (°C)	Substrate temp. (°C)	Growth rate (μm/hr)	Growth rate ratio	Alpha
0.5	1950	536	0.09	1.5	2.6
0.5	1965	563	o.12	1.5	2.6
0.5	1960	590	0.14	1.5	2.6
0.5	1960	627	0.18	1.5	2.6
0.5	1950	646	0.19	1.5	2.6
0.5	1970	704	0.21	1.5	2.6
0.5	1970	736	0.22	1.1	1.9
0.5	1965	766	0.17	0.6	1.0
0.5	1960	815	0.17	0.6	1.0
0.5	1960	908	0.135	0.6	1.0
0.5	1950	946	0.13	0.6	1.0

Table 2 : Growth conditions used, growth rates and growth rate ratios observed for depositions with 1.0% methane concentrations.

Methane conc. (%)	Fil. temp. (°C)	Substrate temp. (°C)	Growth rate (μm/hr)	Growth rate ratio	Alpha
1.0	1950	668	0.24	1.5	2.6
1.0	1980	692	0.36	1.3	2.3
1.0	1970	736	0.38	1.0	1.7
1.0	1985	827	0.57	0.87	1.5
1.0	1980	956	0.43	0.87	1.5
1.0	1980	1037	0.41	0.87	1.5
1.0	1970	1140	0.15	0.8	1.4

Table 3 : Growth conditions used, growth rates and growth rate ratios observed for depositions with 1.5% methane concentrations.

Methane conc.(%)	Fil. temp. (°C)	Substrate temp. (°C)	Growth rate (μm/hr)	Growth rate ratio	Alpha
1.5	1980	578	0.18	1.5	2.6
1.5	1980	612	0.52	1.5	2.6
1.5	1980	692	0.58	1.3	2.3
1.5	1970	729	0.58	0.87	1.5
1.5	1980	1042	0.72	0.87	1.5
1.5	1980	1079	1.04	0.87	1.5

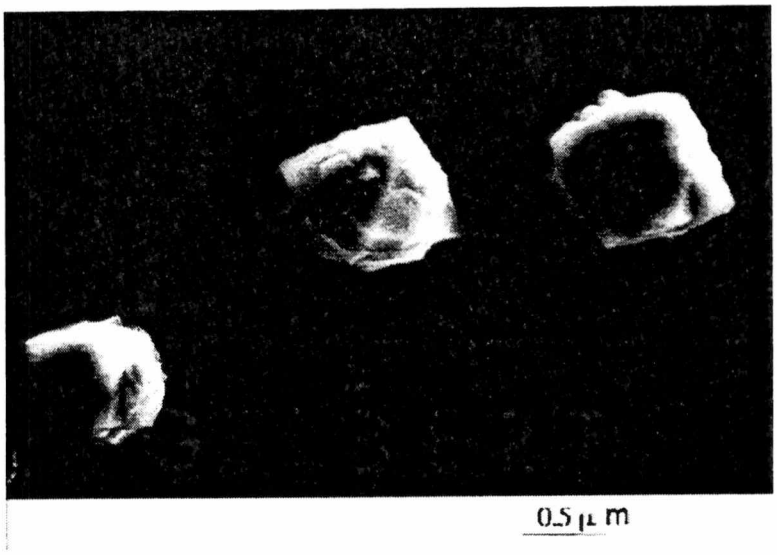

(a)

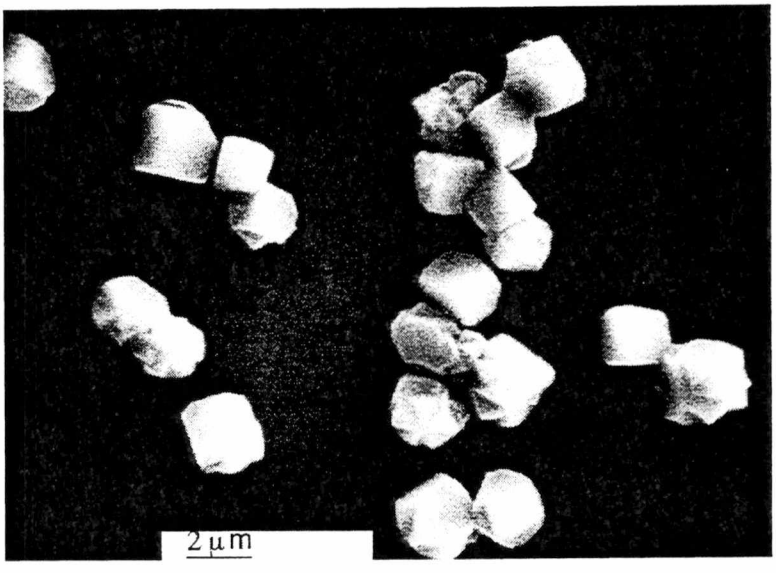

(b)

Figure 1. Scanning electron micrographs of films grown with different combinations of methane concentration and substrate temperatures, with filament temperatures of 1950 °C, resulting in a wide range of growth rate ratios, **r**. The methane concentration, substrate temperature and **r** were : (a) 1.5%, 612 °C and 1.5, (b) 0.5%, 815 °C and 0.60.

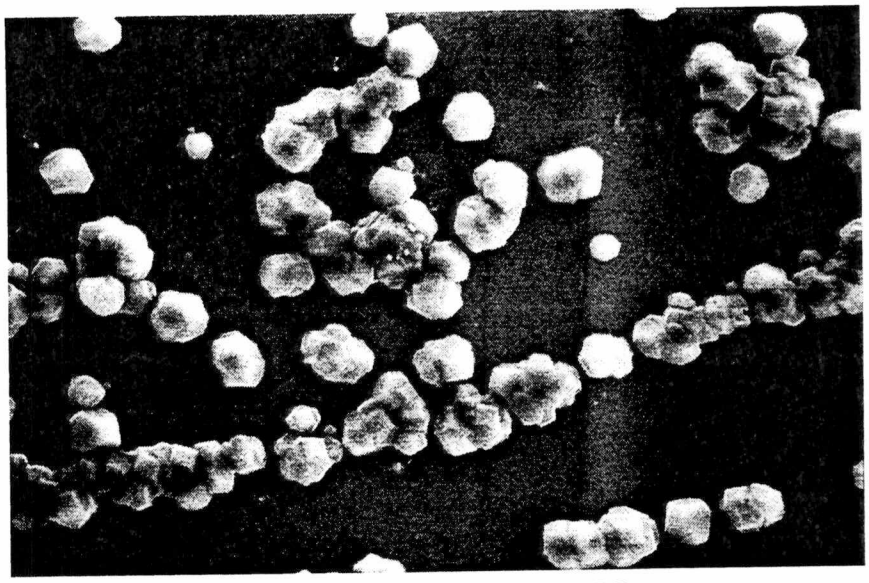

(c)

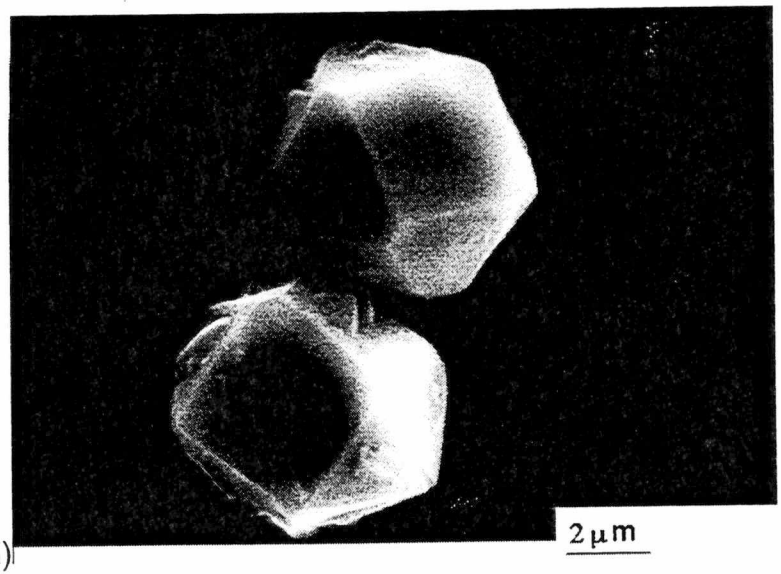

(d)

Figure 1 : Scanning electron micrographs of films grown with different combinations of methane concentration and substrate temperatures, with filament temperatures of 1950 °C, resulting in a wide range of growth rate ratios, **r**. The methane concentration, substrate temperature and **r** were : (c) 0.5%, 736 °C and 1.1, (d) 1.0%, 736 °C and 1.0, respectively.

(b) : 1.0% and 736 °C; (c) 0.5% and 736 °C; & (d) 0.5% and 815 °C. The growth rate ratios, **r** for these films were : (a) 1.5; (b) 1.0; (c) 1.1; (d) 0.60. In general, at low temperatures the individual crystals appear as octahedra. An octahedron is a polyhedron with 8 faces, each face being an equilateral triangle, in this case these are the {111} faces. As the substrate temperature is increased, the {100} faces begin to appear at the corners of the octahedron, so that now the polyhedron is taking the shape of a cubo-octahedron. At this point the crystal has the shape of an irregular cubo-octahedron, with small {100} faces and relatively large {111} faces. A regular cubo-octahedron is a polyhedron that has 6 square faces and 8 equilateral triangular faces where the edge of the square is equal in length to the edge of the triangular face. As the substrate temperature is further increased, the crystal shape goes through the regular cubo-octahedron to (again) irregular cubo-octahedron, but now the square {100} faces are larger than the triangular {111} faces. As the temperature is increased still further, the crystals take the shape of cubes.

It has been observed that the appearance and growth of the twins also follows a trend as a function of the substrate temperature. Since the substrate temperature affects the growth ratio, one could also say that the appearance of twins depends upon **r**. Figure 2 (b) and (c) shows {111} penetration twins as well as contact twins. All the samples shown in fig. 2 correspond to **r** = (1.5-1.3). These samples were grown with different methane concentrations at slightly different substrate temperatures. Figure 3 (a) shows the penetration twins of both types, the {111} as well as the {100}. As the substrate temperature was increased the twinning increased tremendously giving rise to "cauliflower" like morphology, figure 3(b). Further increase in temperature decreased the amount

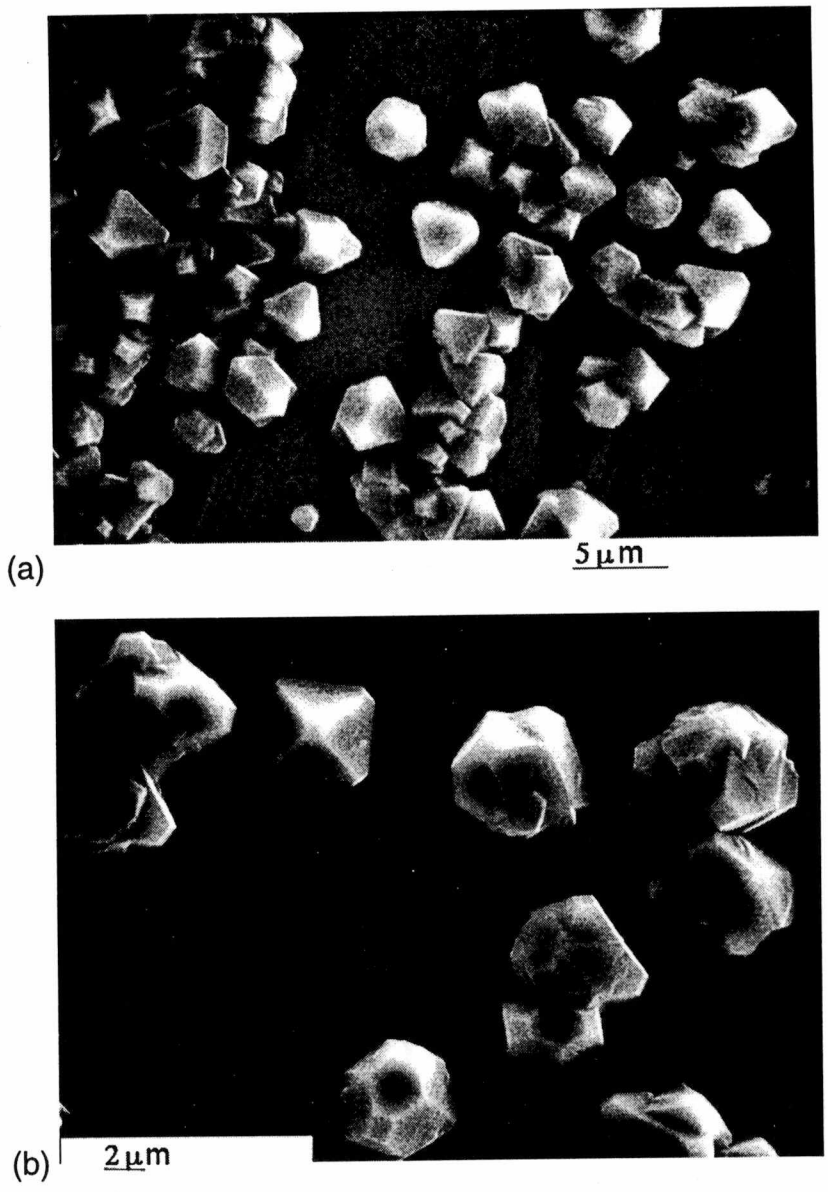

Figure 2 : Scanning electron micrographs showing the {111} penetration twins in the growth region corresponding to **r** > 1.15, or octahedral geometry. The filament temperature used for these depositions were between 1950 and 1980 °C, the methane concentrations and substrate temperatures were : (a) 0.5% and 704 °C, (b) 1.0% and 692 °C.

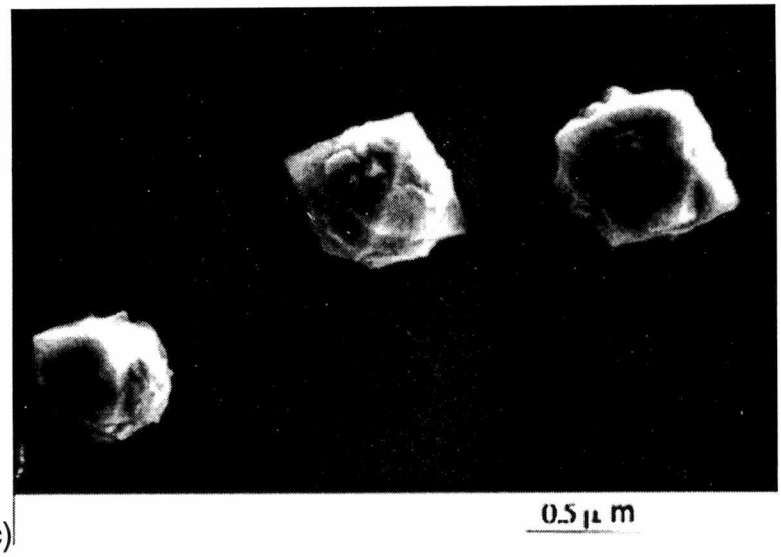

(c)

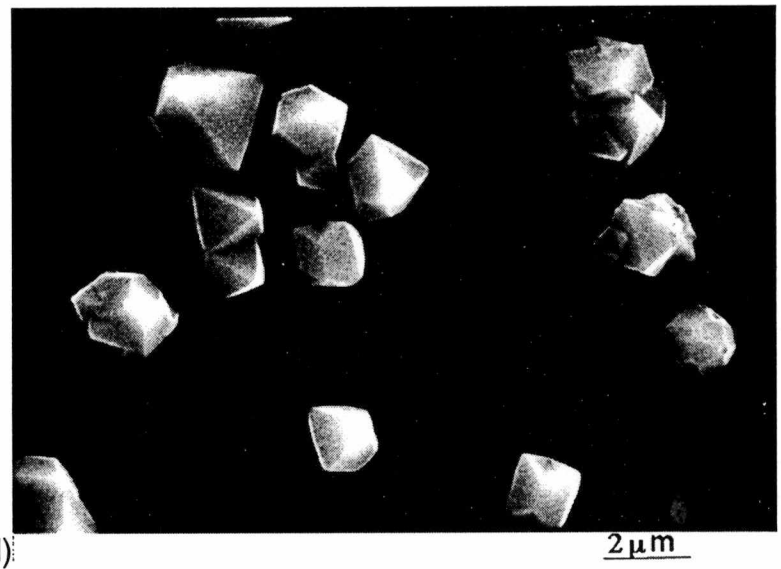

(d)

Figure 2 : Scanning electron micrographs showing the {111} penetration twins in the growth region corresponding to **r** > 1.15, or octahedral geometry. The filament temperature used for these depositions were between 1950 and 1980 °C, the methane concentrations and substrate temperatures were : (c) 1.5% and 612 °C, and (d) 1.5% and 578 °C, respectively.

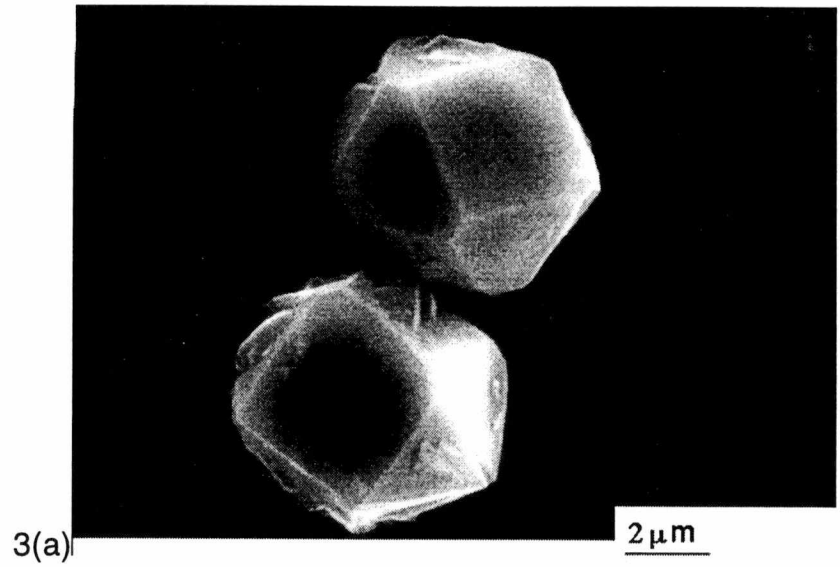

3(a)

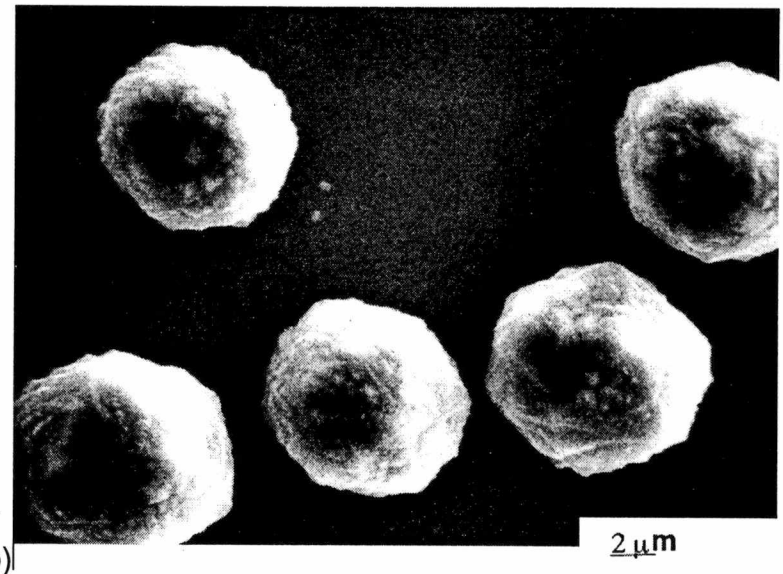

3(b)

Figure 3. The SEM images of the samples showing the {111} and the {100} penetration twins. These crystallites were grown under conditions to have **r** between 1.15 and 0.87, or cubo-octahedral geometry. The growth parameters used were as follows, filament temperature between 1970 and 1985 °C, methane concentration 1.0% and substrate temperatures of : (a) 736 °C, (b) 827 °C.

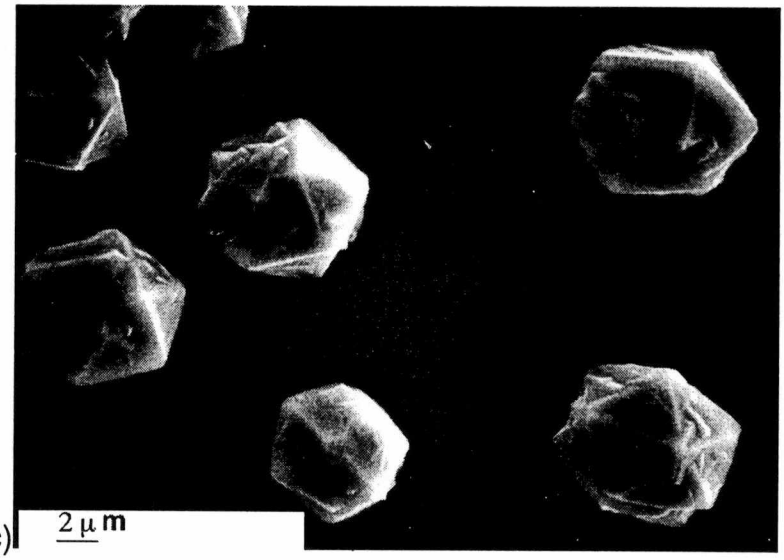

Figure 3 : The SEM images of the samples showing the {111} and the {100} penetration twins. These crystallites were grown under conditions to have **r** between 1.15 and 0.87, or cubo-octahedral geometry. The growth parameters used were as follows, filament temperature between 1970 and 1985 °C, methane concentration 1.0% and substrate temperatures of : (a) 736 °C, (b) 827 °C, and (c) 1037 °C, respectively.

of both the {100} and the {111} penetration twins as can be seen in fig. 3(c), and very clear cubo-octahedra reappear. Figure 4 (a)-(c) shows the appearance of {100} penetration twins and contact twins. Thus the appearance of the penetration twins seems to be dependent upon the growth rate ratio. The contact twins appear at high methane concentrations and substrate temperatures. The classification of the twins on the basis of the growth rate ratio is discussed specifically at the end of this section.

(1) Overall growth rates (**g**)

The growth rate as a function of substrate temperature is summarized in fig. 5 for each of the three methane concentrations studied. For a constant methane concentration of 0.5%, as the substrate temperature was increased, from 536 °C to 946 °C, the growth rate increased from 0.09 μm/hr, reached a maximum at 0.22 μm/hr, and then decreased to 0.15 μm/hr. Similar trends, albeit with a shift in the growth rate maximum to higher temperatures are seen for higher methane concentrations i.e. 1.0 % and 1.5 %. For example, the maximum occurs at 736, 827, and beyond 1079 °C for methane concentrations of 0.5 %, 1.0 % and 1.5 % respectively. For a constant substrate temperature films grown at higher methane concentrations had higher growth rates. For example, films grown at substrate temperature ~730°C with 0.5 %, 1.0 % and 1.5 % had growth rates of 0.22, 0.38 and 0.58 μm/hr respectively.

(2) Growth rate ratios (**r**)

Figure 6 shows the range of growth rate ratios, **r**, seen for a particular methane concentration and the range of temperatures over which a particular morphology is seen. For the HVCVD system used in this study, we observed

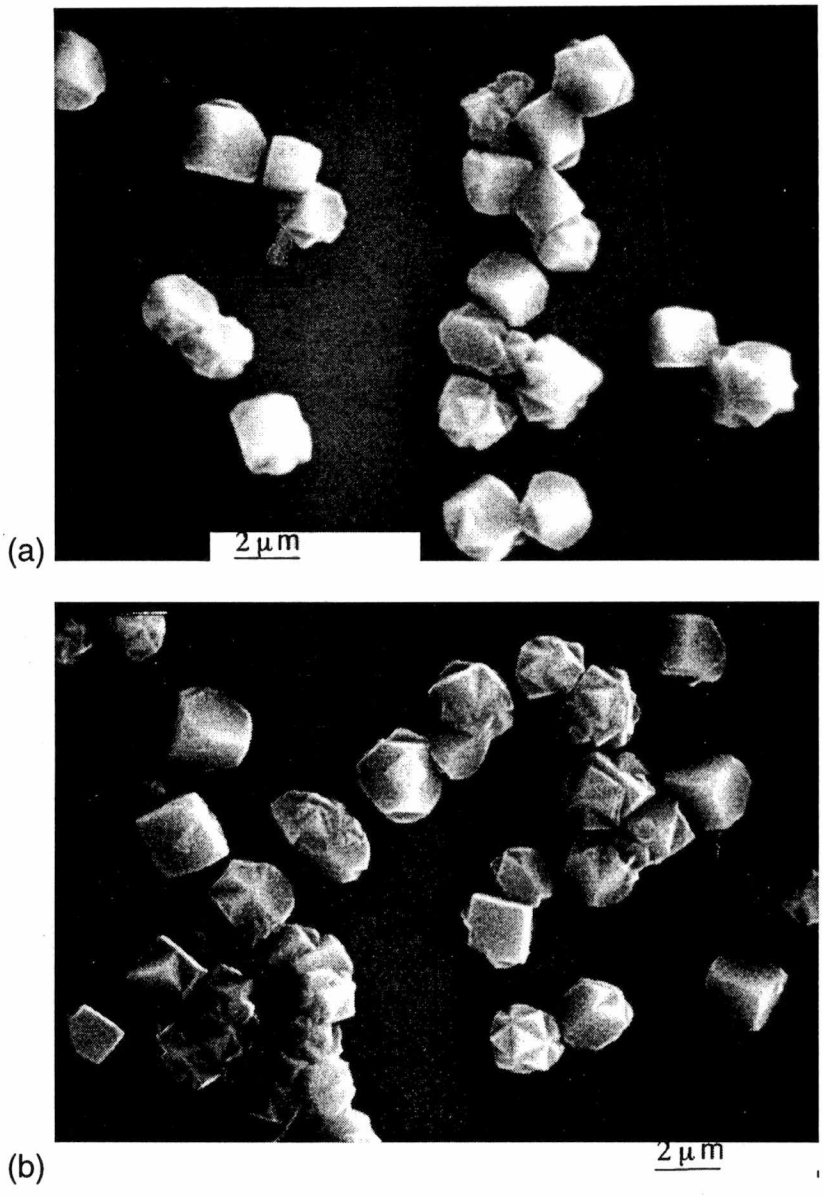

Figure 4 : Scanning electron micrographs of samples showing contact twins in the growth region corresponding to **r** = 0.6, or crystallite geometry of a cube. The growth parameters used were as follows, filament temperature between 1950 and 1965 °C, methane concentration 0.5% and substrate temperatures of : (a) 766 °C, (b) 815 °C.

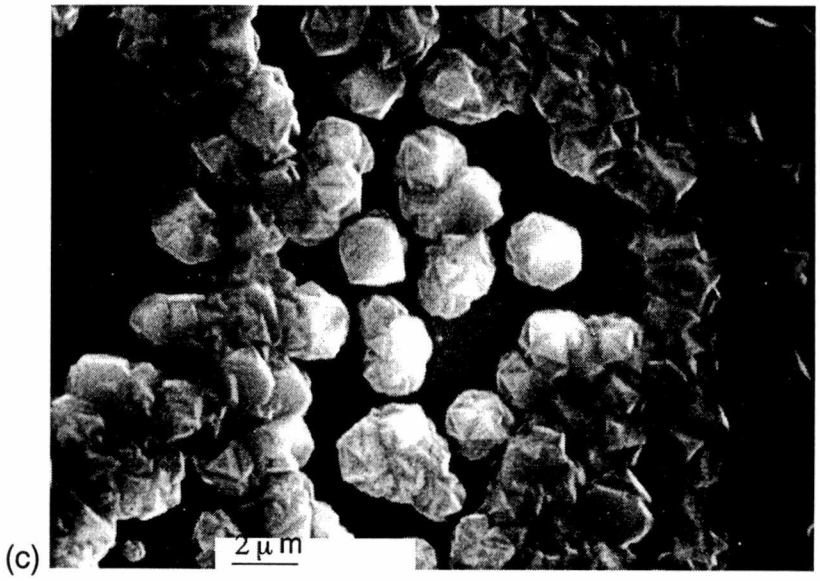

Figure 4 : Scanning electron micrographs of samples showing contact twins in the growth region corresponding to **r** = 0.6, or crystallite geometry of a cube. The growth parameters used were as follows, filament temperature between 1950 and 1965 °C, methane concentration 0.5% and substrate temperatures of : (c) 946 °C.

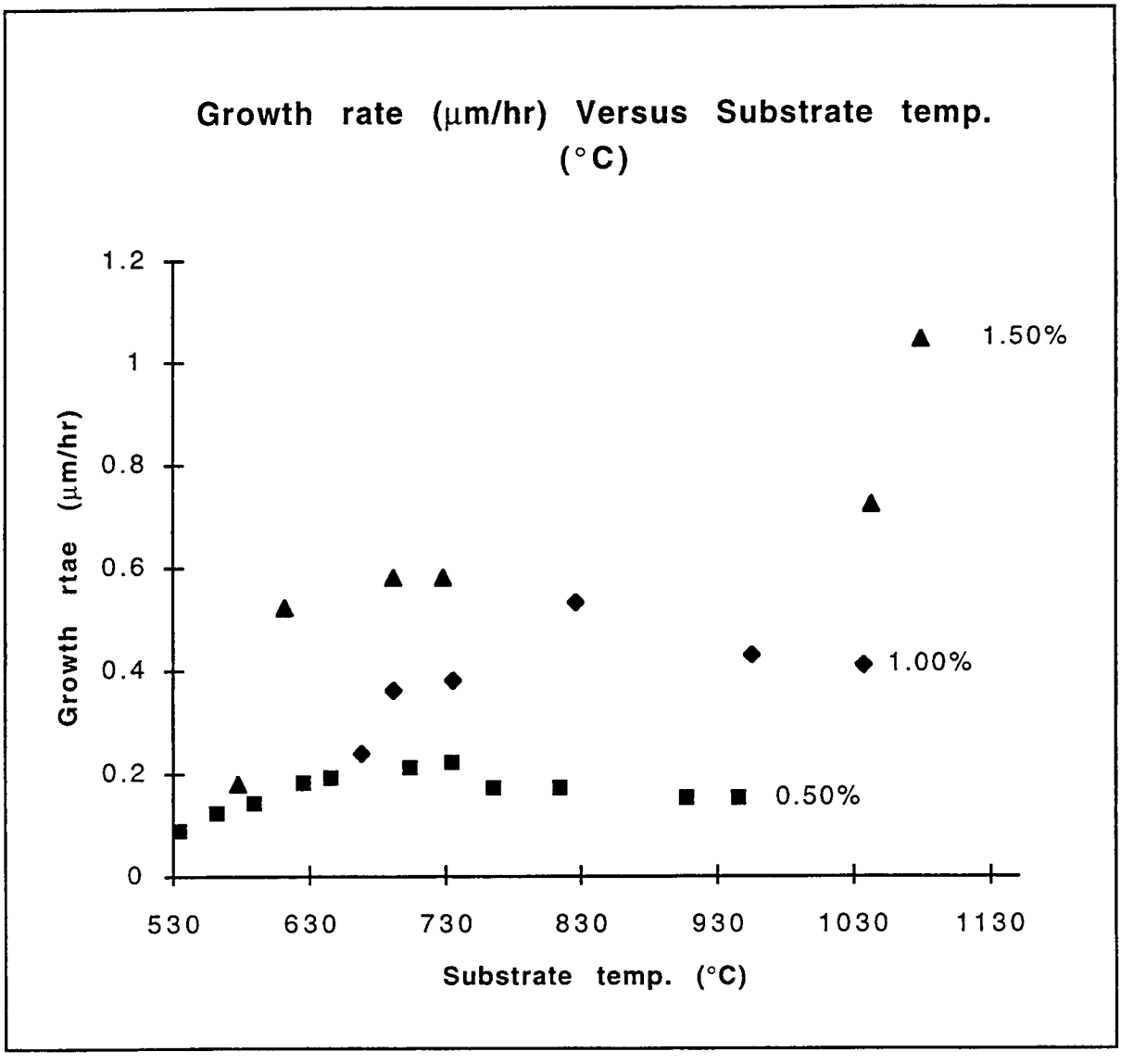

Figure 5 : Growth rate of individual crystals as a function of substrate temperature for the three levels of methane concentrations used. A maximum is observed, at 736 °C and 827 °C for 0.5% and 1.0% methane concentrations, respectively, showing that the maximum shifts towards the higher substrate temperatures for higher methane concentrations. In the case of 1.5% methane concentration, high enough temperatures were perhaps not achieved to observe the maximum.

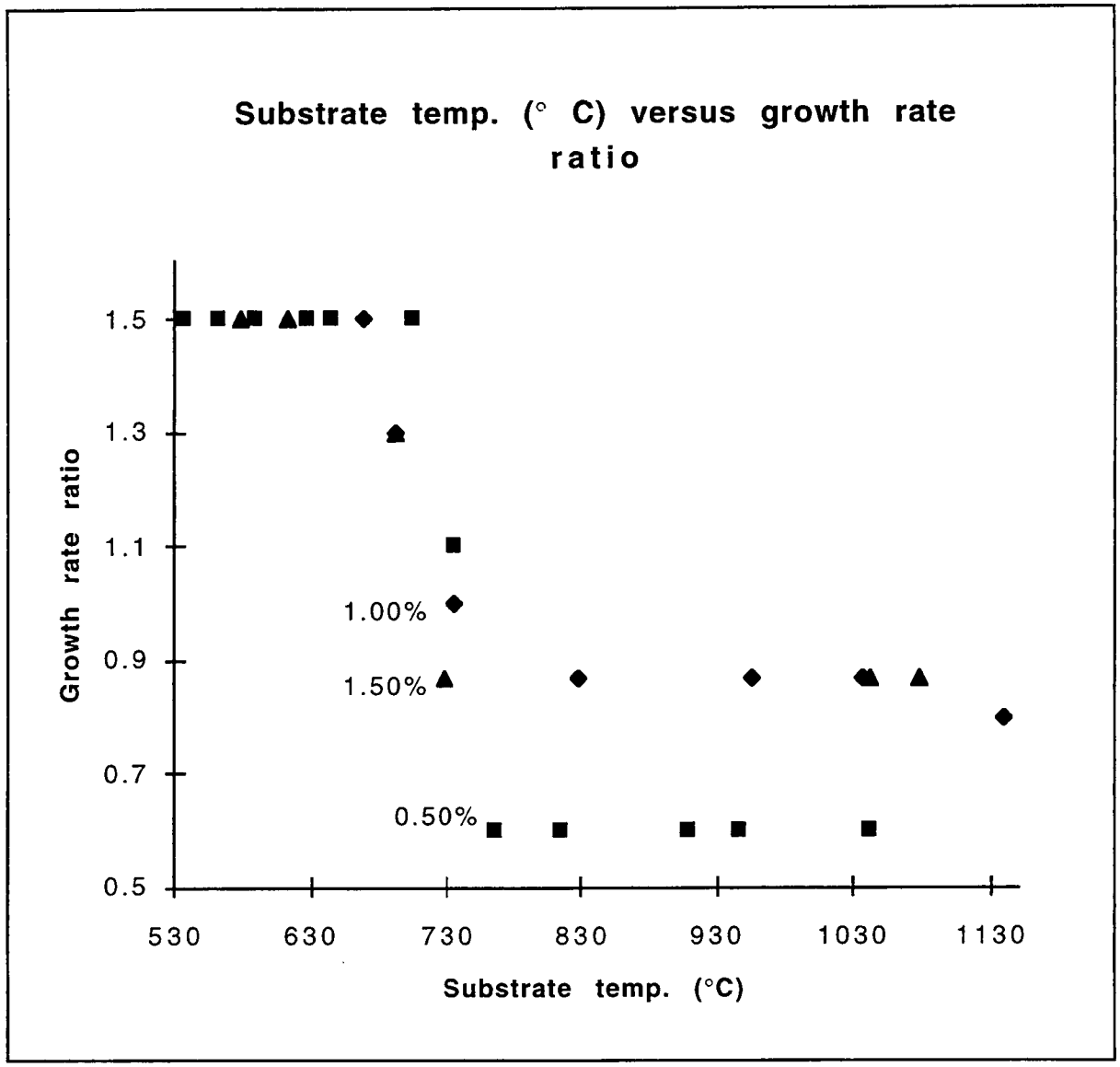

Figure 6 : Growth rate ratio as a function of substrate temperature for three different methane concentrations used. The growth rate ratios show a big drop over a short substrate temperature range. Near cube geometry (**r**=0.6) is observed at lower temperatures for lower methane concentrations, and near octahedral geometry is observed up to higher temperatures for lower methane concentrations.

that for constant methane concentration, **r** decreases overall as the substrate temperature is increased. However, as shown in fig. 6, the majority of the drop in **r** occurs over a relatively small range of substrate temperatures. For example, in depositions done with 0.5% methane concentration, in the substrate temperature range of 536 °C to 704 °C, individual crystals with the shape of octahedra (**r**=1.5) are observed. Between 704 °C and 766 °C, the morphology changes rapidly to irregular cubo-ctahedra at 736 °C, all the way to cubes or near cubes (**r**= 0.6) at 766 °C. For substrate temperatures between 766 and 946 °C the crystals appear as cubes (or near cubes) corresponding to **r**=0.6 (α=1.0).

Similar trends are seen for higher methane concentrations. The temperatures at which the specific crystal shapes appear are, however, slightly different for the three methane concentrations used. It is also observed that for most of the substrate temperature range the crystals appear as regular cubo-octahedra. Irregular cubo-octahedra are seen over a very short intermediate range before the crystal shapes change to octahedra or cubes.

Only for 0.5% methane concentration was the entire span of growth morphology observed; i.e. from octahedron to cube geometry corresponding to **r** = 1.5 to 0.6. For 1.0% methane concentrations the crystal shapes reach as far as **r** = 0.80 but do not make it all the way to cubes or **r** = 0.6. Similarly for 1.5% the crystal morphology did not go beyond the cubo-octahedron geometry, corresponding to **r** = 0.87, in the substrate temperature range used in the experiments. As the methane concentration is increased, the substrate temperature range over which a particular morphology is observed, seems to shift towards lower temperature, however the trends in the crystal shape remain the same. For example, at substrate temperature ~730 °C the three films grown

with 0.5%, 1.0% and 1.5% have crystallites with **r** values of 1.1, 1.0, and 0.87 respectively. At 1040 ° C substrate temperature, the value of **r** for the increasing order of methane concentrations is 0.6, 0.87, and 0.87 respectively.

Figure 7 shows an Isomorphic map for the HFCVD reactor used in this study, with contours corresponding to constant growth rate ratios. This morphology map, for the system used in this study, shows that an increase in the substrate temperature and a decrease in methane concentration has the same effect, namely, a decrease in the value of **r**. The relationship between morphology, growth temperature and gas composition can be expressed in a variety of ways. The isomorphic maps developed simultaneously by Tamor et al. [13] and Wild et al. [14] clearly presents the relationship between morphology and the growth parameters. The substrate temperatures that were used, to achieve the wide range of growth rate ratios, ranged from 536 to 1140 °C and the methane concentrations from of 0.5 to 1.5 %. The filament temperature was in the range 1950 to 1985 °C. This morphology map shows growth conditions which result in crystal morphologies ranging between octahedra to cubes. In comparison with the growth charts available in literature for the microwave plasma systems, one observes that the substrate temperature range is quite different. The range over which all morphologies are observed is much wider for the hot filament system than has been reported for the microwave systems. The three methane concentrations that were used in this study, showed the full range of growth rate ratios in the range of 536 to 1140 °C, whereas the substrate temperature range over which these have been observed by Tamor [13] and Wild [14] is 700 to 1050 °C.

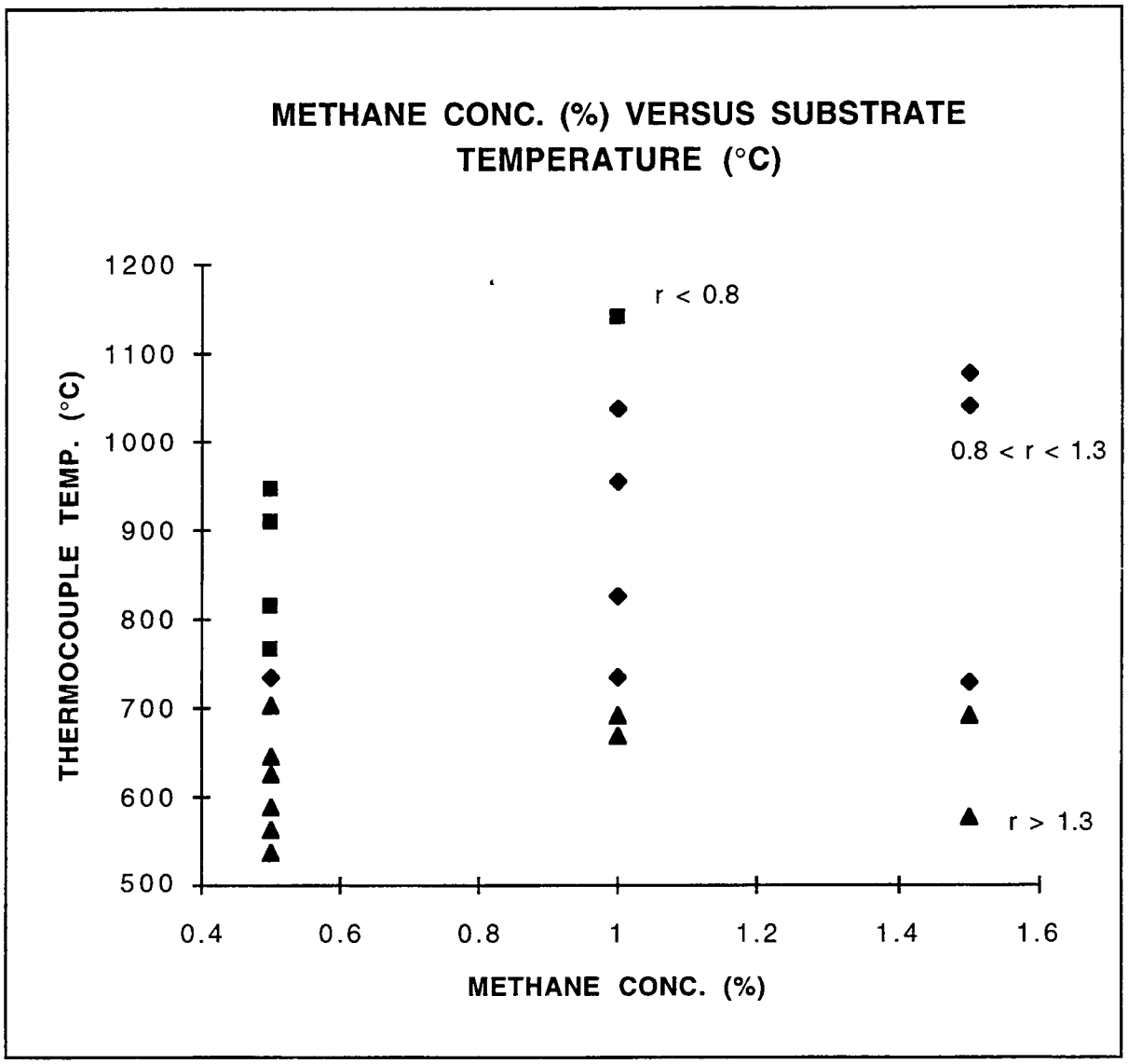

Figure 7 : An Isomorphic map for the HFCVD reactor used in this study, with contours corresponding to constant growth rate ratios. The substrate temperatures ranged from 536 to 1140 °C and the methane concentrations from of 0.5 to 1.0 %. This morphology map shows growth conditions which result in crystal morphologies ranging between octahedra to cubes.

(3) Growth rates in the [100] and [111] directions, **g**<100> and **g**<111>

The trends in the overall growth rate and the growth rate ratios as a function of substrate temperature and methane concentration indicates that the dependence of the growth velocities on the substrate temperature is different for the different crystallographic directions. Figure 8 shows the growth rates in the [100] and [111] directions and the overall growth rate as a function of the substrate temperature for 0.5% methane concentration. At lower temperatures growth in the [100] direction is greater than in the [111] direction, resulting in the near octahedral geometry. As the temperature is increased, the growth rate in both the directions increases almost identically up to the point where the strong change in geometry begins. Once the crystal geometry takes the form of a cubo-octahedron, the overall growth rate and the growth rate in the [100] drop rapidly and then appear to level off. In contrast, the growth rate in the [111] direction continues to increase in the region where there is a rapid drop in the [100] direction, accounting for the rapid change in morphology. After the cube geometry is developed, the growth rate in the [111] direction declines slowly with further increase in temperature. Since the overall growth rate here is based on the longest dimension of the crystal, it parallels the growth rate in the [100] direction over the region where octahedra are grown and parallels that in the [111] when cubes are formed.

Figures 9 and 10 show that similar, though less dramatic, trends are observed at higher methane concentrations. The growth rate in the [100] direction appeared to have a stronger dependence on the substrate temperature than that in the [111] direction. These observations are very similar to the trends that have been reported by Maeda et al. [10] for the homoepitaxial growth in a

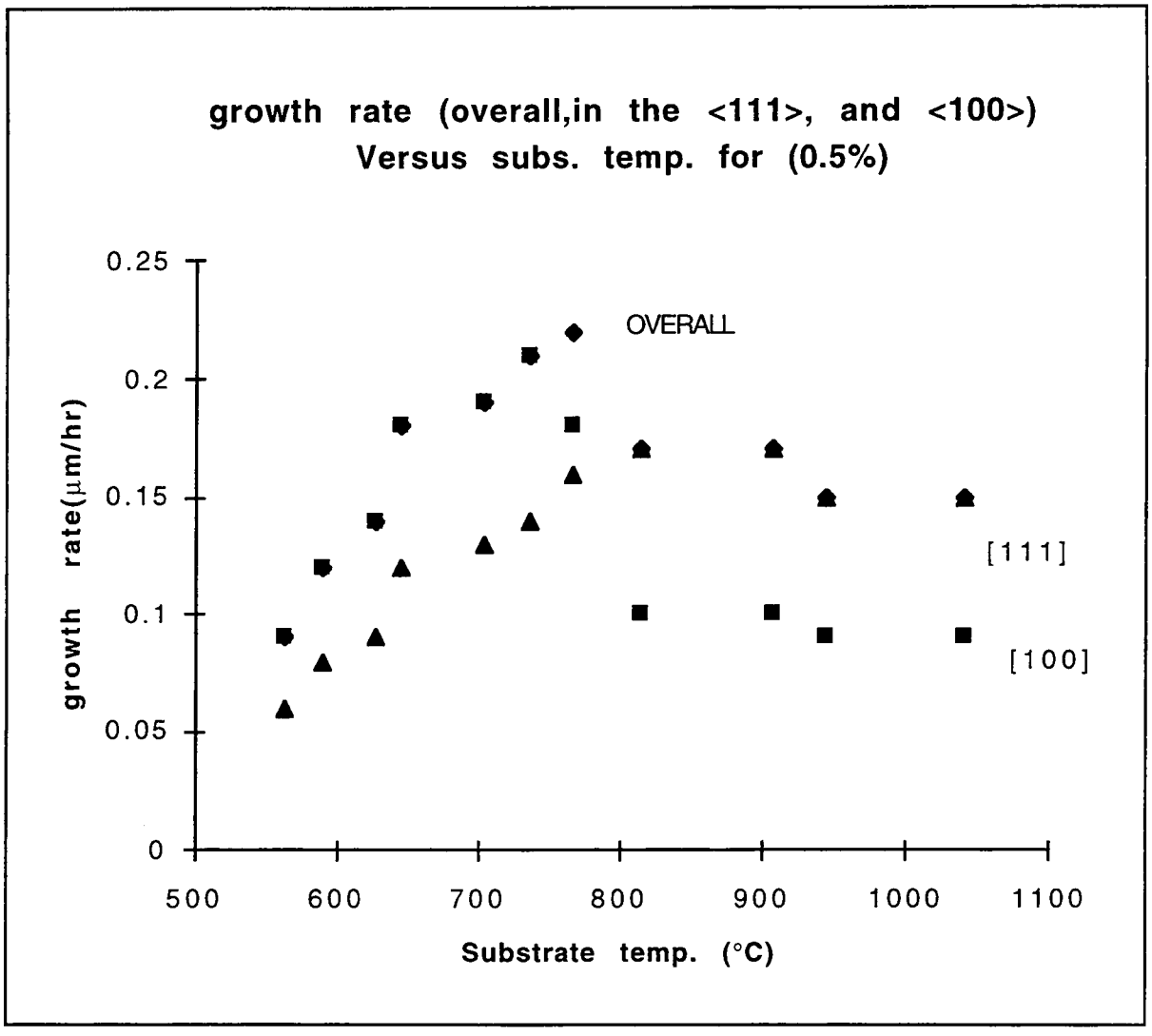

Figure 8 : Overall growth rate and growth rates in the [100] and [111] directions of individual crystallites as a function of substrate temperature for 0.5% methane depositions. The overall growth rate and the growth rates in the [100] direction show a prominent maximum, at 736 and 704 °C respectively, however, the growth rate in the [111] direction shows a steady increase, with a broad maximum at ~850 °C, with the increase in substrate temperature. These trends show that growth on these surfaces is taking place differently.

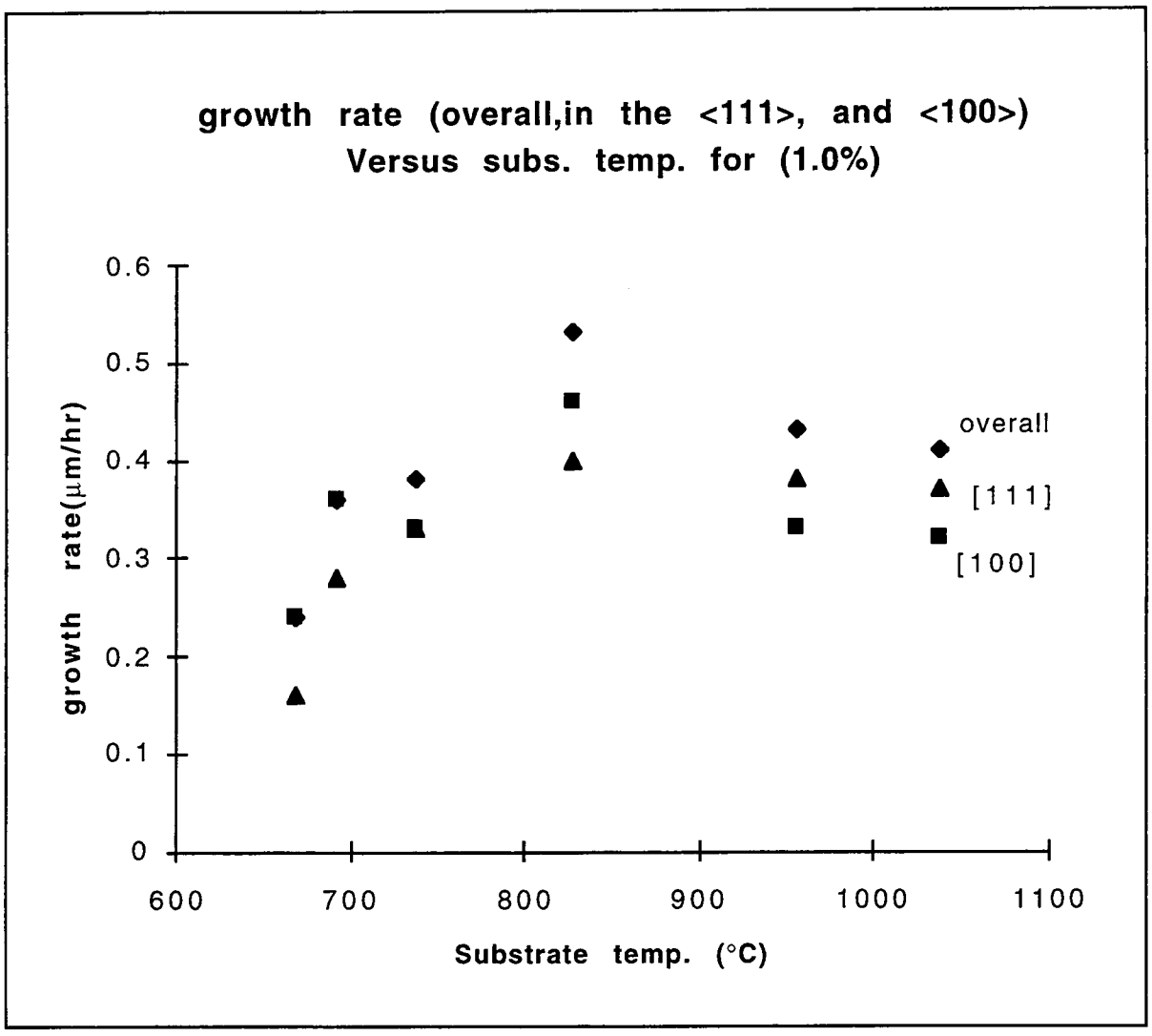

Figure 9 : Overall growth rate and growth rates in the [100] and [111] directions as a function of substrate temperature for 1.0% methane depositions. The overall growth rate and the growth rates in the [100] direction show a drop above 827 °C, after reaching a maximum, whereas the growth rate in the [111] direction shows a gradual increase which levels off at 827 °C, substrate temperature.

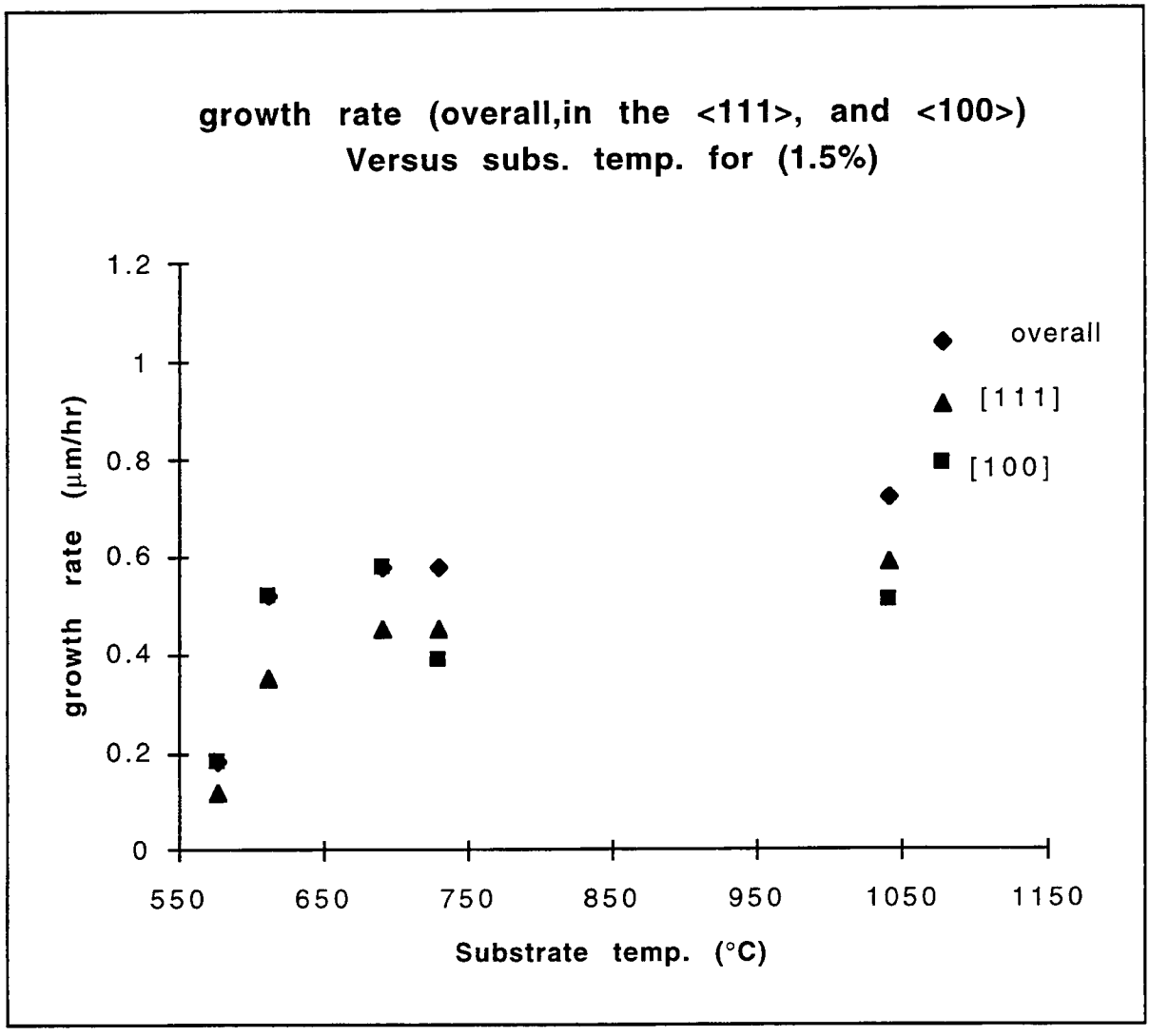

Figure 10 : Overall growth rate and growth rates in the [100] and [111] directions as a function of substrate temperature for 1.5% methane depositions. The growth rates in the [100] direction shows a maximum at 692 °C, then drops off, but shows an increase at 1079 °C. The overall growth rate and the growth rate in the [111] direction shows a gradual increase up to 1042 °C substrate temperature, and then shows a jump at 1079 °C.

microwave plasma system. However, in the present study the growth rates in the specific directions rapidly become limited by the crystal geometry for the cases of cubes and octahedra. This emphasizes the interplay of growth in these directions in determining crystal geometry. The measurements of Maeda et al. [10] show that when geometric constraints are removed, the directional growth rates continue to change even where we can no longer measure them independently due to limiting geometries.

A comparison of our data with that reported by Chu et al. [11] shows very similar trends for the [111] direction (fig. 11), however our data shows a pronounced drop in the growth rate in the [100] direction as the crystal geometry passes through the cubo-octahedron region into the cube region of crystal morphology (fig. 12). The difference in the trends for the growth rates in the [111] and the [100] directions, implies that growth kinetics are different for the different faces. Chu [11] et al. report that these faces have different activation energies. They have determined two activation energies for the substrate temperature regions, above and below 730 °C. They propose that a change in the steady state population of surface species is responsible for the two different activation energies they have calculated. According to these authors, diffusion of adsorbed species, to adjacent surface radical sites may be possible over 730 °C, but is strongly inhibited below it. They have tried to correlate the growth kinetics, for the various faces, on the basis of dihydride coverage.

The absolute values of growth rates reported by Maeda [10] et al. and Chu [11] et al. are also greater than what we have observed. We believe that the distance of the filament from the substrate may be responsible for these

dissimilarities since it is well known that gas phase chemistry changes as a function of the distance from the filament.

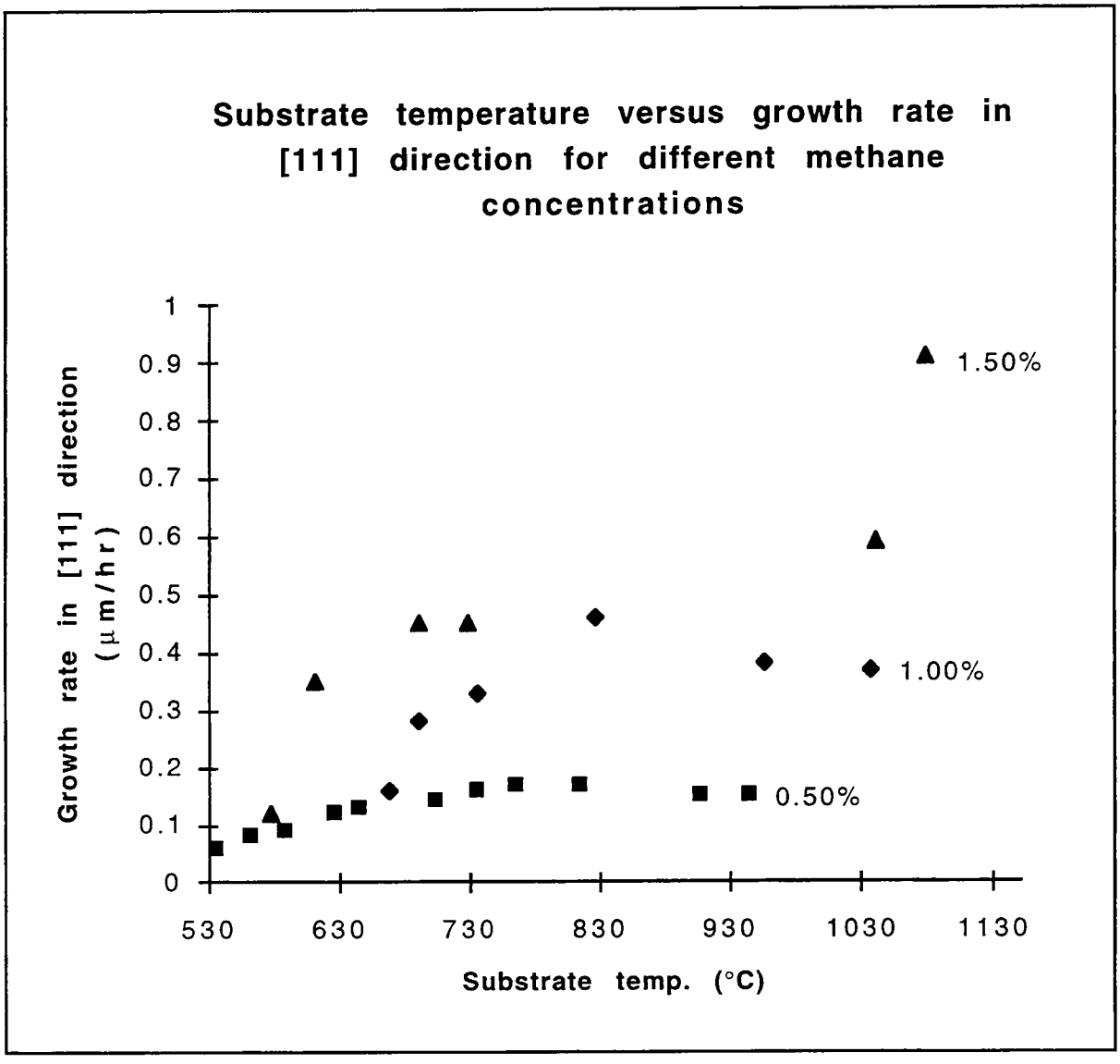

Figure 11 : A plot of growth rate in the [111] direction as a function of substrate temperature for different methane concentrations. The growth rate is observed to increase gradually at lower temperatures but then levels off.

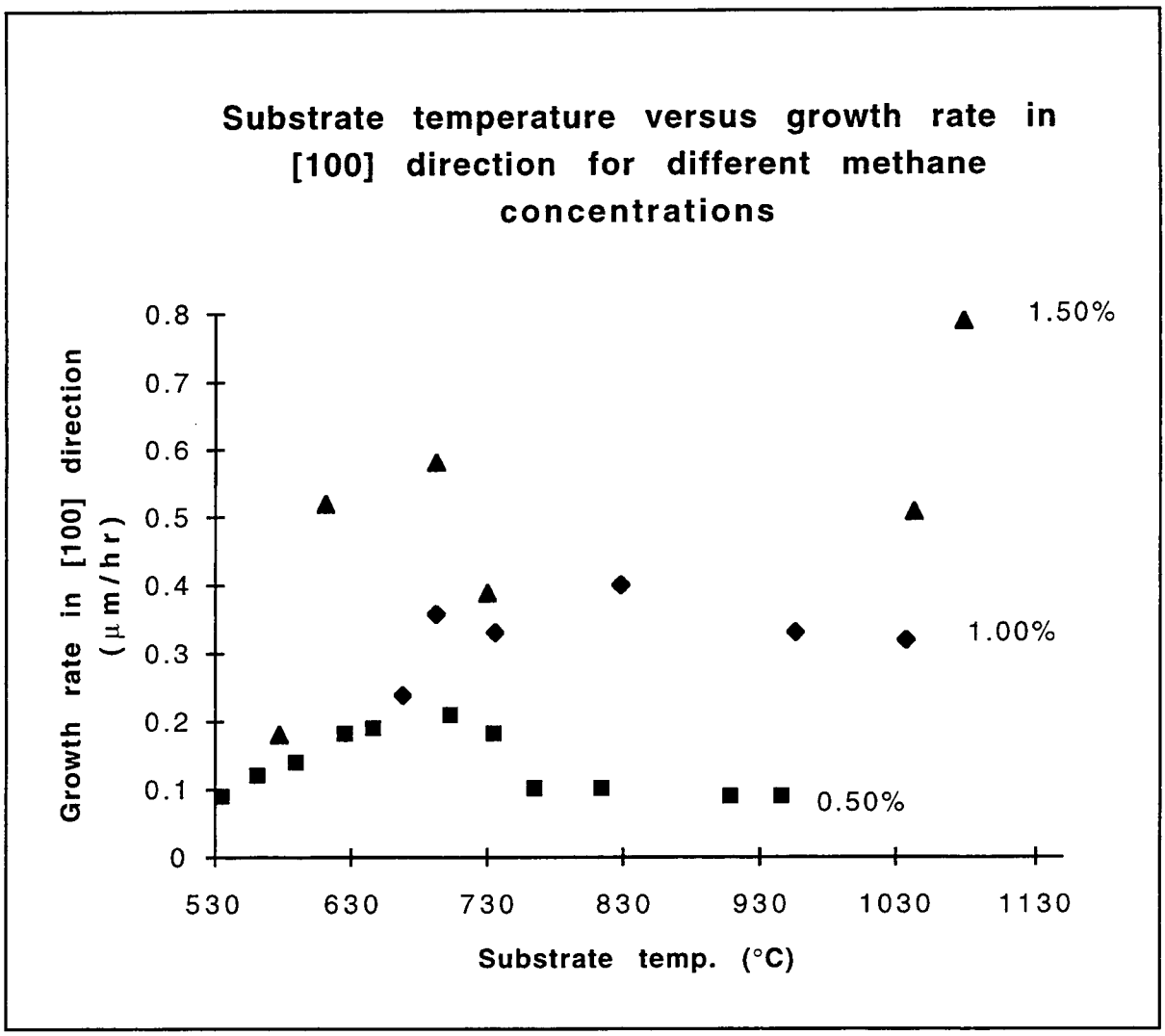

Figure 12 : A plot of growth rate in the [100] direction as a function of substrate temperature for the different methane concentrations used. A maximum is observed, at 704 °C for 0.5% and at 827 °C for 1.0%, which is shifted towards the higher substrate temperature for higher methane concentration. The data for 1.5% methane concentration shows a maximum at ~690 °C, the growth rate then drops between 730 and 1030 °C and then shows an increase beyond 1030 °C.

(4) Twinning

Twinning can be understood on an atomic scale, by considering the growth on a {111} plane. As the atoms are being added a simple rotation of 60° or 180° about the <111> direction leads to the boat configuration of the diamond lattice [12]. This is very common since it does not change the nearest neighbor configuration in the lattice. In a basic sense then, there is no difference between the various types of twins. However, twins have been broadly classified into two categories, the contact twins and the penetration twins, based on their appearance and orientation on the parent faces. Tamor et al. [13] have defined these as " a contact twin always originates on a {111} surface and shares the <111> direction normal to that surface with the parent, while a penetration twin may originate on either a {111} or a {100} surface, and shares a <111> direction that is not normal to that surface". Wild et al. [14] have also recognized these three broad categories and they choose to call them $T\{111\}_p$, $T\{111\}_i$ and T{100}. In this paper, twins have been named according to the definitions of Tamor et al.

The role of penetration twins has been discussed in depth by Tamor et al. [13] who have suggested that they play a major factor in determining the morphology of vapor grown diamond films. They have defined the twins to be {100} or {111} penetration twins based upon the parent face on which they originate and have discussed the orientation of these twins with respect to their parent faces. Based on geometric construction, they have identified growth conditions which suppress one or the other but never both. Wild et al. [14] have performed macroscopic computer simulations to study the influence of the

growth rate ratio on the formation of twins. Their conclusions appear to be consistent with those of Tamor et al. [14].

The discussion regarding twinning, as has been pointed out by Tamor et al. [13] and Wild et al. [14], can be divided into different parts. One is the probability or the rate of twin formation. Another is the ability to outgrow its parent face , and thirdly the ability of the twin to overgrow its parent face and eventually bury it . Tamor et al. [13] find that the rate of twin formation is zero only at $\alpha = 3/2$ ($\mathbf{r} = 0.87$). A {100} penetration twin, according to their study can outgrow its parent face only for $\alpha < 2$ ($\mathbf{r} < 1.15$). A {111} penetration twin, on the other hand can outgrow its parent face only for $\alpha > 3/2$. ($\mathbf{r} > 0.87$). Only <100> penetration twins can overgrow and bury their parent face and only at $\alpha = 3/2$ ($\mathbf{r} = 0.87$). Their argument shows that for $\alpha < 3/2$ ($\mathbf{r} < 0.87$) only the {100} penetration twins persist and for $\alpha > 2$ ($\mathbf{r} > 1.15$) only the {111} persist, which is also supported by the computer simulations of Wild et al. [14] In the region between these two values twins may appear on both the faces.

Interestingly, the observations regarding the presence of twins, fall into three main categories, based on **r**, which are very much comparable with the regions defined by the geometric arguments [13] and computer simulations [14].

(i) $\mathbf{r} > 1.15$ ($\alpha > 2$)

Most of the twins in this growth regime are seen on the {111} faces, i.e. the {111} penetration twins. In this morphology regime {111} faces are the dominating faces . Micrographs of samples with $\mathbf{r} > 1.15$ have previously been shown in fig. 2 (a)-(d). These samples were grown with varying methane concentrations and substrate temperatures. The methane concentrations and

substrate temperatures for these films were : (a) 0.5% and 704 °C; (b) 1.0% and 692 °C; (c) 1.5% and 612 °C; and (d) 1.5% and 578. The growth rate ratios for these samples were close to 1.5. The {100} faces are relatively small in this growth regime and hardly any {100} penetration twins are observed. The samples grown with higher methane content show more {111} penetration twins and contact twins. At constant methane concentration, it was observed that twinning decreased as **r** increased beyond 1.15, for e.g. it was much greater for **r** ~ 1.3 (α ~2.25) than for **r** ~ 1.5 (α ~2.6), for 0.5% as well as for 1.0%. The contact twins, on the other hand, are more abundant in films grown with higher methane content at a constant substrate temperature and towards the higher substrate temperature end for a constant methane level.

(ii) $1.15 > \mathbf{r} > 0.87$ ($2 > \alpha > 1.5$)

In this morphology region, the {100} and the {111} penetration twins were seen in abundance. The SEM images of samples which have **r** between 1.0 and 0.87, corresponding to cubo-octahedral geometry are shown in fig. 3. These films were grown with 1.0% methane concentration and filament temperatures between 1970 - 1985 °C. The substrate temperature was : (a) 736 °C; (b) 827 °C; and (c) 956 °C. At the intermediate temperatures, these twins almost cover the entire crystallite, making it appear like cauliflower like or "microcrystalline", however one can very clearly see an underlying cubo-octahedral shape, i.e. the cubo-octahedron skeleton of the parent crystallite. This cauliflower morphology is seen for ratio exactly 0.87. As one moves away from this range of temperatures (i.e. 736 - 956 °C), the amount of twinning decreases. The appearance of the contact twins increases as the methane

content of the gas mixture is increased. For constant methane concentrations at higher substrate temperatures more contact twins are seen.

(iii) $0.87 > \mathbf{r} > 0.6$ ($1.5 > \alpha > 1.0$)

In this region the crystallites are dominated by {100} faces, as can be seen in figs. 4 (a)-(c). These three films were grown with 0.5% methane concentration with the filament temperature in the range 1950-1965 °C and the total pressure was held constant at 40 torr. The substrate temperature was : (a) 766; (b) 815; (c) 946 °C. The {100} penetration twins can be spotted but are quite uncommon. The contact twins on the other hand are quite common, especially at higher temperatures for a particular methane concentration and at higher methane concentrations.

(5) Texture

Films with **r** between 1.5 and 1.15 ($2.6 > \alpha > 2$) had <100> texture. The films that had **r** ~ 1.5 had the individual crystals in the shape of octahedra. The continuous side of such films showed the corners of the cubes pointing up. However for ratios close to 1.3 (the crystallites were irregular cubo-octahedra with small {100} faces), the continuous film had the {100} faces parallel to the substrate. This was seen for 0.5% as well as the 1.0% methane concentration. For all the other morphological conditions the films showed either a <110> texture or mixed texture.

Conclusions

The effect, on the morphology and texture of diamond films, of the growth parameters, such as, the substrate temperature, and methane concentration

was studied for a HFCVD reactor . The trends in the morphology change observed are very similar to those seen in a microwave plasma system [13,14], however, the temperature regimes are different. The temperature range, within which high quality diamond can be deposited, appears to be wider for the HFCVD system. The observations on the appearance of twins is in good agreement with the geometric and macroscopic computer simulations by Tamor et al. [13] and Wild et al. [14] respectively, and are comparable with the observations for a microwave plasma system [13, 14].

References

1. B. V. Spitsyn, in *Handbook of Crystal Growth*, edited by D. T. J. Hurle, **3**, 403 (1994).

2. W. A. Yarbrough and R. Messier, Science **247**, 688 (1990).

3. W. Piekarczyk and W. A. Yarbrough, J. Cryst. Growth **108**, 583 (1991).

4. J. E. Butler and R. L. Woodin, Philos. Trans. R. Soc. London A **342**, 209 (1993).

5. K. E. spear and M. Frenklach, in *Synthetic Diamond : Emerging CVD Science and Technology*, Edited by K. E. Spear and J. P. Dismukes, 243 (1994).

6. R. E. Clausing, in *Industrial and Scientific Handbook on Diamond,* edited by M. Prelas, G. Popovici, L. K. Bigelow, Marcell Dekker publisher (to be published in summer '97).

7. A. van der Drift, Phillips Res. Rep. **22**, 267 (1967).

8. R. E. Clausing, L. Heatherly, L. L. Horton, E. D. Specht, G. M. Begun and Z. L. Wang, Dia. and Rel. Mat. **1**, 411 (1992).

9. R. E. Clausing, L. Heatherly and E. D. Specht, in *Diamond and Diamond-like films and coatings*, Edited by R. E. Clausing, L. L. Horton, J. C. Angus and P. Koidl, NATO ASI series B **266**, 611 (1991).

10. H. M. Maeda, K. Ohtsubo, M. Irie, N. Ohya, K. Kusakabe and S. Morooka, J. Mater. Res. **10**, 3115 (1995).

11. C. J. Chu, R. H. Hauge, J. L. Margrave and M. P. D'Evelyn, Appl. Phys. Lett. **61**, 1393 (1992).

12 J. C. Angus and C. C. Hayman, Science **241**,913 (1988).

13. M. A. Tamor and M. P. Everson, J. Mater. Res. **9**, 1839 (1994).

14. C. Wild, R. Kohl, N. Herres, W. Muller-Sebert and P. Koidl, Dia. and Rel. Mat. **3**, 373 (1994).

Part 5 : Indexing the hopper shaped {111} face produced in chemical vapor deposited diamond

Introduction

One of the greatest challenges in the field of chemical vapor deposition (CVD) of diamond is the development of methods to limit defects and control morphology in the films produced. The establishment of growth mechanisms which can account for details of growth at a nanometer scale is expected to be instrumental in that development. However, there has been insufficient experimental data on the atomic level structure of the growth surface, on the kinetics of surface processes, and even on the degree to which surface diffusion plays a role, to guide the formulation of suitable growth mechanisms. One area where such data has begun to emerge is the nanometer scale microscopy of the growth surface. Scanning tunneling microscopy (STM) and AFM are being used widely in order to understand different aspects of CVD diamond growth.

STM studies have been conducted by various groups [1-3] to understand the initial nucleation and growth of CVD diamond films. The structure of the developing surface is also being studied using STM and AFM [3-9]. These studies reveal the presence of 2X1 {100} surface reconstruction, step mediated growth on {100} surface and various growth features. Some of the growth features have been investigated quantitatively using these atomic probe microscopies. For example Kreutz et al. [9] report spiral screw dislocations on the {111} face of a boron doped diamond film grown via HFCVD technique, indicating that these faces grow in a layer by layer growth mode. Everson et al. [10] have reported the presence of vicinal surfaces in association with grain boundaries (such as a {313} face where a {111} face terminates at a {100} face on a grain boundary), on boron doped diamond films using STM and AFM. These authors [11] have also used STM and AFM to index the faces and the

orientation of a {111} penetration twin. Their analysis reveals that the <221>' direction of the twin is aligned to the <100> of the parent crystal. They have very elegantly discussed the implications of the penetration twin for the CVD growth of diamond.

The growth feature discussed here, the "hopper" shaped {111} face, has been reported previously [12-14] and is observed in various types of diamond growth. It has been observed in diamonds grown at high pressures in the presence of H_2O as noted by Sunagawa [15]. In low pressure growth of diamond it has been attributed [15] to an increase in the driving force causing {111} faces to develop larger, transforming the hopper faces while {100} faces retain their flatness. Although this feature has been imaged and its implications regarding the growth mechanism discussed, it has not been crystallographically characterized or indexed. Kim et al. [12] have observed this feature and reported it as depression in {111} octahedral face composed of three {110} planes. This assignment of the hopper planes is taken as evidence for the importance of {110} planes in the development of {111} faces, which they suggest derive from (100) and (110) constituent crystallographic planes.

Hirabayashi et al. [13] have studied incompletely formed {111} faces and also characterize the edge walls of these shallow hoppers as consisting of {110} planes. However, the bottom (pit) of the {111} hopper is found to contain numerous {111} triangular tiles rather than constituent {110} and {100} planes. They suggest that the {110} planes at the periphery arise from a lower effective carbon concentration at the center of the {111} surface, which could result in a slow growth rate at the center and creation of a concave shape. According to

this model, the {110} planes appear due to the delay of the growth of the center of the {111} surface and not due to the growth of a {110} surface per se.

Sun et al. [14] have also reported the hopper shaped {111} face and have also labeled these faces to be of the {110} type. It is argued based on geometric grounds that the {110} faces proceed by a step growth mechanism. If credibility is to be established for a growth mechanism for the hopper shaped {111} face, we believe that the faces comprising the hopper must first be correctly indexed.

A quantitative analysis of the "hopper" shaped {111} face is presented here. With the three dimensional information available from the AFM images, we have been able to index the planes comprising the "hoppered {111}" face and find them to contain higher index planes of the {221} and {331} family.

Experimental

The films were grown via hot filament assisted chemical vapor deposition (HFCVD). In these experiments, a 1% CH_4 in H_2 gas mixture was flowed at a rate of 50 sccm into the 25 mm quartz tube which forms the main body of the reactor, as described in part 2. The pressure in the reactor was maintained at ~40 torr by throttling the inlet of the mechanical pump which exhausts the system. A carburized tungsten wire filament was used to activate the gases and to indirectly heat the substrate. Different filament and substrate temperatures were used to determine the conditions which facilitated the appearance of the hopper faces. Table 1 lists the growth conditions used to observe the occurrence of the hopper faces. Typically, the hoppered (111) faces appeared on films that were grown with the filament and substrate brightness temperatures of 2120 °C and 1050 °C, respectively. The temperatures were

measured using a disappearing filament type optical pyrometer without employing any corrections for emissivity or reflections. The films were grown on Si (001) substrates which had half of the growth surface scratched with diamond paste, followed by rinsing with acetone and methanol in an ultrasonic bath. HFCVD growth on such a substrate typically yields a continuous film on the scratched portion and discrete crystallites on the other half, allowing crystal type and film morphology to be studied on a single sample. The substrate was positioned ~10 mm from the filament and films were grown for 16 hours.

The hopper shaped {111} faces appear at relatively high substrate temperatures. During the characterization of the growth chamber, an isomorphic map was generated, which is discussed in Part 4. It was established that, for constant methane concentration and filament temperature (1% and 2120° C respectively, in this case), with the increase in substrate temperature (from 670° C to 1140° C) the morphology of the crystals changed from near octahedra to near cube (i.e. **r** = 1.5 to 0.6 or α = 2.6 to 1.1, where α is defined as $\sqrt{3}$ times the ratio, **r**, of the growth rate in the <100> direction to that in the <111> direction). Over a wide range of substrate temperature (830° C to 1100°C) crystals shaped as cubo octahedra (α=1.5) were observed with varying degree of twinning. Other morphologies did not span such a wide range of substrate temperatures. In this morphology map, the hopper shaped {111} faces appeared towards the high temperature end of the cubo octahedra region.

Two methods were employed to study the film morphology. Scanning electron microscopy (SEM) images were obtained using a Hitachi S-800 microscope. Images of the films were also obtained using a Digital Instruments Nanoprobe III atomic force microscope. AFM images were recorded in air and

at room temperature using the tapping mode of operation. Commercially available micro fabricated silicon cantilevers were used which had a spring constant of ~35 N/m. The AFM images were analyzed quantitatively using Nanoscope III software to determine the geometry of various features and to identify the orientation of the surface facets. All angles were measured from unprocessed images.

Results and Discussion

Figure 1 shows a representative SEM images of a film containing crystallites with hopper shaped {111} faces. Planes with 3-fold and 4-fold symmetry are easily identified as the {111} and {100} faces, and these faces are oriented such that the polycrystalline film appears to be developing a <110> texture. The growth rate for the film in fig. 1 was ~1.3 μ/hr, and the ratio of the growth rate in the <100> to that in the <111> direction was ~0.87 (α=1.5).

Results obtained from the experiments listed in Table 1 can be analyzed as follows. The growth conditions of filament temperature 2120° C and substrate temperature of 1050 °C, which is listed as the first entry in table 1, can be considered to be the standard conditions for growing hopper faces. The scanning electron micrograph of films grown under these conditions are shown in figs. 1 and 2. The films grown with filament temperature that were 100 °C below the standard conditions, i.e. 2020 °C, are shown in fig. 3. The {111} faces appear hoppered but are not as fully developed as seen in fig. 1, which were deposited under standard conditions. If the filament temperature is further lowered to 1980 °C, hopper faces are not observed at all as seen in the micrograph labeled fig. 4. However, if the filament temperature is set approximately at the standard value but the substrate temperature is increased



Figure 1 : An electron micrograph of a (111) face. The <110> edges are seen to be broken. (100) faces appear to be flat.

Table 1 : Growth conditions used for observing the appearance of hoppered {111} faces

Sample	Filament temp. (°C)	Substrate temp. (°C)	Hoppered {111} face
(134) A	2120	1050	yes
(135) B	2020	1052	few
(136) C	1980	1060	none
(132) D	2100	1100	none
(126) E	2020	1030	yes

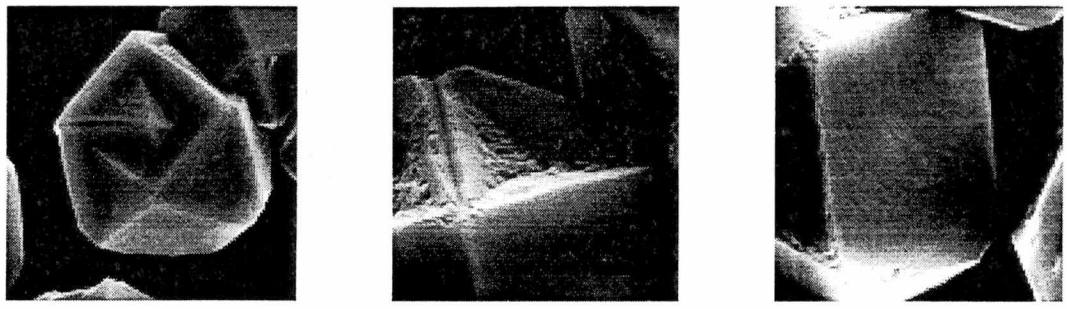

Figure 2 : Scanning electron micrographs of a film grown under the following conditions; filament temperature 2120° C, substrate temperature 1050° C, and 1.0% methane in hydrogen gas mixture.

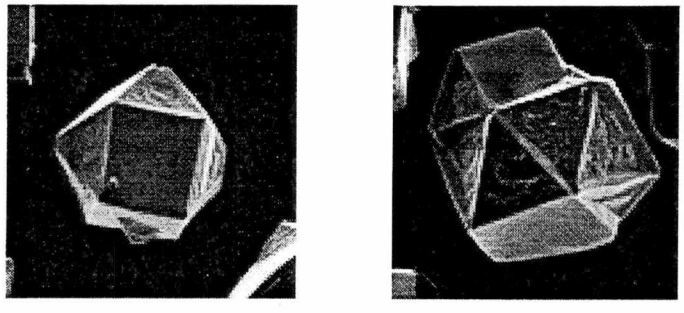

Figure 3 : Scanning electron micrographs of a film grown under the following conditions : filament temperature 2020 °C, substrate temperature 1052 °C, and 1.0% methane in hydrogen gas mixture.

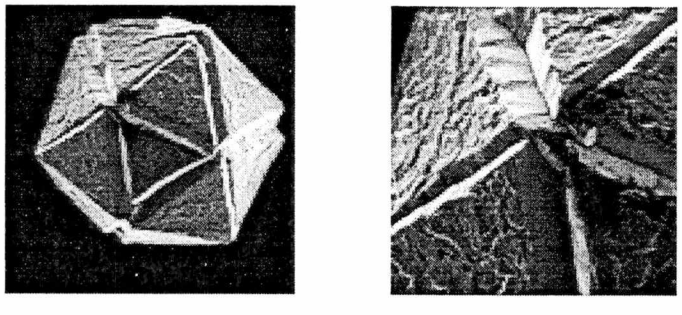

Figure 4 : Scanning electron micrographs of a film grown under the following conditions : filament temperature 1980 °C, substrate temperature 1060 °C, and 1.0% methane in hydrogen gas mixture.

by 50 °C, i.e. 1100 °C, as seen in fig. 5, all of the {111} faces appear to be flat. Filament temperatures of 2020 °C and substrate temperatures of 1030 °C resulted in films that with fully developed hoppered {111} faces as seen in fig. 6.

The hopper {111} faces appear within a range of filament and substrate temperatures (between 2000-2100 °C and no greater than 1055 °C, respectively). Perhaps, a combination of the composition and concentration of gas phase species and, surface phenomenon, such as diffusion and mobility determine the probability of appearance of these hoppered faces. More experiments (gas phase diagnostics near the surface) and theoretical modeling are needed to fully understand the appearance of this morphological feature.

Observations from the scanning electron micrographs of the films with hopper shaped {111} faces instead of flat {111} include : a) the {100} faces appear to be flatter than the {111} faces, b) steps originate from the corners of the {100} faces, as well as the corners enclosed by the three planes comprising the hopper face, c) the edges of the cubo-octahedron, which lie in <110> directions, are broken and not at all sharp, d) the planes comprising the hopper do not meet at clean edges, and e) other growth features are present at the bottom of the hopper which somewhat resemble triangular tiles making up segments of a more or less planar {111} composite feature.

The AFM analysis provides quantitative results of the angles between the faces comprising the hopper shaped {111} and the adjoining faces. Fig. 7 shows an AFM image of a typical hopper shaped {111} face produced in these films. This feature indicates that planes with higher indices than the usual {100} and {111} are forming. The Miller indices for the planes in and surrounding the

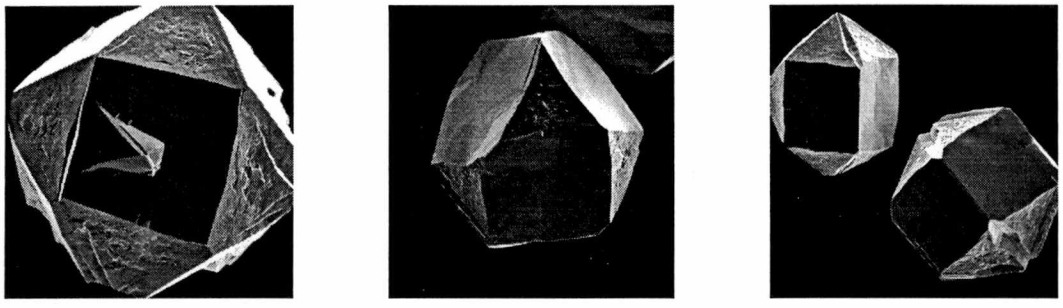

Figure 5 : Scanning electron micrographs of a film grown under the following conditions; filament temperature 2100 °C, substrate temperature 1100 °C, and 1.0% methane in hydrogen gas mixture.

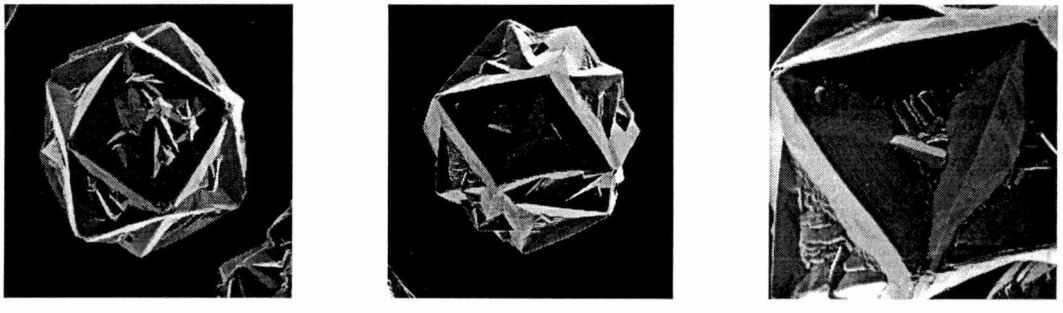

Figure 6 : Scanning electron micrographs of a film grown under the following conditions; filament temperature 2020 °C, substrate temperature 1030 °C, and 1.0% methane in hydrogen gas mixture.

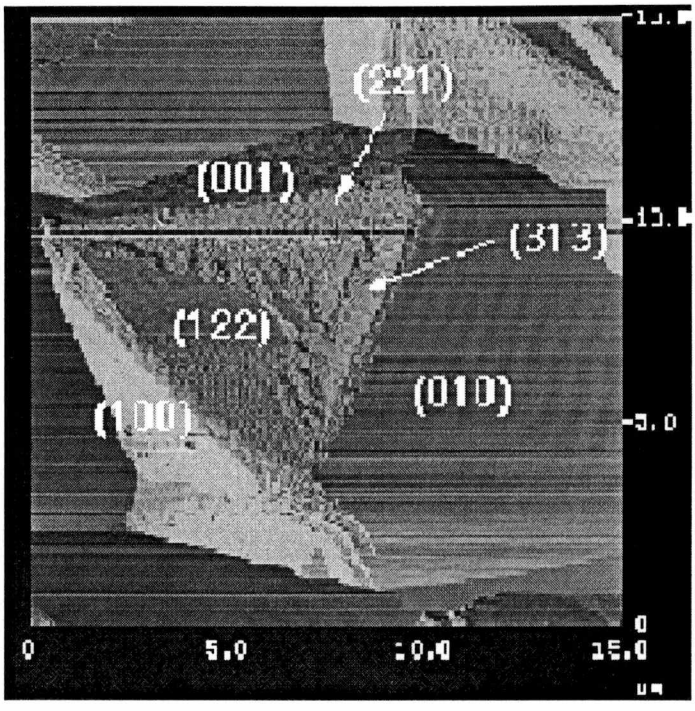

Figure 7 : A 15μm X 15μm tapping mode AFM image of a hopper shaped feature with Miller indices indicated for the feature and the immediate surrounding facets.

hopper are identified in the figure. The indices were determined by measuring the angles between planes and comparing with those obtained from the standard cubic projections shown in fig. 8. For example, the angles between the face identified as the (100) in fig. 7 and the adjacent face inside the hopper (these planes share a common [110] direction) has an average measured value of 68.6°, which corresponds closely to the angle of 70.5° calculated between (100) and (122) faces. Similarly, the angle between the face identified as (010) and the adjacent face inside the hopper (these again share a common [110] direction) is measured to be 75.6°, which corresponds favorably with the value of 76.7° calculated between (010) and (313) faces. Additional angles measured between the interior hopper faces confirm the assignment of the hopper faces belonging to the {221} and {331} family.

The relationship between the low and the high index planes are summarized in the standard (001) projection of a cubic crystal shown in fig. 8. In particular, the {221} and {331} planes fall on the same great circle having a common [110] zone axis.

Table 2 summarizes the angles measured between the various planes and those calculated based upon the crystal structure of diamond. The table is arranged into 3 groups of angles, those between one of the {100} faces and its adjacent hopper face, those between two adjacent hopper faces, and those between one of the {100} faces and the other two non-adjacent hopper faces. The angles being reported have been averaged for different sets of the same face seen on the same or on a different image. For each set, the measurements were repeated about ten times and the indicated errors correspond to the standard deviations of the angles measured. The angles between some of the

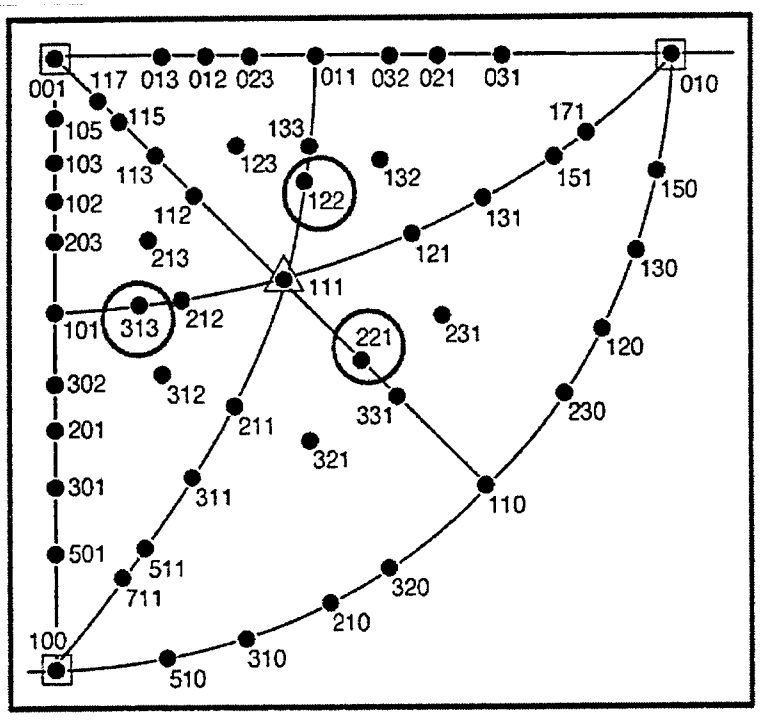

Figure 8 : The standard (001) projection of a cubic crystal illustrating the relationship between low and high index planes.

Table 2 : Comparison of the calculated and measured angles between planes comprising the hopper shaped {111} face. Measured values were obtained by plane fitting of AFM images.

Planes	Calc. Angles (deg.)	Meas. Angles (deg.)	Difference (deg.)
(100)(122)	70.53	68.6 ± 1.5	1.9
(010)(313)	76.74	75.6 ± 3.9	1.1
(001)(221)	70.53	67.5 ± 1.8	3.0
(122)(313)	32.73	29.4 ± 4.0	3.3
(122)(221)	27.26	23.9 ± 1.0	3.4
(221)(313)	32.73	25.5 ± 2.1	7.2
(100)(313)	46.51	42.8 ± 2.0	3.7
(100)(221)	48.19	48.0 ± 2.9	0.2
(010)(122)	48.19	53.1 ± 3.3	-4.8
(010)(221)	48.19	52.0 ± 2.2	-3.8
(001)(122)	48.19	51.3 ± 2.3	-3.1
(001)(313)	46.50	46.6 ± 1.9	-0.1

{100} faces were also measured and were found to give an average value of 90.7°, which is in good agreement with the calculated value of 90°. Sources of error in these measurements could be from the piezo calibration and thermal drift. An error of approximately 0.5 percent in the z-piezo calibration

corresponds to an approximate 3° error in the angle measurements. The angle measurements should be made on the flat area of the face, away from the edges. Since the faces comprising the hoppered {111} face are not completely developed, and have a relatively small completely flat central area, some tip effects creep in. The features seen in an AFM image are convolutions of the tip shape and the shape of the feature itself. The effects of tip have been extensively studied by various groups. Westra et al. [17] have presented the effects of tip shape on surface roughness measurements. Chu et al. [18] have discussed the tip quality, piezo calibration and have proposed a statistical process control approach for tapping mode AFM measurements. These effects were considered and were found to be minimal. The indices for the faces comprising the hopper and its surroundings are summarized in fig. 9.

Conclusions

The presence of near {221} and {331} faces inside the hopper suggests a growth mechanism involving steps [19] nucleated at an outside edge and proceeding inward into the hopper. Such stepwise growth would lead to faces of the type {221}, {331} etc. depending on the relationships between nucleation of steps and their propagation over the underlying {111} face. According to the Periodic Bond Chain (PBC) theory, which has been previously applied to analysis of diamond growth morphology [20], the {111} face is an F or a flat face which makes it a slow growing face. Growth on this face should occur layer by layer due to the difficulty of creating new nucleation sites. The {110} face on the other hand is an S or a stepped face with low barrier to nucleation. It rapidly grows out and therefore is rarely seen. The {221} and {331} are both higher index faces of the type $\{1,1,\pm\delta\}$ and belong to the [110] zone and are also S type

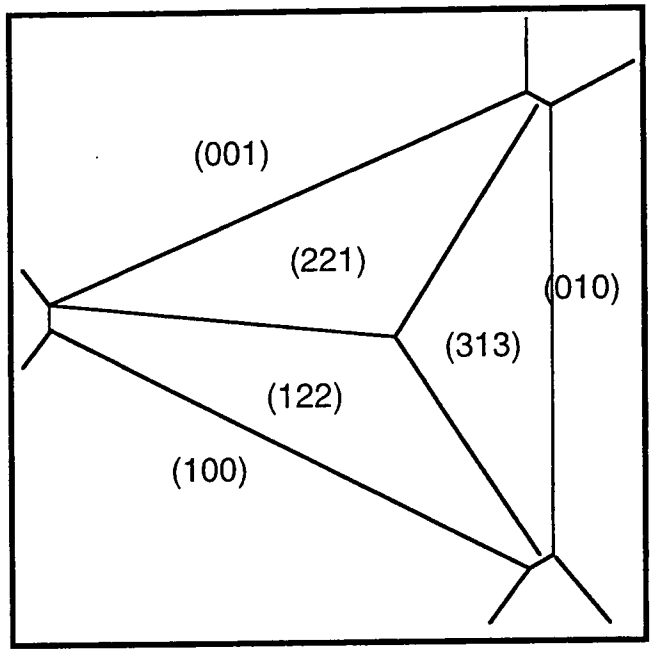

Figure 9 : A schematic of a hopper shaped face showing the miller indices assigned for the identified planes comprising the hoppered {111} faces.

faces but with a lower step density. The facets appear to be relatively flat indicating that surface reconstruction and surface diffusion may play an important role in their growth. The faces could be concave if the edges formed by the intersection of adjacent hopper faces are prolific sources of growth steps or kinks. The fact that the edges to the hopper faces fill in and the bottom of the hopper fills in implies that nucleation and propagation of sites are rate limiting steps for growth in the hopper rather than the arrival of nutrients from the gas phase. The propagation of steps incorporating many crystal layers may be the result of surface reconstruction, surface diffusion, or impurity effects.

In conclusion, it is believed that quantitative crystallographic information such as that presented here can be used to suggest and test models of growth mechanisms, especially when combined with parametric growth studies.

References

1. K. F. Turner, Y. M. LeGrice, B. R. Stoner, J. T. Glass and R. J. Nemanich, J. Vac. Sci. Tech. B **9**, 914 (1991).

2. F. Stubhan, M. Ferguson, H. J. Fusser and R. J. Behm, Appl. Phys. Lett. **66**, 1900 (1995).

3. L. Vazquez, O. Sanchez and J. M. Albella, J. Vac. Sci. Tech. B **12**, 1 (1994).

4. M. A. Tamor and M. P. Everson, J. Mater. Res. **8**, 1770(1993).

5. T. Tsuno, T. Tomikawa, S. Shikata, T. Imai and N. Fujimori, Appl. Phys. Lett. **64**,572 (1994).

6. L. F. Sutcu, M. S. Thompson, C. J. Chu, R. J. Hauge, J. L. Margrave and M. P. D'Evelyn, Appl. Phys. Lett. **60**, 1685 (1992).

7. Y. Kuang, Y. Wang, N. Lee, A. Badzian, T. Badzian and T. T. Tsong, Appl. Phys. Lett. **67**, 3721 (1995).

8. Y. Kuang, N. Lee, A. Badzian, T. T. Tsong, T. Badzian and C. Chen, Dia. and Rel. Mater. **4**, 1371 (1995).

9. T. J. Kreutz, R. E. Clausing, L. Heatherly, Jr., R. J. Warmack, T. Thundat, C. S. Feigerle and K. Wandelt, Phys. Rev. B **51**, 14554 (1995).

10. M. P. Everson and M. A. Tamor, J. Vac. Sci. Tech. B **9**, 1570 (1991).

11. M. P. Everson, M. A. Tamor, D. Scholl, B.R. Stoner, S. R. Sahaida and J. P. Bade, J. Appl. Phys. **75**, 169 (1994).

12. J. S. Kim, M. H. Kim, S. S. Park and J. Y. Lee, J. Appl. Phys. **67**, 3354, (1990).

13. K. Hirabayashi and N. I. Kurihara, Jap. J. Appl. Phys. **29**, 1901, (1990).

14. H. Sun, S. Yu, Z. Jiang, D. Li, L. Liu, Z. Jin and G. Zou, Dia. and Rel. Mat. **5**, 1308, 1996.

15. I. Sunagawa, J. of Cryst. Growth **99**, 1156 (1990).

16. P. Mehta, C. S. Feigerle, L. Heatherly and R. E. Clausing, unpublished.

17 K. L. Westra and D. J. Thompson, J. Vac. Sci. Tech. B **13**, 344 (1995).

18. P. K. Chu, R. G. Brigham and S. M. Baumann, Mat. Chem. and Phy. **41**, 61 (1995).

19. W. K. Burton, N. Cabrera and F. C. Frank, Philosoph. Trans. R. Soc. London A **243**, 299 (1951).

20. L. J. Giling and W. J. P. Enckevort, Surf. Sci. **161**, 567 (1985).

Part 6 : A study of the effect on growth morphology of polycrystalline HFCVD diamond films due to the addition of ammonia in the input gas mixture

Introduction

Nitrogen and boron are the only two known impurities that are naturally incorporated into the diamond lattice. Natural diamond with nitrogen impurities is categorized as Type I whereas Type II contains very little or no nitrogen at all. Type I is further divided into Types Ia and Ib based on the location of nitrogen, as aggregates or on substitutional lattice sites, respectively. Type II is subdivided as IIa if it insulating, or as IIb if it is semiconducting. The presence of nitrogen has been known to affect the optical, mechanical, thermal and electrical properties of diamond [1]. In view of this, until recently, the incorporation of nitrogen into the diamond lattice has been viewed rather pessimistically. Recent observations reveal the beneficial effect that nitrogen incorporation has on the morphology of CVD diamond films. The importance of morphology has been emphasized throughout this work and is an important link between the growth conditions and the applications (properties) of the films. This study details the changes observed in the film morphology as a result of the addition of ammonia and nitrogen to the methane in hydrogen feed gas mixture.

Literature review of the effect of nitrogen on properties

Diamond has very desirable optical properties such as transparency in the infrared region, a refractive index of ~2.42 (in the spectrum between 656 and 486 nm) [2], low optical loss etc. These optical properties when combined with its thermal conductivity and superior mechanical strength makes diamond suitable for a wide range of applications such as windows, lenses, and mirrors. The presence of nitrogen, in the diamond lattice, affects its optical properties, especially in the infrared and ultraviolet region. Optical color centers (e.g. boron

containing diamonds are blue whereas nitrogen containing diamonds are yellow), were probably one of the first properties to be recognized since they are integral to the classification scheme for diamond. The presence of nitrogen in Type Ia can be recognized from the impurity induced infra-red absorption spectrum. It also gives rise to strong absorption in the ultra-violet. It has been noted [1] that nitrogen is not paramagnetic in samples where it exists in aggregate forms. In contrast, Type Ib diamond, where nitrogen is substantial, is found to produce paramagnetic resonance.

Kaiser et al. [3] have studied nitrogen as an impurity in Type I diamond as early as 1959. They have shown that when nitrogen occupies a substitutional position in the lattice, its optical, electrical, and thermal properties depend upon the nitrogen concentration. In particular, these authors have reported the infrared absorption coefficient at 7.8 μm and shown its proportionality to nitrogen content. In the ultraviolet, Type I diamonds have an ultraviolet absorption cut off frequency of approximately 3000 Å, whereas Type II diamonds have a cut off at 2250 Å. They have shown that the shift in the ultraviolet absorption curve for diamond is also proportional to the nitrogen content.

Smith et al. [4] have studied the EPR spectrum of nitrogen donors in natural diamond. Their spin resonance results indicate that nitrogen may be present in a non-paramagnetic form, in adjacent substitutional pairs. Recently, paramagnetic studies have been done [5] on nitrogen containing diamond films grown via microwave assisted chemical vapor deposition. In these growths, nitrogen point defects are favored over aggregate nitrogen formation. Infrared spectroscopy has been used [6] to identify defects and impurities in CVD diamond films. McNamara et al. [6] have shown that nitrogen can have

considerable effect on the optical absorption of diamond in the desirable wavelength region of 8-12 μm in the infra-red region.

One of the most advantageous properties of diamond is its mechanical strength. Commercial applications which utilize this property, e.g. diamond coated tools, are already actively under development. Nitrogen incorporation has been shown [7,8] to generate stress in diamond films, which, affects its mechanical strength. Bergman et al. [7] have used Raman spectroscopy and photoluminescence to study internal compressive stress in diamond films. These authors have implicated nitrogen as being a part of the source of this compressive stress. Stress generated by impurities has been discussed by Anthony [8], who has shown that inhomogenous incorporation of impurities such as nitrogen, boron or hydrogen atoms will generate an overall stress in a film. He notes that the inhomogenous distribution of impurities originates from an uneven incorporation of impurities in the high- and low- order crystal growth sectors and are dependent upon the conditions being used for film growth. The stresses generated in these films can strengthen or weaken the film depending upon their distribution. As noted by Anthony, a positive radial gradient will toughen the film whereas a negative radial gradient will weaken it and make it susceptible to fracture.

It is difficult to say which aspect of its properties is more or less important, when it comes to diamond. As noted by Yoder [2], diamond exhibits extreme values for virtually every material property. It's thermal conductivity is greater than that of any known material. Since thermal conduction takes place by means of phonon propagation (elastic wave), any impurity in the lattice will retard it. It has been reported [9] that the thermal conductivity of diamond

decreases with incorporation of nitrogen in the film. The incentive of nitrogen addition stems from desirable control in morphology, so that, a small trade off in thermal conductivity may not be an overall loss. However, this still needs to be experimentally established.

It is perhaps the electrical properties of diamond that have sustained the highest level of interest in this field. The electrical properties [2] such as its band gap (5450 meV), hole mobility (1800 $cm^2\ V^{-1}sec^{-1}$), electron mobility (2000 $cm^2\ V^{-1}sec^{-1}$), resistivity (10^{16} ohm-cm), breakdown voltage ($10X10^6$), and dielectric constant (5.7) are better than those of any other semiconductor material. Natural semiconducting diamond was discovered to be a p-type by Custers in 1952 [10]. It was then established that in natural p-type semiconductor diamond, boron is the acceptor dopant [11,12]. A combination of its electrical and various physical properties has led to the recognition of diamond as a potential semiconductor for high-temperature, high-frequency and high-power electronic devices. Semiconductor application was first demonstrated by Prins in 1982 [13] using natural Type IIb diamond (p-type semiconducting) and implanting the diamond with C ions to induce n-type region. He was able to demonstrate diode and bipolar transistor action. Geis et al. [14] have used synthetic boron doped diamond obtained by high pressure high temperature synthesis to fabricate point contact transistors and Schottky diodes. The application of diamond in the semiconductor industry has been of tremendous interest to researchers [15, 16, 17]. The negative electron affinity of diamond has made its application as cold cathodes in field emission displays possible. Tremendous efforts are being made to use the p-type semiconductor obtained by doping of diamond with boron. The further development of diamond-based electronic devices is hindered mainly due to the inability of

making an n-type diamond semiconductor. Although nitrogen acts as a donor, it is a deep level donor [18]. As a result n-type doping has been viewed rather pessimistically so far. Wentorf et al. [19] tried ion implantation of nitrogen into a diamond surface. Activation temperatures above 1400 °C result in graphitization of diamond surface making ion implantation an unsuccessful approach for nitrogen doping. Yoder [2] notes that shallow donor impurity may prove difficult, and suggests that hot electron injection from a nearly lattice matched boron nitrite material of even higher bandgap may be possible. Kajihara et al. [20] have investigated potential n-type dopants by ab-initio methods. They find that nitrogen is a deep level donor occupying a substitutional site distorted along the (111) direction, whereas P, Ti, and Na, although shallow donors, have very low solubilities.

Recent reports [21,22] have been made of relatively high conductivity, n-type single and polycrystalline diamond films being produced by doping with phosphorus, which is expected to be a shallow donor (~0.35 eV). Yokota et al. have reported nitrogen doped diamond films via addition of nitrogen gas to the gas mixture used [23]. The nitrogen content of these films is, however, not known. Mort et al. [24] have successfully doped diamond films with nitrogen via addition of NH_3 to the input gas mixture. They have used SIMS and find the nitrogen concentration in these films to be $3X10^8$ atoms/cc. They observe a decrease of several orders of magnitude in the electrical conductivity due to compensation of existing acceptor states in nominally undoped diamond films. This suggests that nitrogen may be used as a probe of these important band-gap states.

Study of the use of nitrogen in the growth of diamond has been limited, perhaps, due to the prevalent pessimism regarding its effect on the properties and its recognition as a deep level donor. However, recently, data is beginning to emerge [9, 25-38] which shows the effects of small additions of nitrogen into the gas phase as being important and potentially beneficial to surface morphology. Most of these experiments have been performed in microwave plasma systems, however, very recently data is also beginning to surface from the HFCVD community. The data available so far is not targeted at semiconductor applications, but is, perhaps, a step forward in understanding the role of nitrogen and may help in solving the problem of obtaining an n- type semiconductor from diamond. Interestingly, nitrogen is being reported to affect the morphology of the growing crystals and may prove very beneficial in producing better quality CVD material.

Literature review of the effect of nitrogen on morphology

Recent studies [9, 25-38] indicate that the addition of nitrogen affects growth rate, morphology, crystalline quality and texture of the films. Small amounts of nitrogen addition to the input gas [9, 28, 32-34] increase the growth rate. Growth rates in the [100] and [111] crystallographic directions have been measured [9, 25-28] and are found to be affected differently by the addition of nitrogen. The amount of nitrogen being incorporated into the films has been determined [26, 27, 31, 32, 34]. Incorporation in the {111} growth sectors is found [26, 27] to be 3-4 times higher than in the {100} growth sectors. Addition of nitrogen is observed to facilitate the growth of <100> fiber textured films [25, 28-30, 34]. Raman spectroscopy shows improvement in crystalline quality [25, 29, 34, 36] for small additions of nitrogen. Higher amounts, in some cases,

deteriorate the crystalline quality of the film [25, 36], whereas others have reported no change in quality with increasing nitrogen concentration [32, 33]. Complete understanding of these effects is possible only after reaction mechanisms are known. Mechanisms for the addition of nitrogen have been proposed [29, 32, 33, 36], however additional work on gas phase chemistry and theoretical modeling is needed before confidence in a mechanistic model can be realized.

Locher et al. [25] have observed that in a microwave plasma system, at low methane concentrations the addition of nitrogen has very little effect, at methane concentration of 1-2 % however, a much more pronounced effect is observed. Wild et al. [28] observe that the homoepitaxial growth rate of {100} film increases by a factor of 1.8 if nitrogen is added in the gas mixture. Muller-Sebert et al. [9] have reported that the growth rates, for polycrystalline diamond film deposited via microwave plasma assisted chemical vapor deposition, increase with increasing amounts of nitrogen, up to 50 ppm, added to the input methane and hydrogen gas mixture. The maximum value being 5 times for 25 ppm addition. Cao et al. [32] have done homoepitaxial diamond film growth co-doping with nitrogen and phosphorous via hot filament chemical vapor deposition and find that addition of N_2 doubled the growth rate. Jin et al. [35] report that the addition of nitrogen during hot filament chemical vapor deposition of diamond films increased the growth rate by a factor greater than two as the N/C gas phase ratio is changed from 0.1% to >10%. Bohr et al. [36] find that change in the growth rate depended upon the filament temperature. Higher N_2 additions resulted in opposing growth rate changes in comparison with low N_2 additions.

Locher et al. [25] observe the transformation of surface morphology from being microcrystalline to well faceted crystals due to the addition of small amounts (40-200 ppm) of nitrogen in microwave plasma enhanced CVD. The effect on the [100] and the [111] crystallographic growth directions has been studied by Wild et al. [4]. they find that the addition of small amounts of nitrogen (0-50 ppm) enhances the growth on the {100} surfaces, especially at high methane concentrations of 1.5%. They find that under these conditions growth in [100] direction is much more than in the [111] direction, resulting in higher values of α.

Locher et al. [25] find that the grain structure for polycrstalline film showed a transition from a <110> fiber texture to a <100> fiber texture with large {100} facets. Their experimental results suggest that the threshold concentration required for the formation of <100> textured films is 200 ppm for 1.0%, 40 ppm for 1.5% and 20 ppm for 2.0%. Cao et al. [33] have studied {100} textured diamond films grown with the addition of nitrogen in the form of NH_3. They find that partially {100} fiber textured films are produced from a nitrogen containing gas mixture. They observe that for homoepitaxial growth the <100> has the slowest growth rate in the absence of nitrogen, however, the <100> directions grows fastest in comparison with the <110> and the <111> directions if 100 ppm nitrogen is introduced into the system during growth. Jin et al. [34] have studied the conductivities of diamond films and find that a strong correlation exists between the electrical conductivity activation energy and habit of growth. Their results suggest that the nitrogen impurities incorporate more efficiently when the growth habit is (100). They also observe [35] that the growth habit changes from (111) to (100) with the increase in the N/C gas phase ratio from 0.1% to 10%. Silva et al. [30] also find that addition of N_2 results in the

{100}<100> textured films instead of {111}{100}<110> films that are obtained without the N_2 addition.

Jin et al. [35] have theoretically calculated the nitrogen doping efficiency to be 10^{-4} which seems to be in good agreement with the experimental results of Samlenski et al. [26] and Spicka et al. [37]. Samlenski et al. [26] have used NRA to determine the incorporation of nitrogen in diamond films grown via microwave plasma. Their results show that the N/C ratios in the films were in the ppm range which was four orders of magnitude lower than the corresponding gas phase ratios. They also report [27] that nitrogen preferentially occupies substitutional sites in the diamond host lattice with a substitutional fraction of 0.8. Their study indicates that nitrogen incorporation in the {111} growth sector is 3-4 times larger than in the {100} growth sector resulting in the incorporation probabilities of $6X10^{-4}$ and $2X10^{-4}$ respectively. Spicka et al. [37] have used SIMS to determine the dopant levels in diamond films grown via HFCVD. Their results indicate the incorporation levels to be really small (below 100 ppma) in films doped with N_2 and note that different results for doping with N_2 can be expected for other gas activation methods such as microwave plasma. Mort et al. [24] have used SIMS to find the nitrogen concentration in diamond films grown via HFCVD and doped with NH_3. Their results indicate these films have incorporated nitrogen concentrations of $3X10^8$ atoms/cc. Cao et al. [32] have grown diamond films co-doped with nitrogen and phosphorus. They have used SIMS to determine the highest concentration of nitrogen to be $6X10^{19}$ atoms/cm^3 in these epitaxial films grown homoepitaxially on natural diamond substrates. Bergmaier et al. [40] have reported the nitrogen content in microwave assisted CVD films using high resolution elastic recoil

detection (ERD) technique. Their results show 0.4% incorporation of nitrogen with respect to carbon.

Raman spectroscopy results of Locher et al. [25] reveal that the films grown at higher methane concentrations (1-2 %) with nitrogen addition in the (10-100) ppm range were of better crystalline quality in comparison with the nitrogen free films. Jin et al. [35] observe that the Raman peak sharpens as the N/C is increased from 0.1% to 40% in the gas phase. Bohr et al. [36] have also studied the influence of nitrogen addition (5%-40% N_2/CH_4) to diamond films grown via HFCVD. Their Raman spectroscopy results indicate that small additions of up to 10% N_2/CH_4 improved the crystalline quality of the film, however the film quality deteriorated for 40%N_2/CH_4. Chatei et al. [29] have studied the effect of varying the concentration of nitrogen introduced in different H_2-CH_4 gas mixtures. They concluded that the crystalline quality is that optimum concentration of nitrogen injected into the reactor may help to improve the quality of diamond films grown via microwave plasma assisted chemical vapor deposition.

May et al. [38] have investigated the effects of the addition of various nitrogen-containing gases such as ammonia, methylamine and HCN, on the chemical composition of diamond films in a HFCVD reactor. They conclude that formation of gaseous HCN seems to be the dominant chemical reaction occurring in the chamber. They report that thermodynamic calculations of Pan et al. [39] confirm that HCN production is highly favored in H-C-N gas mixtures at high gas processing temperatures, however they note that this does not lead to significant incorporation of N into the diamond lattice. They note that addition

of high concentrations of nitrogen did not result in the formation of carbon nitride.

Badzian et al. [31] have reported on the deposition of diamond from methane and nitrogen gas mixtures in a microwave plasma system. They propose that nitrogen becomes an active component of microwave plasma and participates in the abstraction of hydrogen from the diamond surface. They hypothesize that formation of HCN is an indication of hydrogen abstraction allowing diamond growth from CH_4-N_2 gas mixture. They report that the diamond deposited under these conditions shows distortion in its crystalline structure. The sequence of tetrahedral layers shows a tendency towards hexagonal stacking they report. Cao et al. [33] believe that presence of NH_X and CNH_X radicals can significantly change the surface composition of adsorbed species. In particular they believe that these species may break part of the dimers on the (2X1) reconstructed {100} surface and enhance the diamond growth rate of this face relative to the {111} and the {110} faces, by the creation of additional kink sites at the steps. Their observations regarding the surface roughness of the {100} face upon the addition of nitrogen in the gas phase supports the described mechanisms. They [35] explain their observations with the model based on defect-induced stabilization of diamond. Bohr et al. [36] believe that the small N_2 additions were attributable to a reduction of carbon supersaturation due to the abstraction of adsorbed H atoms caused by CN and HCN. At higher N_2 additions the enhanced reconstruction of the diamond surface due to the abstraction of adsorbed H caused the observed growth features. Cao et al. [32] have carried out homoepitaxial diamond film growth doping it with nitrogen and phosphorous simultaneously via hot filament chemical vapor deposition. They report that nitrogen enhances the

incorporation of phosphorus into epitaxial diamond. They believe that large local lattice dilations in caused by single atomic substitutional nitrogen are responsible for the increased doping concentration of phosphorus. Silva et al. [30] have studied the effect of microwave power density and the role of N_2 as impurity in the CH_4-H_2 gas mixture. They have used Raman spectroscopy for film quality, SEM and optical goniometry for studying the morphology, and XRD analysis for texture analysis. They have shown that the plasma power density affects the growth rate and growth rate ratio of the films by controlling the H-atoms concentration, in volume and at the interface. Their results show that higher power densities result in larger range for a parameter and to higher growth rates.

The most important results that have been reported in literature, are perhaps, that the nitrogen addition increases the overall growth rate, and the achievement of the {100} <100> texture. The latter is important because it is now well established that the {111} planes are more defective than the {100}. It is thus desirable to produce {100} oriented films with {100} surfaces. An increase in the overall growth rate as well as a decrease in the growth rate ratio were observed in the course of this study. A careful analysis revealed that the growth rates, in the individual crystallographic directions, increased by different proportions, due to the nitrogen incorporation. The amount of nitrogen incorporated in the different sectors was not measured, however, since the growth conditions used were very similar to those reported by Mort et al. [24], it is expected that these films have similar nitrogen content.

Experimental

The films were grown in a hot filament assisted chemical vapor deposition (HFCVD) reactor which was described in Part 2. In these experiments, the pressure of the growth chamber was maintained at 40 torr, and a mixture of CH_4 and H_2 gas was used at a rate of 50 sccm. Depositions were performed at three levels of CH_4 concentration : 0.5%, 1.0% and 1.5%. A carburized tantalum wire filament was at 2400° C to activate the gases and to indirectly heat the substrate. The films were grown at three distinct substrate temperatures 840 , 980 and 1100 °C. The substrate was mounted on a molybdenum block that was threaded with rhenium wire to resistively heat the sample. The filament and substrate temperatures were measured using a disappearing filament type optical pyrometer without employing any corrections for emissivity or reflections.

The films were grown on Si (001) substrates which had half of the surface scratched with diamond paste, followed by rinsing with acetone and methanol in an ultrasonic bath. The substrate was positioned ~ 10 mm from the filament and the films were grown for 16 hours. The scratched half of the substrate typically developed a continuous diamond film and was used to study the texture. The other half had individual crystallites which provided information regarding the growth rate ratio, appearance of twins and other growth features.

The morphology of these films was studied using scanning electron microscopy (SEM). Film texture was qualitatively determined from the observations of the crystal orientations on the continuous film side of the sample. The growth rates were determined by measuring the dimensions of the individual crystals and dividing the longest dimension by the growth time. The

growth rate ratios were assigned by comparing the individual crystal shapes as seen in the scanning electron micrograph with those in the standard chart. Using simple trigonometric relations, the growth rate ratios and the individual crystal dimensions from the scanning electron micrographs, growth rates in different crystallographic directions were determined. Trends in the overall growth rates and in the different crystallographic directions were then compared.

The first experiments concerned with the effects of nitrogen addition were attempted with the addition of varying amounts of air to the reactor input gases and observing the effect on morphology. Table 1 lists the experimental conditions for those experiments. The addition of air under the normal reactor conditions showed no effect. Change in the substrate temperature (Table 2) was also tried, but showed no effect. Addition of N_2 to the input gas was tried next, the growth parameters used are listed in Table 3. However, that did not seem to have any effect either. Next we tried raising the filament temperature, in order to increase the generation of HCN and other species that were thought to be playing an active role in microwave plasma depositions. Another nitrogen source, more reactive perhaps, was also considered at the same time. TaC filaments were thus used to achieve filament temperatures of ~2400 °C, and ammonia was used as the nitrogen source. Experiments, listed in Tables 4, 5 and 6, were then conducted and showed definite changes as the result of nitrogen additions. Similar experiments were subsequently performed with N_2 additions and showed effects of the same nature, but milder than those obtained with ammonia.

Results and Discussion

(1) Morphology Analysis

(i) Film depositions at conventional filament temperatures

(a) Addition of air

Table 1 lists the results from the addition of different amounts of air to a 1% methane in hydrogen input gas mixture. A WC filament was used at temperatures between 1940 and 1960 °C and the substrate temperature was Table 1 : Addition of air to 1.0% methane in hydrogen gas mixture for filament temperature (1940-1960 °C) and substrate temperature (1015-1040°C)

Air (ppm)	Air (%)	**g** (μm/hr)	**r**	α
19	$1.9X10^{-3}$	0.69	0.80	1.39
63	$6.3X10^{-3}$	0.71	0.90	1.56
168	$1.68X10^{-2}$	0.80	0.87	1.51
3446	$3.446X10^{-1}$	0.65	0.89	1.54
5437	$5.437X10^{-1}$	0.67	0.87	1.51
8269	$8.269X10^{-1}$	0.60	0.90	1.56
14321	1.4321	0.77	0.87	1.51

maintained between 1015 to 1040 °C. The growth rate and the growth rate ratio did not show any appreciable change as the amount of air was increased.

Table 2 lists the experiments that were carried out at several different substrate temperatures with 14,300 ppm (or 1.43%) air being added to a 1% methane in hydrogen input gas mixture. A WC filament was used at ~1950 °C. No appreciable change was observed in the growth rate. The growth rate ratio decreased with the increase in substrate temperature. This however, is an attribute of the change in substrate temperature as has been discussed previously in Part 4.

Table 2 : Addition of 1.43% air to 1.0% methane in hydrogen gas mixture at filament temperature ~ 1950°C

Subs. temp. (°C)	**g** (μm/hr)	**r**	α
1015	0.77	0.87	1.51
1050	0.78	0.78	1.35

(b) Addition of N_2 :

Different amounts of N_2 were added to a 1% methane in hydrogen gas mixture. The filament used was a WC filament at ~1950 °C. The substrate temperature was maintained between 1020 and 1050 °C. The addition of N_2 increased the growth rate. However the amount of N_2 being added did not have

any effect. The growth rate ratio was not affected at all by the addition of N_2. Table 3 lists the growth rates and the growth rate ratios of these samples

(ii) Growth at high filament temperatures

(a) Addition of varying amounts of NH_3 :

A TaC filament was used to achieve higher filament temperatures for the addition of NH_3. The filament was operated at 2400 °C and the substrate temperature was maintained at ~915 °C. Table 4 lists the samples that were grown with the addition of different amounts of NH_3 to a 1.5 % methane in hydrogen gas mixture. A drastic effect was observed in the crystal morphology for 11,200 ppm (1.12 %) and higher ammonia additions. The SEMs of these samples, shown in figure 1(a)-(f), reveal that the crystals maintained a cubo-octahedral geometry with twins on relatively clean underlying facets up to additions of 830 ppm (0.083 %), however for ammonia additions greater than that, the crystals looked microcrystalline.

(b) Addition of NH_3 to three different methane concentrations.

Tables 5, 6 and 7 list the growth conditions for 0.5 %, 1.0% and 1.5% methane in hydrogen gas mixtures. Films were grown under identical conditions, with and without ammonia, for direct comparison. The effects on both r and g at the three temperature levels studied as well as the growth rates in the <100> and <111> directions, g<100> and g<111>, are listed in these tables. Dimensions of the crystals were measured from the SEMs which were then resolved in the different crystallographic directions using trigonometric relations . The input N to C atom ratio in the input gas was kept constant at ~1/6 for all the experiments, resulting in the addition of 2632, 1710 and 789 ppm

Table 3 : Addition of N2 to a 1.0% methane in hydrogen gas mixture at filament temperature ~1950 °C and substrate temperature (1020-1050 °C)

N_2 (ppm)	N_2 (%)	**g** (μm/hr)	**r**	α
0	0	0.91	0.87	1.51
346	$3.46X10^{-2}$	0.74	0.87	1.51
1900	$1.9X10^{-1}$	0.75	0.85	1.47
14530	1.45	0.79	0.85	1.47
18290	1.83	0.75	0.87	1.51
253800	25.38	0.78	0.87	1.51
305600	30.56	0.71	0.87	1.51

Table 4 : Addition of NH3 to 1.5 % methane in hydrogen gas mixture for filament temperature at 2400 °C and substrate temperature of ~915 °C

NH_3 (ppm)	NH_3 (%)	**g** (μm/hr)	**r**	α
0	0	2.2	0.87	1.5
59	$5.9X10^{-3}$	2.3	0.87	1.5
88	$8.8X10^{-3}$	2.5	0.87	1.5
830	$8.3X10^{-2}$	2.7	0.87	1.5
11200	1.1	2.3	microcrystal	----
14500	1.4	2.5	microcrystal	----

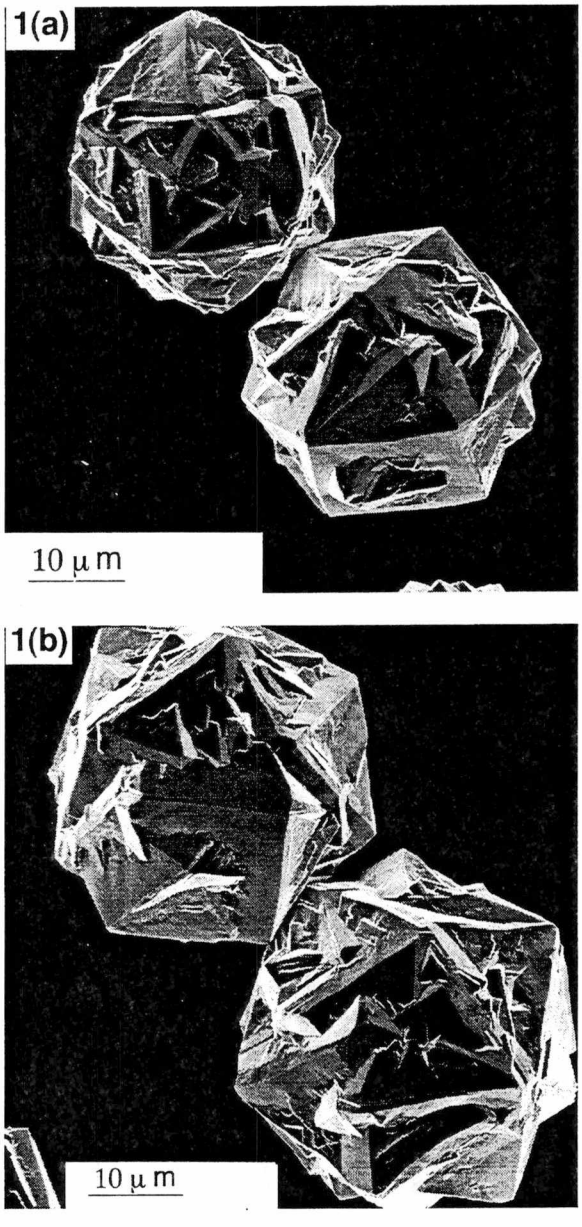

Figure 1 : Scanning electron micrographs showing the effect of addition of NH_3 to 1.5% input CH_4 in H_2 gas mixtures, filament temperature 2400 °C, substrate temperature ~915 °C, Ammonia concentration : (a) 0, (b) 5.9 X 10^{-3}%.

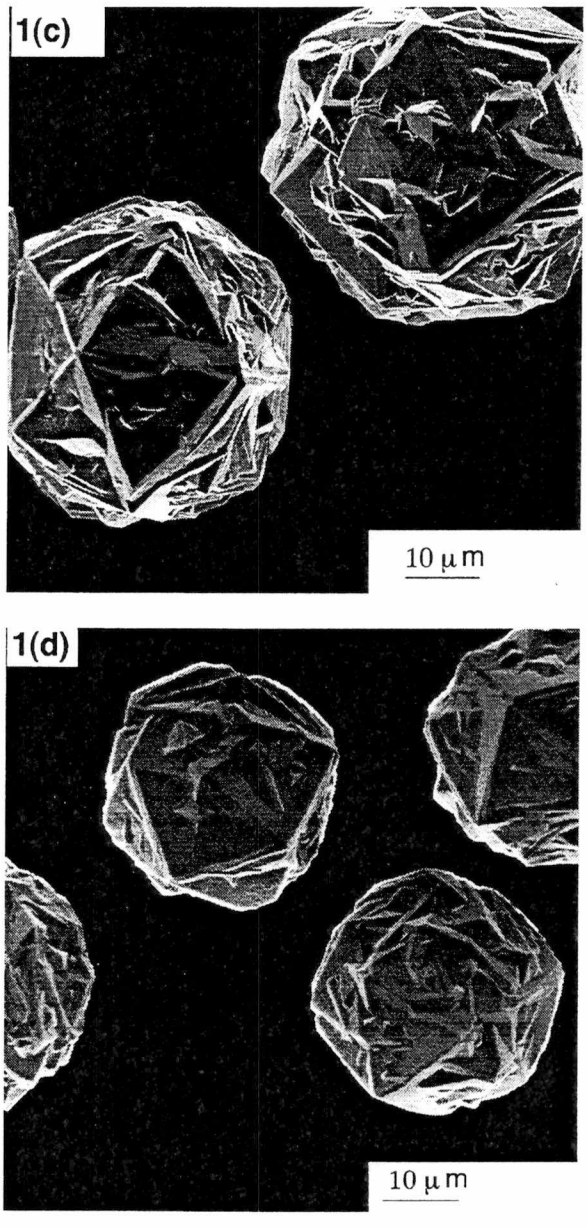

Figure 1 : Scanning electron micrographs showing the effect of addition of NH_3 to 1.5% input CH_4 in H_2 gas mixture, filament temperature 2400 °C, substrate temperature 915 °C, ammonia concentration : (c) 8.8 X 10^{-3}%, (d) 8.3 X 10^{-2} %

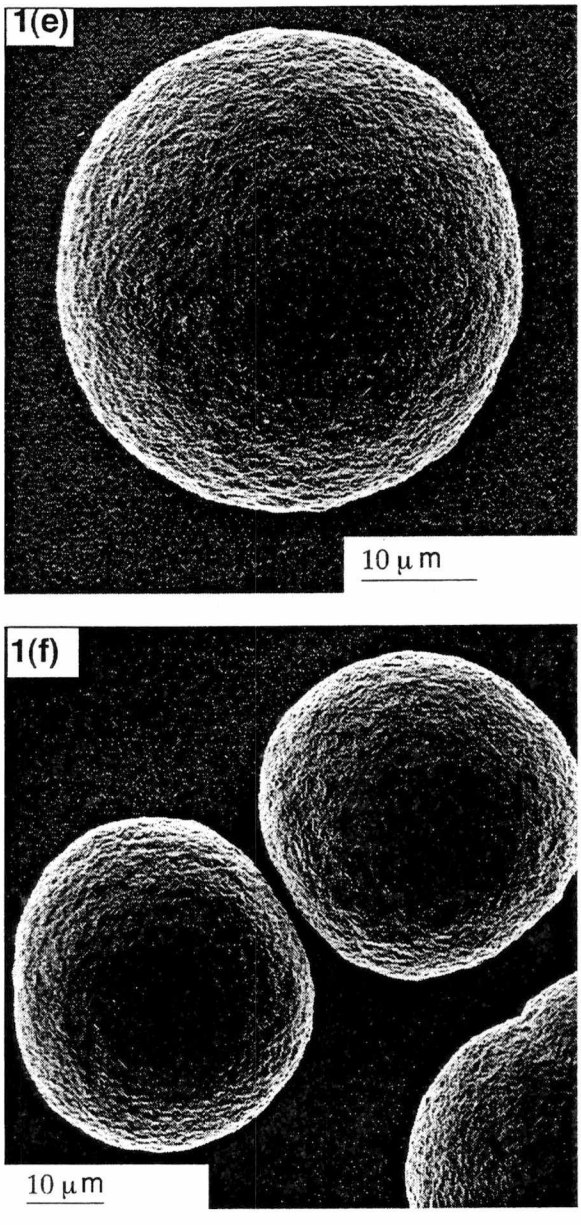

Figure 1 : Scanning electron micrographs showing the effect of addition of NH_3 to 1.5% input CH_4 in H_2 gas mixtures, filament temperature 2400 °C, substrate temperature ~915 °C, Ammonia concentration (%) :(e) 1.12 %, (f) 1.45 %.

Table 5 : Addition of NH3 (N/C=1/6) to 0.5 % methane in hydrogen gas mixture for filament temperature 2400°C

NH_3(%)	Subs. temp. (°C)	**r**	α	**g** (μm/hr)	**g**<100> (μm/hr)	**g**<111> (μm/hr)
0	840	1.15	2.0	0.24	0.20	0.18
0.08	840	1.0	1.7	0.38	0.35	0.35
0	970	0.87	1.5	0.45	0.35	0.41
0.08	990	0.7	1.2	0.96	0.63	0.89
0	1100	0.7	1.2	0.44	0.29	0.41
0.08	1100	0.6	1.0	1.35	0.78	1.31

Table 6 : Addition of NH3 (N/C=1/6) to 1.0 % methane in hydrogen gas mixture for filament temperature 2400°C

NH_3(%)	Subs. temp. (°C)	**r**	α	**g** (μm/hr)	**g**<100> (μm/hr)	**g**<111> (μm/hr)
0	840	0.87	1.5	0.52	0.41	0.47
0.17	840	0.87	1.5	0.74	0.55	0.63
0	1010	0.87	1.5	1.8	1.4	1.6
0.17	1010	0.7	1.2	3.0	2.1	3.0
0	1110	0.7	1.2	1.4	1.1	1.6
0.17	1110	0.6	1.0	2.5	1.2	1.9

Table 7 : Addition of NH3 (N/C=1/6) to 1.5 % methane in hydrogen gas mixture for filament temperature 2400°C

NH_3(%)	Subs. temp. (°C)	**r**	α	**g** (μm/hr)	**g**<100> (μm/hr)	**g**<111> (μm/hr)
0	840	1.15	2.0	0.33	0.31	0.27
0.26	840	0.87	1.5	0.5	0.37	0.43
0	980	0.87	1.5	1.75	1.1	1.2
0.26	980	0.87	1.5	3.25	2.6	3.0
0	1090	0.8	1.4	2.75	2.1	2.7
0.26	1090	0.7	1.2	3.25	2.1	3.0

(0.26, 0.17 and 0.08 %) NH_3 in 1.5%, 1.0% and 0.5% methane concentrations, respectively. Figures 2 (a)-(f), 3(a)-(f), and 4 (a)-(f) show the scanning electron micrographs corresponding to the 0.5, 1.0 and 1.5 % experiments. The (a), (c), and (e) parts of the figures represent micrographs of growths without NH_3 addition, given in order of increasing substrate temperature, whereas, the (b), (d), and (f) parts are the corresponding depositions with NH_3 addition.

(iii) General observations on nitrogen effect on morphology

The scanning electron micrographs, figs. 2 (a)-(f) show the change in morphology for depositions with 0.5% methane. At low temperatures, 840 °C, the film without nitrogen addition showed the crystallites to be cubo-octahedral in shape, with relatively clean (free of twins) facets. The {111} faces were hexagonal shaped, giving the crystal a growth rate ratio of 1.15. However, the addition of ammonia, appeared to deteriorate the crystal shape. The crystallite appeared to have twins on their facets and did not appear to have a geometrically regular shape. Although they looked like a cubo-octahedra, they did not have sharp edges. At the intermediate temperatures, the film grown without nitrogen addition showed crystallites shaped as cubo-octahedra, corresponding to **r**=0.87, with clean facets. The crystallites, however, did include contact twins. The addition of nitrogen, resulted in crystallites, with much smaller {111} faces, having a growth rate ratio of 0.7. This sample had more crystals with contact twins than the corresponding, nitrogen free, sample.

2(a)

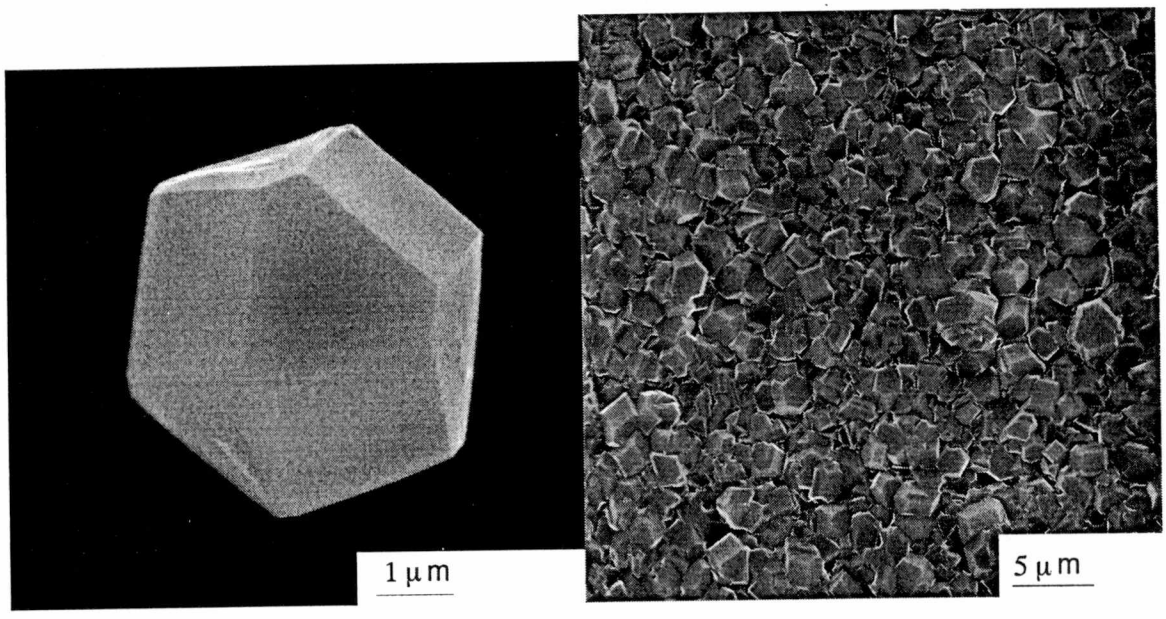

2(b)

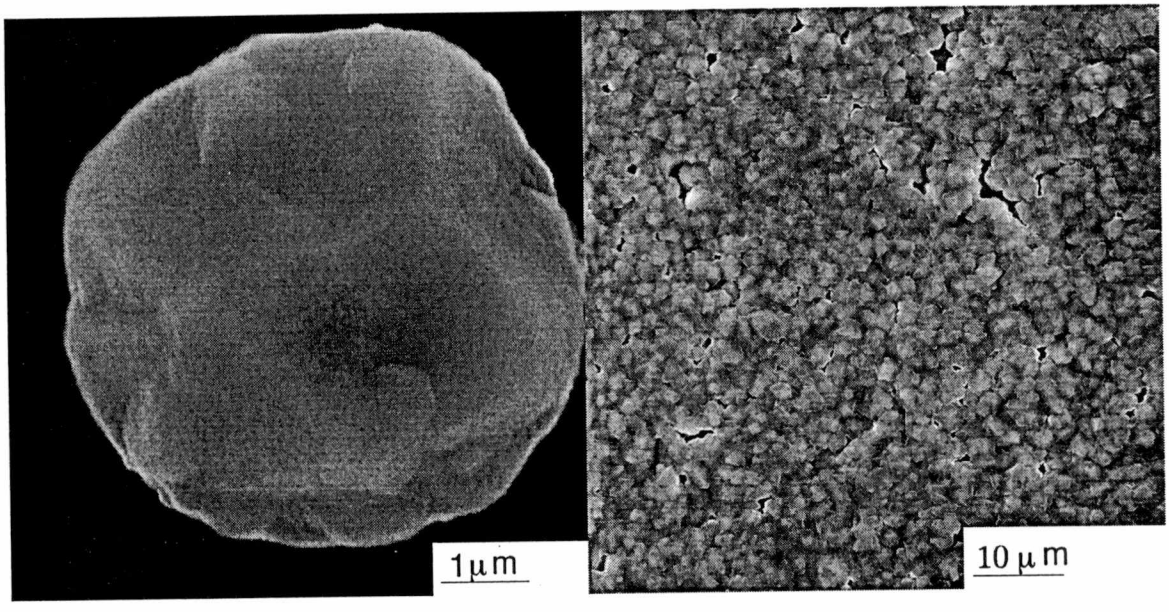

Figure 2 (a)-(b) : Scanning electron micrographs of films deposited with the addition of 0.08 % NH_3 to 0.5 % input CH_4 in H_2 gas mixtures, (N/C=1/6), at filament temperatures 2400 °C, (a) substrate temperature 840 °C without NH_3 addition, (b) substrate temperature 840 °C with 0.08 % NH_3 addition.

2(c)

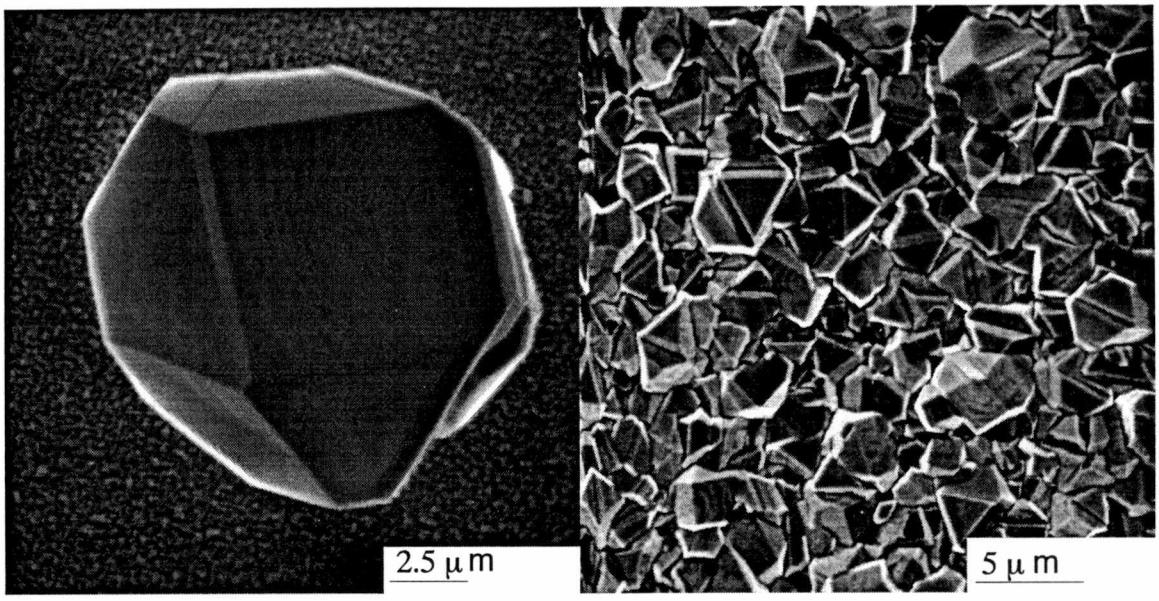

2(d)

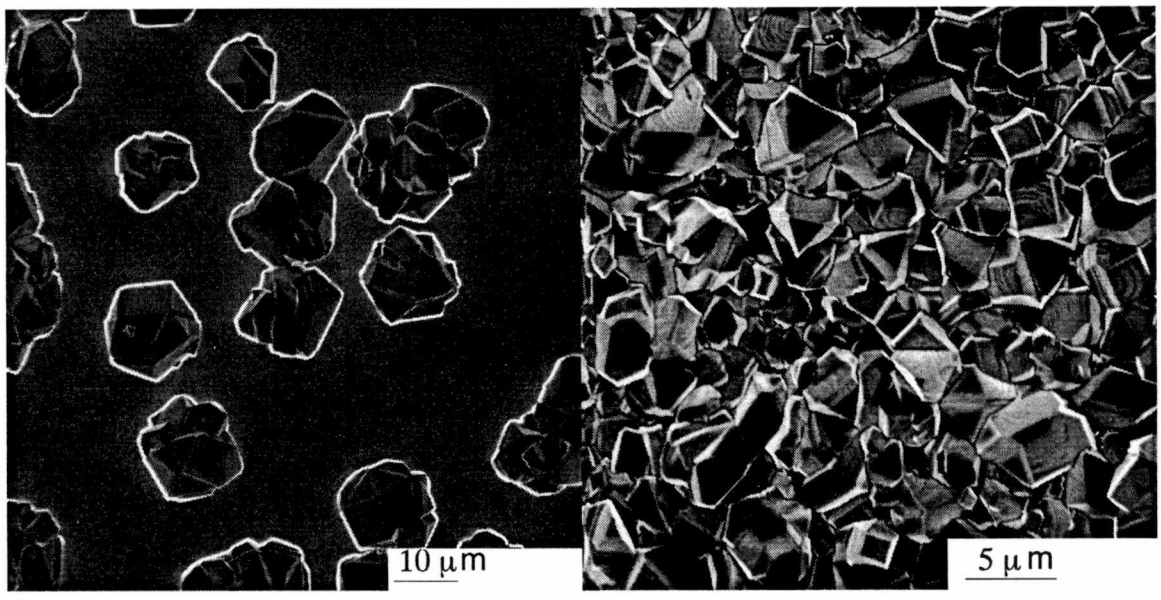

Figure 2 (c)-(d) : Scanning electron micrographs of films deposited with the addition of 0.08 % NH_3 to 0.5 % input CH_4 in H_2 gas mixtures, (N/C=1/6), at filament temperatures 2400 °C, (c) substrate temperature 970 °C without NH_3 addition, (d) substrate temperature 990 °C with 0.08 % NH_3 addition.

2(e)

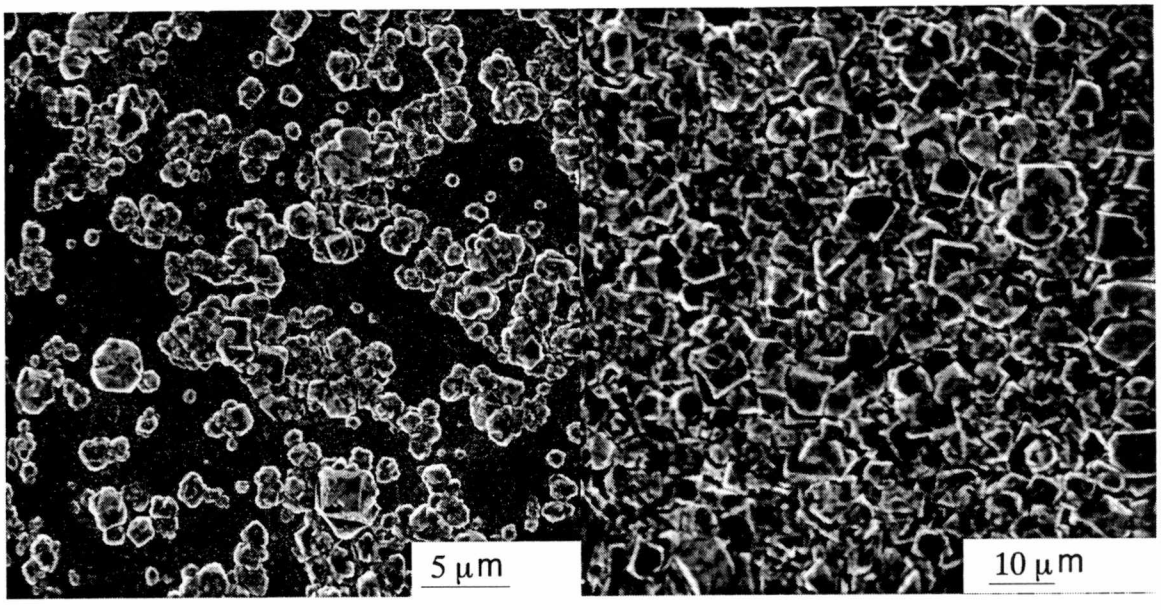

2(f)

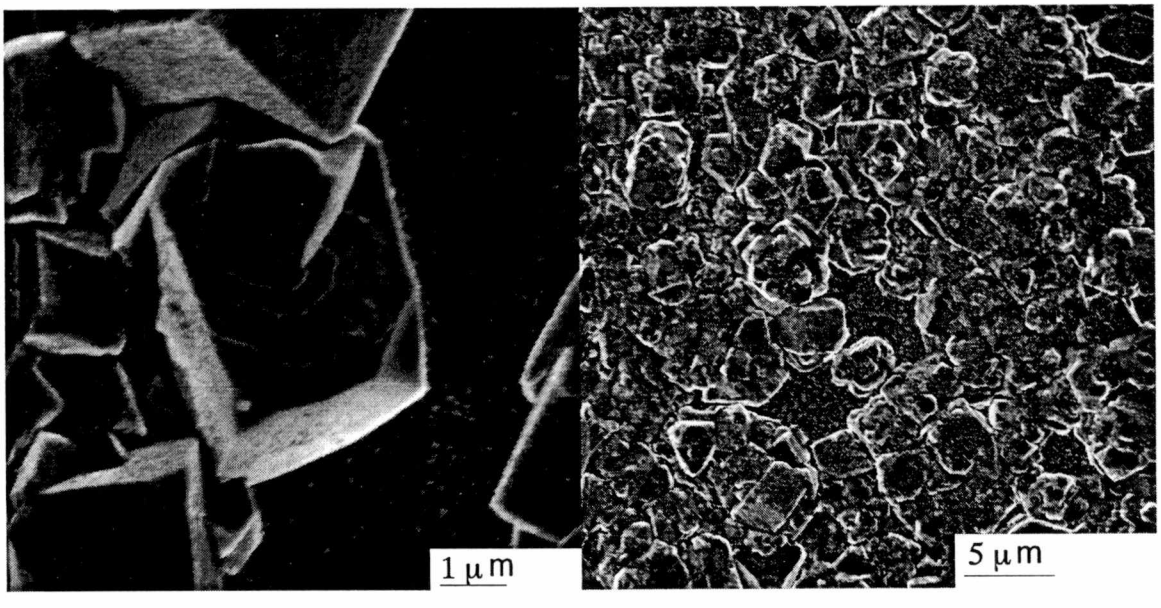

Figure 2 (e)-(f) : Scanning electron micrographs of films deposited with the addition of 0.08 % NH_3 to 0.5 % input CH_4 in H_2 gas mixtures, (N/C=1/6), at filament temperatures 2400 °C, (e) substrate temperature 1100 °C witout NH_3 addition, (f) substrate temperature 1100 °C with 0.08 %NH_3 addition.

At the high temperatures, the nitrogen free film had a wide range of crystal sizes, a growth rate ratio of 0.7, i.e. cubo-octahedral shaped crystals, with smaller {111} faces. The addition of nitrogen, further decreased the size of the {111} faces, giving the crystallites a growth rate ratio value of 0.6, i.e. nearly cube shaped crystals, with very small {111} facets.

The films grown at low temperatures of 840 °C with 1.0% methane showed a large amount of penetration twinning and corresponded to **r**=0.87, i.e. cubo-octahedral shaped crystallites. Addition of nitrogen, resulted in ball like, microcrystalline type, morphology. A closer look revealed, that these crystallites had an underlying cubo-octahedral skeleton and were very highly twinned. The excessive formation of penetration twins gave a ball like appearance. Scanning electron micrographs corresponding to 1.0% CH_4 are shown in figs. 3 (a)-(f). At the intermediate substrate temperatures (1010 °C), the nitrogen free films had very clean facets with cubo-octahedral crystallite geometry still corresponding to **r**=0.87. The films with nitrogen showed smaller {111} faces changing the **r** to 0.7. This sample also showed {100} penetration twins. The films showed {111} faces which were much more rough than the {100}, in both, the nitrogen-free and nitrogen containing films. At the high substrate temperatures (1110 °C), the nitrogen free films had very clean and smooth facets, the crystallites corresponding to **r**=0.7. The nitrogen containing films, were very nearly cube shaped and showed some twin structures running along the diagonal of the {100} face. The shape and orientation of these structures, identifies as {100} penetration twins. The crystallites also show contact twins in the nitrogen containing films.

3(a)

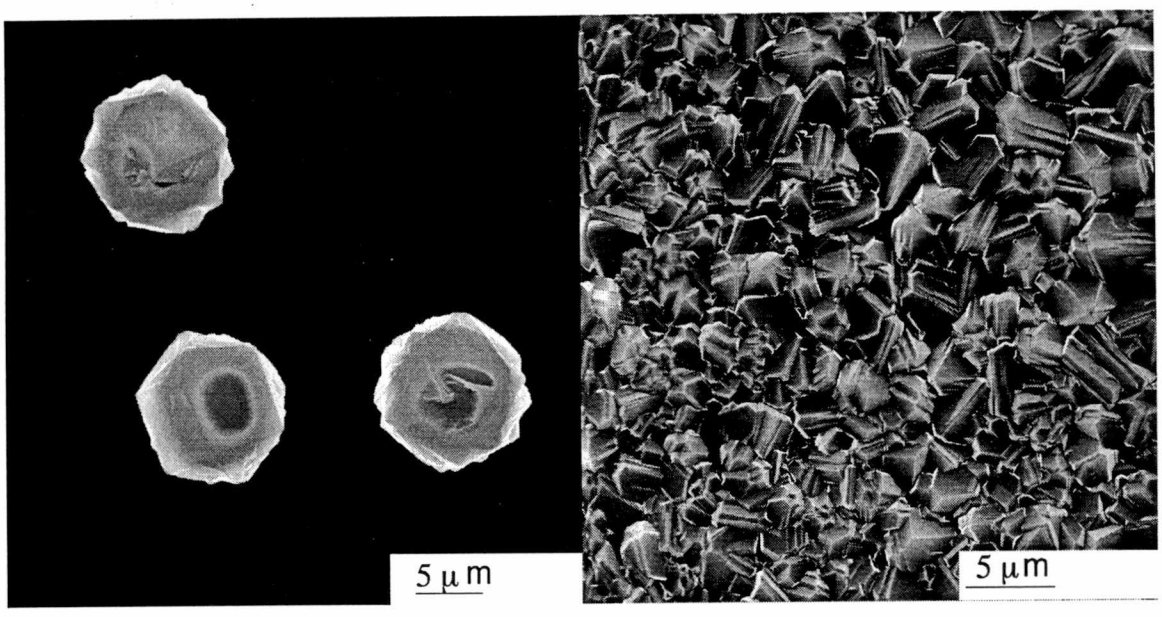

3(b)

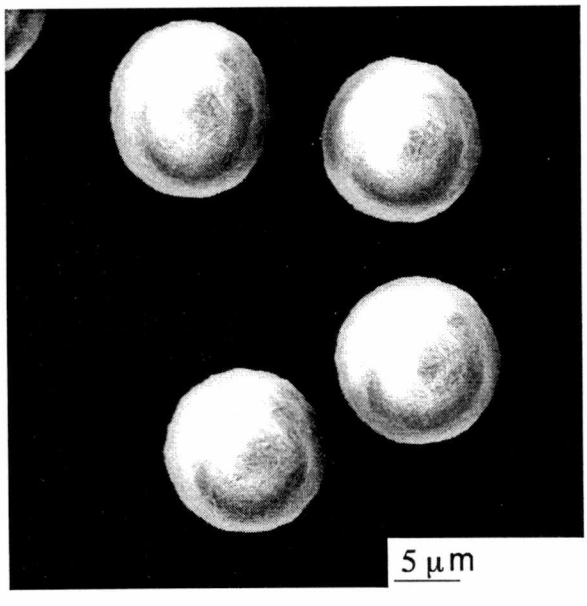

Figure 3 : Scanning electron micrographs of films deposited with the addition of 0.17 % NH_3 to 1.0 % input CH_4 in H_2 gas mixtures, (N/C=1/6), at filament temperatures 2400 °C. (a) substrate temperature 840 °C without NH_3 addition, (b) substrate temperature 840 °C with 0.17 % NH_3 addition.

3(c)

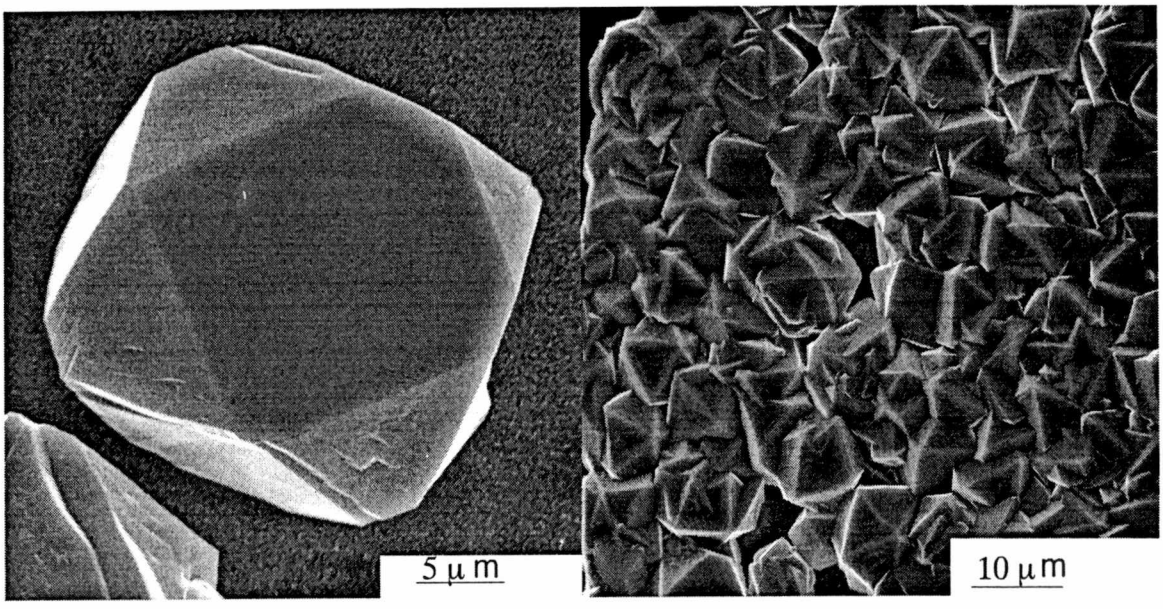

3(d)

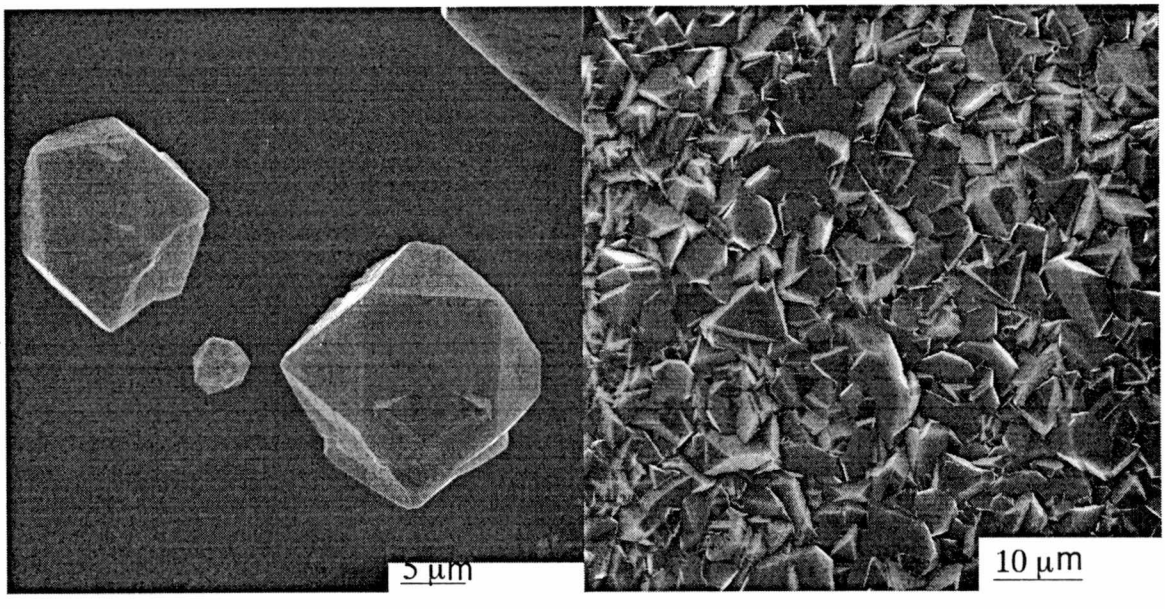

Figure 3 (c)-(d) : Scanning electron micrographs of films deposited with the addition of 0.17 % NH_3 to 1.0 % input CH_4 in H_2 gas mixtures, (N/C=1/6), at filament temperatures 2400 °C: (c) substrate temperature 1010 °C without NH_3 addition, (d) substrate temperature 1010 °C with 0.17 % NH_3 addition.

3(e)

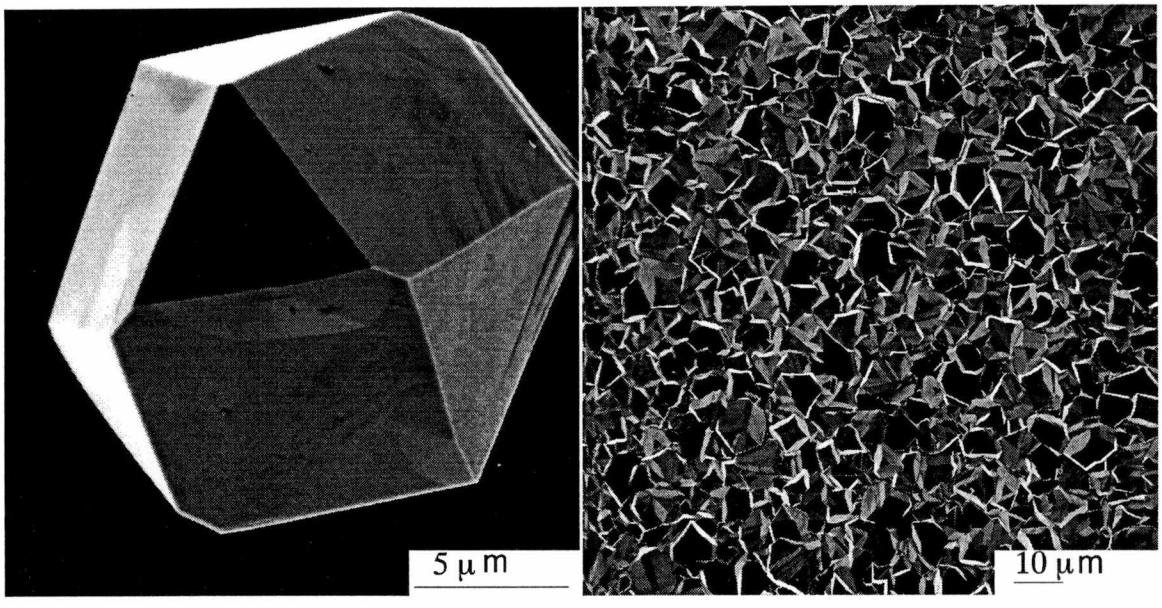

3(f)

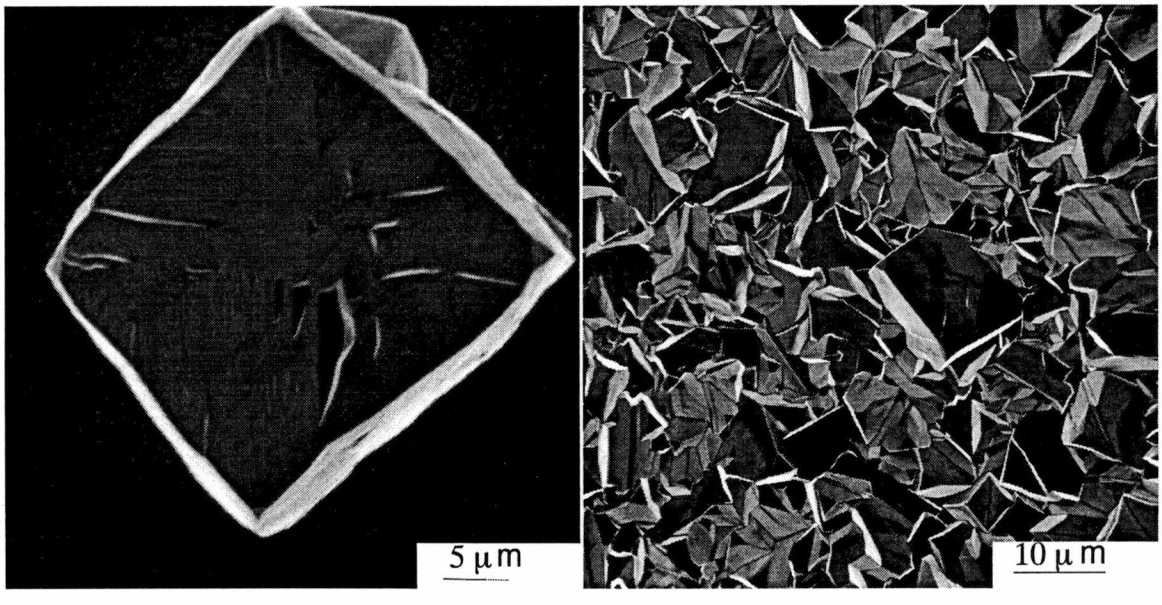

Figure 3 (e)-(f) : Scanning electron micrographs of films deposited with the addition of 0.17 % NH_3 to 1.0 % input CH_4 in H_2 gas mixtures, (N/C=1/6), at filament temperatures 2400 °C : (e) substrate temperature 1110 °C witout NH_3 addition, (f) substrate temperature 1110 °C with 0.17 %NH_3 addition.

The micrographs, corresponding to the 1.5% methane experiments are shown in figs. 4 (a)-(f). At low substrate temperatures (840 °C), the nitrogen free films had small {100} faces and a growth rate ratio value of 1.15. This film also showed {111} penetration twins. The nitrogen containing film, was very highly twinned and showed an underlying cubo-octahedral structure. The growth rate ratio was 0.87. At intermediate temperatures (980 °C), both films, the nitrogen free film as well as the nitrogen containing film, had **r**=0.87. Both of them showed rough {111} and smooth {100} faces. The nitrogen containing film showed a variation in crystallite sizes. At high temperatures (1090 °C), the nitrogen free films showed rough {111} and smooth {100} faces. The {100} penetration twins are also observed. The crystallites have cubo-octahedral shapes with {111} faces smaller than the {100}, with **r**=0.8. The nitrogen containing films, had very small {111} faces, clean facets and very few twins. The {100} faces, however, did not appear flat. They appeared to have curvature to them and some penetration twins.

(b) Analysis of growth rates, **g**

Discussion regarding growth rates and growth rate ratios is based on analysis of the micrographs shown in figs. 2(a)-(f), 3(a)-(f), and 4(a)-(f) and the information listed in the corresponding Tables 5,6 and 7. The growth rates, **g**, and directionally resolved growth rates, **g**<100> and **g**<111>, are compared graphically in figs. 5, 6, and 7 for depositions with and without NH_3 additions.

The addition of NH_3 increased the growth rate for all the three methane concentrations studied at all substrate temperatures used. The change

4(a)

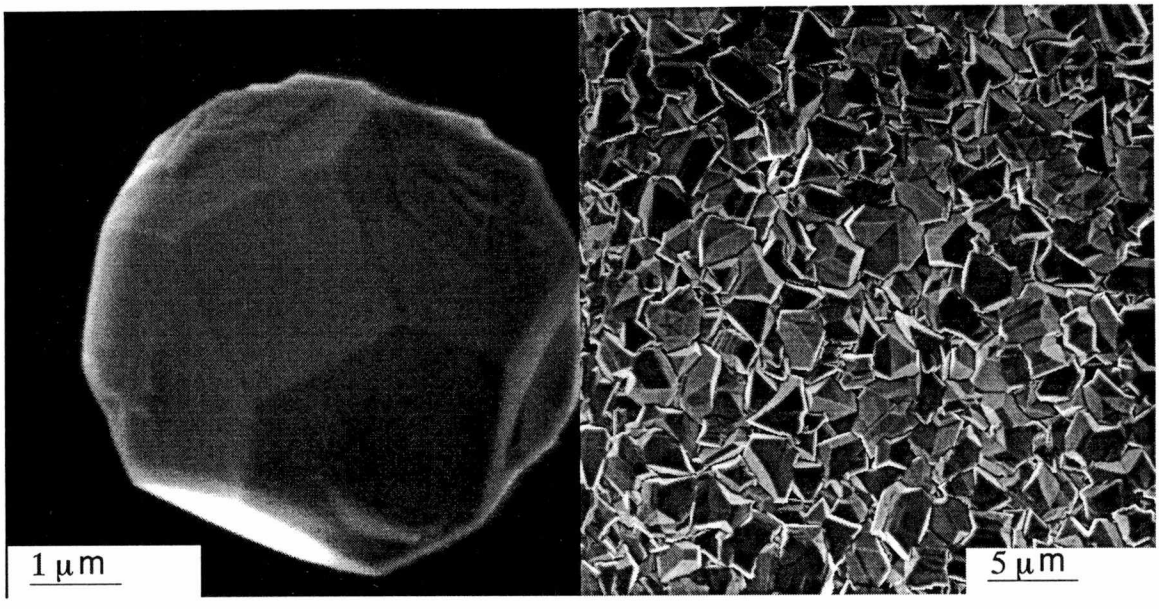

4(b)

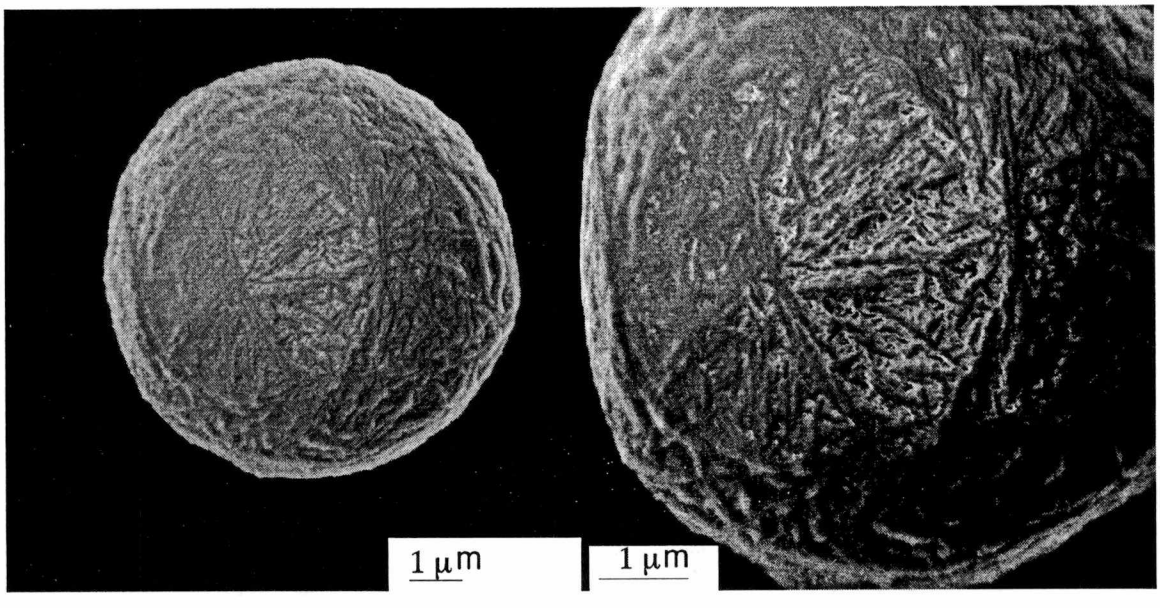

Figure 4 (a)-(b) : Scanning electron micrographs of films deposited with the addition of 0.26 % NH_3 to 1.5 % input CH_4 in H_2 gas mixtures, (N/C=1/6), at filament temperatures 2400 °C. (a) substrate temperature 840 °C without NH_3 addition, (b) substrate temperature 840 °C with 0.26 % NH_3 addition.

4(c)

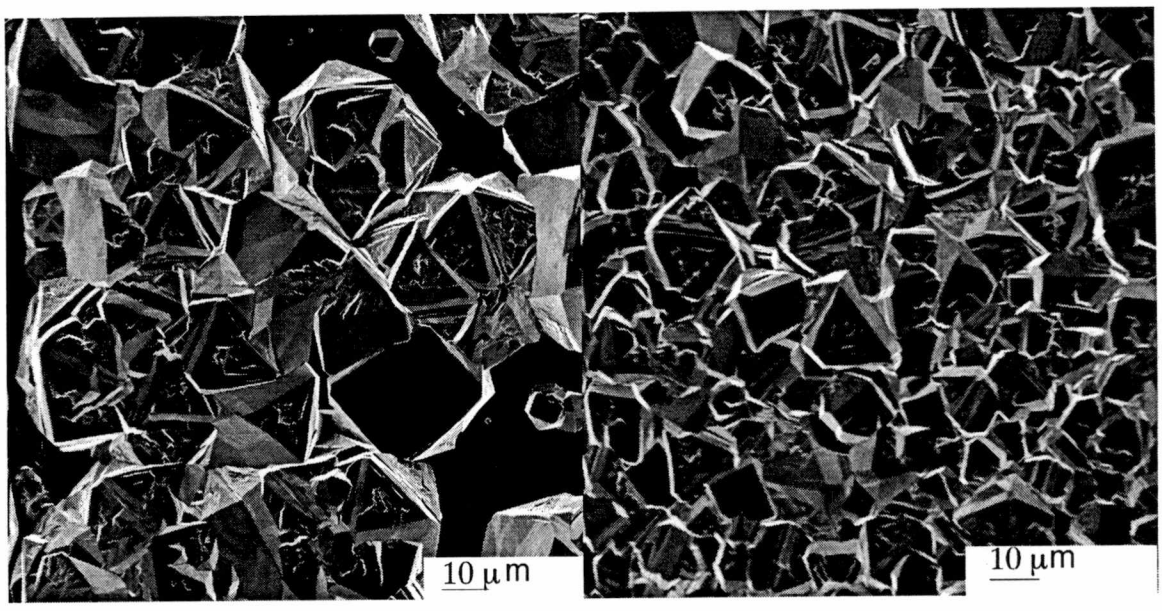

4(d)

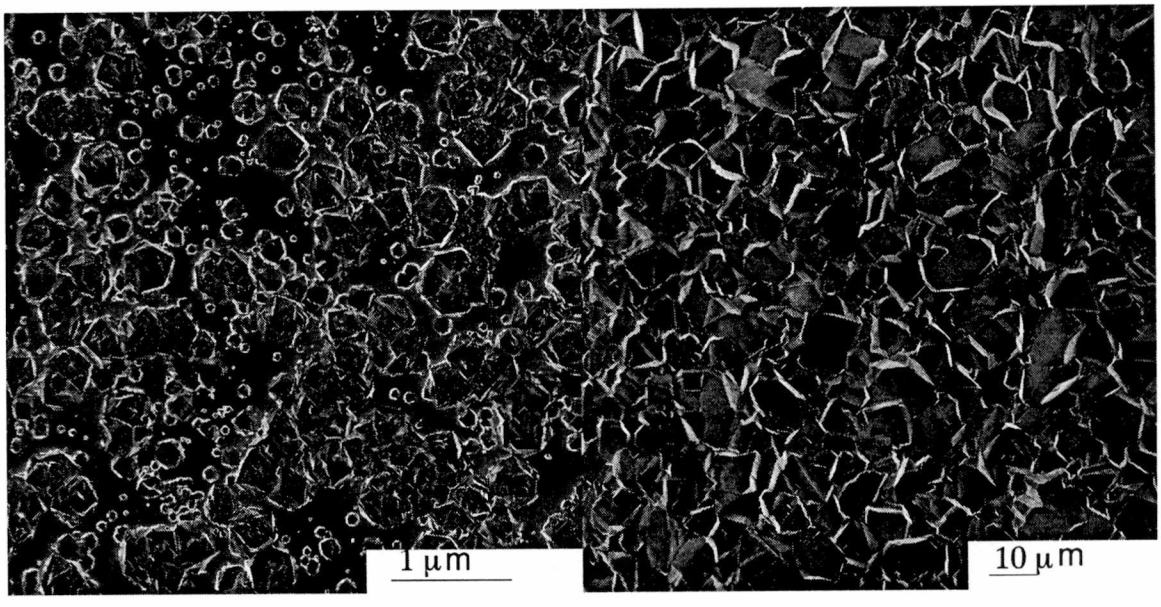

Figure 4 (c)-(d) : Scanning electron micrographs of films deposited with the addition of 0.26 % NH_3 to 1.5 % input CH_4 in H_2 gas mixtures, (N/C=1/6), at filament temperatures 2400 °C : (c) substrate temperature 980 °C without NH_3 addition, (d) substrate temperature 980 °C with 0.26 % NH_3 addition.

4(e)

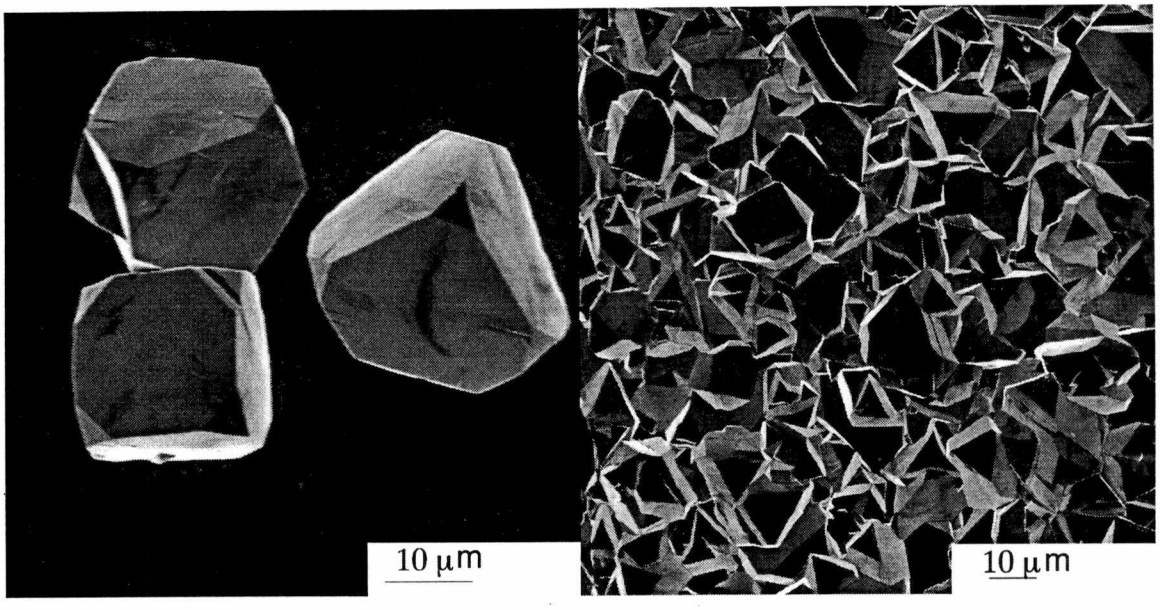

4(f)

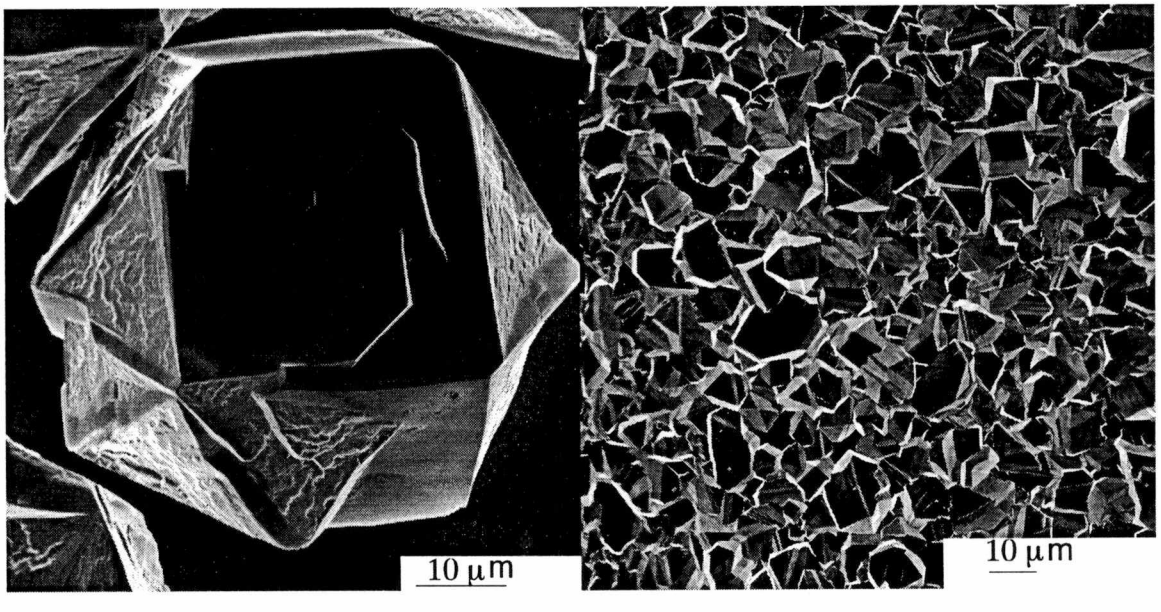

Figure 4 (e)-(f) : Scanning electron micrographs of films deposited with the addition of 0.26 % NH_3 to 1.5 % input CH_4 in H_2 gas mixtures, (N/C=1/6), at filament temperatures 2400 °C : (e) substrate temperature 1090 °C witout NH_3 addition, (f) substrate temperature 1090 °C with 0.26 %NH_3 addition.

observed, however, was dependent on both the methane concentration and substrate temperature.

Figure 5 compares the growth rates for depositions with and without NH_3 addition to a 0.5% methane in hydrogen gas mixture. The results are grouped according to substrate temperature, which are 840, 1010, and 1100 °C. The left two bars in each group correspond to the total growth rate with and without NH_3 addition, whereas, the middle and right pairs of bars in the group compare the NH_3 effect on **g**<100> and **g**<111>, respectively.

It is shown in fig. 5 that for depositions at 0.5% methane concentration, **g** increased at low temperatures from 0.24 to 0.38, (by a factor of 1.6), at the intermediate temperatures from 0.45 to 0.96 (by a factor of 2.1), and at high temperatures from 0.44 to 1.35 (by a factor of 3.1), with NH_3 addition.

Figures 6 summarizes the effect on **g** of NH_3 additions to a 1.0 % methane in hydrogen gas mixture at the three temperature levels -- 840, 1010 and 1100 °C. In fig. 6 it is observed that at low temperatures g increased from 0.52 to 0.74 (by a factor of 1.4), at the intermediate temperatures from 1.8 to 3.0 (by a factor of 1.7), and at high temperatures from 1.4 to 2.5 (by a factor of 1.8).

Similarly fig. 7 shows the increase in the overall growth rate due to the addition of NH_3, for the experiments done with 1.5 % methane in hydrogen gas mixture. The overall growth rate increased from 0.24 to 0.38 μm/hr (by a factor of 1.5), at the low substrate temperatures. It increased from 0.45 to 0.96 μm/hr (by a factor of 1.9) in the intermediate temperature regime, and at high substrate

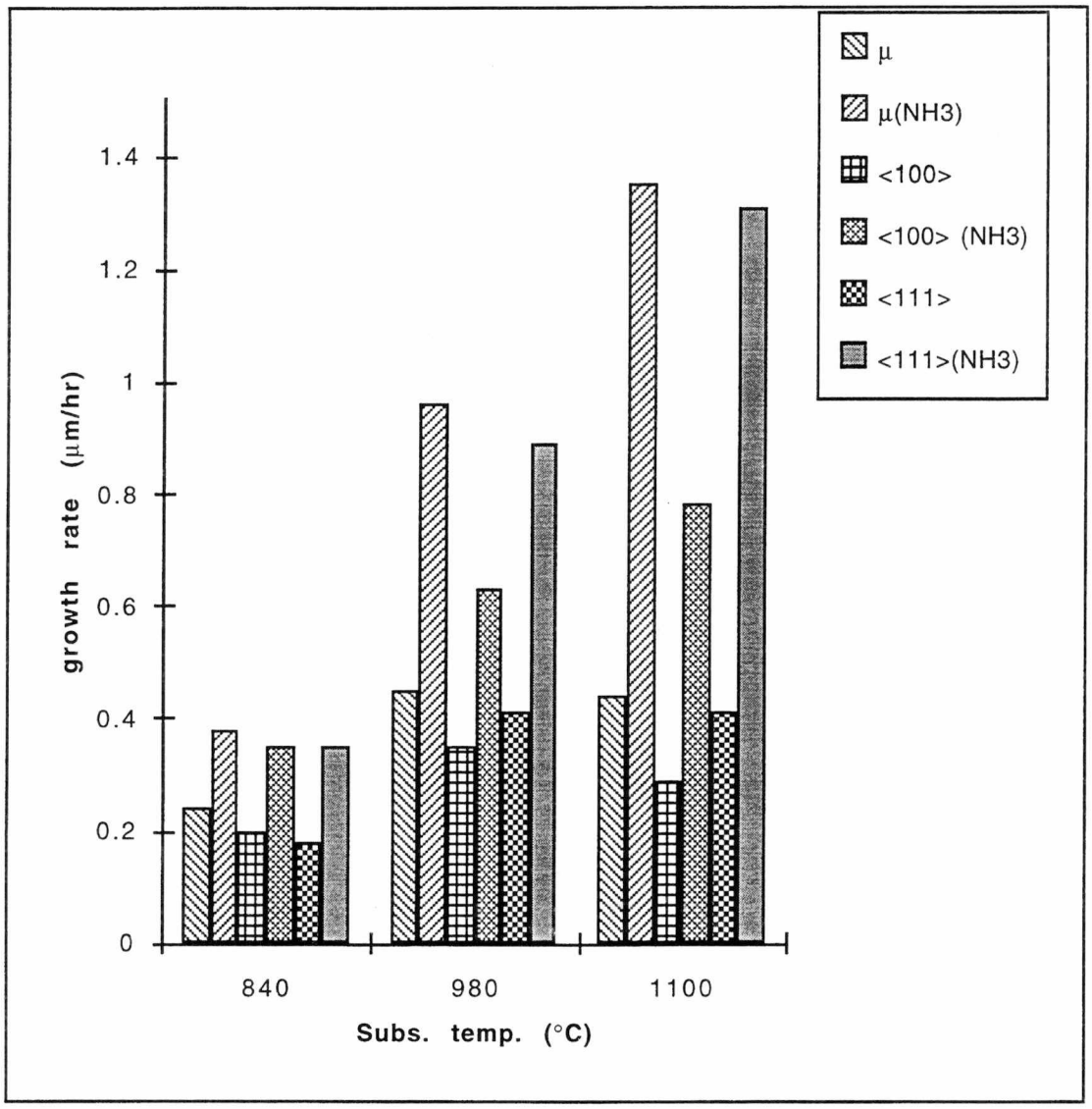

Figure 5 : The effect on the growth rate, g, as a function of substrate temperature with the addition of 0.08 % NH_3 to 0.5 % input CH_4 in H_2 gas mixtures, (N/C=1/6), at filament temperatures 2400 °C.

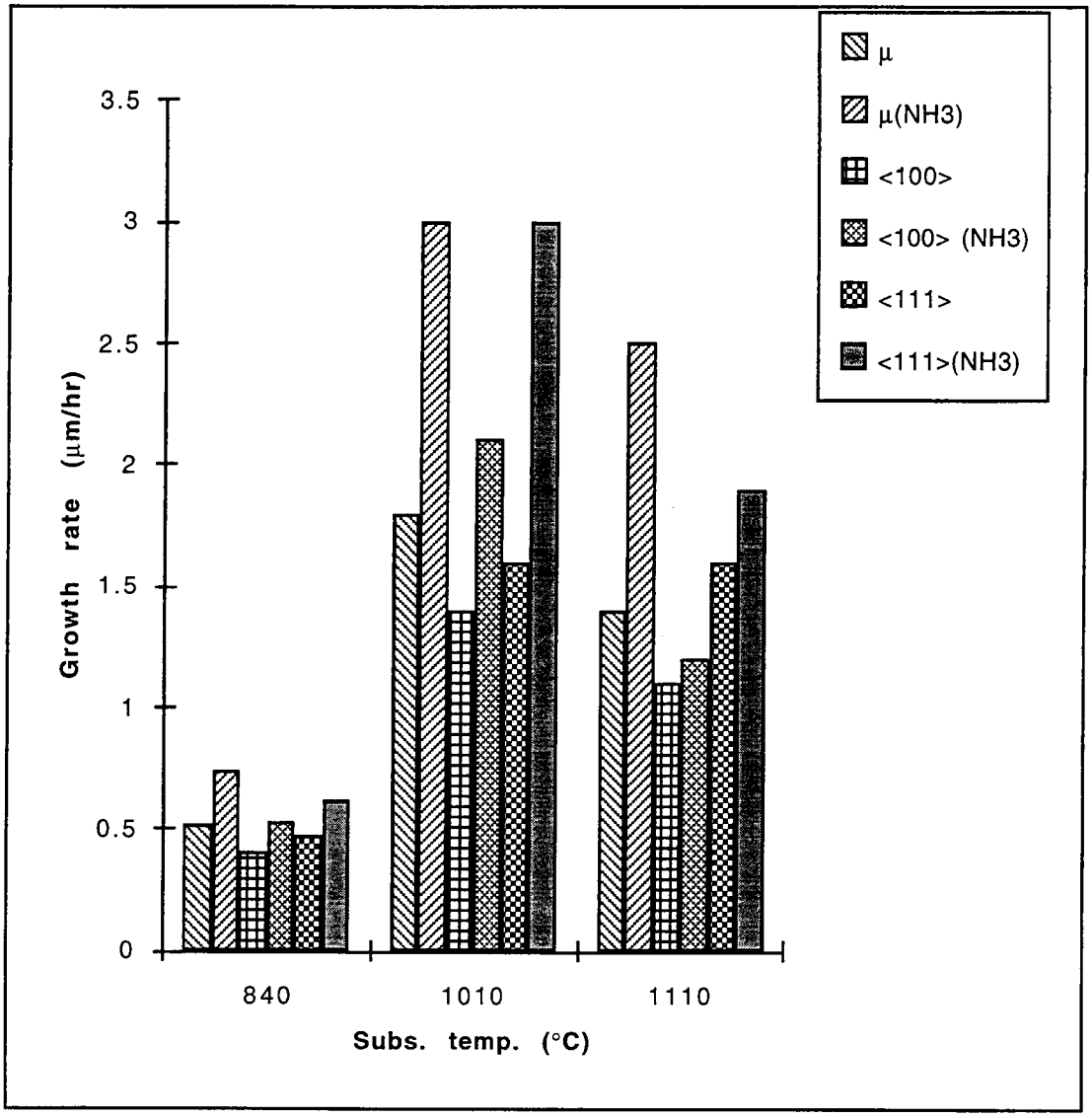

Figure 6 : The effect on the growth rate, g, as a function of substrate temperature with the addition of 0.17 % NH_3 to 1.0 % input CH_4 in H_2 gas mixtures, (N/C=1/6), at filament temperatures 2400 °C.

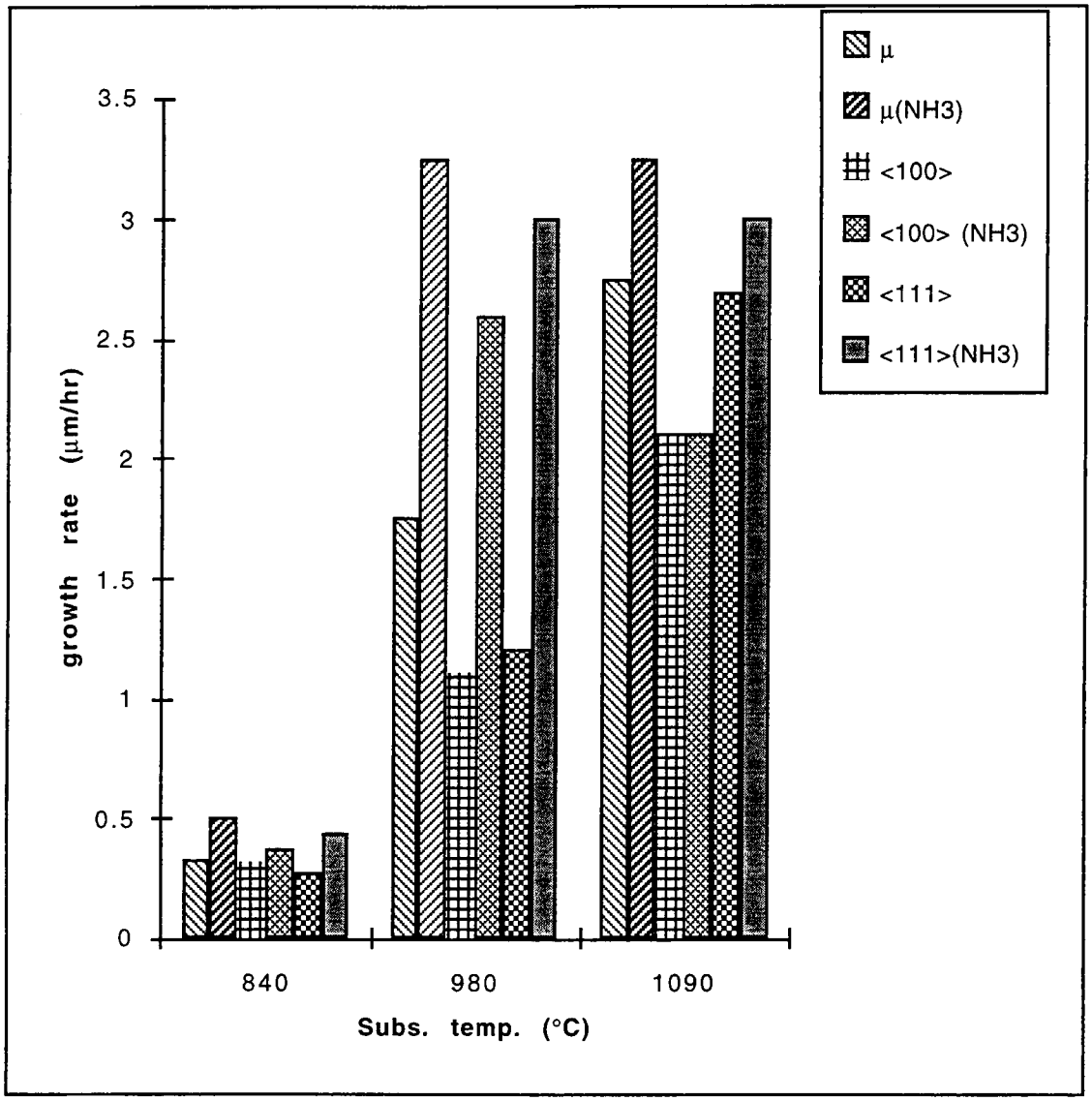

Figure 7 : The effect on the growth rate, g, as a function of substrate temperature with the addition of 0.26 % NH_3 to 1.5 % input CH_4 in H_2 gas mixtures, (N/C=1/6), at filament temperatures 2400 °C.

temperatures the overall growth rate increased from 0.44 to 1.35 μm/hr (by a factor of 1.2) .

Thus addition of NH_3 showed a variation in the increase in growth rates at different methane concentrations and for different substrate temperatures. At 0.5 % methane concentrations the overall growth rate increased by a factor of 1.6, 2.1 and 3.1 at low, intermediate and high substrate temperatures, respectively. At 1.0 % methane concentrations g increased by a factor of 1.4, 1.7 and 1.8 at low, intermediate and high substrate temperatures, respectively. Whereas, at 1.5 % methane concentrations the overall growth rate increased by a factor of 1.5, 1.9 and 1.2 at low, intermediate and high substrate temperatures, respectively.

(c) Growth rates in <100> and <111> directions, **g**<100> and **g**<111>

The addition of NH_3, in general, increased the growth rates in the <100> and <111> crystallographic directions for all methane concentrations and at all substrate temperatures used in this study. However, the increase in the growth rates showed dependence on the methane concentration and the substrate temperature.

For experiments that were done with 0.5 % methane concentrations, fig. 5 shows that at low temperatures, g<100> and g<111> increased by a factor of 1.8 and 1.9, respectively, for the crystals grown with the addition of NH_3, in comparison with crystals grown without ammonia. At intermediate temperatures, the addition of NH_3 increased **g**<100> and **g**<111> by a factor of 1.8 and 2.2, respectively. The high temperature growths showed that the

g<100> changed by a factor of 2.7 as a result of the addition of NH_3; however, the g<111> direction changed by a factor of 3.2.

The experiments done with 1.0 % methane concentrations showed that at low temperatures, the **g**<100> and **g**<111> increased in the same proportion, by a factor of 1.3, due to the addition of NH_3. As shown in fig. 6 at intermediate temperatures, the addition of NH_3 increased the **g**<100> and **g**<111> by a factor of 1.5 and 1.9, respectively. The high temperature growths showed that the g<100> changed by a factor of 1.1 with the addition of NH_3; however, **g**<111> changed by a factor of 1.2.

Figure 7 shows the trends in **g**, **g**<100> and **g**<111> as a function of substrate temperature in the case of 1.5% experiments. At low temperatures addition of NH_3 increased **g**<100> and **g**<111> by a factor of 1.2 and 1.6 respectively. At intermediate temperatures, the addition of NH_3 increased the **g**<100> and **g**<111> by a factor of 2.4 and 2.5 respectively. The high temperature growths showed that **g**<100> and **g**<111> did not change appreciably with the addition of NH_3; by a factor of 1 and 1.1, respectively.

The growth rates in the individual crystallographic growth directions follow different trends for the temperature regimes that were studied. At low methane concentrations (0.5 %), **g**<100> increased by a factor of 1.8, 1.8 and 2.7, whereas **g**<111> increased by a factor of 1.9, 2.2 and 3.2 in the increasing order of substrate temperature. At the intermediate methane concentrations (1.0 %) **g**<100> increased by a factor of 1.3, 1.5 and 1.1, where as, **g**<111> increased by a factor of 1.3,1.9 and 1.2 at low, intermediate and high substrate temperatures, respectively. However, at high methane concentrations (1.5 %),

g<100> increased by a factor of 1.2, 2.4 and 1.0, whereas **g**<111> increased by a factor of 1.6, 2.5 and 1.1 in the increasing order of substrate temperature.

(d) growth rate ratios, **r**

Figure 8 shows the addition of NH_3, in general, decreased **r** at all methane concentrations and for all substrate temperatures. At low methane concentrations (0.5%) **r** decreased from 1.15 to 1.0 at low substrate temperatures, from 0.87 to 0.7 at intermediate temperatures and from 0.7 to 0.6 at high substrate temperatures. At intermediate methane concentrations (1.0%) it did not show a variation at low temperatures, however, at intermediate temperatures it changed from 0.87 to 0.7 and at high temperatures it changed from 0.7 to 0.6. At high methane concentrations (1.5 %) the value of **r** decreased from 1.15 to 0.87 at low substrate temperatures, did not change its value of 0.87 at intermediate temperatures and again decreased from 0.8 to 0.7 at high substrate temperatures.

It is interesting to note that the substrate temperatures at which the addition of NH_3 has no effect on **r** shifts towards higher temperatures for higher methane concentration experiments. For 1.0% and 1.5% methane concentrations, this point (where **r** did not shift) is at ~840 and ~980 °C, respectively. For 0.5 % methane concentrations, this point would probably be observed at substrate temperatures lower than 840 °C.

(c) Addition of N_2 at high filament temperatures

In order to compare the effect of adding nitrogen as N_2 or NH_3 a set of experiments was performed with N_2 being added to the gas mixture using a TaC filament at 2400 °C, and a substrate temperature of 840 °C for all six

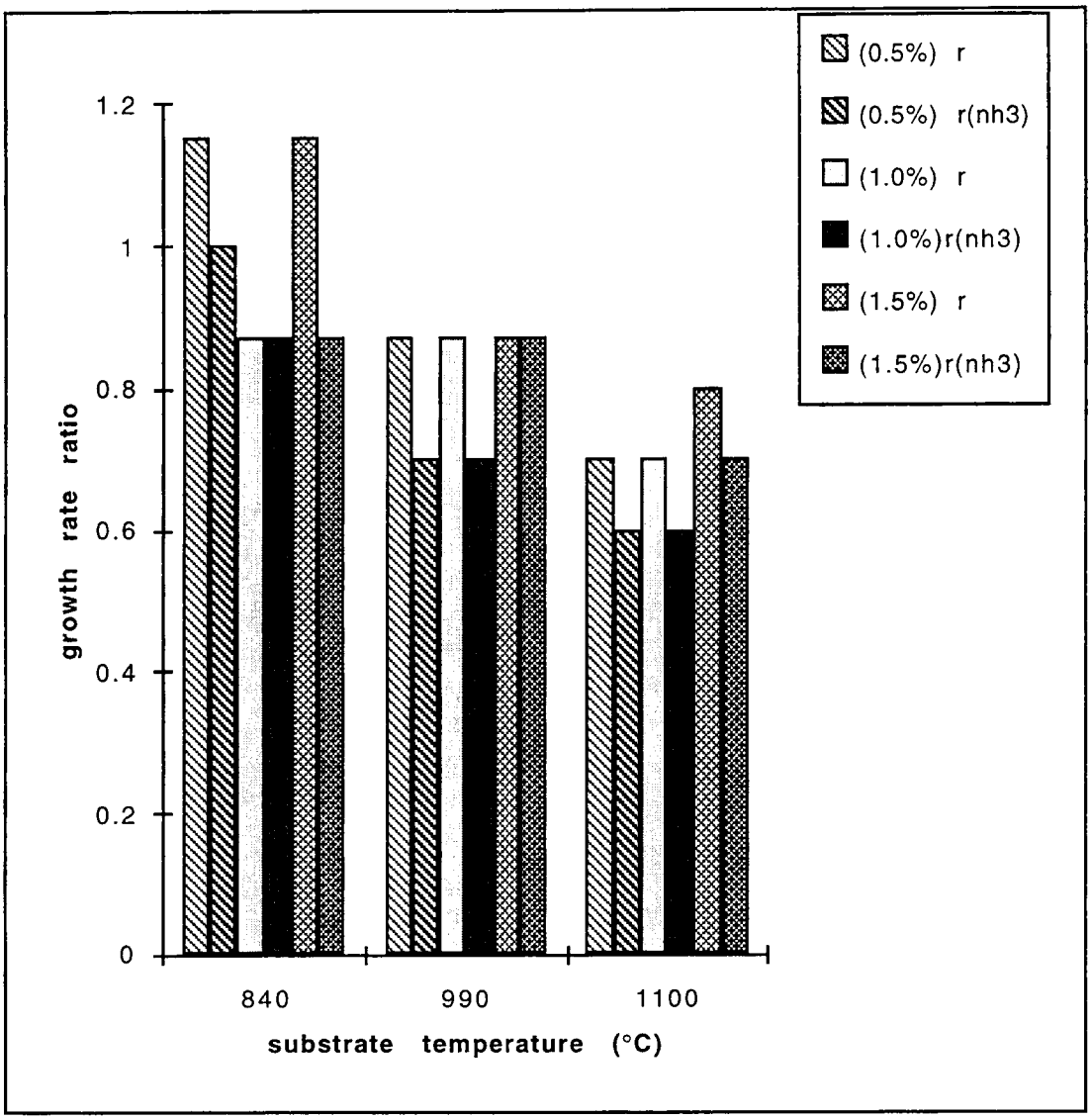

Figure 8 : The effect of addition of NH_3 on growth rate ratio for different methane concentrations at different substrate temperatures.

experiments. Three levels of methane concentration were used --- 0.5%, 1.0% and 1.5%. The amount of N_2 added was calculated so that the C to N atom ratio in the input gas was constant and equal to the value used in the

experiments performed with ammonia, which was, ~1/6. Table 8 lists these growth conditions and calculated parameters.

Table 8 : Addition of N2 (N/C=1/6) to different methane concentrations for substrate temperature 840°C and filament temperature 2400°C

N_2 (%)	Methane conc. (%)	**r**	α	**g** (μm/hr)	**g**<100> (μm/hr)	**g**<111> (μm/hr)
0	0.5	1.15	2.0	0.24	0.20	0.18
0.04	0.5	1.0	1.7	0.31	0.27	0.27
0	1.0	0.87	1.5	0.52	0.41	0.47
0.08	1.0	0.87	1.5	0.67	0.53	0.61
0	1.5	1.15	2.0	0.33	0.31	0.27
0.13	1.5	0.87	1.5	0.5	0.37	0.43

Figure 9 (a)-(f) shows the SEM images of the samples mentioned above in Table 8. Samples grown with low and the high methane concentrations showed a decrease in **r** and an increase in **g**. The intermediate methane concentrations did not appear to show any change in r although **g** increased as a result of the addition of N_2.

6(a)

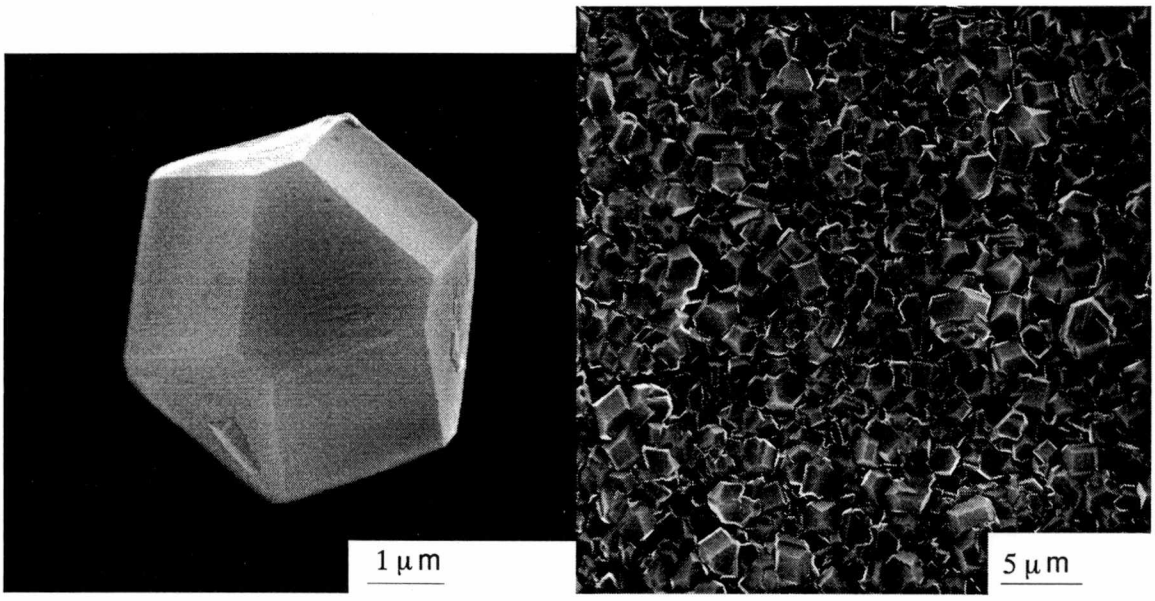

6(b)

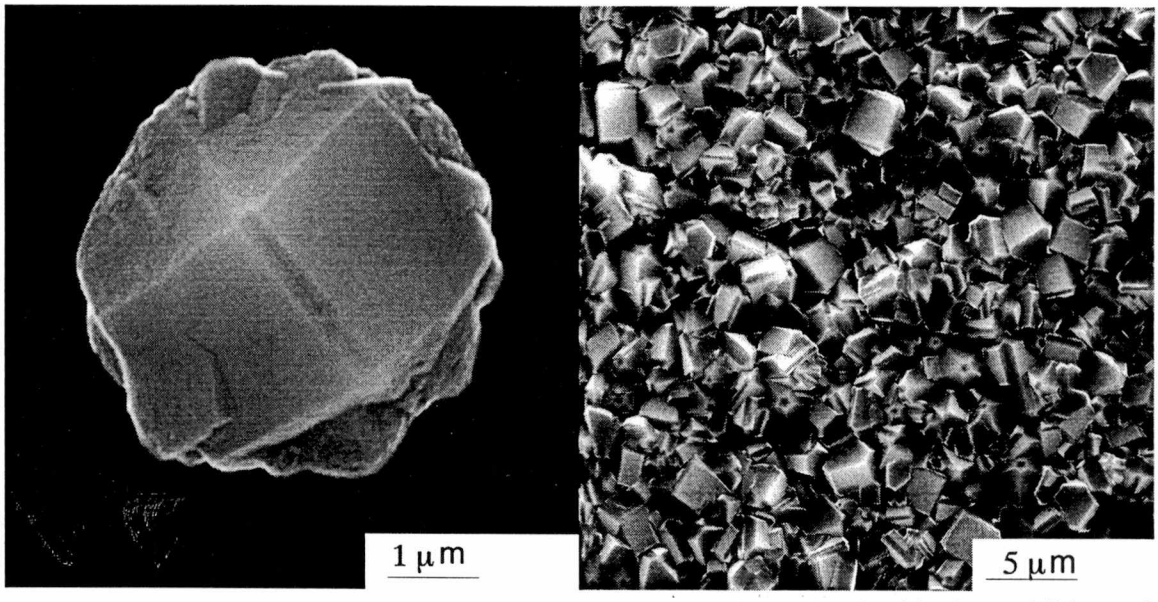

Figure 9 : Scanning electron micrographs of films deposited with the addition of N2 to different input CH_4 in H_2 gas mixtures, keeping the N/C ratio in the input gas mixture constant at ~1/6, at filament temperatures 2400 °C, and at substrate temperature 840 °C (a) for 0.5% CH_4 without N_2 addition, (b) for 0.5% CH_4 with 0.04 % N_2 addition.

6(c)

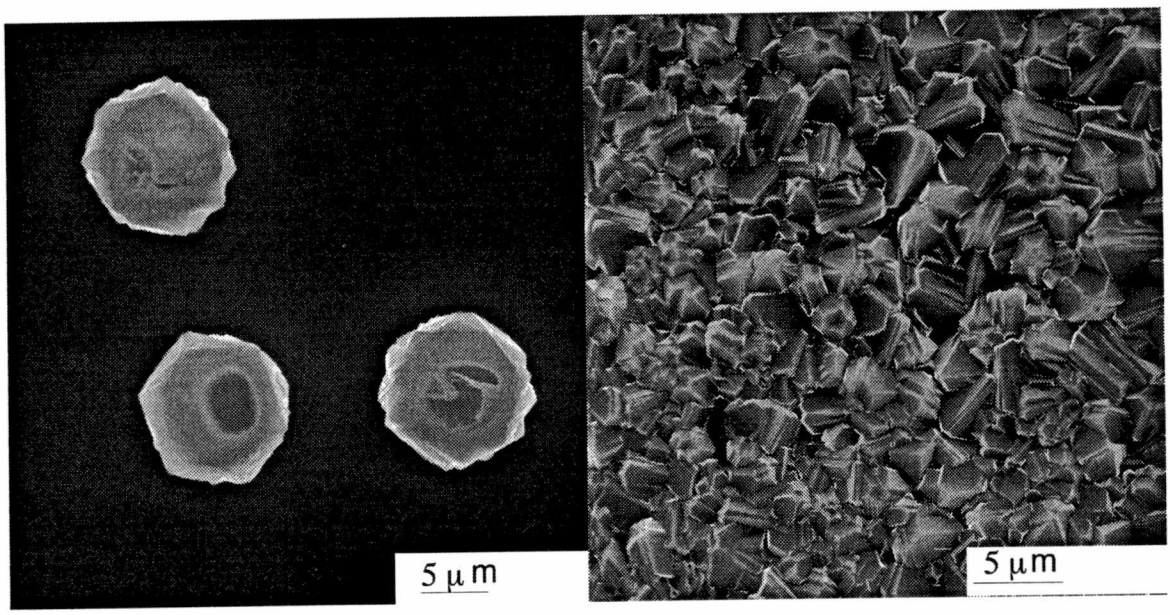

6(d)

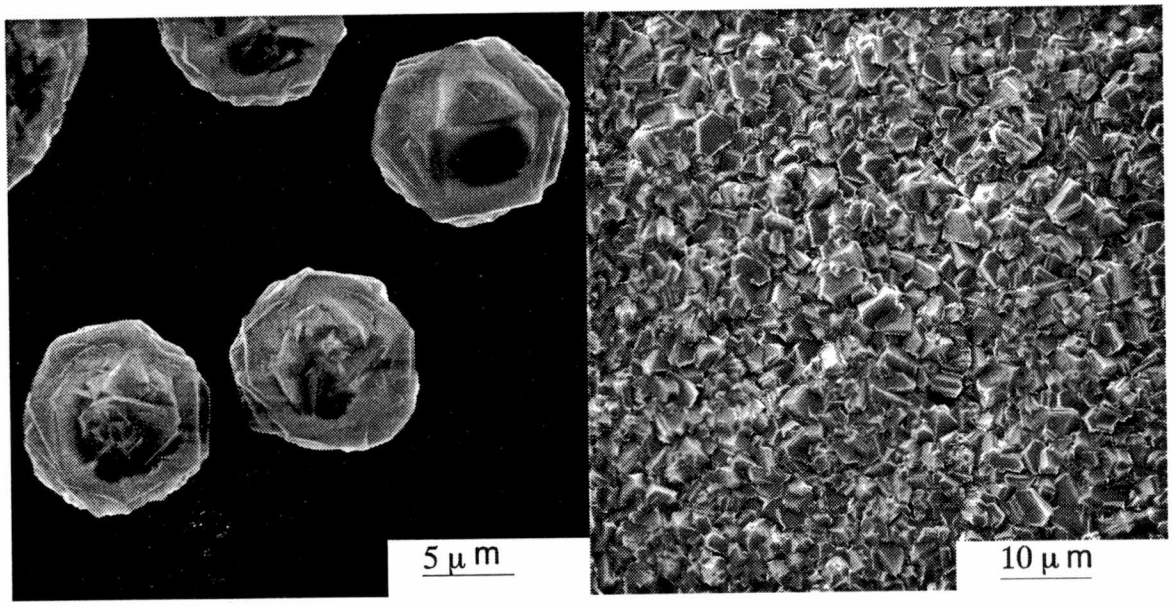

Figure 9 : Scanning electron micrographs of films deposited with the addition of N_2 to different input CH_4 in H_2 gas mixtures, keeping the N/C ratio in the input gas mixture constant at ~1/6, at filament temperatures 2400 °C, and at substrate temperature 840 °C(c) for 1.0 % CH_4 without N_2 addition, (d) for 1.0 % CH_4 with 0.08 % N_2 addition.

6(e)

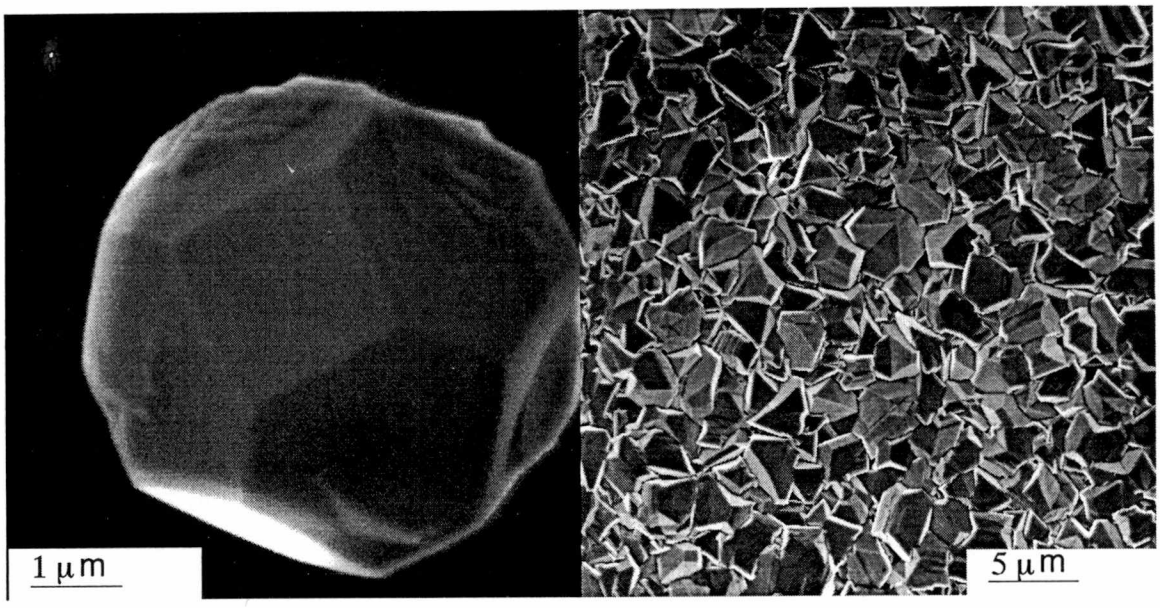

6(f)

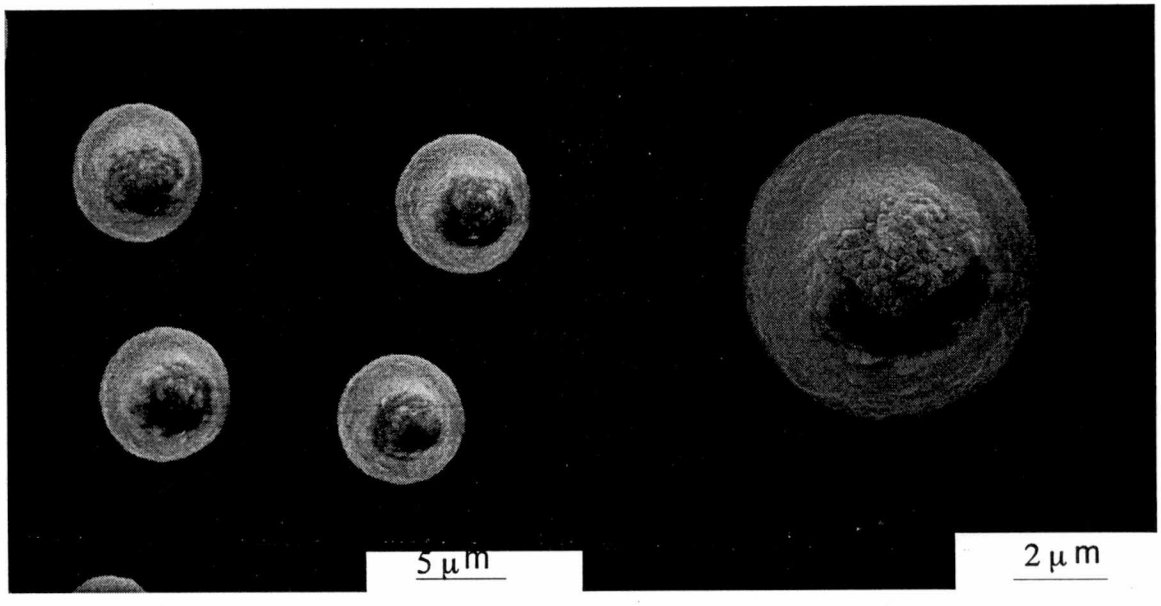

Figure 9 : Scanning electron micrographs of films deposited with the addition of N2 to different input CH_4 in H_2 gas mixtures, keeping the N/C ratio in the input gas mixture constant at ~1/6, at filament temperatures 2400 °C, and at substrate temperature 840 °C(e) for 1.5 % CH_4 without N_2 addition, (f) for 1.5 % CH_4 with 0.13 % N_2 addition.

The scanning electron micrographs, figs. 9 (a) and (b), show that at low methane concentrations (0.5%), the nitrogen free films had crystallites with clean facets, corresponding to **r**=1.15. The films grown with nitrogen, showed crystallites to have twins on their facets and did not have sharp edges. The crystallites exhibited **r**=1.0.

At the intermediate methane concentrations, as in the case of NH_3 addition, the growth rate ratio did not show a change with the addition of N_2. Figures 9 (c)-(d) show that the twinning increased with nitrogen addition, however, the crystallites were very clearly cubo-octahedral in shape, unlike the films grown with NH_3 addition, which had the appearance of ball like crystallites. N_2 had a milder effect on the morphology in comparison with NH_3.

In the case of high methane concentration (1.5%), the films grown with nitrogen addition had a lower growth rate ratio (0.87), than the films grown without nitrogen additions (1.15), as shown in figs. 9 (e) and (f). However, the films grown with nitrogen, had crystallites having the appearance of ball like crystals, i.e. very highly twinned with an underlying cubo-octahedral geometry.

At low methane concentrations (0.5%) the addition of N_2, showed that **g** increased by a factor of 1.3, changing from 0.24 to 0.31. An increase in **g**<100> and **g**<111> was also observed due to the addition of N_2, identical to the effect of NH_3. The values of **g**<100> and **g**<111>increased from 0.20 to 0.27 (by a factor of 1.4) and from 0.18 to 0.27 (by a factor of 1.5), respectively.

At the intermediate methane concentrations (1.0%), **g** increased by a factor of 1.3 as a result of N_2 addition. The values of **g**<100> and **g**<111> increased due to the addition of N_2 by the same amount (by a factor 1.3).

At the high methane concentration levels (1.5%), the addition of N_2 increased **g** from 0.33 to 0.5, (by a factor of 1.5). The values of **g**<100> and **g**<111> increased from 0.31 to 0.37 (by a factor of 1.2) and from 0.27 to 0.43 (by a factor of 1.6), respectively.

A comparison of the effects of the additions of NH_3 and N_2 is made in Table 9. Figure 10 (a) shows graphically that the effect of additions of both N_2 and NH_3 on **g**, **g**<100> and **g**<111>, follow the same trends, however, NH_3 has a much stronger effect than N_2 does. Figure 7 (b) shows the effect of the additions of NH_3 and N_2 on **r**, which are exactly identical.

(2) RGA Analysis

The RGA data for the addition of NH_3 to the input gas mixture (corresponding to table 4) shows that the 27 and 28 amu peak intensities corresponding to HCN and N_2 showed an increase as the amount of NH_3 being added was increased. Figure 8 shows the difference (due to the addition of NH_3) in peak intensities as a function of the amount of NH_3 being added. The 27 and 28 amu peaks increase very slowly up to 0.1% NH_3 additions, and rather drastically beyond that. The strongest effect is seen in the 27 amu peak i.e. production of HCN. The other observation made is that the 15 and 16 amu (CH_3 and CH_4) peak intensities showed a slight decrease whereas 26 amu peak (C_2H_2), showed an increase by about the same amount, implying the conversion of methane into acetylene. The RGA data showed that the system was free of any air leaks and the peak assignments were made accordingly.

Table 9 : Comparison of the addition of NH3 and N2 at different methane concentrations for substrate temperature 840°C and filament temperature 2400 °C

Source of N used	Methane conc. (%)	Δ **r**	Δ **g** (μm/hr)	Δ**g**<100> (μm/hr)	Δ**g**<111> (μm/hr)
N_2	0.5	0.15	0.07	0.07	0.09
NH_3	0.5	0.15	0.14	0.15	0.17
N_2	1.0	0	0.15	0.12	0.14
NH_3	1.0	0	0.22	0.14	0.16
N_2	1.5	0.28	0.17	0.06	0.16
NH_3	1.5	0.28	0.17	0.06	0.16

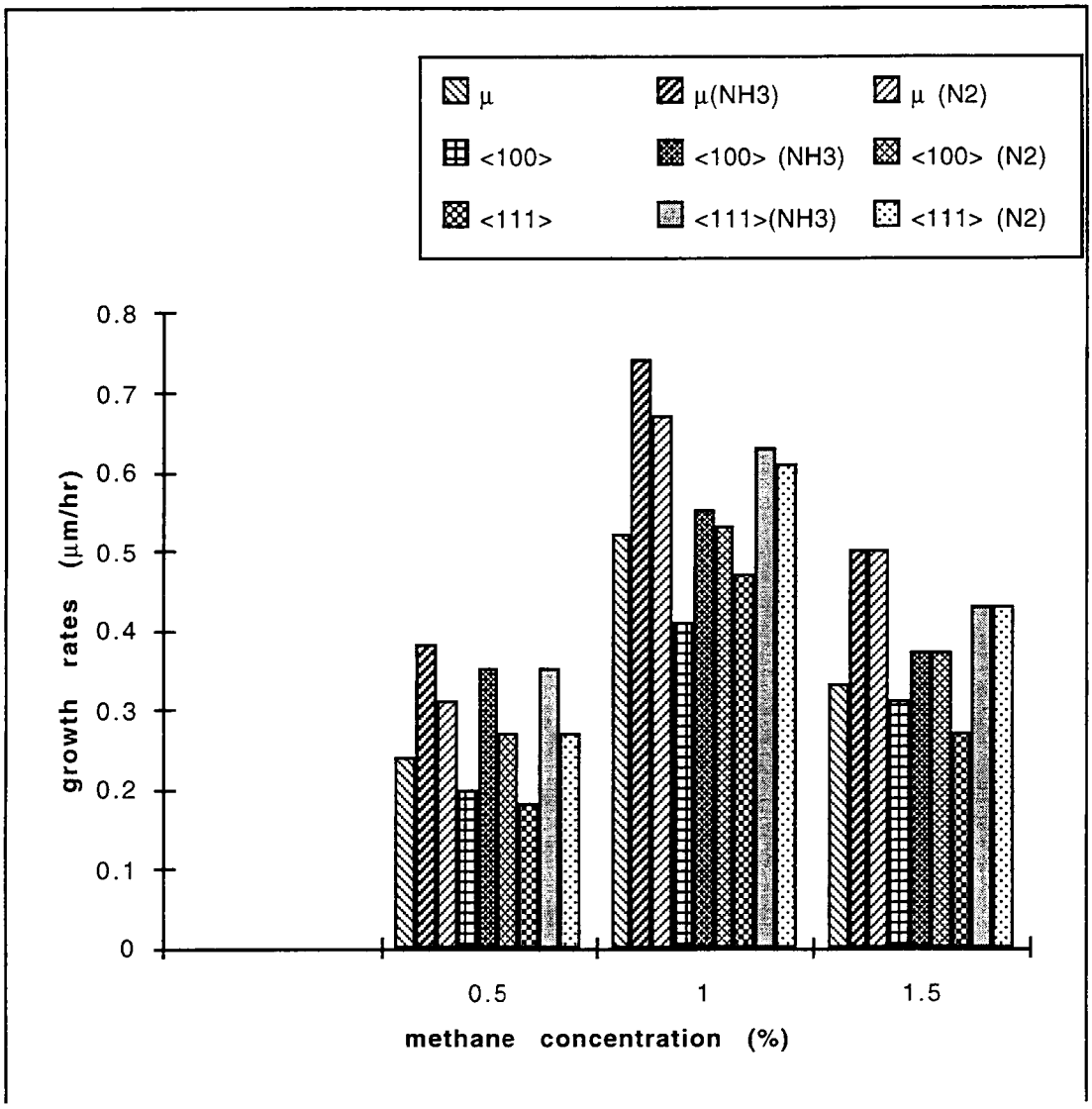

Figure 10 (a) : Comparison of the effect of addition of NH_3 and N_2 on **g**, **g**<100> and **g**<111> for different CH_4 concentrations, substrate temperature 840 °C and filament temperature 2400 °C.

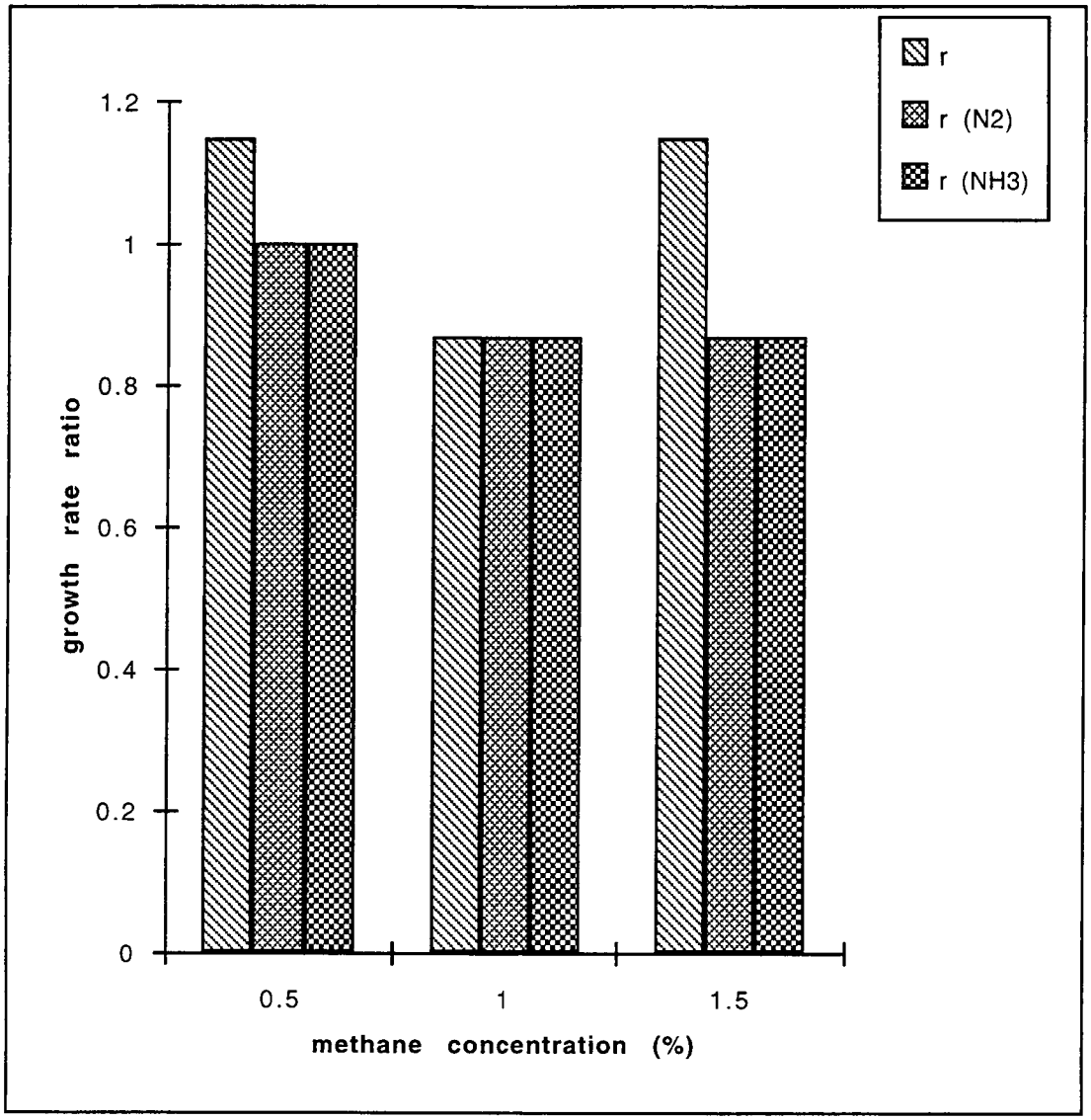

Figure 10 (b) : Comparison of the effect of addition of NH_3 and N_2 on **r** for different CH_4 concentrations, substrate temperature 840 °C and filament temperature 2400 °C.

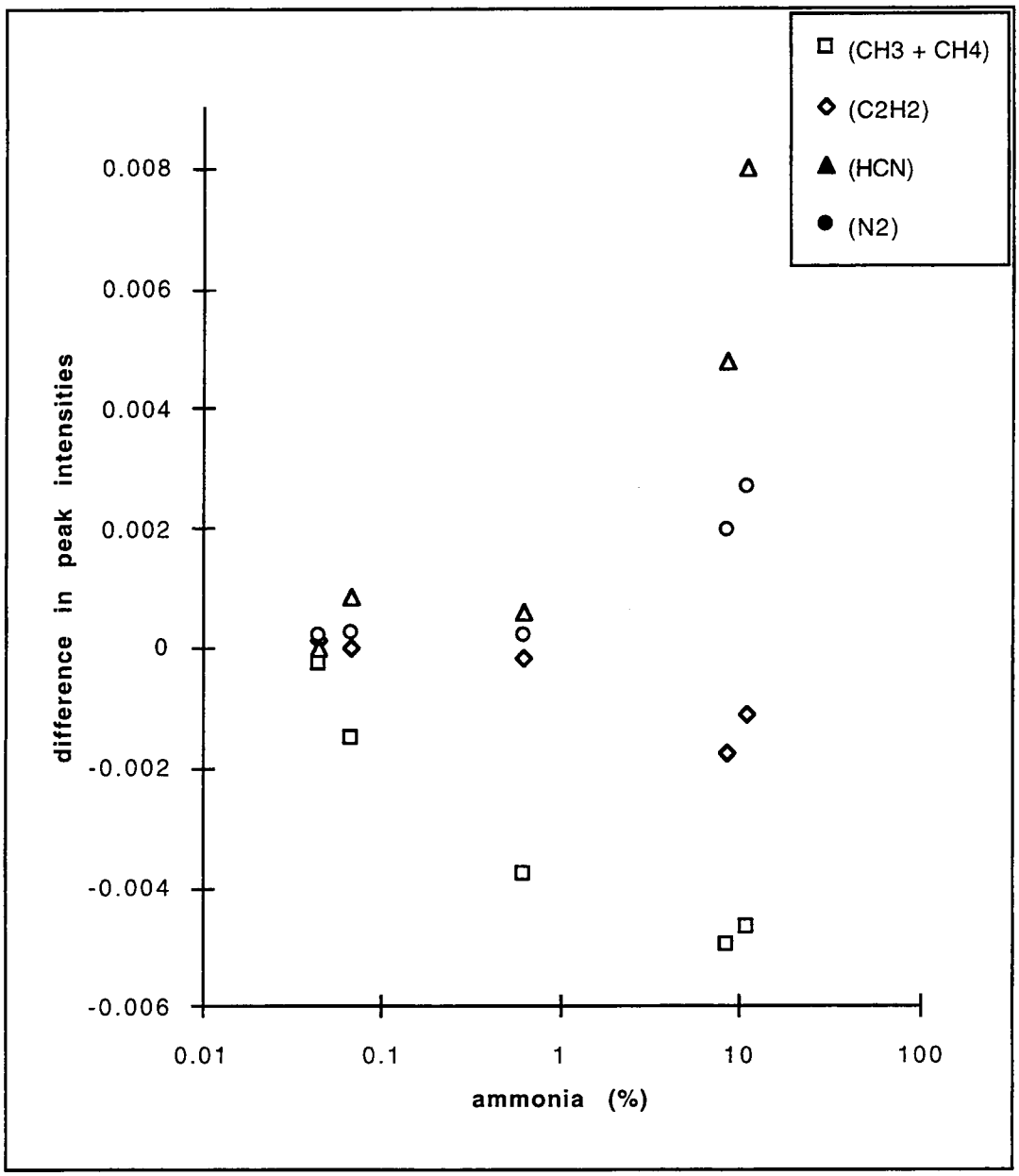

Figure 11 : Change in the RGA peak intensities as a function of addition of NH_3 (%) to 1.5% input CH_4 in H_2 gas mixtures, filament temperature 2400 °C, substrate temperature ~915 °C.

(3) Raman Analysis

Raman spectroscopy was done on the samples listed in table 4. These samples showed that the film quality did not get affected up to 8.3 X 10^{-2} % NH_3 additions. However, additions greater than that deteriorated the film quality drastically. Figure 12 shows the Raman data for these films. Films grown with more than 830 ppm NH_3 showed a tremendous decrease in crystalline quality.

Raman spectroscopy was also done on the samples listed in Tables 5, 6, and 7. The addition of NH_3 caused a variation on the quality of the film. Figure 13 shows Raman spectra of the films grown with 0.5% methane, with and without NH_3 addition, at the three different substrate temperatures. It is observed that the addition of NH_3 deteriorated the quality of the film grown at 840 °C. However, the quality of the films improved at the intermediate (980 °C) and high (1100 °C) substrate temperatures. The films grown with 1.0% methane concentration showed a degradation in film quality at low (840 °C) as well as at the intermediate (980°C) substrate temperatures. However, at high substrate temperatures (1100 °C), the film quality improved with the addition of NH_3. For the 1.5 %, methane concentration, the addition of NH_3 at all three substrate temperatures showed a degradation in the quality of the films. Figure 14 shows Raman spectra of the films grown with 0.5%, 1.0% and 1.5% methane, with and without NH_3 addition, at the intermediate substrate temperature ~980°C.

A comparison of the samples listed in Table 9 showed that the films deposited with the addition of N_2 to 0.5% methane in hydrogen gas mixtures, showed an improvement in the quality of the films, whereas, the addition of NH_3

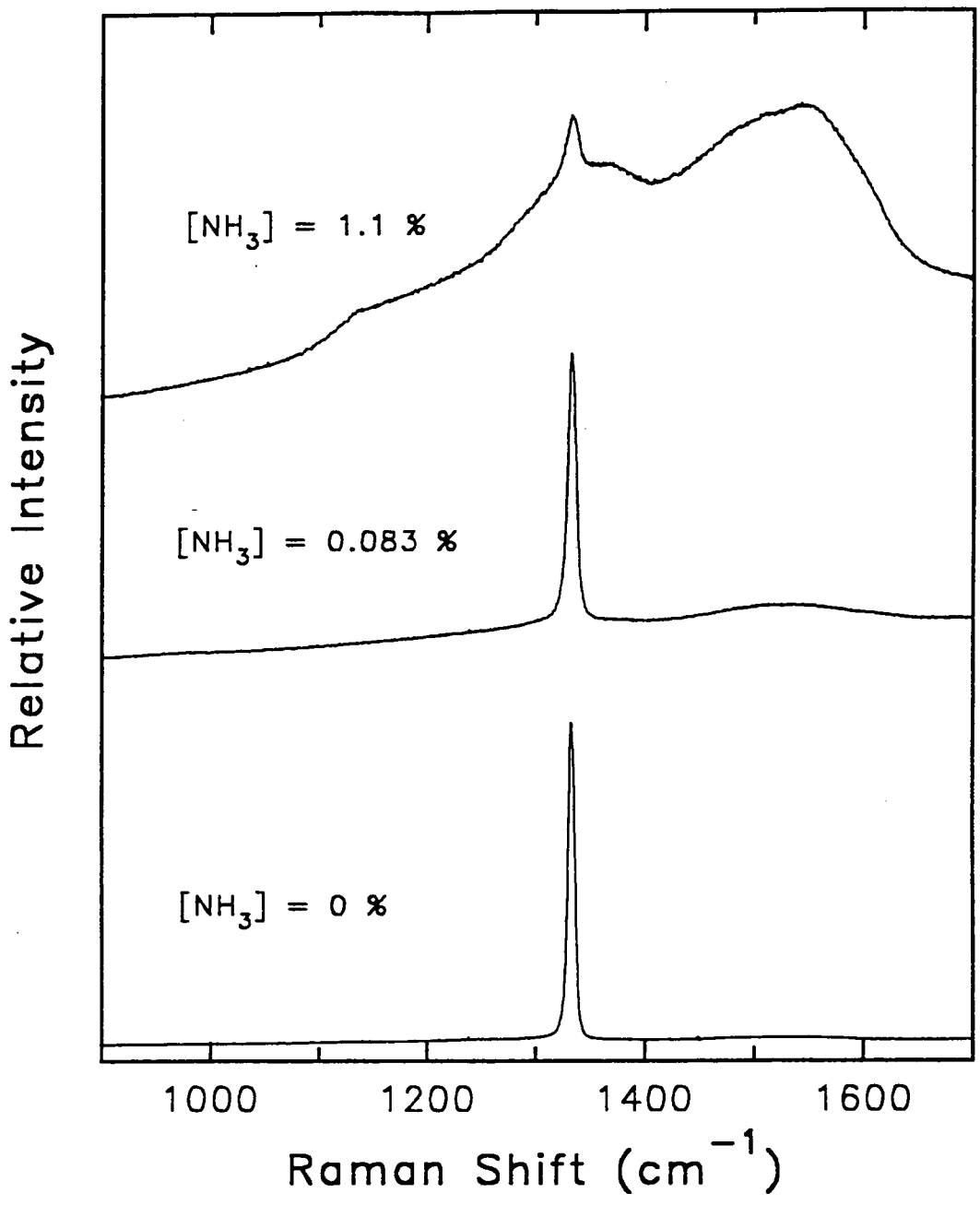

Figure 12 : Raman data reveals that the films grown with more than 830 ppm NH_3 showed a deterioration in crystalline quality of the films.

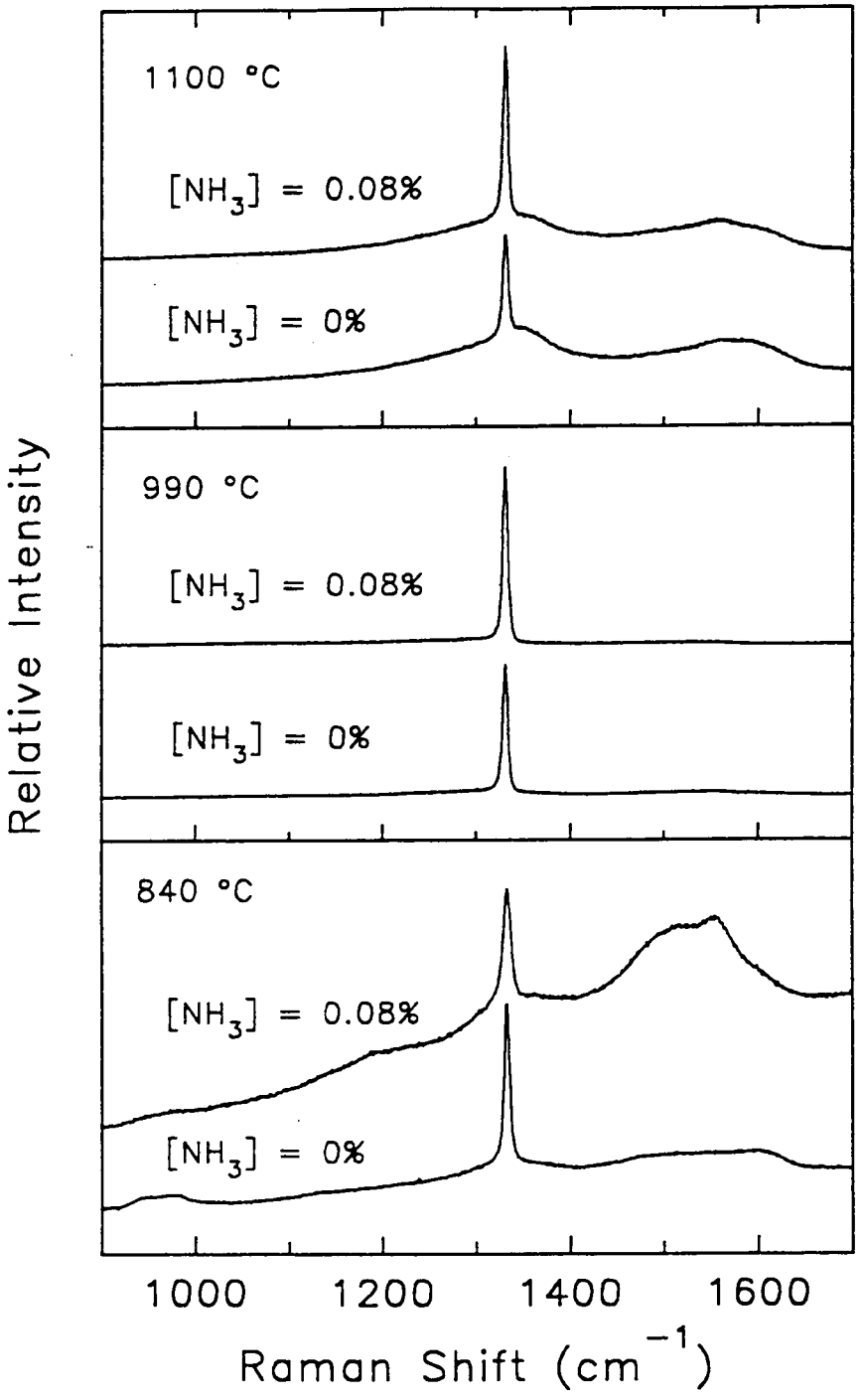

Figure 13 : Raman spectra of the films grown with 0.5% methane, with and without NH_3 addition, at the three different substrate temperatures.

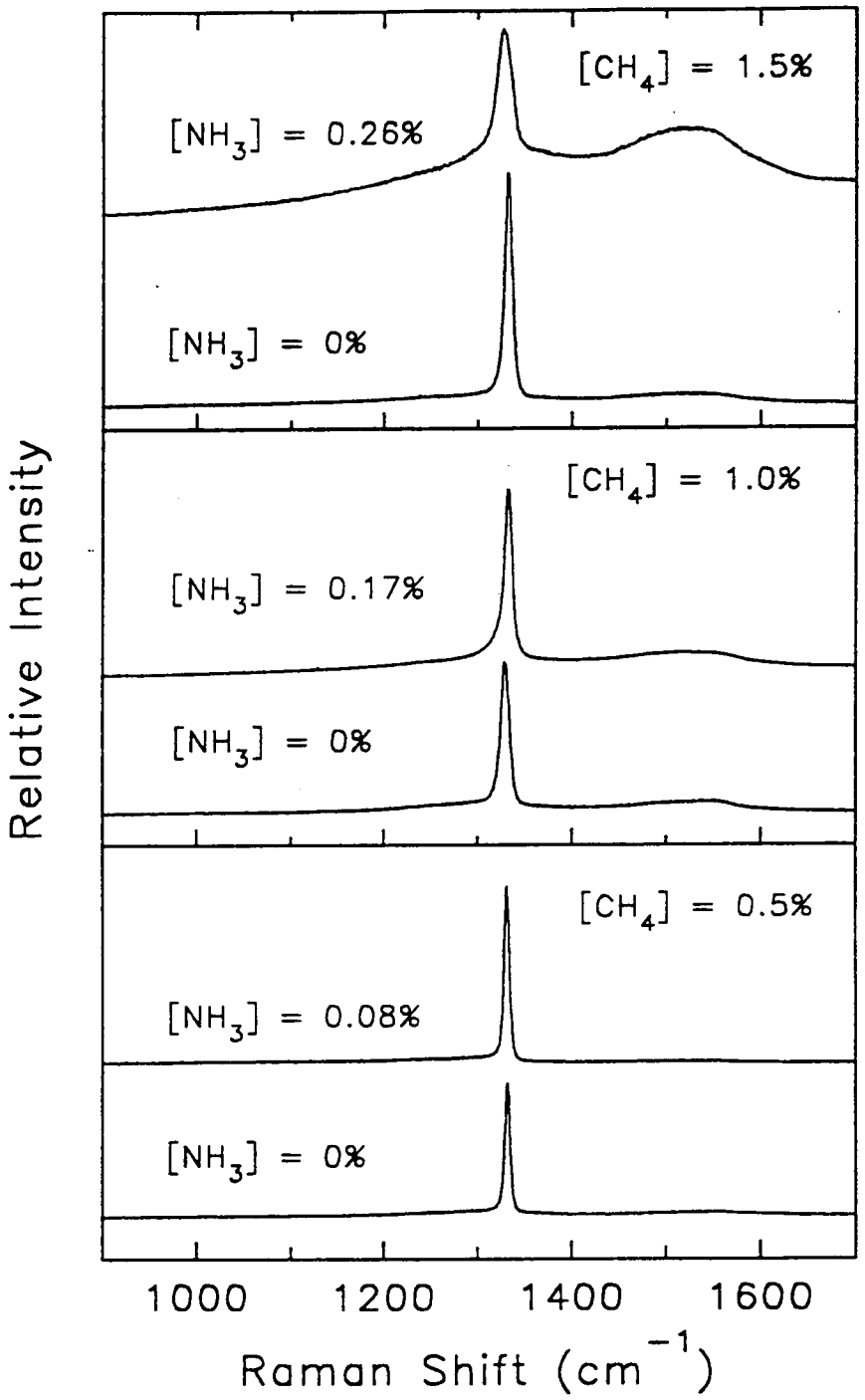

Figure 14 : Raman spectra of the films grown with 0.5%, 1.0% and 1.5% methane, with and without NH_3 addition, at the intermediate substrate temperature ~980°C.

had the opposite effect. The depositions done with 1.0% and 1.5% methane concentrations, showed that the addition of NH_3 deteriorated the film quality. The addition of N_2 did not have as strong an effect on the film quality as the addition of NH_3 did, although the film quality did deteriorate somewhat.

Conclusions

The addition of NH_3 and N_2 to the input gas mixture of CH_4 in H_2 showed a marked effect on the morphology of the crystals. The overall growth rates and the growth rates in the individual crystallographic directions showed an increase. The growth rate ratio decreased due to the nitrogen incorporation in the growth environment. The extent of these effects depends on the growth parameters, especially the filament temperature, the substrate temperature and methane concentration. The data from this study tends to support the hypothesis that HCN is playing an important role in the nitrogen effect, as has been suggested by others for microwave assisted CVD. The data regarding changes in the growth rate ratio shows a decrease in **r** with nitrogen additions which is at variance with what is seen in microwave CVD where **r** increases. More work is needed to understand this difference and its implications for understanding the nitrogen effects.

Future direction

The determination of the nitrogen incorporation ratios into the different growth sectors will benefit the understanding of the mechanism of these processes. Techniques such as nuclear reaction analysis (NRA), elastic recoil detection (ERD), secondary ion mass spectroscopy (SIMS) have been found in the literature to be suitable for determining the nitrogen content in the films.

This study spans a good proportion of the morphology map described in part 4, and some of the effects appear to be quite drastic. Further study, covering all bases of the morphology map, especially regions corresponding to the generation of octahedral crystal geometry would be very useful. Due to the high filament temperatures used, the substrate holder would either have to provide cooling to the substrate or the reactor geometry may have to be altered to facilitate the investigation of octahedral crystal geometry which requires low substrate temperatures and high methane contents.

Raman spectroscopy may be very useful in these films to study the stresses generated which may be correlated with the actual nitrogen content in the films.

Scanning tunneling microscopy (if the films are conducting) or atomic force microscopy may be used to further investigate the growth morphology features in these films. The details provided by these studies will definitely enhance the understanding of the effect of nitrogen addition to diamond films.

References

1. J. E. Field, Ed., *The Properties of Diamond* (Academic, London, 1979).

2. M. N. Yoder, in *Diamond and Diamond -like Films and Coatings*, edited by R. E. Clausing, L. L. Horton, J. C. Angus and P. Koidl, NATO ASI Series B : Physics Vol. **266**.

3. W. Kaiser and W. L. Bond, Phys. Rev. **115**, 857 (1959).

4. W. V. Smith, P. P. Sorokin, I. L. Gelles and G. J. Lasher, Phy. Rev. **115**, 1546 (1959).

5. M. Hoinkis, E. R. Weber, M. I. Landstrass, M. A. Plano, S. Han and D. R. Kania, Appl. Phys. Lett. **59**, 1870 (1991).

6. K. M. McNamara, B. E. Williams, K. K. Gleason and B. E. Scruggs, J. Appl. Phys. **76**, 2466 (1994).

7. L. Bergman and R. J. Nemanich, J. Appl. Phys. **78**, 6709 (1995).

8. T. R. Anthony, Dia. and Rel. Mat. **4**, 1346 (1995).

9. W. Muller-Sebert, E. Worner, F. Fuchs, C. Wild and P. Koidl, Appl. Phys. Lett. **68**, 759 (1996).

10. J. F. H. Custers, Physica **18**, 489 (1952).

11. E. C. Lightowlers and A. T. Collins, Diamond Research 1976 (Supplement to Industrial Diamond Review), 14 (1976).

12. J. P. F. Sellschop, D. M. Bibby, R. J. Keddy, D. W. Mingay, and M. J. Renan, Int. J. Appl. Rad. Isotopes **17**, 277 (1977).

13. J. F. Prins, Appl. Phys. Lett. **41**, 950 (1982).

14. M. W. Geis, D. D. Rathman, D. J. Ehrlichar, A. Murphy and W. T. Lindley, IEEE Elect. Dev. Lett. EDL **8**, 341 (1987).

15. M. W. Geis and J. C. Angus, Scientific American, October, 84 (1992).

16. J. C. Angus and A. T. Collins, Nature **370**, 601 (1994).

17. M. N. Yoder, Nav. Res. Rev. **39**, 27 (1987).

18. A. T. Collins, Phil. Trans. R. Soc. Lond. A **342**, 233 (1993).

19. R. H. Wentorf, Jr. and K. A. Darrow, Phys. Rev. **137**, A1614 (1965).

20. S. A. Kajihara, A. Antonelli, J. Bernholc and R. Car, Phys. Rev. Lett. **66**, 2010 (1991).

21. N. Fujimori, T. Imai, H. Nakahata, H. Shiomi and Y. Nishibayashi, MRS Symposium Proceedings **162**, 23 (1990).

22. K. Okano, H. Kiyoto, T. iwasaki, M. Iida and T. Nakamura, Appl. Phys. Lett. **58**, 840 91991).

23. Y. Yokota, H. Kawarada and A. Hiraki, MRS Symposium Proceedings **162**, 231 (1990).

24. J. Mort, M. A. Machonkin and K. Okumura, Appl. Phys. Lett. **59**, 3148 (1991).

25. R. Locher, C. Wild, N. Herres, D. Behr and P. Koidl, Appl. Phys. Lett. **65**, 34 (1994).

26. R. Samlenski, C. Haug, R. Brenn, C. Wild, R. Locher and P. Koidl, Appl. Phys. Lett. **67**, 2798 (1995).

27. R. Samlenski, C. Haug, R. Brenn, C. Wild, R. Locher and P. Koidl, Dia. and Rel. Mat. **5**,947 (1996).

28. C. Wild, R. Locher and P. Koidl, Proc. MRS Fall meeting '95.

29. H. Chatei, J. Bougdira, M. Remy, P. Alnot, C. Bruch and J. K. Kruger, Dia. and Rel. Mat. **6**,107 (1997).

30. F. Silva, A. Gicquel, A. Tardieu, P. Cledat and T. Chauveau, Dia. and Rel. Mat. **5**,338 (1996).

31. A. Badzian, T. Badzian and S. Tong Lee, Appl. Phys. Lett. **62**, 3432 (1993).

32. G. Z. Cao, F. A. J. M. Driessen, G. J. Bauhuis, L. Giling and P. F. A. Alkemade, J. Appl. Phys. **78**, 3125 (1995).

33. G. Z. Cao, J. J. Schermer, W. J. P. van Enckevort, W. A. L. M. Elst and L. J. Giling, J. Appl. Phys. **79**, 1357 (1996).

34. S. Jin and T. D. Moustakas, Appl. Phys. Lett. **63**, 2354 (1993).

35. S. Jin and T. D. Moustakas, Appl. Phys. Lett. **65**, 403(1994).

36. S. Bohr, R. Haubner and B. Lux, Appl. Phys. Lett. **68**, 1075 (1996).

37. H. Spicka, M. Griesser, H. Hutter, M. Grasserbauer, S. Bohr, R. Haubner and B. Lux, Dia. and Rel. Mat. **5**, 383 (1996).

38. P. W. May, P. R. Burridge, C. A. Rego, R. S. Tsang, M. N. R. Ashfold, K. N. Rosser, R. E. Tanner, D. Cherns and R. Vincent, Dia. and Rel. Mat. **5**, 354 (1996).

39. C. Pan, C. J. Chu, J. L. Margrave and R. H. Hauge, J. Electrochem. Soc., **141**, 3246 (1994).

40. A. Bergmaier, G. Dollinger, T. Faestermann, C. M. Frey, M. Ferguson, H. Guttler, G. Schulz and H. Willerscheid, Dia. and Rel. Mat. **5**, 995 (1996).

Appendix

A1. Diamond lattice showing a unit cell.

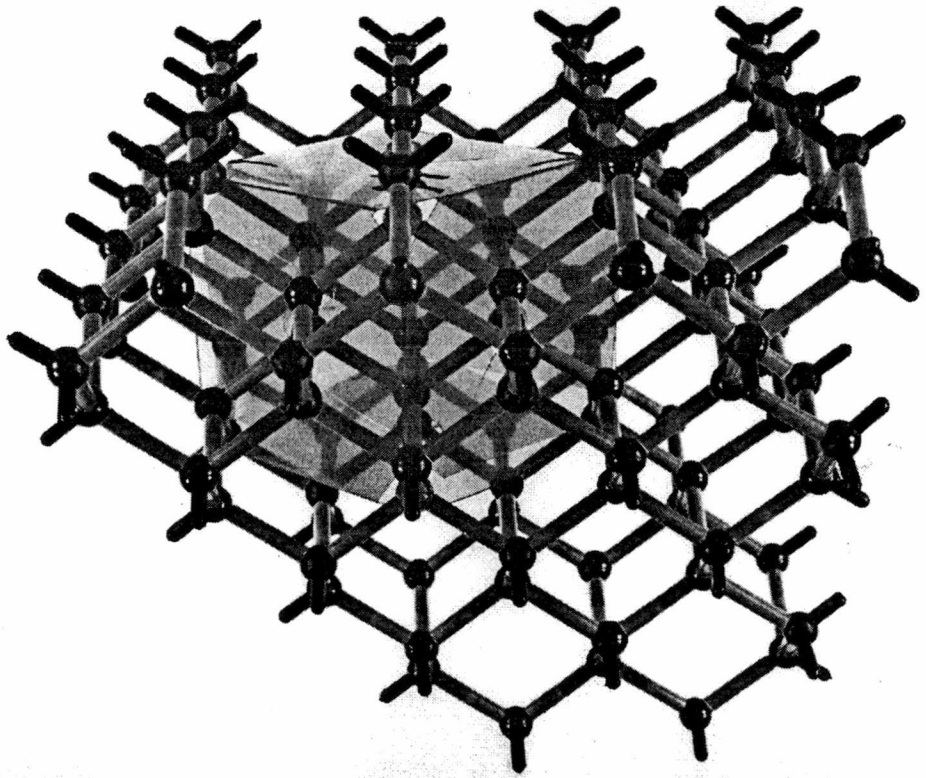

A2. Diamond lattice showing the formation of a twin on a (111) plane.

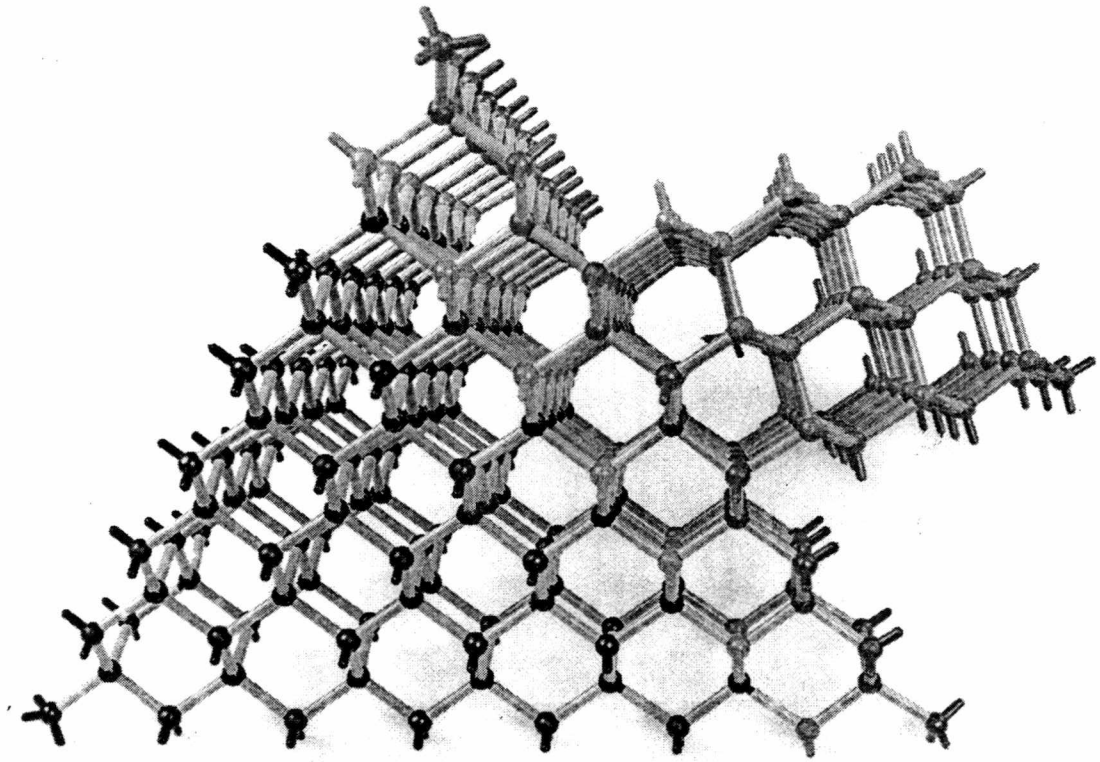

A3. Some characteristics of diamond chemical crystallization from an activated vapor phase.

No	Method of vapour phase activation	Accepted name of method (abbreviation)	Vapour crystallization medium characteristics: Pressure (Torr)	Gas flow (sccm)	Original content	Activated gas content	Vapour phase activation level (kW/cm^3)	Temperature of neutrals and/or ions (10^3 K)	Temperature of electrons (10^5 K)	Ionization degree
1	Thermal	Chemical transport reaction (CTR)	12–400	no	Graphite, H_2	C_2H_2, C_2H, ..., H, H_2	1–5	2.1–2.6	–	–
2	Thermal	Hot filament enhanced CVD (HFECVD)	0.5–760	4–160	CH_4, H_2, C_2H_5OH, H_2	CH_3, C_2H, C_2H_2, C_2H_4, C_2H_5, H, OH, H_2	0.2–5	2.1–3.0	–	–
3	By constant electrical field	DC-discharge	2–200	20–1000	CH_4, H_2	C_1, C_2, CH, CH_2, C_2H, C_2H_2, C_3H, H, H_2	0.2–1.5	4.8–5.3	1.0–1.1	10^{-5}–10^{-7}
4	By constant electrical field	DC-plasma jet	20–400	$(0.5–2) \times 10^4$	H_2, Ar, CH_4	C_1, C_2, CH, CH_3, C_2H_2	1–10	4.0–5.0	7.05–10	10^{-4}–10^{-6}
5	RF-discharge (4–27 MHz)	RF-enhanced CVD (RFE-CVD)	80–760	10^2–10^3	H_2, Ar, CH_4	CH_3, H, ..., H_2	10^2–10^3	4.0–6.0	4.0–6.0	10^{-6}–10^{-5}
6	MW-discharge (2.45 GHz)	Microwave plasma enhanced CVD (MPECVD)	10–50	50–100	CH_4, H_2; CO, H_2O, CH_3OH, H_2	CH_3, CH_2, ..., H, H_2; CH_3, C_2, ..., H, OH, H_2	0.06–0.1	0.8	~10	10^{-5}–10^{-4}
7	Open MW-discharge	Microwave plasma jet	760	$(2.6–5.2) \times 10^4$	CH_4, Ar, H_2	C_1, CH, CH_2, CH_3, H, H_2	0.4–1.0	–	–	–
8	MW-ECR 2.45 GHz	ECR-PACVD	10^{-2}–10^{-1}	1–10	H_2, CO, CH_4, O_2	H, CH_3, OH, H_2	10^{-2}–10^{-1}	0.6–0.9	1–5	10^{-3}–10^{-1}
9	Chemical	Acetylene torch	760	2850–3800	C_2H_2, O_2	C_2, C_2H, ..., H, OH, H_2	10–20	2.8–3.3	–	–
10	Photochemical	Laser enhanced CVD (LECVD)	8–75	–	CO, H_2	C_1, ..., H, OH H_2	–	–	–	–

No	Substrate nature	Substrate area (cm^2)	Crystallization temperature range (K)	Substrate charge	Direct current through substrate ($A\ cm^{-2}$)	Maximal growth rate (μm/h)		Maximal reported thickness (μm)		Refs.
						EDF[a]	PDF[b]	EDF[a]	PDF[b]	
1	Natural diamond	0.5	900–1400	minus	–	3	15	> 5	100	[49, 50]
2	Cu, Au, Si, Mo, W Si, Mo, SiO_2, Al_2O_3, diamond	1–100	1000–1300	minus	–	0.3	15	10	100	[51–54]
3	Mo, W, Re, Si, Al_2O_3	1–4	1000–1300	plus	1–10	5	50	–	10^3	[55–58]
4	Mo, W, Ta, Cu, Si	1	900–1300	plus	–	10	930	–	3×10^3	[59–60]
5	Mo, Ta, W, Si	1–10	800–1100	minus	–	100	1000	–	100	[61, 62]
6	Mo, Ti, Al, Cu, Si, ...	10–30	900–1300	minus or plus	–	4	100	250–1300	> 2000	[63–65]
7	Si	10	1000–1600	minus			30	–	–	[66]
8	Mo, Cu, diamond, Si	1–10	700–1200	plus		1	6–7		–	[67]
9	Mo, Cu, Si	0.5	900–1500	minus	–	150	200	200	1000	[68–69]
10	Si	2	400–1100	minus			0.1–1	–	5–10	[70]

[a] EDF: epitaxial diamond film
[b] PDF: polycrystalline diamond film.

[Source : B. V. Spitsyn, in Handbook of Crystal Growth, edited by D. T. J. Hurle, Vol. 3 (1994)]

A4. RGA data for the addition of Ammonia to 1.5% methane in hydrogen gas mixture using TaC filament at ~2400°C and substrate temperature ~915 °C.

DF #	Fil. temp. (°C)	NH_3 (%)	2 AMU	13 AMU	14 AMU	15 AMU	16 AMU	17 AMU	18 AMU
300	2410	0	5.2E-06	4E-09	9E-09	8.4E-08	1E-07	2E-09	5E-09
300		0	4.5E-06	5E-09	8E-09	1.2E-07	1.4E-07	2E-09	4E-09
301	2400	0.006	5.1E-06	5E-09	9E-09	8.1E-08	1E-07	2E-09	3E-09
301		0.006	4.7E-06	5E-09	9E-09	1.3E-07	1.4E-07	3E-09	4E-09
302	2400	0.009	4.9E-06	4E-09	9E-09	7.6E-08	9.2E-08	2E-09	3E-09
302		0.009	4.6E-06	5E-09	7E-09	1.2E-07	1.4E-07	3E-09	3E-09
305	2430	0.083	4E-06	4E-09	6E-09	5.6E-08	7.2E-08	3E-09	4E-09
305		0.083	4.10E-06	4.00E-09	1E-08	1.3E-07	1.30E-07	4E-09	3E-09
304	2400	1.12	6.20E-06	4.00E-09	1.3E-08	9.1E-08	1E-07	3E-09	3.9E-08
304		1.12	5.3E-06	6E-09	9E-09	1.4E-07	2E-07	3E-09	4E-09
303	2400	1.45	5.5E-06	5E-09	9E-09	7.6E-08	9.5E-08	3E-09	4E-09
303		1.45	5.1E-06	6E-09	1.4E-08	1.4E-07	1.5E-07	2E-08	4E-09

DF #	Fil. temp. (°C)	NH_3 (%)	2 AMU	24 AMU	25 AMU	26 AMU	27 AMU	28 AMU
300	2410	0	5.2E-06	2E-09	7E-09	3.6E-08	2E-09	4E-09
300		0	4.5E-06	0	0	0	0	1E-09
301	2400	0.006	5.1E-06	2E-09	7E-09	3.6E-08	2E-09	5E-09
301		0.006	4.7E-06	0	0	0	0	2E-09
302	2400	0.009	4.9E-06	2E-09	7E-09	3.4E-08	6E-09	5E-09
302		0.009	4.6E-06	0	0	0	0	2E-09
305	2430	0.083	4E-06	1E-09	5E-09	2.7E-08	4E-09	4E-09
305		0.083	4.10E-06	0	0	0	0	2.00E-09
304	2400	1.12	6.20E-06	2E-09	5E-09	3.2E-08	3.2E-08	1.7E-08
304		1.12	5.3E-06	0	0	0	0	2E-09
303	2400	1.45	5.5E-06	2E-09	5E-09	3.2E-08	4.6E-08	1.9E-08
303		1.45	5.1E-06	0	0	0	0	2E-09

Rearranged in increasing order of ammonia content in the gas mixture :

NH_3 (%)	13/2	14/2	15/2	16/2	17/2	18/2
0	0.0008	0.00173	0.01615	0.01962	0.00038	0.00096
0.006	0.001	0.00176	0.01588	0.01961	0.00039	0.00059
0.009	0.0008	0.00184	0.01551	0.01878	0.00041	0.00061
0.083	0.001	0.0015	0.014	0.018	0.00075	0.001
1.12	0.0006	0.0021	0.01468	0.01613	0.00048	0.00629
1.45	0.0009	0.00164	0.01382	0.01727	0.00055	0.00073

NH_3 (%)	24/2	25/2	26/2	27/2	28/2
0	4E-04	0.00135	0.00692	0.000385	0.00077
0.006	4E-04	0.00137	0.00706	0.000392	0.00098
0.009	4E-04	0.00143	0.00694	0.001224	0.00102
0.083	3E-04	0.00125	0.00675	0.001	0.001
1.12	3E-04	0.00081	0.00516	0.005161	0.00274
1.45	4E-04	0.00091	0.00582	0.008364	0.00345

A5. RGA data for 0.5, 1.0 and 1.5 % methane concentration with the addition of NH_3 at diffrent substarte temperatures using TaC filament at 2400 °C. (* addition of N_2)

DF(0.5%)	Fil. (°C)	temp. subs. (°C)	temp. NH_3 (%)	2(AMU)	13(AMU)	14(AMU)
327	2400	840	0	4.6E-06	1E-09	3E-09
328	2400	840	0.08	5.2E-06	2E-09	4E-09
333	2400	840	0.04*	5.7E-06	3E-09	5E-09
314	2400	980	0	5.2E-06	2E-09	3E-09
313	2400	980	0.08	4.8E-06	1E-09	3E-09
321	2400	1100	0	5.1E-06	2E-09	3E-09
322	2400	1100	0.08	5.5E-06	2E-09	3E-09
323	2400	1100	0.04*	4.8E-06	1E-09	3E-09

DF(1.0%)	Fil. (°C)	temp. subs. (°C)	temp. NH_3 (%)	2(AMU)	13(AMU)	14(AMU)
329	2400	840	0	5.4E-06	4E-09	7E-09
330	2400	840	0.17	5.5E-06	4E-09	6E-09
331	2400	840	0.34*	4.9E-06	4E-09	5E-09

DF(1.5%)	Fil. (°C)	temp. subs. (°C)	temp. NH_3 (%)	2(AMU)	13(AMU)	14(AMU)
325	2400	840	0	5.3E-06	5E-09	9E-09
326	2400	840	0.26	5.7E-06	6E-09	0.00000001
332	2400	840	0.52*	5.1E-06	6E-09	0.00000001
317	2400	980	0	5.2E-06	4E-09	8E-09
318	2400	980	0.26	4.9E-06	5E-09	8E-09
320	2400	1090	0	5.2E-06	5E-09	8E-09
319	2400	1090	0.26	5.4E-06	5E-09	8E-09

DF(0.5%)	Fil. (°C)	temp. subs. (°C)	temp. NH_3 (%)	15(AMU)	16(AMU)	17(AMU)	18(AMU)
327	2400	840	0	2.6E-08	3.1E-08	1.00E-09	2E-09
328	2400	840	0.08	3E-08	3.7E-08	1E-09	2E-09
333	2400	840	0.04*	4.5E-08	5.6E-08	1E-09	2E-09
314	2400	980	0	3.1E-08	0.00000004	3E-09	3E-09
313	2400	980	0.08	2.6E-08	3.5E-08	2E-09	3E-09
321	2400	1100	0	2.9E-08	3.6E-08	2E-09	3E-09
322	2400	1100	0.08	3E-08	3.6E-08	2E-09	3E-09
323	2400	1100	0.04*	2.6E-08	3.4E-08	2E-09	2E-09

DF(1.0%)	Fil. (°C)	temp. subs. (°C)	temp. NH_3 (%)	15(AMU)	16(AMU)	17(AMU)	18(AMU)
329	2400	840	0	6.1E-08	7.6E-08	2E-09	2E-09
330	2400	840	0.17	6E-08	7.5E-08	2E-09	2E-09
331	2400	840	0.34*	5.4E-08	6.6E-08	1E-09	2E-09

DF(1.5%)	Fil. (°C)	temp. subs. (°C)	temp. NH_3 (%)	15(AMU)	16(AMU)	17(AMU)	18(AMU)
325	2400	840	0	8.6E-08	1.04E-07	1.04E-07	4E-09
326	2400	840	0.26	9.9E-08	1.21E-07	1.21E-07	2E-09
332	2400	840	0.52*	8.6E-08	1.05E-07	1.05E-07	2E-09
317	2400	980	0	7.5E-08	9.1E-08	9.1E-08	3E-09
318	2400	980	0.26	7.3E-08	8.9E-08	8.9E-08	3E-09
320	2400	1090	0	7.3E-08	9.3E-08	9.3E-08	3E-09
319	2400	1090	0.26	7.3E-08	9.1E-08	9.1E-08	5E-09

DF(0.5%)	Fil. (°C)	temp. subs. (°C)	temp. NH_3 (%)	25(AMU)	26(AMU)	27(AMU)	28(AMU)
327	2400	840	0	1E-09	6E-09	1E-09	2E-09
328	2400	840	0.08	2E-09	0.00000001	4E-09	5E-09
333	2400	840	0.04*	4E-09	2.1E-08	2E-09	9E-09
314	2400	980	0	2E-09	7E-09	1E-09	3E-09
313	2400	980	0.08	2E-09	0.00000001	4E-09	3E-09
321	2400	1100	0	3E-09	1.5E-08	1E-09	5E-09
322	2400	1100	0.08	3E-09	1.4E-08	4E-09	7E-09
323	2400	1100	0.04*	2E-09	9E-09	2E-09	4E-09

DF(1.0%)	Fil. (°C)	temp. subs. (°C)	temp. NH_3 (%)	25(AMU)	26(AMU)	27(AMU)	28(AMU)
329	2400	840	0	4E-09	1.9E-08	1E-09	5E-09
330	2400	840	0.17	4E-09	2.4E-08	8E-09	6E-09
331	2400	840	0.34*	3E-09	0.00000002	3E-09	9E-09

DF(1.5%)	Fil. (°C)	temp. subs. (°C)	temp. NH_3 (%)	25(AMU)	26(AMU)	27(AMU)	28(AMU)
325	2400	840	0	8E-09	4.3E-08	2E-09	4E-09
326	2400	840	0.26	9E-09	4.8E-08	1.00E-08	2.2E-08
332	2400	840	0.52*	6E-09	3.2E-08	4E-09	1.5E-08
317	2400	980	0	5E-09	2.7E-08	2E-09	6E-09
318	2400	980	0.26	6E-09	2.2E-08	8E-09	8E-09
320	2400	1090	0	9E-09	4.3E-08	3E-09	7E-09
319	2400	1090	0.26	6E-09	3.4E-08	1.2E-08	7E-09